Karlsruher Institut für Technologie

Institute for Nuclear Waste Disposal

Inhibition of ferritic steel corrosion in the presence and absence of ionizing radiation

Zur Erlangung des akademischen Grades eines

DOKTORS DER NATURWISSENSCHAFTEN

(Dr. rer. nat.)

von der KIT-Fakultät für Chemie und Biowissenschaften des Karlsruher Instituts für Technologie (KIT)

genehmigte

DISSERTATION

von

M.Eng Justice Enyioma Nwade

aus

Aba, Nigeria

Referent: Prof. Dr. Horst Geckeis

Korreferent: Priv.-Doz. Dr. Frank Heberling

Tag der mündlichen Prüfung: 27.10.2025

Erklärung – Statement of Originality

Hiermit versichere ich, dass ich die vorliegende Arbeit selbstständig verfasst und keine anderen Quellen oder Hilfsmittel verwendet zu haben als die hier angegebenen. Außerdem versichere ich, dass alle Stellen der Arbeit, die aus anderen Quellen wörtlich oder sinngemäß übernommen wurden, als solche kenntlich gemacht worden sind und die schriftliche Version der Arbeit mit der digitalen übereinstimmt. Die Arbeit wurde in gleicher oder ähnlicher Form noch bei keiner anderen Prüfungsbehörde vorgelegt. Die Satzung des Karlsruher Instituts für Technologie zur Sicherung guter wissenschaftlicher Praxis wurde in der jeweils gültigen Fassung beachtet.

I hereby certify that I have written this thesis independently and have not used any sources or aids other than those specified here. I also confirm that all passages in the thesis that have been taken verbatim or in spirit from other sources have been identified as such and that the written version of the thesis corresponds to the digital version. The thesis has not been submitted in the same or a similar form to any other examination authority. The statutes of the Karlsruhe Institute of Technology for safeguarding good scientific practice have been observed in the currently valid version.

Eggenstein-Leopoldshafen

Ort und Datum / Place and Date Unterschrift / Signature

Acknowledgement

"It takes a village to… raise a PhD", and for this training I owe a world of thanks to all of you who made it possible.

First, I would like to express my profound gratitude to Prof. Dr. Horst Geckeis, director of the KIT-INE, for the opportunity to work under his supervision for this PhD research. It has been a privilege to gain invaluable scientific expertise and contribute to high-level scientific research, working in the field of nuclear waste management at the KIT-INE.

I would also like to express my sincere appreciation to Dr. Volker Metz, head of my division, whose constant encouragement, challenge, unwavering belief in and steadfast support throughout this work, kept me motivated to give my best throughout the duration of this research.

A special word of gratitude goes to the project coordinator of this work at KIT-INE, Dr. Frank Becker. Thank you for the invaluable assistance, positive attitude and the academic oversight you provided, from before my doctoral study even started till the end. Your cheerful and kind demeanor made all the difference.

I am very grateful to Dr. Dieter Schild for the SEM-EDX and XPS measurements, for all the fruitful discussions, direction and in fact being a 'co-supervisor' throughout this work. In addition, my heartfelt gratitude goes to other members of the KIT-INE Analytics Department: Dr. Oliver Dieste-Blanco, Dr. Natalie Müller and Ms. Eva Soballa for their assistance with steel samples preparation and FIB-SEM measurements and analysis; Stefanie Kraft for ICP-OES; and to Tanja Kisely for support with essential laboratory materials.

I am grateful to Dr. Markus Plaschke, for his invaluable guidance and critical review of this work.

Dr. Thomas Sittel made significant contributions to the success of this research, particularly through assistance with NMR and MS measurements and analyses.

I extend my gratitude to Dr. Michel Herm, Dr. Tobias König, Ms. Elke Bohnert and Mr. Arndt Walschburger, for their invaluable contributions to the methodology and successful execution of the irradiation experiments.

I am profoundly grateful to Dr. Johannes Lützenkirchen, Dr. Bahram HosseiniMonjezi and Dr. Meike König (KIT-IFG) for providing guidance and support with the QCM and ellipsometry measurements.

I am grateful to Dr. Xavier Gaona for availing his BioLogic potentiostat and to Dr. Nicolas Finck for the Gamry potentiostat that enabled the electrochemical measurements. Also, the support provided by Dr. Pelin Çakir-Wuttke during the early stages of this research was invaluable.

I would like to thank the entire e-SPARK summer school team at the Institute of Physical Chemistry of the Polish Academy of Sciences (IChF) Warsaw, Dr. Damien Feron (CEA, France), Prof. Gerald Frankel (Ohio State University/CorroZoom Series), and the entire European Federation of Corrosion (EFC WP4 – Nuclear Corrosion) for significantly shaping my understanding of electrochemistry and nuclear corrosion science.

I would like to thank the entire NaMaSK Project team and our industry collaborators for the success of this project.

I am very grateful to the INE Workshop group for their meticulous fabrication of my steel samples, and to the Radioprotection group at INE for helping me with samples transfers in and out of the controlled area and their usual collegiality.

I would also like to thank all the colleagues with whom I shared office space, for fostering a congenial atmosphere conducive for research; Dr. Tobias König, Dr. Rosa Guidone, Dr. Peter Szabo, Dr. Giana Baruth, Ms. Sema Ozyagan, Mr. Niels Huber, Mr. Jonas Stracke, Mr. Paul Fürst, and indeed, the entire INE staff and student body.

Finally, I am grateful to my lovely wife, Tochi, and daughters - Deborah and Adara for the endless love, support and understanding.

This doctoral thesis was funded by the German Ministry of Education and Research (BMBF) through the FORKA („Forschung für den Rückbau kerntechnischer Anlagen“) collaborative project NaMaSK, grant agreement number 15S9423B

In memory of my father, Sir D.I. Nwade (1948 – 2022)

“For which cause we faint not; but though our outward man perish, yet the inward man is renewed day by day. For our light affliction, which is but for a moment, worketh for us a far more exceeding and eternal weight of glory”

2 Cor 4:16-17 KJV

Abstract

This doctoral thesis investigates the ferritic steel corrosion during and after Water Abrasive Suspension (WAS) cutting, a method utilized in the dismantling of activated components, specifically Reactor Pressure Vessels (RPVs) and Internals (RPVs), during nuclear decommissioning. One of the drawbacks of this technique is the generation of significant amounts of secondary radioactive waste, which impacts process economics and poses a challenge for radioactive waste disposal of materials which accrue in the process of decommissioning of nuclear facilities. Efficient separation of radioactive steel particles from abrasive particles post-cutting is an essential step for minimizing secondary waste volume and enhancing economic viability. A combined wet sieving and magnetic separation process has been developed for this purpose. However, the corrosive aqueous environment of the WAS, compounded by the presence of ionizing radiation from activated steel, poses a significant threat to the magnetic properties and structural integrity of the steel swarf (used interchangeably with 'steel particles' throughout this work), impeding effective magnetic separation.

The overarching aim of this research was to identify and characterize suitable corrosion inhibitors for a RPV ferritic steel (steel type 20MnMoNi5-5, denoted as 1.6310 according to DIN EN 10027-1) under conditions relevant to WAS cutting and subsequent separation, and to quantify and understand the effects of ionizing radiation on inhibitor performance and steel corrosion.

A multi-faceted experimental approach was employed, combining electrochemical methods (OCP, potentiodynamic polarization, EIS), surface analytical techniques (SEM-EDX, XPS, QCM, Ellipsometry), inhibitor characterization (Chromatography, NMR, Mass Spectrometry), and irradiation experiments utilizing radioactive sources. In addition to the experimental studies, Monte Carlo radiation transport simulations were performed.

Initial screening identified a commercial inhibitor formulation, denoted as C.Inh #4 in this Ph.D. thesis, as highly effective in preventing visible corrosion during immersion tests. Detailed electrochemical studies confirmed its effectiveness as a mixed-type inhibitor that significantly reduced corrosion rates and promoted the formation of a protective surface film. Post-WAS cutting experiments demonstrated that C.Inh #4 successfully mitigated corrosion of steel particles in the actual cutting suspension over extended periods, as demonstrated by SEM-EDX analysis showing the absence of significant corrosion products.

Compositional analysis of C.Inh #4 performed using complementary techniques as well as confirmation from the manufacturer identified Triethanolamine (TEA), of 2,4,6-tri(6-aminohexanoic acid)-1,3,5-triazine (TACT) and 6-(4-Methylphenylsulfonamido) hexanoic acid as the major components of the formulation. Comparative studies of pure TEA and TACT revealed that TACT provided similar corrosion inhibition at significantly 10 times lower concentrations than TEA, which required > 3000 ppm concentration to achieve similar inhibition efficiency. In addition, adsorption studies indicated that while TEA primarily adsorbs via physisorption, TACT utilizes a combination of physisorption and stronger chemisorption, leading to a more stable and durable protective layer, which was supported by QCM and Ellipsometry measurements. Further investigations into the third component, 6-(4-Methylphenylsulfonamido) hexanoic acid, was discontinued due to the presence of sulphur, contrary to the set criteria of using organic compounds having only carbon, hydrogen, oxygen and nitrogen as constituents (CHON principle).

Radiation transport simulations revealed that an annual absorbed dose of about 5 Gy to water is expected from a reference case of 1 m^3 radioactive steel-abrasive mixture in water. Irradiation experiments utilized higher dose values up to 2.5 kGy to obtain discernible radiolysis effects in the inhibitor solutions and to maintain a conservative dose range expected from real scenarios. Investigations into the effects of ionizing radiation demonstrated a dose-dependent decrease in the inhibition efficiency for both TEA and TACT. NMR spectroscopy revealed that both compounds undergo a degree of radiolytic degradation with increasing absorbed dose. Electrochemical and surface analysis of steel exposed to irradiated inhibitor solutions indicated that TEA maintained its protective capabilities slightly more effectively than TACT at higher radiation doses, although some degree of radiation-induced oxidation was observed in both cases. Both inhibitors maintained over 95% inhibition efficiency even after 2.5 kGy irradiation. The presence of bicarbonate ions in irradiated solutions had a positive synergistic effect with ionizing radiation for TEA resulting in a relatively lower corrosion rate, in contrast to TACT.

This research successfully identified a potent inhibitor formulation effective under relevant conditions and provided fundamental insights into the mechanism of corrosion inhibition and influence of ionizing radiation. The findings overall highlight the superior performance and radiation stability of TACT compared to TEA, contributing valuable knowledge for optimizing corrosion inhibition, steel-abrasive separation efficiency in processes like WAS cutting of radioactive steel, and minimizing secondary waste generation in nuclear decommissioning operations.

Zusammenfassung

Diese Doktorarbeit untersucht die Korrosion von ferritischem Stahl während und nach dem Wasser-Abrasiv-Suspensions-Schneiden (WAS-Schneiden), einer Methode, die beim Rückbau aktivierter Komponenten, insbesondere eines Reaktordruckbehälters (Reactor Pressure Vessel, RPV) und dessen Einbauten, eingesetzt wird. Ein Nachteil dieser Technik ist die Erzeugung erheblicher Mengen an radioaktivem Sekundärabfall, was die Prozessökonomie beeinträchtigt und eine Herausforderung für die Entsorgung radioaktiver Abfälle darstellt, die beim Rückbau kerntechnischer Anlagen anfallen. Eine effiziente Trennung radioaktiver Stahlpartikel von Abrasivpartikeln nach dem Schneiden ist ein wesentlicher Schritt zur Minimierung des Sekundärabfallvolumens und zur Steigerung der Wirtschaftlichkeit des Verfahrens. Zu diesem Zweck wurde ein kombiniertes Nasssieb- und Magnetabscheideverfahren für das WAS-Schneiden entwickelt. Das korrosive wässrige Medium der WAS, verstärkt durch die Anwesenheit ionisierender Strahlung aus aktiviertem Stahl, stellt jedoch eine erhebliche Bedrohung für die magnetischen Eigenschaften und die strukturelle Integrität des Stahl-Swarf (im gesamten Text synonym mit „Stahlpartikeln“ verwendet) dar, was eine effektive magnetische Trennung behindert.

Das übergeordnete Ziel dieser Forschung war es, geeignete Korrosionsinhibitoren für das WAS-Schneiden eines ferritischen RPV-Stahls (Stahltyp 20MnMoNi5-5, bzw. 1.6310 gemäß DIN EN 10027-1) und die anschließende Trennung zu identifizieren und zu charakterisieren, sowie die Auswirkungen ionisierender Strahlung auf die Inhibitoren und die Stahlkorrosion zu quantifizieren und zu verstehen.

Es wurde ein vielseitiger experimenteller Ansatz gewählt, der elektrochemische Methoden (OCP, potentiodynamische Polarisation, EIS), oberflächenanalytische Techniken (SEM-EDX, XPS, QCM, Ellipsometrie), die Charakterisierung von Inhibitoren (Chromatographie, NMR, Massenspektrometrie) und Bestrahlungsexperimente unter Verwendung radioaktiver Quellen kombinierte. Zusätzlich zu den experimentellen Studien wurden Monte-Carlo-Simulationen zum Strahlungstransport durchgeführt.

Ein anfängliches Screening identifizierte eine kommerzielle Inhibitorrezeptur, in dieser Doktorarbeit als C.Inh #4 bezeichnet, als hochwirksam zur Verhinderung sichtbarer Korrosion in Immersionstests. Detaillierte elektrochemische Studien bestätigten ihre Wirksamkeit als Inhibitormischung, die die Korrosionsraten signifikant reduzierte und die Bildung eines

schützenden Oberflächenfilms förderte. Experimente nach dem WAS-Schneiden zeigten, dass C.Inh #4 die Korrosion von Stahlpartikeln in der tatsächlichen Schneidsuspension über längere Zeiträume erfolgreich minderte, was durch SEM-EDX-Analysen, die das Fehlen signifikanter Korrosionsprodukte zeigten, bestätigt wurde.

Die Zusammensetzungsanalyse von C.Inh #4, die mittels komplementärer Analysetechniken ermittelt und letzlich vom Hersteller bestätigt wurde, identifizierte Triethanolamin (TEA), 2,4,6-Tri(6-aminohexansäure)-1,3,5-triazin (TACT) und 6-(4-Methylphenylsulfonamido)hexansäure als Hauptbestandteile der Rezeptur. Vergleichende Studien von reinem TEA und TACT ergaben, dass TACT eine ähnliche Korrosionshemmung bei einer um das Zehnfache geringeren Konzentrationen als TEA bot, wobei TEA Konzentrationen von > 3000 ppm benötigt wurden, um eine ähnliche Inhibierungswirkung zu erreichen. Darüber hinaus zeigten Adsorptionsstudien, dass TEA primär durch Physisorption adsorbiert, während TACT eine Kombination aus Physisorption und stärkerer Chemisorption nutzt, was zu einer stabileren und dauerhafteren Schutzschicht führt, welches durch QCM- und Ellipsometrie-Messungen bestätigt wurde. Weitere Untersuchungen der dritten Komponente, 6-(4-Methylphenylsulfonamido)hexansäure, wurden aufgrund des Vorhandenseins von Schwefel eingestellt, denn dies widersprach den festgelegten Kriterien der Verwendung von organischen Verbindungen, die nur Kohlenstoff, Wasserstoff, Sauerstoff und Stickstoff als Bestandteile aufweisen sollen (CHON-Prinzip).

Strahlungstransportsimulationen ergaben, dass eine jährliche absorbierte Dosis von etwa 5 Gy in Wasser für einen Referenzfall einer radioaktiven Stahl-Abrasiv-Mischung in 1 m3 Wasser zu erwarten ist. In den Bestrahlungsexperimente wurden höhere Dosiswerte bis zu 2,5 kGy verwendet, um mögliche Radiolyseeffekte in den Inhibitorlösungen deutlich zu erkennen und einen konservativen Dosisbereich aufrechtzuerhalten, der in realen Szenarien zu erwarten ist. Untersuchungen der Auswirkungen ionisierender Strahlung zeigten eine dosisabhängige Abnahme der Inhibierungseffizienz für sowohl TEA als auch TACT. Ergebnisse der NMR-Spektroskopie ergaben, dass beide Verbindungen mit zunehmender absorbierter Dosis einen gewissen Grad an radiolytischem Abbau erfahren. Elektrochemische und Oberflächenanalysen von Stahl, der bestrahlten Inhibitorlösungen ausgesetzt war, zeigten, dass TEA seine schützenden Eigenschaften bei höheren Strahlungsdosen etwas effektiver beibehielt als TACT, obwohl in beiden Fällen ein gewisser strahlungsinduzierter Oxidationsgrad beobachtet wurde. Beide Inhibitoren behielten selbst nach 2,5 kGy Bestrahlung eine Inhibierungseffizienz von über 95% bei. Die Anwesenheit von Bicarbonationen in bestrahlten Lösungen bewirkte einen synergistischen Effekt für TEA im Gegensatz zu TACT.

Diese Untersuchungen identifizierten erfolgreich eine potente Inhibitor, der unter relevanten Bedingungen für eine Anwendung mit radioaktiven Stählen wirksam ist, und lieferte grundlegende Einblicke in die Mechanismen der Korrosionshemmung und deren Beeinflussung durch ionisierende Strahlung. Die Ergebnisse unterstreichen insgesamt die höhere Leistungsfähigkeit und Strahlenresistenz von TACT im Vergleich zu TEA und liefern wichtige Erkenntnissen zur Optimierung der der Stahl-Abrasiv-Trennung in Prozessen wie WAS schneiden von radioaktive Stählen und zur Minimierung der Sekundärabfallerzeugung bei der Stilllegung von Kernkraftwerken.

Table of Contents

List of Figures

List of Tables

List of Abbreviations

(aq)	Aqueous species
(l)	Liquid
cps	Counts per second
EDX	Energy Dispersive X-ray Spectroscopy
EI-MS	Electron Ionization Mass Spectrometry
EIS	Electrochemical Impedance Spectroscopy
Eqn.	Equation
IAEA	International Atomic Energy Agency
ICP-OES	Inductively Coupled Plasma Optical Emission Spectroscopy
IE	Inhibition Efficiency
INE	Institut für Nukleare Entsorgung / Institute for Nuclear Waste Disposal
KIT	Karlsruhe Institute of Technology
LWR	Light Water Reactor
MOX	Mixed Oxide Fuel
m/z	mass-to-charge ratio
NaMaSK	Nasssiebung und Magnetseparation von Korngemischen zur Minimierung von Sekundärabfällen im Rückbau Kerntechnischer Anlagen/ Wet screening and magnetic separation of grain mixtures to minimize secondary waste in nuclear facility dismantling.
n.d.	Not detected
NPP	Nuclear Power Plant
OCP	Open Circuit Potential
PWR	Pressurized Water Reactor
RN	Radionuclide
QCM	Quartz Crystal Microbalance
RPV	Reactor Pressure Vessel
r.t.	Room temperature
SEM	Scanning Electron Microscopy
TACT	2,4,6-Tri (6-aminohexanoic acid)-1,3,5 triazine
TEA	Triethanolamine
WAS	Water Abrasive Suspension
XPS	X-ray photoelectron spectroscopy

List of Parameters

Parameter	Quantity Name	Unit(s)	Notes
A	(1) Source Activity	Bq	Used for total activity of radioactive sources (e.g., Co-60, SAM).
	(2) Exposed Surface Area	cm^2	Used in electrochemical corrosion rate calculations (Eq. 2.5).
	(3) Arrhenius Pre-exponential Factor	depends on CR unit	Used in Arrhenius equation (Eq. 3.5).
ΔA	Change in Absorbance	(dimensionless)	Used in Fricke dosimetry.
C	Inhibitor Concentration	ppm, vol.%, mol/dm^3	Used for inhibitor concentration in solution.
CR	Corrosion Rate	mm/yr	Quantifies the rate of metal loss due to corrosion.
C_{dl}	Double Layer Capacitance	µF	Represents the capacitance of the electrical double layer.
C_{H2O}	Molar Concentration of Liquid Water	mol/dm^3	Used in Langmuir isotherm calculation (Eq. 1.17).
D	(1) Absorbed Dose	Gy, kGy, mGy	Quantifies the energy absorbed per unit mass.
	(2) Density (in CR calculation)	g/cm^3	Density of the metal in corrosion rate formula.
ΔD	Energy Dissipation Change	(dimensionless)	In QCM, related to viscoelastic properties of adsorbed layer.
D_F	Absorbed Dose to Fricke Solution	Gy	Specifically absorbed dose measured by Fricke dosimetry.
D_W	Absorbed Dose to Water	Gy	Absorbed dose converted to water equivalent.
DSMAX	Maximum Step Length	(cm)	PENELOPE simulation parameter.
E	(1) Equilibrium Cell Potential	V	In thermodynamic equations (Eq. 1.12, 1.15).
	(2) Electrode Potential (general)	V	General term for potential difference.
E_{corr}	Corrosion Potential	V, mV	The stable potential at which net current is zero (OCP value).

E_{OCP}	Open Circuit Potential	V, mV	Synonym for corrosion potential, specifically from OCP measurement.
E_p	Passivation Potential	V	Potential at which passivation begins.
E_b	Film Breakdown Potential	V	Potential at which protective film breaks down.
E_a	Activation Energy	kJ/mol	From Arrhenius plot (Eq. 3.5).
EW	Equivalent Weight of Corroding Metal	(dimensionless, based on atomic weight)	Used in corrosion rate calculations.
F	Faraday Constant	C/mol	Used in electrochemical equations.
f	Frequency	Hz, MHz, mHz	Used in EIS and general signal description.
Δf	Frequency Change	Hz	In QCM, related to mass change.
f_0	Resonant Frequency (QCM)	Hz	Fundamental resonant frequency of the quartz crystal.
G	Radiation Chemical Yield	mol/J, molecules/100 eV	Number of molecules formed/consumed per unit absorbed energy.
ΔG	Gibbs Free Energy Change	kJ/mol	Thermodynamic driving force for reactions.
ΔG_{ads}^{θ}	Standard Adsorption Gibbs Free Energy	kJ/mol	Quantifies the spontaneity and strength of adsorption.
h	Film Thickness	nm	Measured thickness of adsorbed layers (QCM, Ellipsometry).
i_{corr}	Corrosion Current	μA	The current at the corrosion potential.
IE%	Inhibition Efficiency	%	Measures the percentage reduction in corrosion rate.
j	Imaginary Unit	(dimensionless)	$j^2 = -1$ in complex impedance notation.
	Overall Current Density	μA/cm², mA/cm²	Net current density flowing at the electrode.
j_a, j_c	Anodic, Cathodic Current Densities	μA/cm²	Partial current densities of anodic and cathodic reactions.

j_o	Exchange Current Density	$\mu A/cm^2$	Rate of forward and reverse reactions at equilibrium.
K	Constant (in CR calculation)	mm/(A·cm·yr)	Unit conversion constant in corrosion rate formula.
K_{eq}	Adsorption Equilibrium Constant	(variable, depends on C unit)	Relates inhibitor concentration to surface coverage at equilibrium.
l	Path Length	mm	In UV-Vis measurements.
n	(1) Number of electrons	(integer)	e^- transfer in electrochemical reactions.
	(2) Harmonics of fundamental frequency	(integer)	In QCM Sauerbrey equation (Eq. 2.8).
pH	pH value	(dimensionless)	Measure of acidity/basicity.
Q	CPE Parameter	$Fs^{(\alpha-1)}cm^{-2}$	CPE parameter (units vary based on α).
R	Molar Gas Constant	J/(molK)	Used in thermodynamic and kinetic equations.
R_p	Polarization Resistance	Ω, kΩ, MΩ	Resistance of electrochemical processes, often ≈ $R_{ct.}$
R_s	Solution Resistance	Ω, kΩ, MΩ	Ohmic resistance of the electrolyte.
R_{ct}	Charge Transfer Resistance	Ω, kΩ, MΩ	Resistance to charge transfer at the interface.
T	Temperature	K, °C	Absolute temperature
$t_{1/2}$	Half-life	s	For radioactive isotopes.
α	(1) Transfer Coefficient	(dimensionless)	In Butler-Volmer equation.
	(2) CPE Exponent	(dimensionless)	In CPE impedance formula.
β_a, β_c	Anodic, Cathodic Tafel Slopes	mV/dec	From potentiodynamic polarization curves.
ε	Molar Extinction Coefficient	m^2/mol	For Fe^{3+} in Fricke dosimetry.
η	Overpotential/Overvoltage	V, mV	Deviation of potential from equilibrium.
η_{CT}	Charge Transfer Overpotential	V, mV	Overpotential due to slow charge transfer.
η_R	Resistive Overpotential	V, mV	Overpotential due to ohmic losses.
η_T	Mass Transport Overpotential	V, mV	Overpotential due to mass transport limitations.

θ	Surface Coverage	(dimensionless)	Fraction of surface covered by adsorbed inhibitor.
μ_q	Shear Modulus of Quartz	$g \cdot cm^{-1}s^{-2}$	For AT-cut crystal in Sauerbrey equation.
ρ	(1) Density (of metal or solution)	g/cm^3	Used for both metal density (CR) and solution density (Fricke).
ρ_q	Density of Quartz	g/cm^3	For quartz crystal in Sauerbrey equation.
ϕ	Phase Angle	deg, °	In Bode plots (EIS).
ω	Angular Frequency	rad/s	In EIS impedance formulas.
δ	(1)Chemical shift (2)Standard deviation	ppm -	In NMR spectroscopy In SEM-EDX analysis
Ψ, Δ	Ellipsometric Parameters	deg, °	Measured in ellipsometry.
$\chi 2$	Chi-squared	(dimensionless)	Goodness of fit for EEC modeling.

CHAPTER ONE: INTRODUCTION

1.1 Motivation of the Study

Nuclear power plants play a vital role in the energy systems of many countries, supplying low-carbon electricity and heat for other industrial applications. Most nuclear reactors have a service life of about 40 years, after which the decommissioning and dismantling phase of the lifecycle commences [1]. The decommissioning of nuclear power plants and other nuclear facilities is a complex process involving the removal of spent nuclear fuel and other radioactive materials, segmentation of the reactor pressure vessel and internals, removal of the secondary systems, demolition of containment structures, and site remediation. Decommissioning represents one of the most significant challenges facing the nuclear industry in the coming decades. As one of the key processes in the decommissioning program, the safe and efficient dismantling of reactor pressure vessels (RPVs) and its internals is crucial. RPV structural materials, primarily low alloy ferritic steels [2–4], become activated due to prolonged exposure to neutron irradiation [5,6], necessitating remote handling for dismantling and packaging during decommissioning.

As of early 2024, 213 nuclear power reactors worldwide had been officially shutdown for decommissioning, yet full dismantling and decommissioning had been completed for only 22 of them [7]. This represents a global challenge requiring innovative, sustainable, and cost-effective methodologies for RPV segmentation – the process of cutting the RPV into smaller pieces for efficient removal and storage. Various techniques are employed in the industry to segment reactor pressure vessels and internals, including abrasive waterjet cutting, plasma arc, mechanical cutting, electrical discharge machining, and metal disintegration machining [8,9]. The use of plasma saw, and laser cutting methods has been proposed recently but has not been used to date [10]. Wire sawing and abrasive waterjet cutting are widely used methods in segmentation projects [11–13]. However, abrasive waterjet cutting and other underwater cutting techniques are particularly well-suited for this application due to the additional radiation shielding effect in compliance with the ALARA (As low As Reasonably Achievable) principle [14]. Also, cold-cutting methods prevent aerosol formation, offering advantages such as reduced personnel exposure and minimal secondary waste generation [15].

The abrasive waterjet cutting method (Water-Abrasive-Suspension (WAS) cutting process) utilizes a high-pressure water jet mixed with suspended abrasive particles to cut through thick

metal structures, including reactor internals and high-strength steel components of RPVs [16], as shown in Figure 1.1. It has thus emerged as a highly effective method for RPV internals segmentation due to its precision, versatility, cost and the ability to minimize radiological exposure [17,18]. Despite its technical advantages, the considerable generation of radioactive secondary waste - the mixture of steel swarf (steel particles) and abrasive particles, hampers its economic competitiveness compared to conventional cutting methods [9,10,13]. WAS cutting has been employed in Germany for the dismantling of the Stade and Würgassen nuclear power plants (NPP) RPV internals [19,20]. Strategies for reducing the attendant radioactive secondary waste after dismantling remain a crucial open question for sustainability and enhanced economic efficiency [21,22]. Hence, separating the radioactive steel swarf and reusing the abrasive grains would represent a further possible improvement to the WAS cutting process.

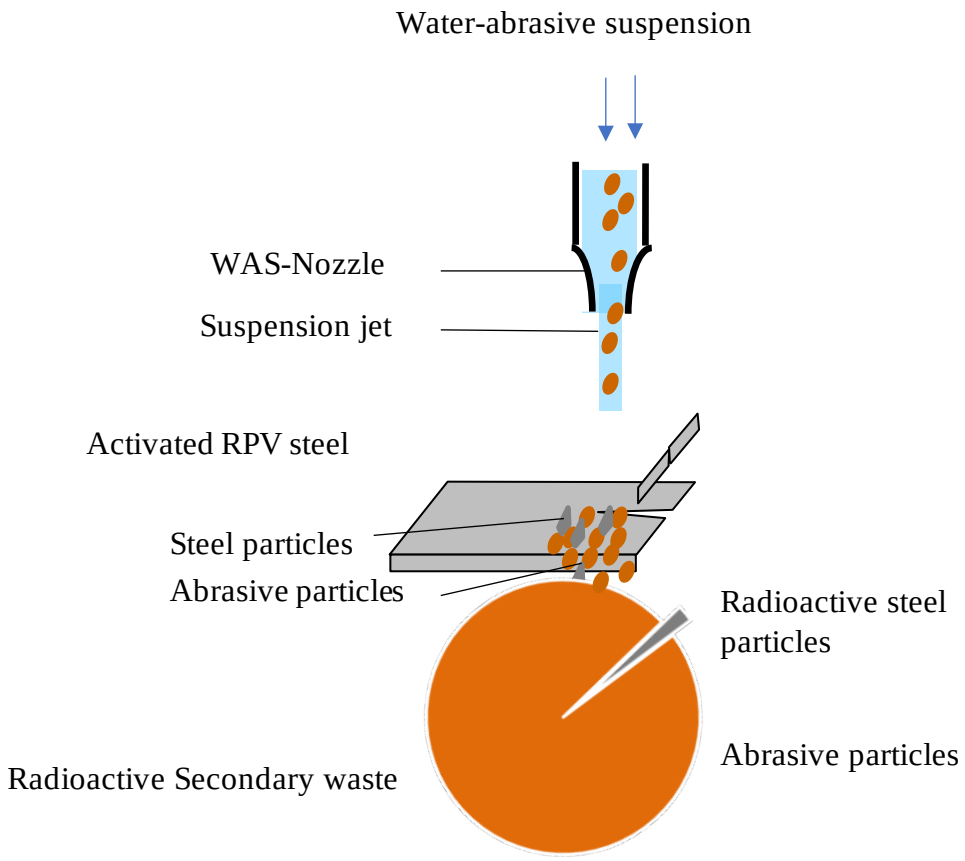

Figure 1.1: Schematic of water-abrasive suspension jet cutting of RPV steel, which produces radioactive secondary waste (abrasive particles and activated steel particles). For details, see references [3, 16].

Efforts have been made to recycle the abrasives used in the WAS cutting of conventional materials [23,24]. However, the NENAWAS project (Neuartige Entsorgungswege für

Abrasivmittel aus der Wasserstrahl-Schneidtechnikan. In English, novel disposal routes for abrasives from waterjet cutting technology) [25], MaSK project (Magnet-Separation von Korngemischen zur Minimierung von Sekundärabfällen im Rückbau kerntechnischer Anlagen. In English, magnetic separation of granular mixtures for minimizing secondary waste in the decommissioning of nuclear facilities) [26] and the present work in the NaMaSK project (***Na***sssiebung und ***Ma***gnet***s***eparation von ***K***orngemischen zur Minimierung von Sekundärabfällen im Rückbau Kerntechnischer Anlagen. *In English, wet screening and magnetic separation of grain mixtures to minimize secondary waste in the dismantling of nuclear facilities*) [27] have been research efforts to address the challenge of minimising the volume of secondary waste generated in the WAS cutting process applied to nuclear systems and structures. The overarching motivations for these projects are the recycling of abrasives and the reduction of the volume of radioactive waste which would limit the cost of radioactive waste disposal and the improved economics of the WAS cutting process.

The NENAWAS and MaSK projects, funded by the German Ministry of Education and Research (BMBF) and developed jointly by the Institute for Nuclear Waste Disposal (KIT-INE) and the Institute for Technology and Management in Construction (KIT-TMB), developed a separation process for the post-treatment of grain mixtures generated during the cutting of reactor pressure vessel steels [25,26,28]. Figure 1.2 shows the separation scheme, which entails that fine steel and abrasive particles are removed using the sieves, the larger steel particles further separated using the magnetic filter and disposed, while the larger abrasive particles are reused. Detailed separation experiments were initially carried out with the development of a prototype separation system (Patent No: DE102018110204A120191031), and thereafter, process parameters such as concentration of the grain mixture, time of a filter cycle and flowrate were systematically examined.

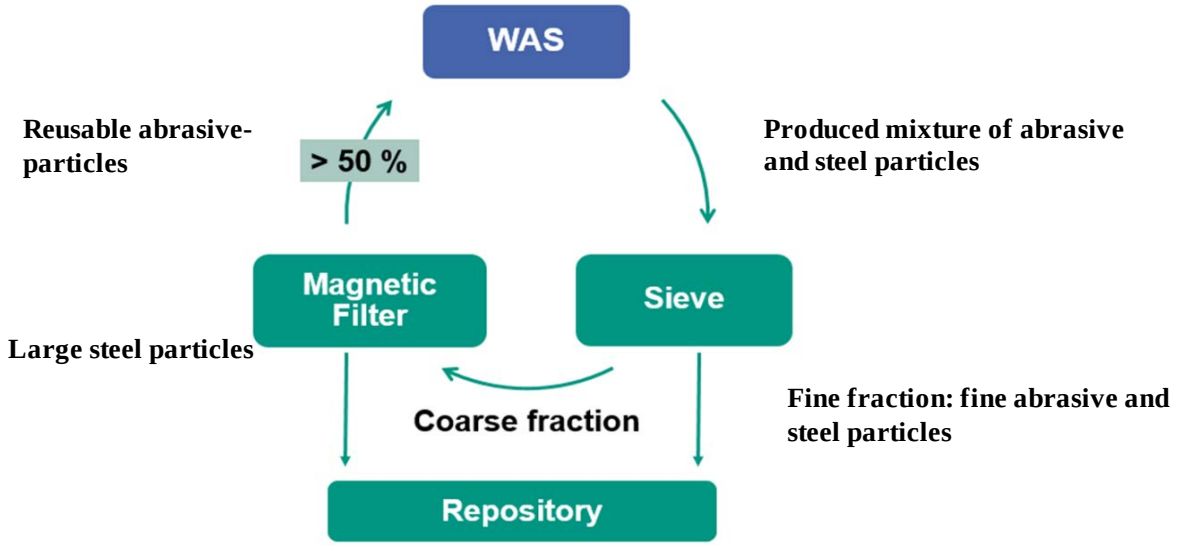

Figure 1.2: Overall scheme for abrasive-steel mixture separation in the NaMaSK system adapted from Heneka, 2021[29].

Chemical and microscopic analyses of the grain mixtures were performed to determine the grain characteristics and separation efficiency. The separation system separated the steel particles from the abrasive-steel mixture generated during the cutting process. This prototype unit utilizes filters of varying mesh sizes and magnetic separation, specifically a magnetic rod filter, and exploits the ferromagnetic properties of the steel particles, enabling their efficient separation from the non-magnetic abrasive material [28,29].

The MaSK pilot plant was developed to enhance the separation efficiency from 90% obtained in the NENAWAS system to > 98%. The plant separates steel from abrasives in a batch process, combining wet screening and magnetic filtering. The preliminary experimental design and investigation of the magnetic filtration system required for separating the radioactive steel and abrasive mixture have been reported in the doctoral theses of Brandauer, 2017 [30] and Krauß, 2021 [31].

The NaMaSK project - is a successor of the two previous projects, developed jointly by KIT-INE and KIT-TMB, supported by ANT Lübeck, Orano and EnBW [32–34]. The overall goals of the project are the minimization of steel corrosion prior to separation, optimization of the separation parameters and the development of a continuous separation cycle to achieve the highest possible radioactive secondary waste reduction and abrasive reuse rate. The later has been reported in the doctoral thesis of Heneka, 2024 [27]. The secondary radioactive waste volume reduction is estimated to be between 50-70%.

In NaMaSK, improvements to the separation of steel-abrasive mixture with sieving and magnetic separation has been implemented while the present study addresses the limiting factor of steel corrosion in the cutting suspension. The steel particles are expected to be intact prior to separation, corrosion of the steel particles in aqueous solution presents an impediment. The corrosion of the RPV ferritic steel particles in the aqueous environment during and after the waterjet cutting is particularly complex due to mechanical stress, the aqueous environment, and ionizing radiation from activated components. While corrosion inhibitors could be used to address the challenge of corrosion, their application in nuclear decommissioning presents unique issues - the effectiveness of corrosion inhibitors may be compromised by radiation-induced degradation, hence the limited understanding of inhibition mechanisms under combined corrosion-radiation conditions presents an opportunity for further study.

1.2 Problem Statement and Aim of Study

Effective separation of the steel swarf from the abrasive grains in the separation system under study depends on the corrosion resistance of the materials. RPVs are typically made from low-allow ferritic steels with a thin inner lining of austenitic stainless steel. The choice of materials is due to mechanical properties, neutronic properties, cost etc. However, the corrosion susceptibility of the RPV low-alloy steels, such as 1.6310 (20MnMoNi5-5), poses a challenge to the minimization of secondary radioactive waste in the NaMaSK system. Corrosion is a chemical and electrochemical process that leads to the deterioration of materials and the formation of corrosion products such as oxides and hydroxides. This corrosion-induced degradation can negatively impact the effective separation of RPV ferritic steel particles in our process.

First, the corrosion of steel and rust formation strongly affects the Fe-bearing material resulting in non-magnetic iron corrosion products. The corrosion of iron in aqueous solutions produces rust, which consists of several phases, e.g., Fe_2O_3, α-, β- and γ-FeOOH, that are anti-ferromagnetic [35,36]. Studies have shown that the presence of corrosion products on ferromagnetic materials leads to increased magnetic hysteresis losses, a phenomenon characterized by energy dissipation within the material as its magnetization cycles through a magnetic field. This energy loss manifests as a reduction in the efficiency and strength of magnetization, directly suggesting a degradation or weakening of the material's magnetic properties due to rust formation [37,38]. This degradation is problematic because it can impede the effective magnetic separation of steel particles. Corrosion can alter the orientation and

strength of the net magnetic moment and the spatial distribution of the internal magnetic field in a ferromagnetic material [39]. The influence of alloying elements on the magnetic properties of iron alloys has also been observed, highlighting that corrosion influences the magnetic properties of a material because these properties are susceptible to the condition of the material's surface [40,41]. While corrosion may not affect the overall magnetic properties of bulk metal samples (given that corrosion is a surface phenomenon and the base metal is largely unaffected), the impact becomes significant for micrometer-sized steel particles as encountered in this study.

Furthermore, the corrosion of the RPV steel particles in the aqueous environment could release radioactive ions and particulates into the cutting fluid. This increases the risk of contamination, poses environmental and health hazards to workers, and requires more stringent containment measures. In addition, corroded steel particles produce loose oxide particles and sludge, which contaminate the abrasive slurry. These corrosion by-products could inadvertently increase the volume of radioactive waste, complicating waste management and increasing disposal costs. Therefore, preventing corrosion ensures more efficient separation processes and reduced secondary waste generation.

The use of corrosion inhibitors provides a strategy for protecting steel particles during the WAS cutting process and before filtration and magnetic separation. In contrast with other corrosion mitigation methods such as using oxygen scavengers or cathodic protection systems (which cannot be applied to metal particles in suspension as they cannot be contacted), corrosion inhibitors act directly in the aqueous cutting fluid, providing real-time protection to steel particles in suspension, as they are generated. This is particularly critical in the turbulent and high-pressure environment of the WAS cutting process, where exposed steel surfaces are continually created and subjected to the corrosive aqueous environment. Corrosion inhibitors are not expected to adversely affect the magnetic properties of steels. In contrast, inhibitors can preserve the magnetic properties essential for efficient separation by preventing the formation of non-magnetic corrosion products. This makes them highly compatible with the downstream separation process after the cut. Moreover, corrosion inhibitors are quickly introduced into the cutting fluid without significantly modifying the setup. They are cost-effective and less toxic, especially compared to alternative strategies like replacing cutting fluids with inert media/oxygen scavengers [42] or implementing complex cathodic protection systems [43]. Corrosion inhibitors can also be tailored to specific operational conditions like pH,

temperature, and radiation fields. This flexibility ensures their effectiveness across various scenarios, making them suitable for large-scale industrial applications.

While corrosion inhibitors offer a potential solution, their application in nuclear decommissioning presents unique challenges. The RPV materials typically undergo neutron activation over many years of operational life and emit ionizing radiation as a result, and thus their interaction with the inhibitors requires understanding of the effects of ionizing radiation on inhibitor effectiveness. Ionizing radiation, characterized by high-energy particles or electromagnetic waves capable of causing ionization in atoms, presents unique challenges in terms of material degradation and corrosion. The effectiveness of conventional corrosion inhibitors may be compromised by radiation-induced degradation, and the limited understanding of inhibition mechanisms under combined corrosion-radiation conditions has hindered the development of suitable protective systems. Obtaining relevant insights into how radiation may impact these inhibitors' stability, reactivity, and protective properties is crucial for developing robust corrosion prevention strategies for the steel swarf separation. Many studies have focused on the effects of irradiation on corrosion inhibitors used for nuclear power plants to limit oxygen concentration in the reactor coolant at high temperatures and high-pressure values and in very alkaline or acidic conditions during plant operations or maintenance [42,44,45]. In contrast, others have studied inhibitors utilized in the extraction processes for the partitioning and transmuting of minor actinides in highly acidic conditions and requiring radiolytic and hydrolytic stability under extreme radiation fields [46,47]. The present study focuses on inhibitors for RPV steel in near-neutral environments and the influence of ionizing radiation on their performance.

This thesis presents a systematic investigation into the selection and characterization of corrosion inhibitors and their behavior in the presence of radiation fields. These inhibitors find application in RPV ferritic steel corrosion inhibition during waterjet cutting operations and post-cutting separation using a developed wet-filtration and magnetic separation system. The research follows a strategic progression from initial inhibitor screening through detailed mechanistic studies and culminates in evaluating radiation effects on inhibitor performance. By combining electrochemical methods, surface analytical techniques, and radiation chemistry approaches, this work provides comprehensive insights into the complex relationship between corrosion inhibition mechanisms and radiation-induced effects.

Aim of the study:

The doctoral thesis aims to:

1. Select suitable corrosion inhibitor(s) for minimizing the corrosion of ferritic steel corrosion during and after cuts with the water-abrasive suspension to ensure efficient steel-abrasive separation.

2. Quantify the effects of ionizing radiation on the corrosion of ferritic steels in the presence and absence of the inhibitors and understand the chemical processes involved.

The study combines electrochemical and surface analytical techniques with irradiation experiments to better understand inhibitor behavior. Separation and characterization methods elucidate inhibitor compositions, while Monte Carlo simulations and irradiation experiments simulate radiation field effects during real-world WAS cutting of steels.

1.3 Overview on Relevant Corrosion Inhibition Processes and their Modelling

The unique environment of the WAS – characterized by the presence of fine steel particles, abrasive material (garnet), water, and ionizing radiation, likely at near-ambient temperatures post-cutting – is explicitly differentiated from the high-temperature, high-pressure conditions and specific water chemistries encountered during LWR operation [48]. The review aims to synthesize current knowledge, identify significant research gaps, and thereby provide a foundation for developing effective corrosion control strategies to optimize secondary waste management in RPV decommissioning projects.

The corrosion of ferritic steels in aqueous environments, such as the WAS, is fundamentally an electrochemical process. It involves the simultaneous occurrence of oxidation (anodic) and reduction (cathodic) reactions at anodic and cathodic sites on the metal surface. Compositional differences, grain boundaries, and surface heterogeneities lead to the formation of anodic and cathodic sites on steel surfaces, creating potential differences between these areas. In the presence of an ionically conductive medium, a certain charge transfer develops between the steel and solution due to the potential difference [49,50]. This charge transfer or current is referred to as the corrosion current. The charge is transferred from the anodic sites of the steel into the solution and back to the steel through the cathodic sites.

1.3.1 Steel Corrosion in Near-neutral Solutions

As stated previously, the steel corrodes in the aerated, near-neutral solution of a water abrasive suspension via reduction-oxidation partial (half) reactions. At the steel anode, the anodic reaction is generally represented as the oxidation of iron since iron is the main constituent of steels, leading to the formation of metal ions in the solution.

The half-cell reactions are described as follows:

1. Anodic Reaction: Metallic iron dissolution

$$Fe \rightarrow Fe^{2+} + 2e^{-} \quad (1.1)$$

2. Cathodic Reaction: Dissolved oxygen reduction at cathodic sites leading to localized increase in pH, and possibly passivation of the metal.

$$O_2 + 2H_2O + 4e^{-} \rightarrow 4OH^{-} \quad (1.2)$$

Rust formation can occur through the interaction of cathodic and anodic products.

$$Fe^{2+} + 2OH^{-} \rightarrow Fe(OH)_2 \quad (1.3)$$

Since the corrosion process is a consecutive reaction chain, the overall corrosion rate is governed by the kinetics of the slowest of these partial reactions and is influenced by several factors. The rate is directly influenced by temperature, pH, include the electrochemical potential difference driving the reactions, temperature, the concentration of dissolved species (like oxygen or aggressive ions), and the electrical conductivity of the solution facilitating ion movement. Critically, the formation and properties of surface films – either passive layers (thin, protective oxides) or thicker corrosion product layers – significantly moderate the corrosion process by acting as barriers to ion or electron transport.

Under ambient conditions, the corrosion product, $Fe(OH)_2$ from Eqn. 1.3, is unstable and oxidizes to ferric hydroxide (also known as 'yellow rust') in the presence of sufficient dissolved oxygen under oxic conditions:

$$2Fe(OH)_2 + H_2O + \frac{1}{2}O_2 \rightarrow 2Fe(OH)_3 \quad (1.4)$$

Yellow rust could undergo dehydration to form hydrated ferric oxide FeOOH or hematite Fe_2O_3 (red rust).

$$Fe(OH)_3 \rightarrow FeOOH + H_2O \quad (1.5)$$

Two forms of hydrated ferric oxide are observed in the corrosion of iron in water: α-FeOOH (geothite) and γ-FeOOH (lepidocrocite) [51].

The stability of different corrosion products in the iron-water system at various pH values and potentials is illustrated in a Pourbaix diagram [52]. The major applications of Pourbaix diagrams have been to predict the spontaneous direction of corrosion reactions for a given metal-electrolyte system, to predict possible ways to drive the corrosion reaction in a desired direction by adjusting environmental conditions, and to estimate the composition of corrosion products.

For the fine steel swarf generated during WAS cutting and residing in the suspension, the most pertinent corrosion mechanisms are likely Uniform Corrosion and Pitting Corrosion.

- **Uniform Corrosion:** This involves a relatively even dissolution of the metal surface across the exposed area. While often considered less insidious than localized forms, the extremely high surface area of the fine steel swarf means that even a low uniform corrosion rate can lead to significant metal loss and corrosion product generation in a short time. The mechanism in high-temperature water often involves outward diffusion of metal ions and inward diffusion of oxygen species through a growing oxide layer. At the lower temperatures relevant to the WAS cutting, the kinetics will be slower, but the fundamental process of surface oxidation and dissolution remains active.
- **Pitting Corrosion:** This is a localized form of attack characterized by the formation of small pits or holes, initiating at points where the protective passive film breaks down [53]. Initiation sites can include surface defects, scratches (potentially abundant due to cutting/abrasion), or inclusions within the steel matrix, such as manganese sulphides (MnS). Pitting is often promoted by the presence of aggressive anions, particularly chlorides (Cl^-), which may be present as impurities in the process water or the abrasive material [54,55]. Once initiated, pit growth can be autocatalytic: the localized dissolution within the pit leads to an accumulation of metal cations, which hydrolyze to lower the local pH, and migration of anions (like Cl^-) into the pit to maintain charge neutrality, creating an aggressive microenvironment that hinders repassivation and accelerates further dissolution. Given the potential for surface damage from cutting and the possible presence of contaminants, pitting represents a significant concern for the steel particles.

Additionally, Galvanic Corrosion could play a role at a microstructural level. RPV steels typically possess a tempered bainitic or martensitic microstructure, which may contain different phases or carbide precipitates or inclusions like MnS [3]. Potential differences between

these microstructural features (e.g., ferrite vs. cementite in pearlite remnants, or matrix vs. inclusions) can establish micro-galvanic cells when exposed to the electrolyte, accelerating the corrosion of the more anodic phase.

For steels in near-neutral solutions, the half-cell potentials of the electrochemical cell deviate from their equilibrium values with the consequent development of an irreversible electrode potential. This deviation in potential is called an overpotential or overvoltage η.

$$\eta = E(i) - E \qquad (1.6)$$

where E is the half-cell potential at equilibrium as given by the Nernst equation and E(i) is the measured potential represented as a function of current density [56,57].

Overpotential arises due to slow charge transfer, resistance losses and mass transfer losses in the system, all of which contribute to the overall overpotential. Charge transfer or activation overpotential (η_{CT}) is overpotential arising from maintaining the rate of the electrode reactions. Resistive or Ohmic overpotential (η_R) develops as a result of electronic or ionic conduction. Mass transport overpotential (η_T), is observed as a result of mass transport limitations [58,59].

The change in potential gives rise to electrode reaction resulting in current flow. The cathodic half-cell potential becomes more negative than its equilibrium value while the anodic half-cell potential shifts to more positive values. This phenomenon is called polarization. The resulting polarization of the anodic and cathodic sites leads to anodic and cathodic net currents exceeding the exchange current density (j_o).

If the electrochemical system is such that electrode process is completely determined by charge transfer at the metal surface, typical for corrosion measurements around the corrosion potential, then the relationship between the current and voltage is described by the Butler-Volmer equation [57,60]:

$$j = j_a + j_c = j_o\left\{\exp\left(\frac{\alpha n F}{RT}\eta\right) - \exp\left(-\frac{(1-\alpha)nF}{RT}\eta\right)\right\} \qquad (1.7)$$

Where j = overall current density of the reaction, j_a & j_c = anodic and cathodic current densities respectively, j_o is the exchange current density at equilibrium, α = transfer coefficient, which describes the charge transfer kinetics ($0 \leq \alpha \leq 1$), F = Faraday constant (96485 $Cmol^{-1}$), R = universal gas constant (8.314 $Jmol^{-1}K^{-1}$), T = absolute temperature in Kelvin (K) and n = number of electrons transferred.

Two limiting cases of the Butler–Volmer equation occur; at the high overpotential regime (when for $> 50mV$) resulting in an approximation to the Tafel equation, and at the low potential regime from which an expression for the polarization resistance, R_p, may be derived (also known as the Stern–Geary relationship) [61,62].

When the overpotential η is significantly greater than RT/nF = 25.7mV at $25°C$ (i.e. $\eta > 50mV$), the respective counter reaction is neglected.

For the cathodic reaction, we neglect the anodic current density contribution and thus have:

$$j = -j_o \exp\left\{\left(-\frac{(1-\alpha)nF}{RT}\eta\right)\right\} \quad (1.8a)$$

For the anodic reaction, we neglect the cathodic current contribution and have:

$$j = j_o\left\{\exp\left(\frac{\alpha nF}{RT}\eta\right)\right\} \quad (1.8b)$$

Solving the above two equations for η yields;

For the cathodic reaction, $\eta = -\frac{RT}{(1-\alpha)nF}2.3\log j_o - \frac{RT}{(1-\alpha)nF}2.3\log|j|$ (1.9a)

For the anodic reaction, $\eta = -\frac{RT}{\alpha nF}2.3\log j_o + \frac{RT}{\alpha nF}2.3\log|j|$ (1.9b)

The above equations for the overpotentials can be expressed as a linear equation of the form

$$\eta = A + B \bullet \log|j| \quad (1.10)$$

The above linear equation is known as the Tafel equation, which describes the rate of metal dissolution as a function of the overpotential.

From the Tafel equation, A is the Tafel constant while B can be defined as the Tafel slopes for both the anodic and cathodic reactions as B_a and B_c (commonly β_a & β_c) where;

$$\beta_a = \frac{2.3RT}{\alpha nF} \text{ and } \beta_c = \frac{2.3RT}{(1-\alpha)nF} \quad (1.11)$$

From the Tafel equation, it can be seen that shifting the anodic potential towards positive values results in a higher rate of metal dissolution.

If the steel electrode is anodically polarized at a certain positive potential or in the presence of an oxidizing agent, a sudden decrease in the rate of anodic dissolution is observed [53]. This occurs because of the formation of a protective oxide film on the metal surface. This protective film is called a passive film and this process is called passivation by an oxide film. In a few cases, the excess accumulation of metal ions near the electrode layer can lead to the

precipitation of salts on the electrode covering a portion of the surface and leading to passivation. This type of passivation could be seen at higher pH values [63,64]. The presence of corrosion inhibitors could also introduce a passive layer blocking active sites on the metal surface, ennobling the corrosion potential and ultimately reducing the kinetics of the electrode processes [65].

1.3.2 Thermodynamics of Steel Corrosion

The electrochemical processes that produce steel corrosion differ from typical chemical reactions in that their energetics depend on the difference in potentials between the steel and the contacting phase e.g. an electrolyte solution. Changes in the free-energy of reaction, ΔG, accompanying the corrosion reaction determine the driving forces and progression of the anodic half-reactions. In principle, it must be thermodynamically favourable for a given corrosion reaction to occur spontaneously. For such, the change in Gibb's free energy, ΔG, must be negative, where:

$$\Delta G = -nFE \quad (1.12)$$

The sum of the associated free energy changes of the oxidation and reduction half-reactions must be negative, for the reaction to proceed i.e.

$$\Delta G_{ox} + \Delta G_{red} < 0 \quad (1.13)$$

Where ΔG_{ox} and ΔG_{red} are the changes in free-energy associated with the anodic oxidation reaction and the cathodic reduction reactions respectively.

Both oxidation and reduction free-energy changes are related to the equilibrium cell potential, E, as given below:

$$\Delta G^{\circ}_{ox} = nFE^{\circ} \quad (1.14a)$$

$$\Delta G^{\circ}_{red} = -nFE^{\circ} \quad (1.14b)$$

Where E° = Standard electrode potential.

The standard electrode potential for the cathodic reduction reaction of hydrogen evolution has a value of 0 V assigned to it. This is known as the Standard Hydrogen Electrode (SHE) used as a reference in electrochemical reactions. The standard electrode potential for Iron oxidation has a value of +0.44 V [57].

The Nernst equation given below describes the relationship between the electrode potential and the standard electrode potential under non-equilibrium conditions. The standard cell potentials describe cells in which all dissolved substances are at an effective concentration of 1 moldm^{-3} or unit activity. The 'effective activity' (denoted as a_i) accounts for the non-ideal behavior of ions and molecules in real solutions, where intermolecular interactions can deviate from ideal dilute conditions. For ideal solutions or very dilute solutions, the activity of a species is approximately equal to its molar concentration. Therefore, the Nernst equation gives a relationship between the cell potential, the effective activities of the dissolved electroactive species and the standard electrode potential [66].

$$E = E^{\circ} - \frac{RT}{nF} \ln Q \qquad (1.15a)$$

$$\text{and, } Q = \frac{\prod a_{ox}}{\prod a_{red}} \qquad (1.15b)$$

where Q is the reaction quotient, relating the activities of oxidized and reduced species.

The difference in potentials of the anodic and cathodic half-cell reactions drives the corrosion reaction.

While the application of thermodynamics in the study of corrosion has been successful in establishing the tendency of corrosion for a given metal-electrolyte system, a major limitation is the inability to predict the rate of the corrosion process.

1.3.3 Corrosion Inhibition of Steel

Corrosion inhibitors are chemical substances that, when added in small quantities to a corrosive environment, significantly decrease the rate of metal corrosion [67]. Their primary function is typically to interact with the metal surface or the corrosive medium to impede the electrochemical reactions driving corrosion manifesting as alterations in the anodic or cathodic polarization behavior (reducing slopes of the Tafel plot), impeding the transport or diffusion of aggressive ions to the steel surface, and increasing the overall electrical impedance of the steel surface and double-layer [68]. Inhibitors are broadly classified based on their effect on the electrochemical half-reactions: anodic inhibitors slow the metal dissolution (anodic) reaction, cathodic inhibitors slow the reduction (cathodic) reaction, and mixed-type inhibitors affect both.

The mechanisms of inhibition action are diverse. Anodic inhibitors often promote the formation or stabilization of a passive oxide film on the metal surface (passivators). Cathodic inhibitors

may poison the cathodic reaction sites (e.g., hindering oxygen reduction in aerated, near-neutral or alkaline media) or precipitate as insoluble compounds on cathodic areas, forming a barrier layer [69]. Many inhibitors, particularly organic compounds, function by adsorbing onto the steel surface. This adsorbed layer acts as a physical barrier, blocking active corrosion sites and preventing access of corrosive species to the metal surface. Organic inhibitors often possess heteroatoms (such as Nitrogen (N), Oxygen (O), Sulfur (S)) with lone pair electrons, and/or multiple bonds or aromatic rings (π-electron systems), which facilitate their interaction with the unfilled d orbital of iron to form coordinate bonds [70,71].

The adsorption of an organic inhibitor to a steel surface leads to the formation of a protective film that acts as a barrier between the metal and the corrosive environment. The nature of this adsorption can be categorized as physical adsorption (physisorption) or chemical adsorption (chemisorption), or often a combination of both [72,73]. For organic inhibitors with heteroatoms (N, O, S), this involves the sharing of lone pair electrons from the inhibitor with vacant d-orbitals of the metal atoms (e.g., iron). π-electrons from aromatic rings or multiple bonds can also participate. Chemisorption leads to stronger bonding and often more effective inhibition, and its rate may increase with temperature up to a certain point. The adsorption process is often described mathematically using adsorption isotherms (e.g., Langmuir, Freundlich, Temkin, Frumkin), which relate the inhibitor concentration in solution to the degree of surface coverage. A detailed review of the mechanism of the inhibition of steel corrosion in near-neutral media is found in the works of Verma and coworkers [69], Quraishi and coworkers [74] and by Mansfeld and coworkers [75].

Dissolved O_2(aq) concentration, pH, temperature, and composition of corrosive medium all affect the inhibition of steel corrosion in neutral, oxic solutions. For iron/steel immersed in acid solutions, the metal surfaces are usually free of oxides due to the higher solubility of the iron corrosion products such as Fe_2O_3(s), $Fe(OH)_2$(s) and FeOOH(s) at low pH, whereas metal surfaces corroding in neutral solutions are covered with coatings of oxides, hydroxides, or salts due to their lower solubility at higher pH. These variations mean that compounds that inhibit steel corrosion in acidic solutions by adhering to oxide-free surfaces may not be adequate for preventing corrosion in neutral solutions. A number of organic compounds have been investigated for the corrosion inhibition of mild steel and low alloy steels in near neutral media. Azole and triazoles derivatives [76–79], amines and amino acids derivatives [70,80–82] and triazine derivatives [83,84] have been reported as satisfactory corrosion inhibitors of mild steel corrosion in near-neutral oxygen-saturated solutions.

1.3.4 Corrosion Inhibitor Adsorption Modelling

In corrosion studies, most organic inhibitors act primarily by adsorption onto the metal surface and providing a protective covering [58,85]. Inhibitor-Metal adsorption is defined as a surface phenomenon that results in an accumulation of inhibitor molecules, atoms, and/or ions (adsorbate) onto the metal surface (adsorbent). Adsorption typically occurs by physical/physisorption, chemical/chemisorption or a combination of both mechanisms [72,73,86]. Physical adsorption mechanism is facilitated by the electrostatic forces between the charges on the metal surface and dipoles or ions groups of the inhibitor [87,88], chemisorption on the other hand leads to the formation of stronger bonding via covalent bonds. An adsorption isotherm models the relationship between the adsorbate (inhibitor molecules) in the surrounding phase (electrolyte solution) and adsorbate adsorbed on the surface of the adsorbent (metal electrode) at equilibrium and constant temperature. The Langmuir [77,84,89–91], Freundlich [92,93] and Temkin [94] adsorption isotherms have been frequently used to model corrosion inhibitor adsorption on metal surfaces.

The Langmuir adsorption isotherm assumes monolayer adsorption on a homogenous surface, a dynamic equilibrium state with all adsorption sites being equivalent, and no interactions between adsorbed molecules and is expressed by the relation [95–97]:

$$\theta = \frac{K_{eq}C}{1+K_{eq}C} \tag{1.16}$$

Where: C is the inhibitor concentration in mol/dm^3, K_{eq} is the adsorption equilibrium constant and θ is the surface coverage.

When fitted to the Langmuir Isotherm, the standard Gibbs free energy of adsorption (ΔG^{θ}_{ads}) can be calculated using the thermodynamic relation:

$$K_{eq} = \frac{1}{c_{H_2O}} \exp\left(-\frac{\Delta G^{\theta}_{ads}}{RT}\right) \tag{1.17}$$

Where: c_{H_2O} is the molar concentration of liquid water (55.34 mol/dm^3 at 25°C)

The $\frac{1}{c_{H_2O}}$ factor in the equation above considers the aqueous-phase adsorption of the inhibitor molecules as substitutional adsorption where an inhibitor molecule replaces a water molecule on the surface.

1.3.5 Radiolysis of Organic Corrosion Inhibitors

Radiolysis of organic corrosion inhibitors occurs when these compounds are exposed to ionizing radiation, such as alpha particles, gamma rays or high-energy electrons. Organic corrosion inhibitors often contain functional groups with heteroatoms (e.g., nitrogen, oxygen, sulfur) that facilitate adsorption onto metal surfaces, forming a protective barrier. However, these functional groups are also susceptible to radiation damage. When exposed to ionizing radiation, organic corrosion inhibitors can undergo various transformations, including: bond cleavage leading to fragmentation and the formation of smaller, potentially less effective or even corrosive byproducts [98], generation of highly reactive free radicals that can further react with the inhibitor or with the metal surface, potentially accelerating corrosion [99], as well as polymerization which can induce the formation of larger, less soluble species that may lose their inhibitive properties [100].

While radiolysis of various molecules has been a subject of interest for a long time, specific research on the effect of radiolysis on the performance of corrosion inhibitors has been limited to organic compounds used in the operation of nuclear power plants, in decontamination [101] and in solvent extraction in partitioning of actinides from dissolved spent nuclear fuel [102]. When ionizing radiation interacts with a solution of an organic compound, the immediate reaction is the radiolysis of water which forms the bulk of the solution. The primary products of water irradiation are $H_2O_2(aq)$, $H_3O^+(aq)$, $OH^-(aq)$, $H_2(g)$, $OH\cdot(aq)$, $H\cdot(aq)$, $O_2(aq)$, and $e^-(aq)$[103]. Of all these products, solvated electrons (e^-_{aq}), hydrogen (H·) and hydroxyl (OH·) radicals are the most reactive species which rapidly react with organic compounds to form organic free radicals. The resulting radicals affect the inhibition performance of the corrosion inhibitors [104–106].

Radiation-induced chemical change is quantitatively expressed by the G-value, defined as the number of molecules formed or consumed per 100 eV of absorbed energy. For water radiolysis, the primary G-values for species like e_{aq}^- (~2.7), OH• (~2.8), and H• (~0.5) are well-established [103,107]. G-values for the formation of all individual radiolysis products of complex organic molecules used as corrosion inhibitors are often not readily available in the literature due to the analytical challenges of identifying and quantifying a myriad of potential products. However, existing studies on similar compounds provide valuable insights into typical yields. These yields are essential in quantifying the degree of degradation expected from a molecule based on the absorbed energy from ionizing radiation.

1.4 Thesis Structure

The thesis is structured to ensure a cohesive narrative. The initial chapters establish a foundational understanding of RPV steel corrosion, corrosion inhibitors, and a detailed description of the experimental methods. The results and discussion chapter presents findings from inhibitor selection, a test cut of the steel with WAS, long-term corrosion inhibition monitoring of the steel swarf, and experiments with unirradiated and irradiated inhibitors. Finally, the thesis concludes with a comprehensive outline of major findings and their implications for secondary waste minimization after reactor decommissioning.

CHAPTER TWO: MATERIALS AND METHODS

This chapter details the materials, experimental and numerical methods employed in this study, which can be broadly categorized into two main areas: experiments utilizing non-radioactive steel samples and unirradiated inhibitor solutions, and numerical simulations coupled with experiments involving irradiated samples.

Experiments involving non-radioactive steel coupons and unirradiated inhibitors were conducted at the KIT-INE with three primary objectives: (a) Selection of suitable inhibitors for RPV steel cutting in the WAS process, and determination of their corrosion inhibition kinetics and mechanism using electrochemical measurements. (b) Gaining insights into their surface adsorption behavior through surface analytical techniques, including X-ray Photoelectron Spectroscopy (XPS), Scanning Electron Microscopy/Energy-dispersive X-ray spectroscopy (SEM-EDX), Quartz Crystal Microbalance (QCM), and Ellipsometry. (c) Observation of the inhibition behavior following use in a WAS cutting process.

Monte Carlo simulations of radiation transport aided the estimation of realistic dose-rates from a steel-abrasive mixture to be separated after a WAS cut. Inhibitor samples and steel coupons were irradiated in specifically designed setups utilizing alternative radiation sources available at the KIT-INE shielded box line. Post-irradiation experiments included electrochemical testing of the irradiated inhibitor solutions and solution characterization via Nuclear Magnetic Resonance spectroscopy (NMR). Additionally, surface analysis of coupons irradiated with the inhibitors was performed to determine the effect of ionizing radiation on the inhibition of RPV steel corrosion under post-WAS cutting conditions.

2.1 Materials

2.1.1 RPV Steel

The reactor pressure vessel material under investigation, 20MnMoNi5-5, is a low-alloy ferritic-bainitic steel, designated as 1.6310 according to the German DIN standard (equivalent to ASTM A533 Grade B Class 1). This material is typically used in the manufacturing of the RPV shell, coolant lines and jacket plates [108]. The microstructure of 1.6310 steel consists primarily of tempered bainite, with a small amount of ferrite. This microstructure provides a good balance of strength and toughness, essential for the RPV's operational requirements [109].

However, it is also susceptible to various forms of corrosion in aqueous solutions and especially under irradiation conditions.

A block of the steel obtained from the previous MaSK project is shown in Figure 2.1 and used throughout the experiments. Cylindrical coupons were cut from the steel block for immersion tests and as working electrodes for electrochemical measurements. The 1.6310 steel block was also transported to the project partner site, ANT Lübeck, for WAS cutting with the selected inhibitor (C.Inh #4) added to the process water.

The composition of the steel shown in Table 2.1 was obtained from the acceptance test certificate of the steel conducted by Edelstahl Rosswag (D-76327 Pfinztal-Kleinsteinbach) attached in the appendix section (A1).

Table 2.1: Chemical composition of 1.6310 steel in weight (wt.) %

Element	Fe	C	Mo	Si	Mn	Ni	Cu	Cr	(P, N, V)
Comp. (wt %)	balance	0.19	0.43	0.28	1.31	0.67	0.03	0.12	0.06

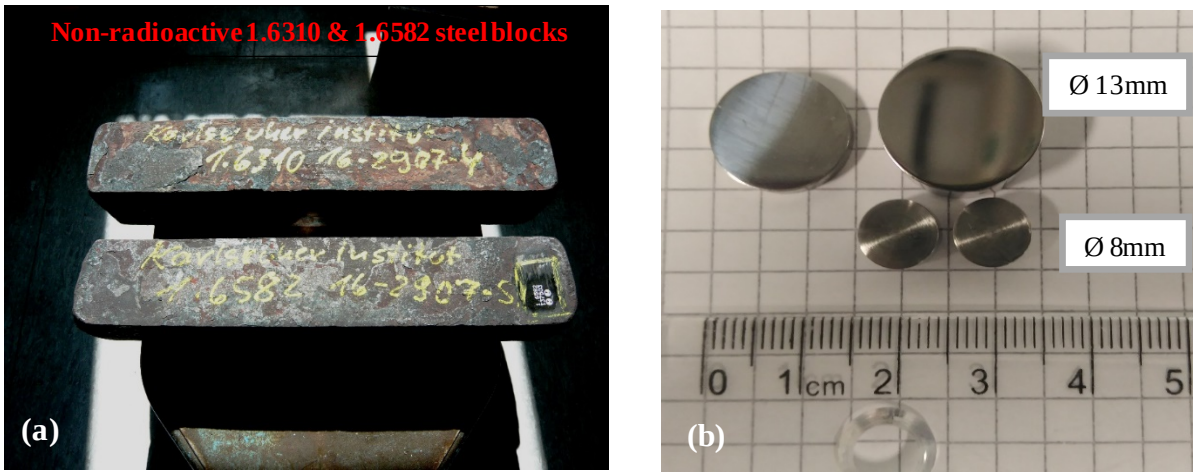

Figure 2.1: Steel samples used for the WAS cutting trial and electrochemical experiments: (a) Blocks of non-radioactive 1.6310 and 1.6582 steel (b) Coupons of 1.6310 steel produced at the KIT-INE workshop.

Steel Sample Preparation:

Cylindrical coupons of the investigated steel, with dimensions of Ø 13mm x 15mm and Ø 8mm x 5mm (shown in Figure 2.1), were cut from the steel block. Before use in corrosion experiments, the surfaces of the steel coupons were prepared according to ASTM standards [110]. The steel was abraded with p240, p600, and p1000 Silicon Carbide (SiC) papers on a Buehler EcoMet30 Twin Semi-Automatic grinder-polisher machine to provide a uniform

surface area. Abrasion was followed by polishing with a diamond paste, progressing from 3µm and 1µm roughness, to achieve a mirror surface finish. After polishing, the coupons were cleaned with isopropanol in an ultrasonic bath, washed with de-ionized water to remove any attached carbon paste and fine steel particles, and then dried with Argon before storage in an Argon-filled box to prevent oxidation.

2.1.2 Abrasive

As described in the introduction, the WAS cutting process employs a high-pressure water jet mixed with abrasives. Garnet sand is the most frequently used abrasive for the WAS process. As a naturally occurring mineral, its composition and particle size distribution can vary depending on the extraction site, processing methods and manufacturer. In the present study, Barton™ 80 HPX (High-Performance Hard Rock) garnet sand was utilized as the abrasive. While garnet is a natural product whose chemical composition may vary with product batch, the average composition of the sand components is detailed in Table 2.2. The designation 80 HPX is derived from the particle size of the abrasive, sorted with screens of 80 meshes per inch, resulting in a mesh size of 177 µm. Some properties of HPX80 garnet abrasive include 7.5 – 8.5 hardness (Mohs), 3.9 – 4.1 specific gravity (g/cm^3) and red to slightly pink in color [111].

Table 2.2: Average chemical composition (wt. %) of the Barton 80 HPX abrasive [111].

Component	SiO_2	Al_2O_3	FeO	Fe_2O_3	TiO_2	MnO	CaO	MgO
Composition. (wt %)	36	20	30	2	2	1	2	7

2.1.3 Corrosion Inhibitors

Preliminary selection of corrosion inhibitors for this study was based on a number of criteria as seen in Figure 2.2. Inhibitors which had been reported in literature as suitable for inhibiting mild/low alloy steel corrosion were considered. The selected inhibitors were required to be relatively non-toxic (with respect to environmental regulations), readily available, and low cost. While organic compounds containing heteroatoms such as P, N, O and S have been shown to be excellent corrosion inhibitors for metals including Fe, the C-H-O-N (Carbon, Hydrogen, Oxygen, Nitrogen) principle was applied. The C-H-O-N principle, applied in nuclear waste processing, establishes a basis for selecting molecules for extraction and for waste handling where molecules containing only carbon, hydrogen, oxygen and nitrogen are focused on. As a

result, all secondary organic process waste can be treated via incineration without increase in final waste volumes as well as radioactive solid residues [112–114].

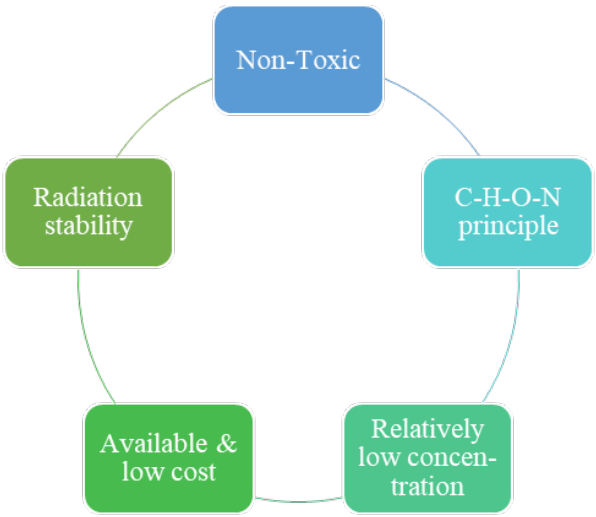

Figure 2.2: Criteria for the selection of inhibitors to be used for WAS cutting of RPV steel.

The tested pure compounds, AnalaR grade 5-Methylbenzotriazole, 5-Aminobenzimidazole, 3,4-Dihydroxybenzoic acid, and L-Tryptophan were purchased from Merck Chemicals GmbH (Darmstadt, Germany) and used as purchased. Aqueous solutions of chemicals were prepared using deionized water (Milli-Q water) from a Merck Advantage A10 device, which filters water to a 3 ppb TOC value and provides a resistivity of 18.2 MΩ·cm at 25.00±1.00 °C. For the immersion tests, a 0.004 mol/dm^3 NaCl solution was prepared as the blank. Different concentrations of the inhibitors were added to the blank to give the inhibited solutions. pH values were measured with a laboratory pH meter (inoLab® pH7110) and a semi-micro pH electrode (Orion™ 8103BN ROSS™, Thermo-Fisher Scientific). The pH meter calibration was performed at room temperature with standard buffers (NIST Standard, Merck, Germany) at pH values 4, 6, 8 and 10. Steel coupons were added to each solution in glass vials under aerated conditions and monitored for steel corrosion. In addition, four commercial inhibitor formulations were obtained from various manufacturers and named as C.Inh #1, C.Inh #2, C.Inh #3 and C.Inh #4 respectively with properties given below according to the manufacturers:

C.Inh #1: non-toxic, organic, polyamine mixture.

C.Inh #2: fatty amine mixture, non-ferrous metal inhibitors, dosage 0.2%

C.Inh #3: 99% Octadecylamine, <1% Salicylic acid.

C.Inh #4: Alkaline pH, polyamine mixture, dosage 0.5-2.5%

For the electrochemical tests using the C.Inh #4, 0.004 mol/dm^3 NaCl solution (Fischer Scientific, Darmstadt, Germany) was used as the blank solution. Further electrochemical tests were also performed using a blank solution of 0.06 mol/dm^3 $NaHCO_3$, as informed by the industrial partner of the project, representing the typical cutting solution utilized for RPV segmentation. This was prepared by dissolving a weighted quantity of analytical grade $NaHCO_3$ purchased from Merck Chemicals GmbH in Milli-Q water.

2.2 Experimental & Analytical Methods

2.2.1 Immersion Tests

The pure inhibitor compounds and commercial formulations were tested as potential inhibitors via immersion tests at different concentrations. Ø 8 mm steel coupons were added to vials containing each of the inhibitors and visually observed for corrosion after a period of up to 7 days. A summary of the immersion test and conditions are given in Table 2.3:

Table 2.3: Immersion test experimental conditions

No.	Inhibitor	Inh. Conc (ppm)	Electrolyte (NaCl) conc. (mol dm^{-3})	T ± 1 °C	pH ± 0.1	Duration
1	5-Aminobenzimidazole	1000	0.004	25	8.4	24 hours
2	3,4-Dihydroxybenzoic acid	1000	0.004	25	3.1	24 hours
3	L-Tryptophan	1000	0.004	25	5.9	24 hours
4	5-Methylbenzotriazole	1000	0.004	25	8.9	24 hours
5	C.Inh #1	10000	0.004	25	8.7	7 days
6	C.Inh #2	10000	0.004	25	8.8	7 days
7	C.Inh #3	10000	0.004	25	9.1	7 days
8	C.Inh #4	10000	0.004	25	8.2	7 days

2.2.2 Electrochemical Analyses

The corrosion of 1.6310 steel investigated in this study is fundamentally an electrochemical process. Consequently, electrochemical techniques were applied to understand the mechanisms of corrosion and for quantitatively evaluating the efficiency of corrosion inhibitors. These methods allowed for the probing of electrical and chemical transformations at the interface,

providing insights into reaction kinetics, surface film properties, and the overall corrosion rate. The techniques employed were specifically Open Circuit Potential (OCP) measurements, Potentiodynamic Polarization (PDP), and Electrochemical Impedance Spectroscopy (EIS), to comprehensively investigate the corrosion behavior of 1.6310 steel and the performance of selected inhibitors. The combined utilization of OCP, PDP, and EIS enabled a cross-correlation of results, with a consistency across the different electrochemical methods strengthening the conclusions drawn regarding the inhibitor performance and mechanism.

A BioLogic VMP3® Multichannel potentiostat/galvanostat (BioLogic France) was used for electrochemical measurements performed on unirradiated samples. Subsequent data analyses were performed with the accompanying EC-Lab® software. A sealed three-electrode cell was used with a 13 mm diameter 1.6310 steel coupon as the working electrode (WE) having an exposed surface area of 0.84 cm^2. The working electrode was fastened to a sample holder, exposing only the polished surface area, and secured with an O-ring. A high purity graphite rod was used as the counter electrode (CE), and Ag/AgCl in saturated 3 mol dm^{-3} NaCl was used as a reference electrode (RE). A Luggin capillary tube was used alongside the reference electrode to minimize the distance between the RE and WE surface, thereby minimizing ohmic voltage drops [115,116]. The electrodes were placed in the 500ml glass three-electrode electrochemical cell from BioLogic® containing 200 – 500 ml of each solution, and connected to the potentiostat for each experiment. A schematic representation of the 500 ml three-electrode cell is shown in Figure 2.3. The potentiostat measures the flow of current between the WE and the CE, while the potential is measured between the WE and RE.

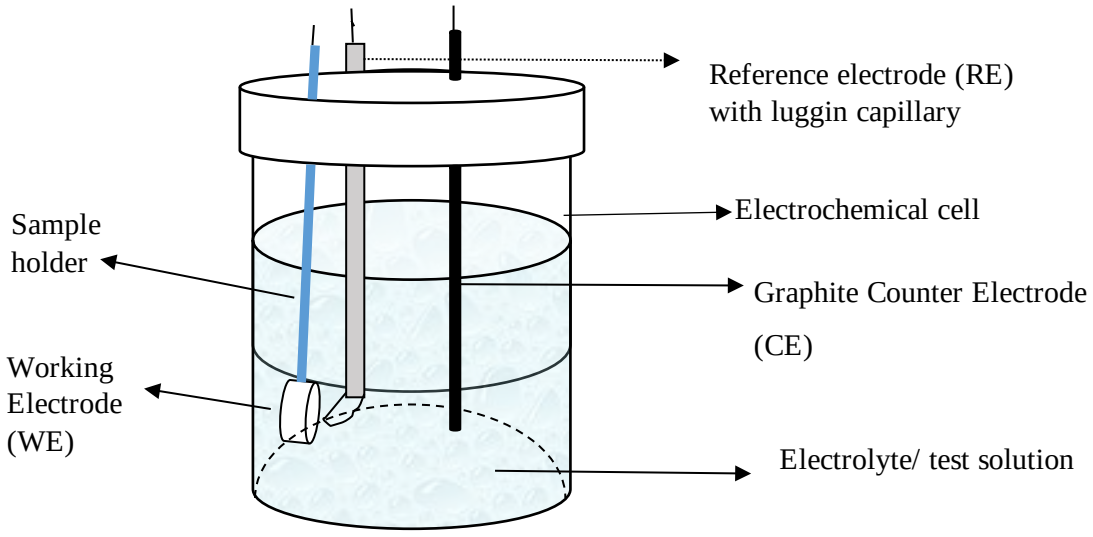

Figure 2.3: Three-electrode corrosion cell showing reference electrode, working electrode and graphite counter electrode.

While initial screening and preliminary electrochemical tests utilized a 0.004 mol dm^{-3} NaCl solution as the blank, subsequent electrochemical investigations involving the individual constituents of the selected inhibitor discussed in Chapter 3.4, employed a 0.06 mol/dm^3 $NaHCO_3$ solution as the blank electrolyte. This decision was informed by an industrial partner involved in the project, who indicated that a 0.06 mol dm^{-3} $NaHCO_3$ solution is typically added to their demineralized water for use as the cutting fluid in their WAS cutting operations. The use of sodium hydrogen carbonate likely serves multiple purposes in the cutting fluid. Bicarbonate/carbonate solutions are known to act as buffering agents [117], helping to maintain a stable pH in the cutting fluid despite potential acidic or alkaline contaminants introduced during the cutting process. Furthermore, carbonate ions can contribute to the passivation of steel surfaces by promoting the formation of protective iron carbonate or oxide/hydroxide layers [118], thereby offering a degree of inherent corrosion protection to the steel swarf even before the addition of any corrosion inhibitor.

2.2.2.1 Open Circuit Potential

The Open Circuit Potential (OCP), also referred to as the free corrosion potential (E_{corr}) or rest potential when no net external current flows, is defined as the electrical potential difference measured between the working electrode (in this study, 1.6310 steel) and a stable reference electrode, both immersed in the corrosive electrolyte. This potential spontaneously develops due to the establishment of a dynamic equilibrium where the total rate of all anodic (oxidation) reactions equals the total rate of all cathodic (reduction) reactions occurring simultaneously on the electrode surface [119]. The magnitude of the OCP is a direct thermodynamic indicator of the propensity of the steel to corrode in the specific medium; generally, a more negative OCP value suggests a greater driving force for corrosion [58].

Monitoring the OCP over a period of time is a critical preliminary step in electrochemical corrosion studies. It allows for the assessment of the stability of the metal/electrolyte system before initiating more perturbative techniques like PDP or EIS. The OCP versus time curve provides information about real-time processes occurring at the electrode surface. These can include the formation or breakdown of passive layers or inhibitor films, as well as the adsorption or desorption kinetics of inhibitor molecules on the steel surface [120].

Furthermore, the direction and magnitude of the OCP shift observed upon the introduction of a corrosion inhibitor can offer preliminary insights into the inhibitor's primary mode of action

(i.e., whether it predominantly affects anodic reactions, cathodic reactions, or both) even before conducting more detailed polarization experiments [79,121].

OCP Experimental Procedure:

All three electrodes described in Figure 2.3 were immersed in the test electrolyte and the potential difference between the WE and the RE measured using a high-impedance voltmeter, which is an integral part of the potentiostat. The high impedance of the measuring instrument is crucial to ensure that negligible or no current is drawn from the electrochemical cell. This is vital to prevent any unintended polarization of the WE, which would otherwise perturb the system's natural equilibrium potential and lead to an inaccurate OCP measurement. The OCP was then monitored as a function of time, typically for a duration sufficient to allow the system to reach a quasi-equilibrium state (e.g., 3600 seconds or longer). Stabilization was considered achieved when the potential variation became minimal over a defined period (less than 5 mV over 5 minutes or 1 mV/min).

The analysis of OCP data provided information regarding the corrosion behavior of 1.6310 steel in each test environment, including the stabilized OCP value (E_{corr}) and insights into surface film dynamics.

2.2.2.2 Electrochemical Impedance Spectroscopy

Electrochemical Impedance Spectroscopy (EIS) is a non-intrusive electrochemical technique employed to investigate the complex properties of the metal/electrolyte interface and the various electrochemical and physical processes occurring there. These processes include non-faradaic phenomena such as the charging of the electrical double layer, and faradaic processes such as charge-transfer reactions (corrosion), diffusion of electroactive species, and the behavior of surface films (e.g., passive layers or adsorbed inhibitor films) [57].

The technique involves applying a small amplitude (5-10 mV root mean square, rms) sinusoidal alternating current (AC) potential (or current) perturbation to the working electrode, which is usually held at its OCP. This perturbation is applied over a wide range of frequencies, typically spanning several orders of magnitude. The electrochemical system responds to this sinusoidal input with an AC current (or potential) output that is also sinusoidal but may differ in amplitude and be phase-shifted relative to the applied signal [122].

The impedance (Z), a complex quantity analogous to resistance in direct current (DC) circuits, is then calculated as the ratio of the AC potential (E) to the AC current (I) as a function of angular frequency (ω)

$$\omega = 2\pi f \tag{2.1}$$

$$Z(\omega) = \frac{E(\omega)}{I(\omega)} \tag{2.2a}$$

where f is the frequency.

Impedance can be expressed in complex notation as

$$Z(\omega) = Z'(\omega) + jZ''(\omega) \tag{2.2b}$$

where $Z'(\omega)$ is the real (resistive) component and $Z''(\omega)$ is the imaginary (reactive) component of the impedance, and $j^2 = -1$, is a complex number that enables the representation and calculation of phase differences in both the resistive and reactive aspects of the system's impedance response to the applied signal.

The frequency-dependent impedance spectrum provided a detailed "fingerprint" of the electrochemical interface.

EIS is relatively non-destructive due to the small amplitude of the perturbation signals, allowing for in-situ monitoring of corrosion processes and the formation or degradation of inhibitor films over extended periods on the same electrode sample. This capability is particularly valuable for studying the long-term stability and performance of corrosion inhibitors and for tracking dynamic changes at the interface [123,124].

EIS Experimental Procedure:

In the present study, EIS measurements were conducted using a three-electrode electrochemical cell, identical in configuration to that used for OCP and PDP studies, containing the 1.6310 steel working electrode, RE and CE. The experiments were performed at the stabilized OCP of the working electrodes to investigate the corrosion behavior under freely corroding conditions. To do this, a small amplitude AC voltage perturbation, 5 mV (rms), was superimposed on the chosen DC potential (OCP). The frequency of this AC signal was then swept logarithmically between 1 MHz and 1 mHz. Measurements were made at 10 points per decade of frequency to adequately resolve the impedance spectrum.

Data Representation and Interpretation:

The complex impedance data obtained from EIS experiments are commonly visualized and analyzed using two types of plots:

(a) Nyquist Plot: which plots the negative of the imaginary component of impedance ($-Z''$) against the real component (Z') for each frequency measured. Each point on the plot corresponds to the impedance at a specific frequency, with frequency decreasing from left to right.

(b) Bode Plot: which consists of two graphs plotted against the logarithm of frequency (log f) - Bode Magnitude plot (logarithm of the impedance modulus |Z| versus log f) and the Bode Phase Plot (phase angle, $\phi = \arctan(Z''/Z')$ versus log f).

Nyquist plots exhibit one or more semicircles. In a system dominated by a single time-constant (e.g., charge transfer resistance in parallel with double-layer capacitance), a single semicircle is observed. The diameter of this semicircle, when it intercepts the real axis, is related to a resistance value, most commonly the charge transfer resistance (R_{ct}). The observed semicircles tend to be "depressed," meaning their centers lie below the real axis, indicating a deviation from ideal capacitive behavior and is often attributed to factors such as surface roughness, porosity of surface films, non-uniform current distribution, or a distribution of time constants at the interface [123,125].

The Bode plot explicitly shows the frequency dependence of both the impedance magnitude and the phase shift. For a purely resistive element, it would show a frequency-independent |Z| and a phase angle of 0°. A purely capacitive element would exhibit a slope of -1 in the log |Z| vs. log f plot and a constant phase angle of -90° [126].

In corrosion studies, the impedance at very low frequencies in the Bode magnitude plot is often taken as an indicator of the overall corrosion resistance (approaching $R_s + R_{ct}$ for simple systems). The shape and maximum value of the phase angle peak in the Bode phase plot, as well as the frequency at which it occurs, provide valuable information about the capacitive nature of the interface and the presence of protective films. For instance, a broad phase angle peak approaching -90° over a wide frequency range often suggests good capacitive (barrier) properties of a film [127].

The combination of Nyquist and Bode plots provides complementary information that facilitates detailed interpretation of EIS data. While Nyquist plots are effective for visualizing time constants as semicircles and are widely used for fitting data to equivalent electrical circuits, they do not explicitly display frequency information for each data point. Bode plots,

on the other hand, clearly illustrate the frequency dependence of |Z| and φ, making it easier to identify frequency ranges dominated by specific electrochemical processes (e.g., solution resistance at high frequencies, capacitive behavior at intermediate frequencies, diffusion-controlled processes at low frequencies) and to assess the quality of the experimental data (e.g., by observing noise levels, particularly at low frequencies).

Equivalent Electrical Circuit (EEC) Modelling:

Analysis of EIS data using EEC models provides parameters for the corrosion process and inhibitor behavior. An EEC is a theoretical circuit composed of ideal electrical components such as resistors (R), capacitors (C), and sometimes inductors (L), along with more specialized electrochemical elements like the Constant Phase Element (CPE) and the Warburg impedance (Z_W). These elements are arranged in a specific configuration to represent the plausible electrochemical and physical processes occurring at the metal/electrolyte interface. The experimental impedance spectrum is then fitted to the chosen EEC using complex non-linear least squares (CNLS) fitting algorithms to determine the values of the circuit elements with chi-squared values (χ^2) indicating goodness of fit [128].

In the EIS results obtained from the corrosion and inhibition studies on 1.6310 steel:

- R_s (Solution Resistance): Represents the ohmic resistance of the electrolyte solution between the working electrode and the tip of the reference electrode's Luggin capillary. Its value depends on the electrolyte conductivity, cell geometry, and electrode spacing.
- R_{ct} (Charge Transfer Resistance): Represents the resistance to the Faradaic corrosion reactions (electron transfer) occurring at the metal/electrolyte interface. R_{ct} is inversely proportional to the corrosion rate; a higher R_{ct} value signifies a lower corrosion rate and thus better corrosion resistance. A significant increase in R_{ct} upon addition of an inhibitor is a primary indicator of effective inhibition.
- C_{dl} (Double Layer Capacitance): Represents the capacitance of the electrical double layer formed at the interface due to charge separation. The value of C_{dl} is affected by the dielectric constant of the interfacial region, the thickness of the double layer, and the electrochemically active surface area. Changes in C_{dl} upon inhibitor addition indicate adsorption of inhibitor molecules (which may alter the dielectric constant or layer thickness) or changes in surface roughness. A decrease in C_{dl} often demonstrates effective inhibitor adsorption, as inhibitor molecules (typically having a lower

dielectric constant than water) replace water molecules at the interface, or due to an increase in the effective thickness of the dielectric layer.

- CPE (Constant Phase Element): This element is used in place of an ideal capacitor (C_{dl}) to account for non-ideal capacitive behavior, which manifests as a depressed semicircle in the Nyquist plot. This non-ideality can arise from surface heterogeneity, roughness, porous electrode structures, or a distribution of relaxation times.

The impedance of a CPE is given by:

$$Z_{CPE} = \frac{1}{Q(j\omega)^{\alpha}} \quad (2.3)$$

where Q is a CPE parameter (with units of $Fs^{(\alpha-1)}\ cm^{-2}$), ω is the angular frequency, and α is an empirical exponent, ranging from 0 to 1, that reflects the degree of deviation from ideal capacitive behavior. If α =1, the CPE behaves as an ideal capacitor with capacitance Q. If α = 0, it behaves as a resistor [129].

While not used for the modelling, the Warburg impedance (Z_W) is a circuit element used in EIS models to represent mass transport limitations of electroactive species. It arises when the rate of the electrochemical reaction is governed by the speed at which reactants (e.g., dissolved oxygen for corrosion, or an inhibitor molecule) can diffuse through the solution to the electrode surface. It appears in the Nyquist plots as a straight line with a 45° angle to the abscissa.

The Randles Circuit, consisting of R_s, C_{dl}, and R_{ct} (without Z_W), was chosen as the EEC to represent the electrochemical processes occurring at the 1.6310 steel/electrolyte interface under the specific experimental conditions. For simplicity, the inhibitor film resistance and capacitance were respectively evaluated as part of R_{ct} and C_{dl}, with C_{dl} modeled as a CPE to account for surface non-ideality. Experimental data were fit to the model using proprietary software from the potentiostat manufacturer (assessed by a low χ^2 value from the fitting software) [130,131].

EIS, coupled with EEC modelling, provided qualitative information about the corrosion of 1.6310 steel and the effects of inhibitors such as the mechanism of corrosion, the inhibitor adsorption and film properties, and the Inhibition Efficiency (IE %) evaluated as:

$$IE\ (\%) = \frac{R_{ct,inh} - R_{ct,uninh}}{R_{ct,inh}} \times 100 \quad (2.4)$$

Where $R_{ct,inh}$ and $R_{ct,uninh}$ are the charge transfer resistances measured in the presence and absence of the inhibitor, respectively.

2.2.2.3 Potentiodynamic Polarization

Potentiodynamic polarization (PDP) involves systematically varying the potential of the working electrode (1.6310 steel) away from its OCP, typically scanning in both the positive (anodic) and negative (cathodic) directions, at a controlled, constant rate, while simultaneously measuring the resultant current flowing through the electrode[132]. This method directly interrogates the kinetics of the constituent anodic (metal dissolution) and cathodic (oxygen reduction) reactions that collectively govern the overall corrosion process. PDP as an accelerative technique, forces the electrochemical system away from its natural equilibrium state (OCP). While this allows for the rapid assessment of corrosion kinetics and the extraction of parameters like i_{corr}, the application of significant polarization can, in some cases, irreversibly alter the electrode surface. Such alterations might include the formation of thick corrosion product layers, the initiation of pitting (if scanned to sufficiently high anodic potentials), or the stripping of adsorbed inhibitor films [57,123].

The relationship between the applied potential (E) and the logarithm of the measured current density (log j) is plotted to generate a polarization curve. In many corrosion systems under activation control, this curve exhibits linear regions, known as Tafel regions, at potentials sufficiently displaced (typically >50 – 100 mV) from the E_{corr}. The theoretical basis for this current-potential relationship is provided by the Butler-Volmer equation (See Eqn. 1.7 and 1.8), which describes the kinetics of electrode reactions when the rate is limited by the charge transfer step.

The PDP curve can reveal distinct characteristic regions reflecting the electrochemical behavior of the steel across the scanned potential range. These include: Active Dissolution Region – where the rate of metal dissolution increases exponentially with increasing anodic potential; Passive Region – characterized by a significant decrease in current density despite further increases in anodic potential, due to the formation of a protective surface film (e.g., an oxide layer or adsorbed inhibitor layer) and Transpassive Region – characterized by very high anodic potentials which may result in the passive film break-down, leading to a renewed increase in current density, often associated with pitting corrosion or oxygen evolution [54,62,132].

The overall shape of the PDP curve provided qualitative information which pertains to the steel's corrosion mechanism (e.g., general corrosion, tendency to passivate) and its susceptibility to localized forms of attack like pitting corrosion in the specific test environment, both in the absence and presence of inhibitors.

Due to this potentially "destructive" aspect of PDP, electrochemical experiments in this study were sequenced thus: OCP → EIS → PDP.

PDP Experimental Procedure:

PDP experiments were conducted using the same three-electrode electrochemical cell configuration as described for OCP measurements, comprising the 1.6310 steel WE, RE, and a CE. Prior to initiating the polarization scan, the OCP of the working electrode was monitored until stability was achieved, establishing the E_{corr} of the system. The potential scan was initiated at a potential significantly cathodic to the OCP (-500 mV relative to OCP) and then swept in the anodic direction, passing through the OCP, up to a predetermined anodic potential limit (to +500 mV relative to OCP). The scan was performed at a constant, slow scan rate of 0.2 mV/s. The choice of scan rate allowed the electrochemical system to approach a quasi-steady state at each applied potential, a prerequisite for accurate Tafel extrapolation and kinetic parameter determination. Faster scan rates could introduce distortions due to capacitive charging currents or may not allow sufficient time for surface concentrations or film properties to equilibrate, leading to skewed Tafel slopes and corrosion current, i_{corr}, values [119,132].

PDP Data Analysis: Tafel Extrapolation

Tafel extrapolation is applied to PDP curves to determine corrosion kinetic parameters. The method relies on the observation that, under activation control, the relationship between overpotential and log |i| becomes linear at potentials sufficiently far from E_{corr}. These linear segments are known as Tafel regions. The Tafel regions on both anodic and cathodic branches of the polarization curve are typically at least 50 – 100 mV, away from the measured E_{corr}[133,134]. Straight lines were fitted to the identified linear (Tafel) regions using linear regression. The slopes of these fitted lines yield the anodic Tafel slope (βa) and the cathodic Tafel slope (βc). These slopes are characteristic of the kinetics of the anodic and cathodic reactions, respectively, and represent the change in potential required to alter the current density by one order of magnitude. The corrosion potential (E_{corr}) and the logarithm of the corrosion current density are determined from the point of intersection of the extrapolated anodic and cathodic Tafel lines.

PDP analysis, through Tafel extrapolation, yielded several critical parameters that enabled the characterization of corrosion inhibitor performance: E_{corr}, i_{corr}, βa, βc, passivation parameters and corrosion rate and inhibition efficiency.

Calculation of Corrosion Rate:

The reported corrosion rates were evaluated with the BioLogic EC-Lab® software using the Tafel Fit method. EC-Lab® applies the Nelder and Mead Simplex method to improve the goodness-of-fit (represented by minimized χ^2 values), fitting the data in the selected Tafel region to the Stern-Geary equation [131]. Four adjustable electrochemical parameters: i_{corr}, E_{corr}, β_c and β_a, were optimized till stable values were obtained and the i_{corr} finally used to calculate the corrosion rates (CR) according to the formula [132]:

$$CR = \frac{i_{corr} \bullet K \bullet EW}{\rho \bullet A} \quad (2.5)$$

Where K = 3272 mm A^{-1} cm^{-1} yr^{-1}, is a constant that specifies the unit of the corrosion rate, EW is the equivalent weight of the corroding metal, calculated by dividing the atomic weight of the pure metal by the number of electrons (n) involved in the corrosion process (n = 2 for Fe → Fe^{2+}). EW for steel was therefore 28.25. ρ is the density of the metal 7.85 g cm^{-3} [132] and A is the exposed surface area of the metal coupon during the experiment.

The corrosion inhibition efficiency of the tested inhibitor is calculated from the i_{corr} and CR according to the formulae below:

$$IE\ (\%) = \frac{i_{corr}(blank) - i_{corr}(inhibitor)}{i_{corr}(blank)} \bullet 100\% = \frac{CR(blank) - CR(inhibitor)}{CR(blank)} \bullet 100\ \% \quad (2.6)$$

Uncertainties associated with these directly determined or fitted parameters were obtained from statistical analysis of replicate measurements or the fitting software's output. These uncertainties were then propagated to derived quantities, such as the CR and IE, following standard error propagation principles for fundamental arithmetic operations.

Post-irradiation electrochemical measurements were performed with a Gamry 1010E™ potentiostat (Gamry Instruments Inc., USA) in the conventional three-electrode cell configuration. The working electrode was a 5mm-diameter 1.6310 coupon with 0.50 cm^2 exposed surface area. A platinum wire was used as counter electrode while Ag/AgCl in saturated 3 mol/dm^3 KCl was used as a reference electrode.

Before each measurement, the polished WE was polarized for 10 min with −1 V vs Ag/AgCl potential to remove intrinsic surface oxides and to create a more reproducible initial test surface. The electrochemical measurements were performed in triplicates to ensure reproducibility, at room temperature (25 ± 2 °C) and in aerated condition.

2.2.3 Water Abrasive Suspension Cutting

To evaluate the effectiveness of the selected corrosion inhibitor, a non-radioactive steel block (Figure 2.1) was transported to ANT Lübeck, where it underwent a controlled WAS cutting process (ConSUS) [32]. This technique, patented by ANT, is specifically used for segmenting structural materials such as RPV and its internals.

After preliminary immersion tests followed by electrochemical analysis, an optimal concentration (1.5 vol.%) of the selected inhibitor was used for the WAS cutting of the steel block. WAS cutting involves directing a high-pressure jet of water mixed with abrasive particles—typically 80 HPX garnet—onto the steel surface. The resulting jet, comprising approximately 97.5% water and 2.5% abrasive by volume, effectively cuts through the steel block. A schematic overview of the WAS cutting setup is presented in Figure 2.4.

In the process described in Figure 2.4, a portion of the pressurized water is diverted into an Abrasive Mixing Unit, where it is combined with the abrasive material to form a suspension. This suspension is then forced through a high-pressure hose and nozzle, producing a stable and focused cutting jet. The steel block is securely fixed underwater within a cutting basin, ensuring immersion throughout the process. The cutting water—ordinary tap water dosed with a commercial additive (Liquitech 227P), is also mixed with a 1.5 vol.% concentration of the selected corrosion inhibitor prior to the cut. Liquitech 227P is a dimethyl phosphonate-based sequestering agent for removing $CaCO_3$, MgOH, dirt and solids from water prior to use in WAS cutting operations. The primary purpose of this additive as stated in the technical datasheet is the protection of cutting nozzles and other equipment from premature wear [135].

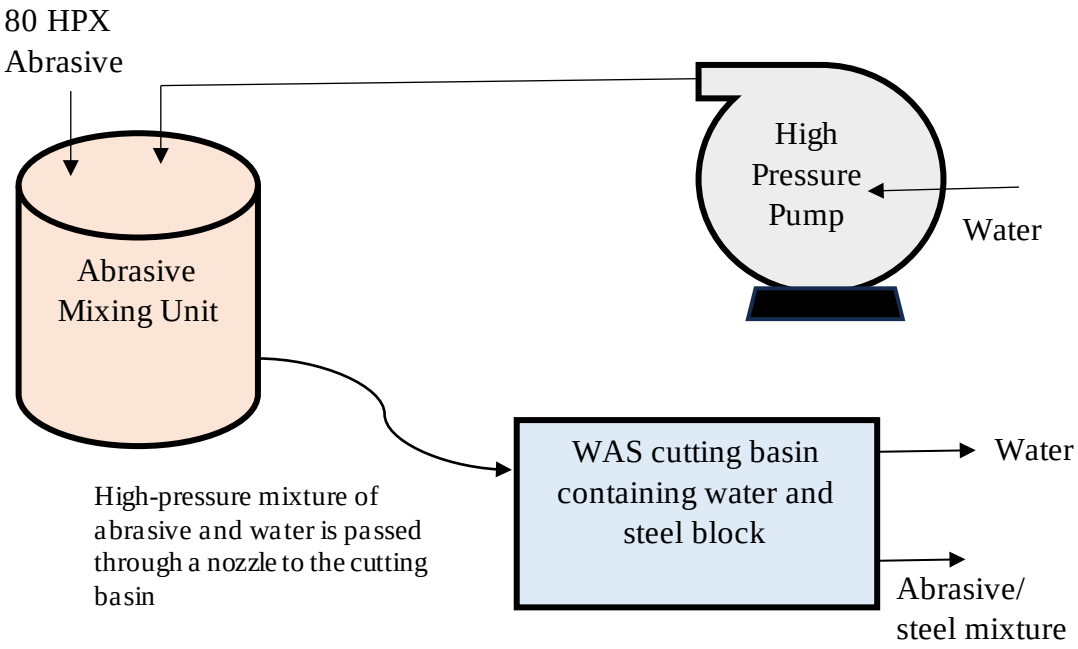

Figure 2.4: Schematic of the components of the WAS cutting process at ANT Lübeck.

Typical operational parameters during cutting included:

- **Water pressure:** 500–1500 bar
- **Water flow rate:** 3–10 l/min
- **Abrasive feed rate:** 0.2–1 kg/min

The WAS cutting process generated a secondary waste stream consisting of steel and abrasive particles. These were collected after the cut, along with liquid samples including the untreated tap water, inhibitor-dosed tap water, and the cutting suspension (WAS). Surface characterization of the sampled steel-abrasive mixture was performed over an 18-month period to observe the corrosion inhibitor performance. This integrated experimental approach allowed for both the segmentation of the RPV steel and the evaluation of corrosion inhibition under near-process conditions.

2.2.4 Surface Analyses of Studied Steel Samples

2.2.4.1 X-ray Photoelectron Spectroscopy and Scanning Electron Microscopy

XPS and SEM with Energy Dispersive X-ray Spectroscopy (SEM-EDX) were performed in the controlled area of the KIT-INE to characterize the exposed surfaces of the steel coupons post-potentiometric experiments and to monitor the corrosion of the steel particles post-WAS cut with the selected inhibitor over some time.

Chemical composition and surface morphology of the coupons and steel particles were obtained by scanning electron microscopy using a FEI QUANTA 650 FEG, with a field emission electron gun allowing a 1 nm resolution at 30 kV with secondary electrons. Scanning electron microscopy involves focusing a tiny electron probe on the surface of a sample in a two-dimensional raster. Images created by secondary electrons (SE) provide information on surface morphology at lateral resolution down to a few nanometers. Backscattered electron (BSE) images provide a material contrast because of different electron backscatter efficiencies of the elements. Moreover, the detection of X-ray emissions enabled the quantification of atomic concentrations on a micrometer scale, a capability offered by energy-dispersive X-ray spectroscopy (EDX). Data analysis was performed using the Pathfinder software (Thermo

Fisher Scientific Inc.) for the QUANTA 650 FEG Instrument. Elemental compositions are reported with associated uncertainties expressed as ±3σ (three standard deviations). This statistical notation indicates a 99.73% confidence interval for the measurement, reflecting the precision and detection limits of the quantitative EDX analysis.

XPS analysis provides a very surface-sensitive technique for the characterization of the surface chemistry of solid phases without the need for elaborate sample preparation. It was used to obtain a detailed elemental composition of the exposed surface of the steel surfaces used throughout this study with and without the corrosion inhibitor. XPS measurements were performed on a VersaProbe II ULVAC-PHI spectrometer with an Al Kα (1486.7 eV) monochromatic X-ray source (see Figure 2.5). XPS measurements were performed in an ultra-high vacuum chamber within the device allowing measurements under vacuum and in strictly anoxic conditions. The PHI MultiPak program v9.9 was used for data analysis and spectra fitting.

Figure 2.5: X-ray photoelectron spectrometer at KIT-INE (ULVAC-PHI, model VersaProbe II). Courtesy of Dr. Dieter Schild.

To calibrate the binding energy scale of the spectrometer, established binding energies of elemental lines from pure metals were utilized (Cu $2p_{3/2}$ at 932.62 eV, Au $4f_{7/2}$ at 83.96 eV). The binding energies of elemental lines of samples are charge-referenced to O 1s of hydroxide at 531.4 eV as an internal binding energy reference, comparable to referencing to C 1s of

hydrocarbon at 284.8 eV. Molar fractions of oxygen species were determined through curve fitting of the O 1s spectra using a Shirley background and Gaussian functions. Using soft X-rays from Al means that the information depth (95% of signal) of the Fe 2p spectrum for e.g. magnetite is ~2.7 nm (angle sample surface – analyzer: 45°), determined from the inelastic mean free path (IMFP) of photoelectrons [136,137]. The estimated relative error of molar fractions falls within ± 10%, while the error of elemental lines' binding energies is estimated to be within ± 0.2 eV. In this study, relevant reference binding energies for O 1s are specified as follows: 529.6 eV (Fe_2O_3), 530.0 eV (Fe_3O_4), 530.1 eV (FeO*OH), 531.2 eV (FeOO*[1]H). Reference binding energies for the S $2p_{3/2}$ elemental lines are 169 eV (sulphate), 167 eV (sulfite), 167.6 eV (sulfone), and 400.4 eV (organic matrix amine) for the N 1s.

The XPS spectra presented in this study are plots of electron intensity given as counts versus the binding energy, E_B,[138] from which information regarding the chemical states of the steel surfaces with and without corrosion inhibition and in the presence and absence of ionizing radiation were obtained.

2.2.4.2 Quartz Crystal Microbalance

QCM experiments were performed to study the adsorption/desorption behavior of the components of the selected corrosion inhibitor (C.Inh #4) on iron as surrogate for 1.6310 steel, and to determine the thickness and other properties of adsorbed films. The QCM measurement principle is based on the Sauerbrey equation that establishes a linear relationship between frequency shift and mass change for the detection of molecule-surface interactions especially for rigid, thin and evenly distributed films. The Sauerbrey equation may no longer hold for thick, viscoelastic films. As hydrated inhibitor molecules are adsorbed on the Fe-coated quartz crystal surface and ordered, the mass gain causes a drop in its fundamental frequency change while the change in energy dissipation (energy loss due to internal friction and deformation within the layer) could increase [139]. A typical measurement result is illustrated in Figure 2.6.

The Sauerbrey equation is given as [140]:

$$\Delta f_n = -n\frac{2f_{0,n}^2}{A\sqrt{\mu_q \rho_q}}\Delta m \qquad (2.8)$$

$$\Delta f = -n\frac{1}{C}\Delta m \qquad (2.9)$$

[1] * Denotes the oxygen of the corresponding binding energy.

Where:

f_0 is Resonant frequency of the fundamental mode (Hz), Δf is the normalized frequency change (Hz), Δm is the mass change (g), n is the harmonics of the fundamental frequency, Δf_n is the change in the frequency harmonics, A is the Piezoelectrically active crystal area (area between electrodes, cm^2), ρ_q is the density of quartz (ρ_q = 2.648 g cm^{-3}), μ_q is the shear modulus of quartz for AT-cut crystal ($\mu_q = 2.947 \cdot 10^{11}$ g $cm^{-1} \cdot s^{-2}$) and C is the mass sensitivity constant, related to the properties of the oscillating quartz QCM substrate. For a 5 MHz crystal, C equals 17.7 ng/($cm^2 \cdot$ Hz).

The change in energy dissipation (ΔD) quantifies the energy lost per oscillation cycle due to internal friction and deformation within the adsorbed layer and the coupled solvent. The Sauerbrey equation is a simplified model that assumes the adsorbed inhibitor layer is perfectly rigid and elastic. Under these ideal conditions, the energy dissipated by the oscillating crystal remains constant, or the changes are negligible.

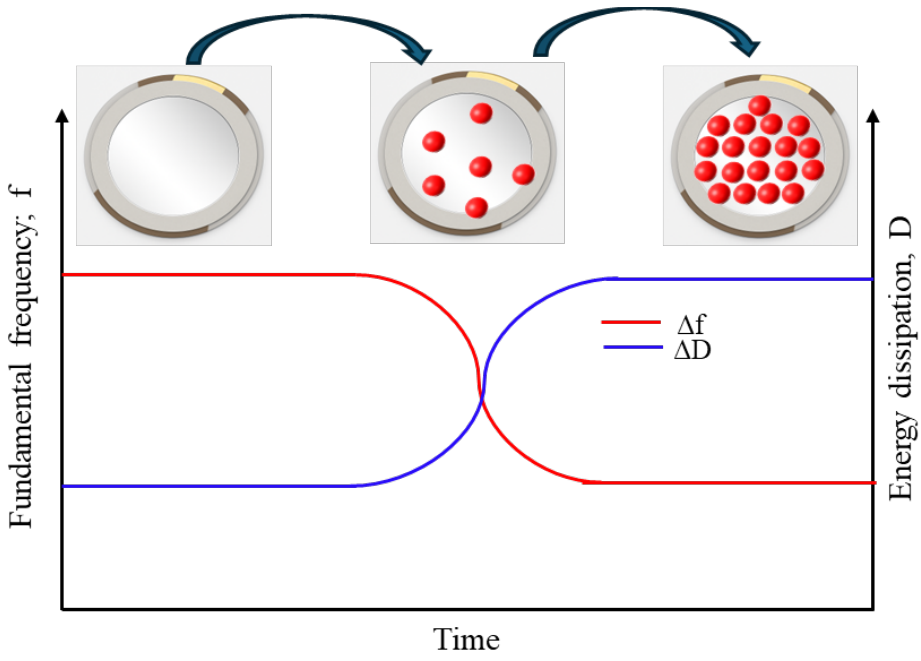

Figure 2.6: Effect of mass deposition and arrangement on the fundamental frequency and energy dissipation changes of a quartz crystal. Δf and ΔD represent measured fundamental frequency and energy dissipation changes respectively. When inhibitor molecules are added, Δf starts to decrease & ΔD increases. A stable Δf & ΔD is reached when full surface coverage is attained.

The QCM setup (Fig. 2.7 and 2.8) used in the present study included the following: a two-channel QCM-I device (SEMILAB, Budapest, Hungary) with temperature control (4°C – 80°C ± 0.02°C), AT-cut Fe-coated QCM sensors (Quantum Design GmbH) with nominal frequency

5.000 MHz ± 20 kHz, a peristaltic pump for flowrate control and a selection valve for solutions when running parallel experiments. Figure 2.7 shows the setup of the devices used for the QCM experiments for defined inlet of solutions. The QCM device is connected to a Gamry 1010E potentiostat for data acquisition and program control. Figure 2.8 shows the connection of the flow cell assembly and gives the dimensions of an AT-cut Fe-sensor. AT-cut quartz are cut at a specific crystallographic angle (35.25° from z-axis), vibrate in the thickness shear-mode, optimized for temperature stability and have a frequency sensing range of 0.5 – 300 MHz [141].

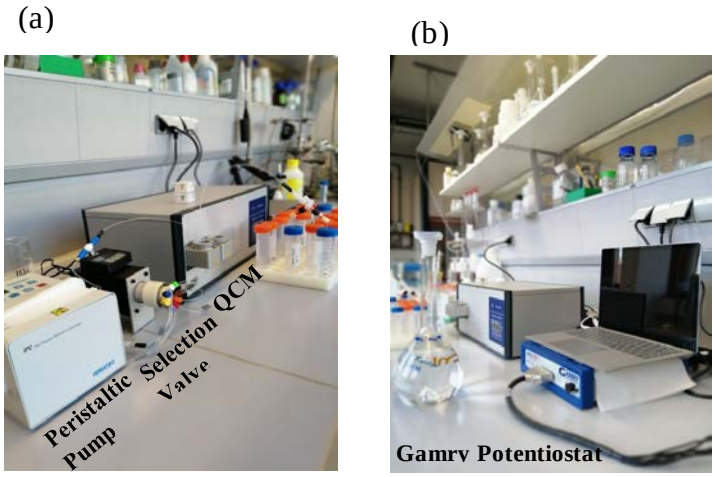

Figure 2.7: QCM-I setup at the KIT-INE. (a) A peristaltic pump, selection valve and the QCM device (Left). (b) A Gamry potentiostat and PC serving as interface with the QCM device (Right).

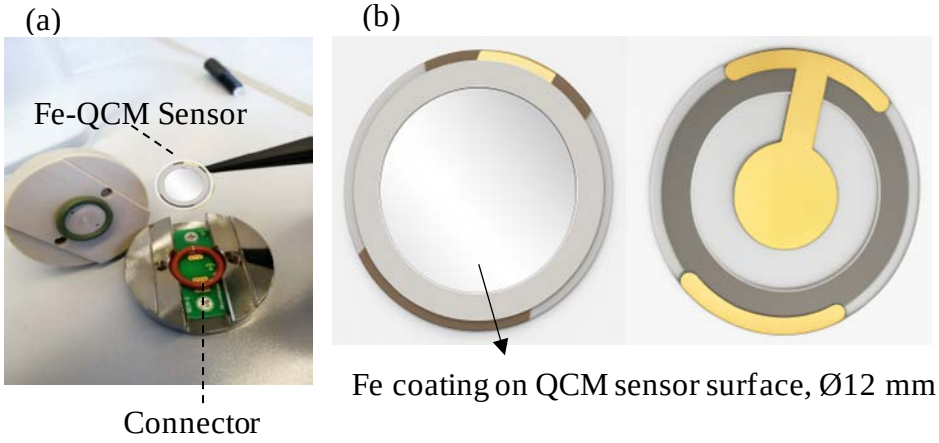

Figure 2.8: (a) Standard flow cell assembly showing QCM sensor and electrode connections (b) Left – Fe-coated QCM sensor: central region represents quartz areas with Fe coating. Right – backside of the quartz with golden contact areas.

Experimental Procedure: Inhibitor adsorption on Fe-QCM

Initially, the Fe-QCM sensor was cleaned with ethanol and dried with Argon. Concurrently, the inhibitor solutions were prepared at the required concentrations (300 ppm TACT and 5000 ppm TEA, both identified components of the selected inhibitor – C.Inh #4). To establish a

stable baseline, ultrapure water was introduced into the system at a flow rate of 0.1 ml/min, and the QCM sensor was allowed to stabilize until a steady baseline reading was achieved. Once stability was confirmed, the selection valve was switched to the inhibitor solution, and the frequency shift (Hz) on the QCM sensor was continuously monitored. A decrease in frequency indicated the adsorption of the inhibitor onto the Fe-QCM sensor surface. Following the observation of adsorption, the flow was switched back to ultrapure water for a rinsing period. This cycle (water → inhibitor solution → water) was subsequently repeated twice to verify the consistency and reproducibility of the adsorption and desorption processes.

Furthermore, effects of flow rate variation were investigated. A schematic diagram showing sample injection into the flow cell via the peristaltic pump and selection valve is given in Figure 2.9. Samples were pumped at a known flowrate from the "Running buffer" into the flow cell containing the QCM sensor. Prior to this, the connection lines were purged by selecting the "Sample load/prime" via the selection valve to remove trapped air bubbles from the line, which could affect measurements and prime the line for sample injection.

QCM experiments were performed in 'static mode' and in 'dynamic mode'. In static mode, the Fe-coated QCM sensor was immersed in the inhibitor solution, allowing adsorption under equilibrium conditions. In 'dynamic mode,' the sensor was placed in the flow cell, with an inhibitor solution pumped through it while frequency changes were monitored

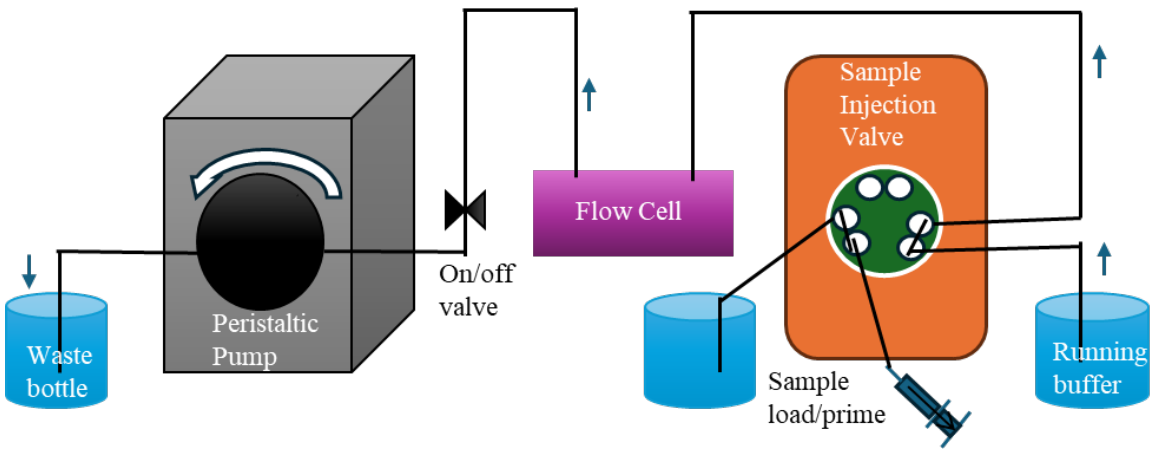

Figure 2.9: Schematic diagram for 10-port valve with sample sucked up from a sample vial.

2.2.4.3 Ellipsometry

To further characterize the thickness of the adsorbed inhibitor films, spectroscopic ellipsometry measurements were performed at the KIT Institute of Functional Interfaces (IFG) using an in-house ellipsometer. The samples analyzed were the Fe-coated QCM sensors that had previously been exposed to TEA and TACT solutions, as described in the QCM methodology.

Ellipsometry quantifies the change in the polarization state of light upon reflection from a surface, which is expressed by two fundamental parameters which are highly sensitive to the refractive index and absorptive properties of films on the surface [142,143]:

(a) Psi (Ψ): Representing the change in the ratio of the amplitudes of the p-polarized (parallel to the plane of incidence) and s-polarized (perpendicular to the plane of incidence) components of the electric field.
(b) Delta (Δ): Representing the change in the phase difference between the p-polarized and s-polarized components upon reflection.

This approach allowed for a complementary analysis of the inhibitor film thickness, providing insights into the optical properties and physical dimensions of the adsorbed layers. Film thickness was determined by fitting the measured Ψ and Δ to an appropriate optical model of the film-substrate system.

2.2.5 Characterization of the Selected Inhibitor

A composition analysis of the selected inhibitor, C. Inh #4, was performed via a series of experiments to determine the active components of the formulation.

The XPS spectra of the pure inhibitor and that of a steel surface treated with the inhibitor were analyzed. In addition, Electron Ionization Mass spectrometry (EI-MS), column chromatography and NMR spectroscopy - including proton (^{1}H), Carbon (^{13}C), and 2D NMR (Homonuclear Correlation Spectroscopy - COSY) were all performed to qualitatively characterize the composition of the inhibitor formulation.

2.2.5.1 Column/Paper Chromatography

The corrosion inhibitor (C.Inh #4) was stripped in a column using a Water – Isopropanol (Fischer Scientific, Darmstadt, Germany) mixture in a 1:20 ratio. Different fractions of the

eluent were collected in 10 ml glass vials and numbered accordingly. For each of the collected fractions, paper chromatography was used to determine the number of distinct components present. Fractions with single/similar species were collected and further purified in a Schlenk Line, removing trace amounts of the stripping solvent mixture present. The purified fractions were further analyzed with NMR spectroscopy in order to identify distinct compounds isolated.

2.2.5.2 NMR Spectroscopy

Deuterated water (D_2O) was purchased from VWR International and used as purchased. 50 µl of the tested sample was pipetted into a high-resolution NMR tube followed by the addition of 550 µl of D_2O. All NMR spectra were measured using a Bruker Avance III 400 MHz spectrometer at 300 K. ^{1}H spectra were recorded at a transmitter frequency of 400.13 MHz and ^{13}C spectra at 100.63 MHz. A BBFO^{plus} sample head with z-gradient and direct x-detection was used. The chemical shifts (δ) were internally referenced to TMS (δ(TMS) = 0 ppm). ^{1}H and ^{13}C spectra were recorded with 32,000 datapoints for improved resolution. Signal multiplicities are typically given as follows: s (singlet), d (doublet), t (triplet), q (quartet), quin (quintet), sex (sextet), sept (septet), m (multiplet) and br. s (broad signal).

2.2.5.3 Mass Spectrometry

The electron ionization mass spectra (EI-MS) were measured using a JEOL AccuTOF GC-Alpha coupled to an AGILENT 7890B Gas Chromatography (GC) (Santa Clara, CA, United States) system. All mass spectra were recorded in the mass spectrometry department of the Organic Chemistry Institute of the Ruprecht-Karls-University Heidelberg [144].

2.2.6 Irradiation Experiments:

To investigate the effect of ionizing radiation on the effectiveness of TEA and TACT inhibitors, irradiation experiments were conducted in the KIT-INE shielded boxline (INE-ABL). Given the absence of a dedicated gamma-irradiation source as a surrogate for activated RPV steel within the institute, initial experiments were performed to identify and characterize suitable alternative radiation sources for sample irradiation. Two primary candidates were considered: an activated stainless steel spring section from the plenum of the spent nuclear fuel rod – SBS 1108-N0204 irradiated at PWR Gösgen, and a spent MOX fuel segment from a fuel rod (KWU 14.28 5813) irradiated at Obrigheim NPP. To accurately determine the expected dose rates from these sources and to select an optimal irradiation configuration for the inhibitor solutions,

a series of preliminary experiments were conducted. These involved irradiating deionized water samples, deploying Thermoluminescent Dosimeters (TLDs) in both autoclaves and specialized irradiation vials, and utilizing Fricke dosimetry. The data from these preliminary experiments were essential for ensuring controlled and quantifiable radiation exposure for the subsequent inhibitor irradiation studies.

In the first setup, the solution-filled autoclave was wrapped in a nylon bag and placed in the INE ABL. This was a precaution against sample contamination and to guarantee safe handling post-irradiation. The activated steel sample was placed underneath the nylon-wrapped autoclave at the exact position for each experiment. In the second setup, a carousel made from polyethene was constructed to handle 16 glass vials radially positioned around a central hole containing the source as shown in Figure 2.10.

2.2.6.1 Sample Preparation

50ml of deionized water was used as a blank solution before the irradiation of the inhibitor solutions. Fricke solution with composition 1 mM $Fe(NH_4)_2(SO_4)_2$, 1 mM NaCl, and 0.4 M H_2SO_4 was prepared for use as a chemical dosimeter according to the E61 Committee ASTM Standard [145]. 5000 ppm TEA and 300 ppm TACT solutions were prepared by dissolving weighed quantities of high-purity TEA and TACT in deionized water to prepare the needed concentrations. 10ml of each solution was loaded into borosilicate irradiation glass vials. Each solution was prepared in an argon-saturated glovebox and degassed with argon before irradiation to reduce the presence of dissolved oxygen.

2.2.6.2 Irradiation of Inhibitors

For the first experiment irradiating the blank solution, 50ml of deionized water was loaded into the autoclave in an argon-saturated glovebox. Gamma irradiation was performed using a piece of the activated stainless-steel spring as shown in Figure 2.10 (steel spring itself) and within the setup in Figure 2.11. Source properties include:

1. Main gamma contributor: Co-60
2. Source specific activity: $8.4 \cdot 10^7$ Bq/g [146]
3. Mass of steel spring: 10 g
4. Gamma dose rate at contact: 1.6 Gy/h at contact (measured at the European Commission Joint Research Center, Karlsruhe, JRC-KA)

Higher dose irradiation was performed with a spent MOX fuel segment (Figure 2.12) as a radiation source. Source properties are highlighted below [146]:

1. Fuel type: Mixed Oxide fuel (MOX) with 3.2% Pu_{fiss}
2. Pellet length and diameter: 11 mm/9.08 mm
3. Mass of fuel: 49.1 g_{HM}
4. Contact dose: ~ 6 Gy/h

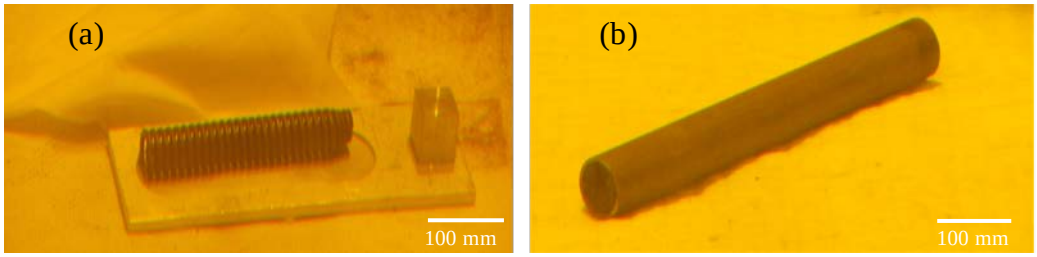

Figure 2.10: Radiation sources for irradiation experiments in the INE-ABL: (a) Activated stainless steel spring from the plenum of irradiated UO_x fuel rod segment (SRS 1108-N0204) (b) Cladded spent MOX fuel rod (KWU 14.28 5813). Images courtesy of Dr. Tobias König.

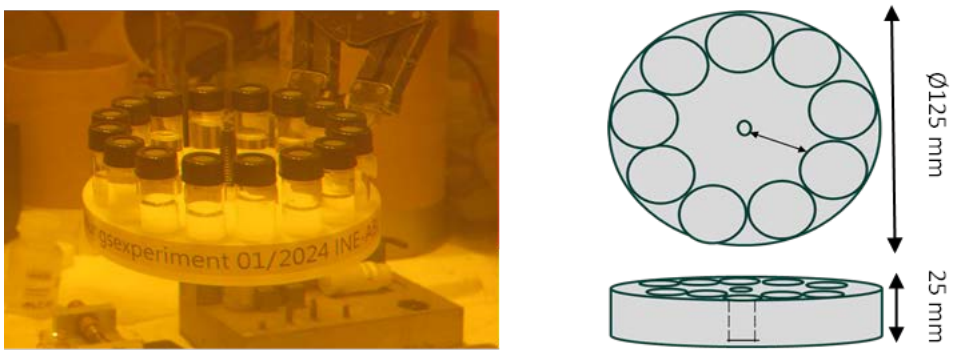

Figure 2.11: Carousel with samples and activated spring source at the center in the INE-ABL. Image courtesy of Dr. Tobias König (left). Schematic of the sample holder showing dimensions, not drawn to scale (right)

2.2.6.3 Dosimetric experiments

Absorbed dose to the samples and the irradiation dose rate from the available sources in the INE-ABL were experimentally determined utilizing solid-state dosimetry with TLDs and chemical dosimetry using Fricke solution. The absorbed dose from the activated spring was measured using TLDs and Fricke solution while the absorbed dose from the spent MOX fuel segment was measured exclusively using Fricke solution due to the relatively high contact dose rate from the source.

Solid-State Dosimetry:

Twenty pre-annealed TLDs of size $3 \times 3 \times 0.9$ mm made from LiF crystals, were positioned inside the autoclave (at the bottom, cylindrical surface, and at the top), up to the expected water level in the autoclave to measure absorbed dose to the blank solution in the autoclave. For the second setup, eleven TLDs were put inside the glass vials as shown in Figure 2.12, to measure the absorbed dose in the inhibitor solutions in the low-dose irradiation experiment. An extra unirradiated TLD was included in each case to measure and account for background dose during handling and transport. Irradiation of TLDs was for a period of 4 hours to prevent saturation after which evaluation was performed to determine the absorbed dose and dose rate. After irradiation, the TLDs were evaluated at the KIT-SUM laboratory using a Toledo 654 TLD reader. The TLDs were heated up to 300 °C at a heating rate of 10 °C/s to anneal irradiation-induced defects. Photons are emitted in the process yielding a glow curve which shows glow impulses per channel. The total number of impulses correlates with the absorbed dose per detector. Two reference TLDs irradiated with defined doses, were used for drift correction in the photomultiplier. Two TLDs were also evaluated to correct for background radiation during the transport of the detectors between the irradiation and read-out.

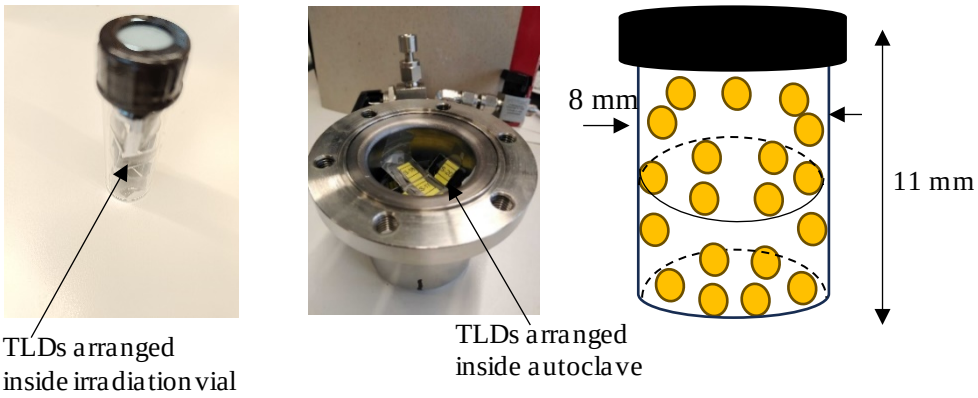

Figure 2.12: TLDs arranged in irradiation vial and in autoclave (left and middle images). Schematic of TLD arrangement inside an irradiation vial (right).

Fricke Dosimetry:

To determine experimentally the absorbed dose to the inhibitor solutions and the blanks in the experiments, as well as the validation of the numerical computation of radiation field around the solutions using Monte Carlo simulation, Fricke dosimetry was performed.

Dosimeter Readout:

A Fricke dosimeter is a chemical dosimeter that measures ionizing radiation by detecting changes in the absorption of light caused by the oxidation of ferrous ions (Fe^{2+}) to ferric ions (Fe^{3+}). The extent of this change is proportional to the radiation dose received. When evaluation is done with a spectrophotometer, the absorbed dose to the Fricke solution is calculated following the procedure outlined by ASTM E61 Committee [145], with Eqn. 2.10

$$D_F = \frac{\Delta A}{\rho \bullet l \bullet \varepsilon \bullet G} \tag{2.10}$$

where ΔA is the difference in absorbance value of the Fricke solution before and after irradiation, ρ is the density of the Fricke solution which is approximately 1.024 g/cm^3 [144], l is the path length through the photometric cell i.e. the cuvette used for the UV-Vis measurements. The molar extinction coefficient, ε, measured at the wavelength of 304 nm is 217.4 m^2/mol. G is the radiation chemical yield (G-value) of Fe^{3+}. G-values for Fe^{3+} were taken from the literature [147] with the assurance that the G-value was unaffected by photon dose rates for instantaneous dose rates below 10^7 Gy/min [148]. The absorbed dose of water, D_W, can be calculated from ΔA and D_F by using the relation:

$$D_W = 1.004\ D_F \cong 278\ \Delta A \tag{2.11}$$

Dosimeter preparation:

The Fricke solution was prepared using ultrapure water from a Milli-Q system. The Fricke solution was prepared before the start of the experiments and stored away in a borosilicate glass bottle covered with aluminum foil in a dark cupboard to protect the solution from light and minimize self-oxidation processes [149]. Before each experiment and readout, a sample was placed near the UV-spectrophotometer and measured as a control to verify the stability of the Fricke solution.

Irradiation and Calibration:

The Fricke solutions were irradiated over the same period as the irradiated samples to measure to total absorbed dose during irradiation. For calibration, a 10 ml Fricke solution sample was also irradiated with Cs-137 at the KIT-SUM calibration facility with 30 and 50 Gy nominal dose values, and readout was performed afterwards. The irradiation setup is shown in Figure 2.14 where the vials are placed on an irradiation stand. Cs-137 sources are shielded and located underneath the irradiation stand. The rotating source holder brings the desired source into the irradiation position. Collimators define the irradiation cone.

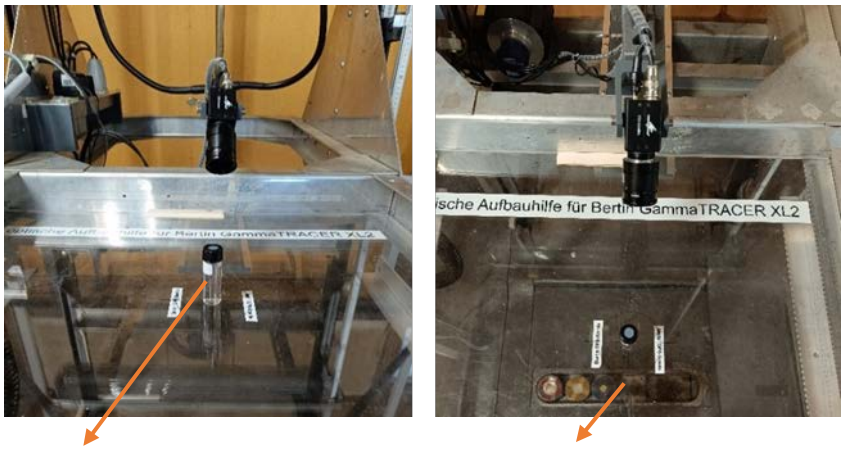

Figure 2.13: Fricke solution irradiation set up at the KIT-SUM irradiation facility: (a) sample on irradiation stand (b) opening aperture for Cs-137 source underneath the irradiation stand.

The Suprasil Quartz (QS) cuvette used for the UV-Vis measurements had a path length of 10.00 $\pm$ 0.01mm as described by the manufacturer. Given that the measurements were made with the same solution, cuvette and spectrophotometer, the denominator ($\rho \bullet l \bullet \varepsilon \bullet G$) was a constant.

Absorbance measurements were performed using an Agilent Cary 6000i UV-Vis NIR Spectrophotometer with measurements made between 600 nm and 190 nm. The cuvette compartment was maintained at 25.00 $\pm$ 0.01°C during measurement. Baseline correction was implemented by measuring the spectra of the matrix solution and subtracting from that of the Fricke solution in each case.

The temperature during each irradiation was recorded and temperature corrections to the reference temperature of 25°C were applied in line with the ISO/ASTM 51026-23E1 standard.

The absorbed dose of water (D_W) was obtained from D_F by applying the correction factors described in the standard. The corrections involve a dose conversion from Fricke solution to water, accounting for non-uniformity over the Fricke solution volume, the difference in radiation absorption properties of the Fricke solution and water and the sample holder wall effects. The experiments were made in duplicates to ensure reproducibility.

2.4 Numerical Simulations

Numerical simulations were performed using the PENELOPE/penEasy ("PENetration and Energy LOss of Positrons and Electrons") Monte Carlo particle transport code [150,151].

The objectives of the numerical simulations in this study were (a) to make estimates of dose rates from the radiation sources in the KIT-INE, complementing experimental dosimetry values and (b) to establish a reference case of radioactive steel-abrasive-water mixture, for estimating the expected absorbed dose range for inhibitor radiolysis.

For the simulations, a reference case was established and conservative estimates were made for RPV specific activity values.

Given that RPV steels are activated by neutron irradiation during their service life, the steel composition, neutron flux and the position of the steel relative to the core determine the type and quantities of activation products to be found in the steel. In the context of decommissioning RPVs, Cobalt-60 (Co-60, $t_{1/2}$ = 5.27 yrs) and Nickel-63 (Ni-63, $t_{1/2}$ = 100 yrs) are major concerns due to their long-term radiological hazard [6,152]. Specifically, Ni-63 is the most abundant activation product expected in a Light Water Reactor (LWR) on the timescale of deferred dismantlement [152]. Its century-long half-life makes its production optimal for this long-term perspective. While it is produced by direct neutron capture on the relatively low abundance natural isotope Ni-62 (3.6%), this is offset by the substantial amounts of nickel present in stainless steel components within the reactor. Ni-63 decays by emission of a relatively low-energy beta particle with a 66 keV endpoint energy, resulting in negligible Bremsstrahlung production for this isotope [152]. Co-60 on the other hand decays by emitting a medium-energy beta particle (0.32 MeV, 99%) to the 2.51 MeV level of excited Ni-60 which further decays to the ground state by emitting gamma rays (1.17 MeV & 1.33 MeV, 100%) [153]. Co-60 is thus crucial for assessing immediate dose rates and gamma shielding requirements, while Ni-63 dominates the long-term radiological inventory. Co-60 is therefore the radionuclide of interest in the present study.

A survey of specific Co-60 activity values for some decommissioned RPVs are outlined in Table 2.4.

Table 2.4: Estimated specific activity of Co-60 activity in the RPV from different PWR Nuclear Power Plants (NPP) after shutdown. The numbers are quoted from the references given.

NPP	RPV section	Specific Co-60 activity range (Bq/g)	Reference
Stade	RPV – Flange:		(Loeb et al, 2011) [154]
	Base body	9.90E+02 – 4.38E+03	
	Plating	2.02E+03 – 9.12E+03	
	RPV Core:		
	Base body	1.43E+05 – 2.09E+05	
	Plating	4.74E+05 – 6.15E+05	
	RPV Calotte:		
	Base body	4.96E+01 – 1.36E+02	
	Plating	1.21E+01 – 1.19E+02	
Forsmark (1.6 yr decay time)	RPV Body	1.12E+03	(Anunti et al, 2013) [155]
	Core shroud	2.01E+07	
Oskarshamn 3 (4yrs decay time)	RPV	2.28E+03	(Larsson et al, 2013) [156]
	Core shroud	5.5E+07	
Trino (30 years decay time)	RPV – Flange:		(Rossini et al, 2018) [157]
	Base body	2.08E+01	
	Plating	6.62E00	
	Vessel wall (core height)	2.86E+04	*Co-60 had 10.3% total radioactivity contribution 30 years after shutdown.
	Inner cladding (core height)	8.69E+06	

Prior to RPV segmentation, the reactor primary system undergoes decontamination. This operation removes surface contamination as well as oxide layers, which could contain significant activity levels. The specific activity of RPV activation products is determined based on factors including years of operation, total burnup and decay time after reactor shutdown. For the Kori-1 reactor (607 MW PWR) in South Korea, RPV Co-60 activities of $2.23 \cdot 10^{12}$ Bq in the core region and $5.25 \cdot 10^{6}$ Bq in the lower region were reported after 40 years of operation [158]. Moreover, the stainless-steel cladding of the RPV (core region), as seen in Table 2.4, is generally more activated than other regions. In addition, the specific activity of activation products in RPV materials are two orders of magnitude higher in BWRs than in PWRs [152].

2.4.1 Reference Case of Steel-Abrasive-Water Mixture

The PENELOPE Monte Carlo code was employed to simulate radiation transport from a Co-60 source with an activity of 10^{9} Bq. A total activity of 10^{9} Bq (1GBq) was chosen for the Co-60 source in the SAM reference case simulation, based on specific activity figures in Table 2.4,

as a conservative estimate to encompass a relevant range of radiological conditions expected in real WAS cutting scenarios and the reference case under consideration. The specific system to be simulated consists of a cylindrical water drum with a total volume of 1 m^3. The primary volume (97.5% of the total, i.e., 0.975 m^3) is occupied by liquid water. The bottom 2.5% of the drum volume (0.025 m^3) contains a steel-abrasive mixture (SAM) layer. This layer is composed of garnet abrasive and activated steel particles (see Figure 2.14). The steel particles constitute 1.29% of the mass of the steel-abrasive mixture and have a characteristic size of 106 µm. The characteristics of the steel-abrasive mixture are taken from the extensive characterization experiments performed in the thesis of Heneka [27]. These activated steel particles are assumed to be the sole source of radiation, behaving as Cobalt-60 (Co-60).

The simulation tracked photon and electron transport through the medium, accounting for all relevant physical interactions including photoelectric absorption, Compton scattering, pair production, and bremsstrahlung radiation. The energy cutoffs were set at 1 keV for photons and 10 keV for electrons to balance computational efficiency with limits for energy deposition in the range of molecular bonding energies.

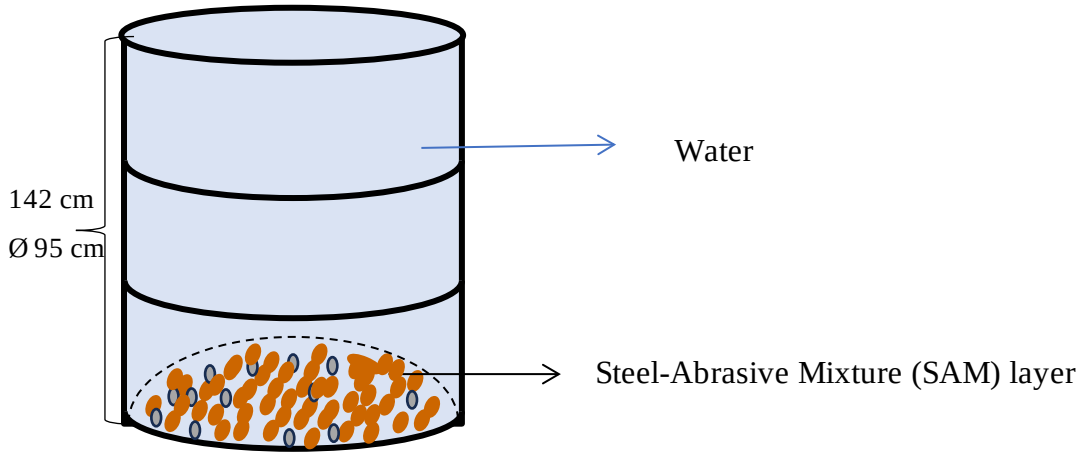

Figure 2.14: Sketch of reference case of steel-abrasive mixture in 1m^3 water volume for PENELOPE simulation. SAM layer is assumed to be a homogenous body with water directly above.

In addition, simulations were made for the setup described in Figure 2.11 which estimates the dose rate from an activated stainless steel spring section from a spent nuclear fuel plenum, around which are vials containing the inhibitor solutions. The source is modeled as a hollow cylinder of Co-60 while the solutions and irradiation vials are modelled as shown with materials defined as glass and water respectively. The dimensions of the irradiation vial and autoclave are also described in the code and modeled as quadrics. The absorbed dose of water was e estimated by utilizing the "Energy Deposition" tally. This tally records the total energy

deposited by all particles (photons, electrons, and positrons) within specified volumes (e.g., the water regions of the vials or the 1 m^3 water phantom). The output of this tally is typically presented in units of energy per history (e.g., keV/history). A "history" refers to the complete life of a single particle (an electron, positron or a photon) from its generation at the source until it is either absorbed, escapes the simulated geometry, or reaches a predefined cutoff energy. The simulation tracks each particle's path, including all its interactions (e.g., scattering, energy loss, new particle creation), as an individual "history". To convert the energy deposition into absorbed dose (Gy or MeV/g), the total energy deposited is then divided by the mass of the scored volume and multiplied by appropriate conversion factors, as detailed in Section 3.5.1 on Radiation Transport Simulations.

2.4.2 PENELOPE Code

The Monte Carlo simulations in this work were performed using the PenEasy code version 2019-09-21 which operates with PENELOPE code (Version 2018). The main features, characteristics and physics behind the code are extensively discussed in the manual of the code [150]. The code is implemented in FORTRAN 77 with its structure based on a set of subroutines that are invoked from a main program written by the user. It applies to energies ranging from 10^3 eV to 10^9 eV for photons and from 0.1 keV to 10^9 eV for electrons. The code simulates different interaction mechanisms for charged particles and photons such as elastic scattering, inelastic scattering, pair production and Bremsstrahlung X-ray production. The electron binding effects and Doppler broadening are taken into account for incoherent scattering in addition to the characteristic k-shell X-rays and Auger electrons emission following photoelectric absorption. Electron and positron histories are generated based on a mixed algorithm that combines the detailed simulation of hard events (e.g., strong elastic scattering, inelastic collisions resulting in characteristic X-rays or Auger electrons, or bremsstrahlung emission above a certain energy threshold) with the condensed simulation of soft events (e.g., distant inelastic collisions or weak elastic scattering). In this mixed algorithm, hard and soft interactions are classified by defining suitable cutoff values for energy loss and angular deflection.

Both condensed and mixed simulation schemes reduce computing time by reducing the number of events to be simulated [159]. PenEasy is a general-purpose main program for PENELOPE, which includes a set of source models, tallies and variance-reduction techniques invoked from a structured code [151]. All the Monte Carlo simulations performed throughout this work were

conducted on a PC-type computer of 1.9 GHz Intel Core i7 vPro 8th Gen processor with a RAM size of 16 GB.

2.4.2.1 Materials and Geometry

To construct the material files, the PENGEOM subroutines package was used. This package is included in PENELOPE for designing material systems. In the package, quadric surfaces delineate homogenous bodies. The different materials used in the simulation were created with their specified compositions, using the executable binary *material.exe* found in the accompanying Pendbase database.

In the geometry file, bodies are defined by surfaces which are defined by quadrics. The materials of the different bodies were also numbered accordingly and would be defined in the PenEasy code. The origin was taken to be the center of the water phantom or irradiation vial in each case. Their lower and upper ends were defined as planes, with z-shift equidistant from the center on both z+ and z-axes, corresponding to their overall length. Their sides were defined with cylindrical quadrics, with dimensions on the x and y axes corresponding to their radii. The material and body corresponding to each of the modelled materials are numbered accordingly. The geometry file in each simulation case was modified to specify the quadrics and dimensions of all the surfaces and bodies involved in the simulation. In the case of irradiation vials, a visualization of the modeled geometry can be visualized using PENGEOM's geometry 2D and 3D viewers as seen in Figure 2.15.

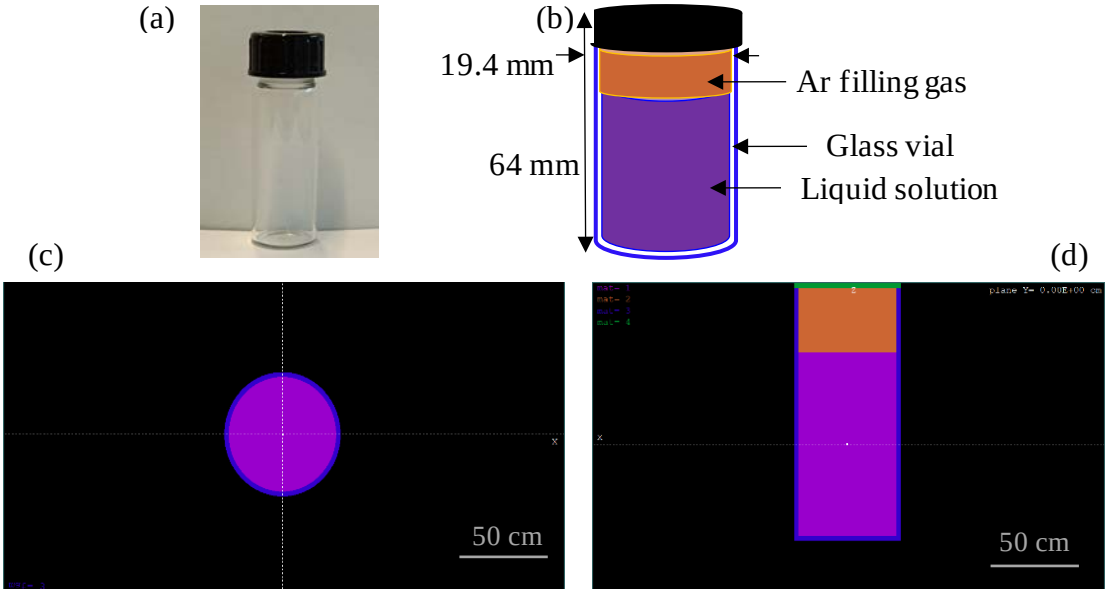

Figure 2.15: Glass vial for sample irradiation. (a) Picture of glass vial (b) Schematic of glass vial with dimensions and content. (c) x-y cross-section and (d) z cross-section of the geometry model of water in the glass irradiation vial created with PENGEOM Geometry viewer.

2.4.2.2 Simulation

The PENELOPE/penEasy input file was modified for source transport physics and spatial position, the geometry file for bodies and materials created with PENGEOM, and tallies for scoring physical quantities (energy deposition, particle track structure, photon/electron fluence, cylindrical dose distribution). Source particle was defined using Co-60.nuc file which inherently accounts for the full decay scheme, including all gamma and beta emissions as pre-processed from evaluated nuclear data libraries and integrated into PENELOPE's internal radionuclide database [150]. Absorption energies for transported particles (EABS e^+, γ and e^-) define the kinetic energy thresholds below which electrons, photons and positrons are considered locally absorbed, were modified to account for more interactions. Additionally, a Maximum Step Length (DSMAX) was applied, imposing an upper limit on the geometric length of any single transport step within a specific material body. The geometry input file and sections of the PENELOPE/penEAsy input file for simulating particle transport in the SAM reference case are provided in Appendix C.

CHAPTER THREE: RESULTS AND DISCUSSION

3.1: Evaluation and Selection of an Appropriate Corrosion Inhibitor

3.1.1 Immersion Test Results

Images of immersion tests of 1.6310 steel coupons (produced as described in Section 2.1.1) in inhibitor solutions are shown in Figure 3.1 and Figure 3.2. The steel coupons were exposed to 1000 ppm of aminobenzimidazole, 3,4-dihydroxybenzoic acid, L-tryptophan, 5-methylbenzotriazole (Figure 3.1) and commercial inhibitors denoted as C.Inh #1, C.Inh #2, C.Inh #3 and C.Inh #4 (Figure 3.2).

Steel coupons immersed in 1000 ppm solutions of each four pure compounds (Fig. 3.1) showed discoloration of the solutions and visible formation of corrosion products on the steel coupons after 24 hours of immersion (Figure 3.1). These organic compounds have been reported in the literature to be effective in the inhibition of mild steel corrosion in different media [89,120,160–164]. ICP-OES analysis of the discoloration observed in the 3,4-Dihydroxybenzoic acid solution revealed the presence of elevated concentration of iron from the dissolution of the steel coupon.

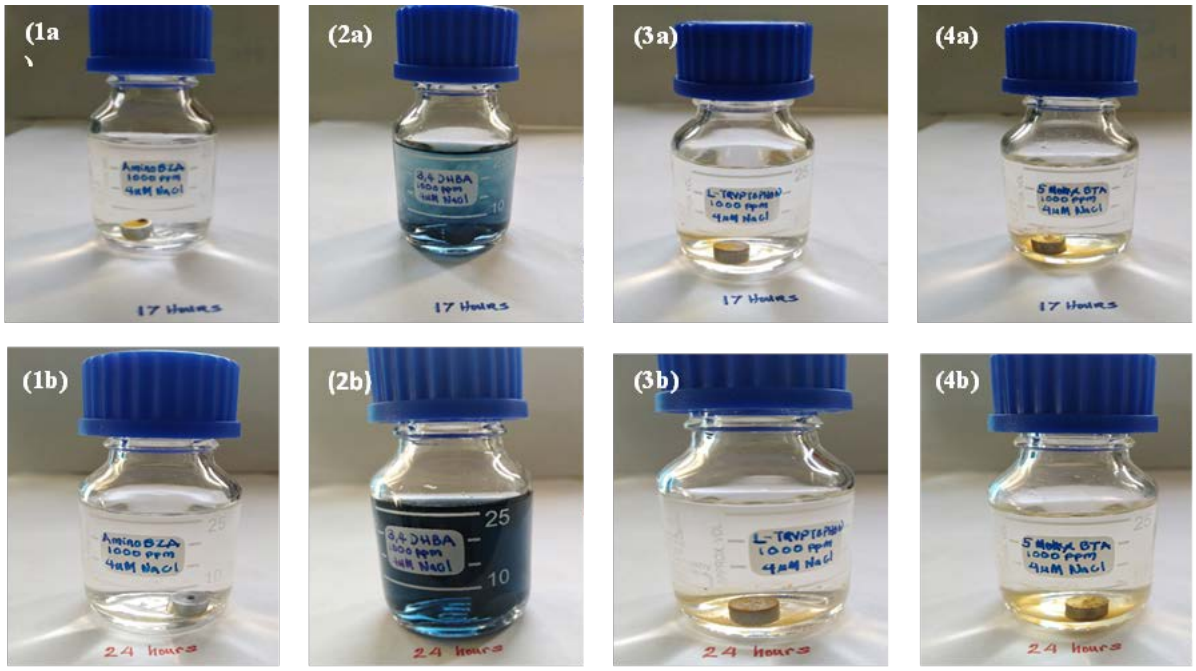

Figure 3.1: Steel coupons immersed in 4 different inhibitor solutions after 17 hours (top row: 1a-4a) and 24 hours (bottom row: 1b-4b). (1) Aminobenzimidazole; (2) 3,4-Dihydroxybenzoic acid; (3) L-Tryptophan; (4) 5-Methylbenzotriazole

The immersion test results for 1 vol.% of the four commercial inhibitor formulations denoted as C.Inh #1, C.Inh #2, C.Inh #3 and C.Inh #4, are presented in Figure 3.2. Iron corrosion was observed in all solutions except C.Inh #4 after a 7-day immersion period. Over the 7-day immersion period, C.Inh #3, an octadecylamine-based formulation, provided only partial inhibition of steel corrosion, failing to prevent visible corrosion over the full duration. Observation after 24 hours revealed localized pitting corrosion on the steel surface. Further literature review suggested that the application of this inhibitor is best suited for reactor secondary circuit operating conditions of high temperature (250 – 350 °C), high pH, and high pressure [165–168].

C. Inh #4 showed excellent corrosion inhibition after the 7-day immersion period via optical inspection, with no visible signs of corrosion product formation. This qualitative observation is significant, as it indicates that C.Inh #4 possesses superior inhibitory properties under the experimental conditions compared to the other seven candidates. Based on this initial screening, C.Inh #4 was selected for more detailed quantitative analysis using electrochemical techniques. The aim of these subsequent experiments was to determine the optimal concentration for effective inhibition and to gain mechanistic insights into how C.Inh #4 protects the 1.6310 steel surface.

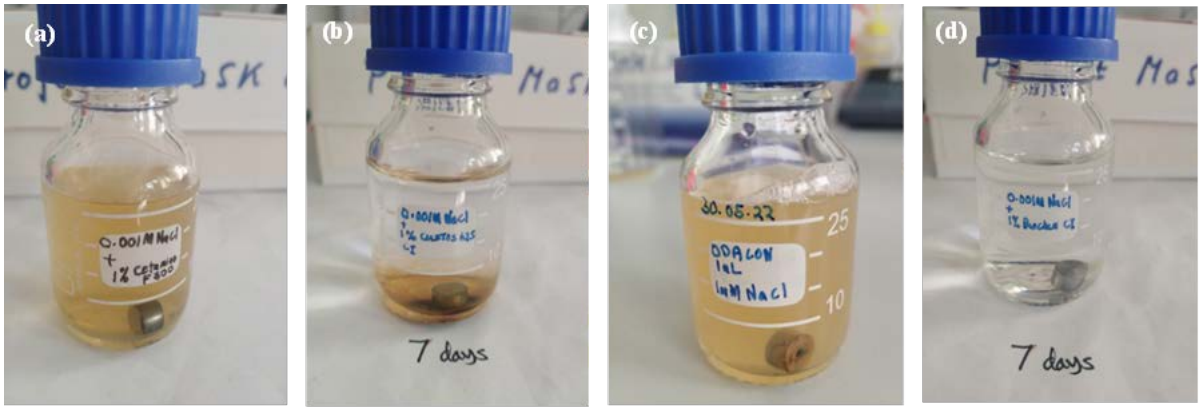

Figure 3.2: Steel coupons immersed in 4 different commercial inhibitor solutions after a 7-day immersion. (a) C.Inh #1; (b) C.Inh #2; (c) C.Inh #3; (d) C.Inh #4.

3.1.2 Electrochemical Measurements with C.Inh #4 Inhibitor

Electrochemical techniques were applied to systematically study the effect of varying concentrations (0.5 vol.%, 1.0 vol.%, 1.5 vol.%, 2.0 vol.%, and 2.5 vol.% solutions) of the best performing inhibitor from the immersion tests, C.Inh #4, on the corrosion inhibition of 1.6310

steel in 0.004 mol/dm^3 NaCl solution. The evolution of the Open Circuit Potential (OCP) at room temperature (r.t), measured relative to a Ag/AgCl reference electrode over a period of 4 hours, is shown in Figure 3.3, while Figure 3.4 illustrates the potentiodynamic polarization curves of the electrode.

3.1.2.1 Open Circuit Potential

The evolution of the OCP for 1.6310 steel in solutions with the studied five concentrations of C.Inh #4 is presented in Figure 3.3. The measured values were reported relative to the Ag/AgCl reference electrode. The measured OCP values vs RE primarily depend on the nature of the electrolyte/solution (redox couple, pH, etc.) and are also influenced by the impedance of the potentiostat [169].

The OCP for all the WE in each of the concentrations of c.Inh #4 starts at a relatively negative potential (approximately -0.95 V vs. Ag/AgCl, as shown in Figure 3.3) and rapidly shifted towards more positive values within the initial few minutes. This initial negative potential reflects the -1 V applied potential used for surface pre-treatment to ensure measurement reproducibility (as described in Section 2.2.2). The subsequent positive shift indicates the rapid formation of a surface film, which kinetically hindered both anodic metal dissolution and cathodic oxygen reduction reactions. This film formation led to a partial passivation of the steel surface, establishing a new, more noble mixed potential and significantly reducing the overall susceptibility to corrosion.

The OCP for the blank solution shifts positively, primarily attributed to the spontaneous formation of a native oxide/hydroxide layer on the freshly depassivated steel surface upon exposure to the aerated blank solution. This initial oxidation partially passivates the steel, hindering further anodic dissolution and shifting the electrochemical equilibrium towards a less active state. The OCP however stabilizes at a relatively negative value (around -0.7 V vs. Ag/AgCl), indicating that the steel surface remains to some extent susceptible to corrosion in the blank chloride solution over the experimental duration.

For 0.5 vol.% - 2.5 vol% concentrations of C.Inh #4, the initial OCP values are considerably more positive compared to the blank solution. The steady-state OCP values generally become more positive with increasing inhibitor concentration. Figure 3.3 strongly suggests that C.Inh #4 effectively inhibits the corrosion of 1.6310 steel in the 0.004 mol/dm^3 NaCl solution. The positive shift in OCP with increasing inhibitor concentration indicates a reduction in the

thermodynamic driving force for corrosion. The formation of a more stable and noble potential plateau at higher inhibitor concentrations implies the development of a protective surface film.

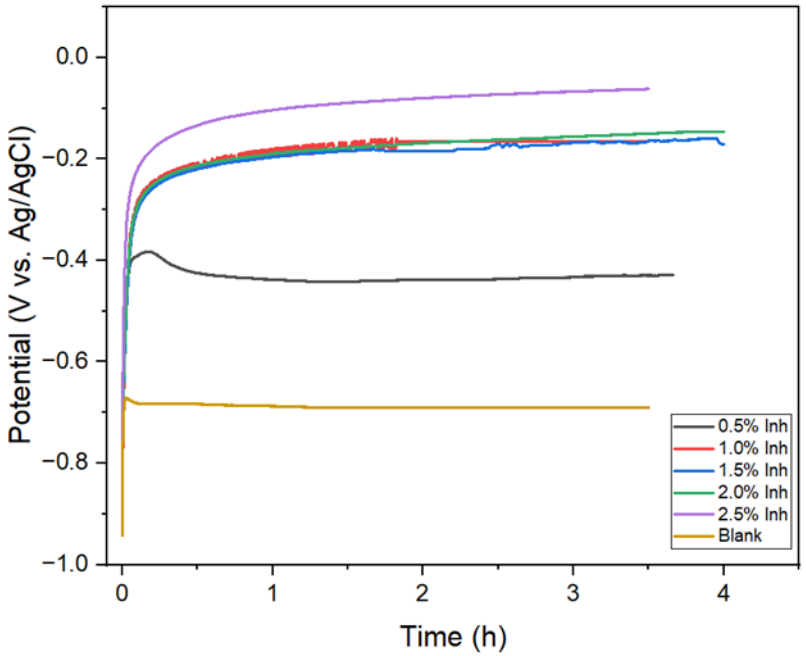

Figure 3.3: Open Circuit Potential (OCP) measurements at different C.Inh #4 concentrations in 0.004 mol/dm^3 NaCl solution, at r.t.

This steeper and larger initial potential increase in the presence of the inhibitor strongly suggests a fast interaction kinetics between the inhibitor molecules and the metal electrode. This rapid interaction likely involves the swift adsorption of inhibitor molecules onto the active sites of the steel surface and/or the rapid formation of a protective film. The subsequent stabilization at more noble potentials (e.g., around -0.15 V to -0.05 V vs. Ag/AgCl for higher inhibitor concentrations) indicates the development of a more persistent and effective protective layer, which could involve strong adsorption of inhibitor molecules, or promotion of a more stable passivation layer compared to the blank.

3.1.2.2 Potentiodynamic Polarization

The potentiodynamic polarization curves in Figure 3.4 reveal the electrochemical kinetics of the 1.6310 steel in 0.004 mol/dm^3 NaCl solution used as blank and as background electrolyte with the inhibitor solutions. The blank solution exhibits a typical active corrosion behavior, characterized by a well-defined Tafel region indicating charge-transfer control of the anodic and cathodic reactions. The corrosion potential (read off at the intercept of the two arms of the curve on the electrode potential axis) is relatively negative, and the corrosion current density,

estimated by extrapolating the Tafel slopes, is comparatively high, signifying a significant corrosion rate in the absence of the inhibitor.

It can be observed from Figure 3.4 that with increasing inhibitor concentration, a notable shift in the polarization curves towards more positive potentials (as observed in the OCP plot) and lower current densities is observed across all concentrations. This indicates that the inhibitor effectively suppresses both the anodic (metal dissolution) and cathodic (oxygen reduction) reactions. The current density is lowered with increasing inhibitor concentration with observed alterations to both the cathodic and anodic branches compared to the blank, suggesting that the inhibitor is a Mixed-type Inhibitor – which forms a highly resistive surface layer, simultaneously restricting access of corrosive species to the steel's anodic sites and impeding the diffusion of dissolved oxygen from the bulk solution to the cathodic sites, effectively reducing the overall corrosion current (rate).

The polarization curves for 1.0 vol.%, 1.5 vol.%, and 2.0 vol.% inhibitor concentrations were similar. It is likely that the surface coverage of the inhibitor on the steel electrode approaches a saturation limit within this concentration range. As the inhibitor concentration increases from 1.0 vol.% to 2.0 vol.%, most of the available active corrosion sites on the metal surface are already occupied by inhibitor molecules. The mechanism of protection is assumed to involve the formation of a monolayer or a thin multi-layer adsorbed film of the inhibitor, and once this layer is substantially formed, additional inhibitor in the bulk solution has a limited impact on further improving its effectiveness. This observation could indicate that the optimal performance of the inhibitor under the experimental conditions is achieved within the 1.0 vol.% to 2.0 vol.% range. Beyond this concentration, a significant shift is observed at 2.5 vol.%, which could result from an improved packing density of the inhibitor, multilayer adsorption forming a robust diffusion barrier for oxidative species, or enhanced cathodic inhibition (as observed in the slope of the cathodic branch), all contributing to further improvements in corrosion protection.

The anodic curves show the presence of two distinct sections; a near-linear region close to the E_{OCP} where the slope is near-zero and a breakaway region towards higher current densities with a steeper slope. The flat region indicates the passivation of the surface or the formation of a protective layer over a potential range. The breakaway region suggests passivation breakdown with increasing polarization. Tafel extrapolation around the linear region close to the E_{OCP} is used for the estimation of Tafel constants and corrosion kinetics.

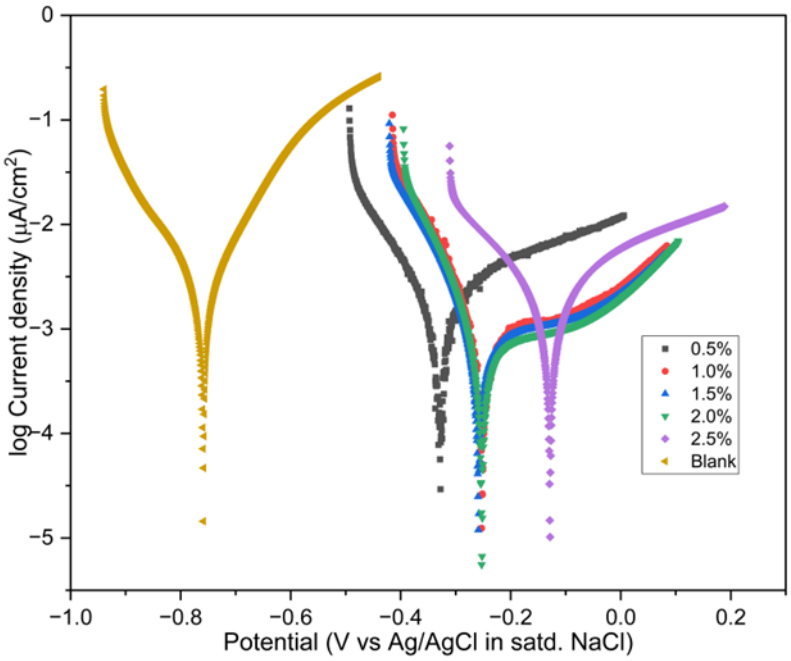

Figure 3.4: Potentiodynamic polarization curves of blank and different C.Inh #4 inhibitor concentrations in 0.004 mol/dm^3 NaCl at 25°C.

The electrochemical parameters obtained from the polarization curves; β_a and β_c Tafel slopes, corrosion current, corrosion potential, corrosion rate, and inhibition efficiency are given in Table 3.1.

Table 3.1: Electrochemical parameters for C.Inh #4 at different concentrations.

Soln.	β_a (mV/dec)	β_c (mV/dec)	i_{corr} (μA)	E_{corr} (mV)	CR (mmpy)	IE (%)	θ
Blank	171.7 ± 3.5	206.6 ± 4.7	11.3 ± 1.3	667.6 ± 32.2	0.16 ± 0.02	-	-
0.5%	224.4 ± 5.2	123.2 ± 3.7	1.39 ± 0.5	332.2 ± 23.5	0.11 ± 0.04	87.7 ± 4.7	0.88
1%	214.8 ± 1.7	97.8 ± 4.0	1.0 ± 0.1	252.6 ± 15.5	0.08 ± 0.01	90.8 ± 1.5	0.91
1.5%	66.2 ± 1.2	82.8 ± 2.0	0.7 ± 0.1	259.2 ± 18.9	0.05 ± 0.01	93.8 ± 1.1	0.94
2%	91.6 ± 2.3	86.1 ± 1.9	0.7 ± 0.1	252.8 ± 20.2	0.0 5± 0.01	94.0 ± 1.3	0.94
2.5%	80.4 ± 2.1	73.8 ± 2.1	0.6 ± 0.1	129.0 ± 11.2	0.05 ± 0.01	94.4 ± 0.9	0.94

The degree of surface coverage (θ) has been reported in the literature [77,160,170,90] as equivalent to the measure of inhibition provided by the corrosion inhibitor and calculated as the ratio of the corrosion current density of the inhibited solution and the blank.

$$\text{Surface coverage } (\theta) = \frac{i_{corr}(\text{blank}) - i_{corr}(\text{inhibitor})}{i_{corr}(\text{blank})} = \frac{IE(\%)}{100} \qquad (3.1)$$

It is assumed that inhibitor molecules stack onto the metal surface to form a continuous layer of protection corresponding to the extent of corrosion inhibition. A plot of inhibition efficiency as a function of inhibitor concentration is given in Figure 3.5.

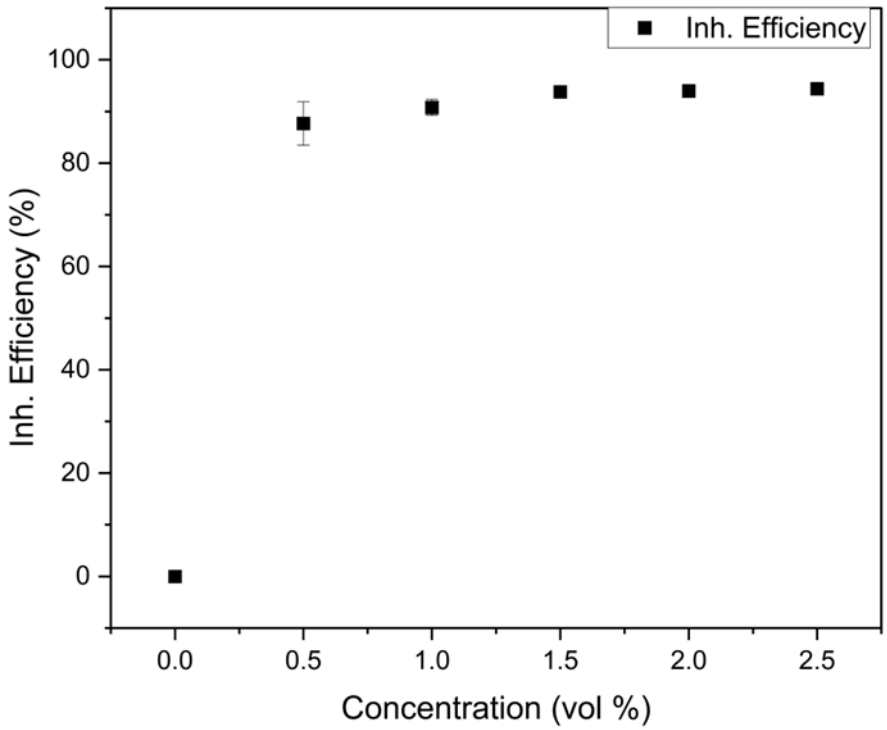

Figure 3.5: Plot of corrosion inhibition efficiency as a function of C.Inh #4 concentration.

A threshold in inhibition efficiency is observed at an inhibitor concentration of 1.5 vol.%. Above this concentration, the introduction of additional inhibitor molecules provides only a marginal increase in inhibition efficiency. Specifically, a 0.2% increment in inhibition efficiency using 2.0 vol.% and a 0.7% increment using 2.5 vol.% inhibitor concentration. The data suggest that >90% inhibition efficiency and thus corrosion mitigation is already achieved within the 1.0% to 2.0% range, and adding more inhibitor molecules beyond this point provides very little additional protective benefit, making it less optimal from a practical cost-benefit standpoint. For practical applications therefore, the optimal concentration of this inhibitor for protecting the steel in similar environments would be between 1.0% and 2.0%.

3.1.2.3 Electrochemical Impedance Spectroscopy

EIS spectra were acquired at open-circuit potential (E_{OCP}), with a frequency range from 1 MHz to 1 mHz. The sinusoidal input voltage amplitude was set at 5 mV with measurements of 6

points per frequency decade. Measurements with the 1.5 vol.% of C.Inh #4 were made after a 3-hour immersion period, ensuring a stable open-circuit potential. The selection of the voltage amplitude was aimed at enhancing the signal/noise ratio, particularly at lower frequencies, without substantial influence on the system's overall state.

Nyquist and Bode plots were generated from the obtained EIS experimental data. EEC modeling of the EIS data was fitted with the Randles Circuit, consisting of a solution resistance, charge transfer resistance and a double-layer capacitance representing the film capacitance. The modified Randles circuit has been applied in modeling inhibitor systems with mild steel and other low-alloy steels [77,171,172]. Based on the behavior observed in the Nyquist and Bode plots in the present study (depressed and sometimes incomplete semicircles), modifications to the Randles circuit were necessary to accurately represent the impedance response. This involved replacing the ideal double-layer capacitance with a Constant Phase Element (CPE/Q) to account for non-ideal capacitive behavior arising from factors such as surface roughness, non-uniform current distribution, or a distribution of time constants. A schematic of the equivalent electrical circuit model with physical features for the electrochemical system under review is represented in Figure 3.6.

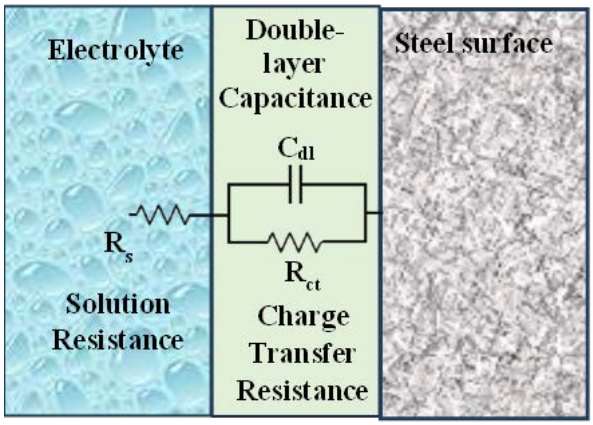

Figure 3.6: Typical equivalent circuit model of a metal in an inhibited electrolyte solution.

Figure 3.7 presents the Nyquist plots (Complex-plane plots) for the 1.6310 steel electrode in the blank 0.004 mol/dm^3 NaCl solution (Figure 3.7a) and in the presence of 1.5 vol.% C.Inh #4 inhibitor (Figure 3.7b). These plots, which display the negative imaginary impedance (-Z'') versus the real impedance (Z'), visualize the electrochemical impedance response and identify time constants associated with corrosion processes.

For the blank solution, Figure 3.7(a) shows a depressed semicircle when the real and imaginary impedance axes are plotted with the same scale. The intercept of this semicircle with the real axis at high frequencies (the leftmost point) represents the solution resistance (R_s). The diameter of the semicircle, extending from R_s to its intercept with the real axis at low frequencies, corresponds to the charge transfer resistance (R_{ct}). This resistance is inversely proportional to the corrosion rate. The relatively small diameter of the semicircle for the blank solution indicates a low R_{ct}, consistent with a high corrosion rate in the absence of an inhibitor [123].

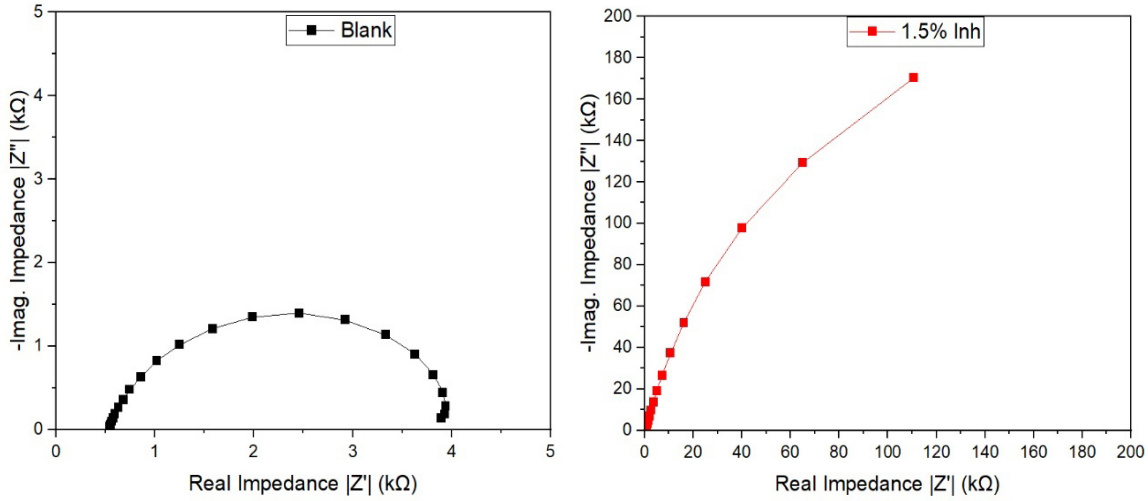

Figure 3.7: Nyquist plots of (a) left plot - blank solution and (b) right plot - 1.5 vol.% C.Inh #4 solution.

In contrast, the Nyquist plot for the 1.5 vol.% inhibitor solution shows an enlarged and developing semicircle. The solution resistance (R_s) remains similar to that of the blank, as expected, since the inhibitor primarily affects the electrode-electrolyte interface, not the bulk solution conductivity. The diameter of the semicircle is significantly larger than that of the blank solution. This directly indicates a substantial increase in the charge transfer resistance (R_{ct}). A larger R_{ct} signifies a much slower electron transfer rate at the interface, demonstrating a significant reduction in the corrosion rate due to the inhibitor's protective action.

The Nyquist plot for the 1.5 vol.% inhibitor solution shows an apparent incompleteness of the semicircle at the low frequency end, suggesting that the full relaxation processes, potentially involving very slow charge transfer reactions or the onset of mass transport limitations (e.g., diffusion of oxygen or inhibitor molecules to/from the surface), were not entirely captured within the measured frequency range. Had the frequency range been extended to even lower

frequencies, these processes might manifest as additional capacitive loops or a Warburg impedance (a straight line with a 45-degree slope), but their partial manifestation within the experimental window resulted in the incomplete semicircle. Constraints with experimental time and instrumentation made it difficult to measure at even lower frequencies.

At the steel-electrolyte interface, there is the formation of an electrical double layer (EDL) due to the interaction between the steel surface and the ions from the solution [173,174]. At the interface between the steel and the aqueous solution, two layers develop: a Stern Layer (Inner Helmholtz Plane), which consists of ions strongly adsorbed onto the steel surface due to electrostatic attraction, forming a compact layer in direct contact with the steel surface. Beyond the Stern layer lies the Diffuse Layer (Outer Helmholtz Plane), where ions from the electrolyte solution are loosely associated with the steel surface [175,176]. This layer extends into the solution and is characterized by a gradient in ion concentration. With the adsorption of inhibitor molecules, water molecules are displaced from the steel surface, decreasing the dielectric constant of the EDL and directly leads to a decrease in the $C_{dl.}$ In addition, a higher R_{ct} value, suggests slower electron transfer kinetics, due to the reduction in the active surface area and increase in thickness of the EDL.

The Bode plots in Figure 3.8, comprising impedance magnitude (|Z|) and phase angle (ϕ) as functions of frequency, provide a comprehensive representation of the electrochemical response of the 1.6310 steel electrode in the blank 0.004 mol/dm^3 NaCl solution and in the presence of 1.5 vol.% C.Inh #4 inhibitor.

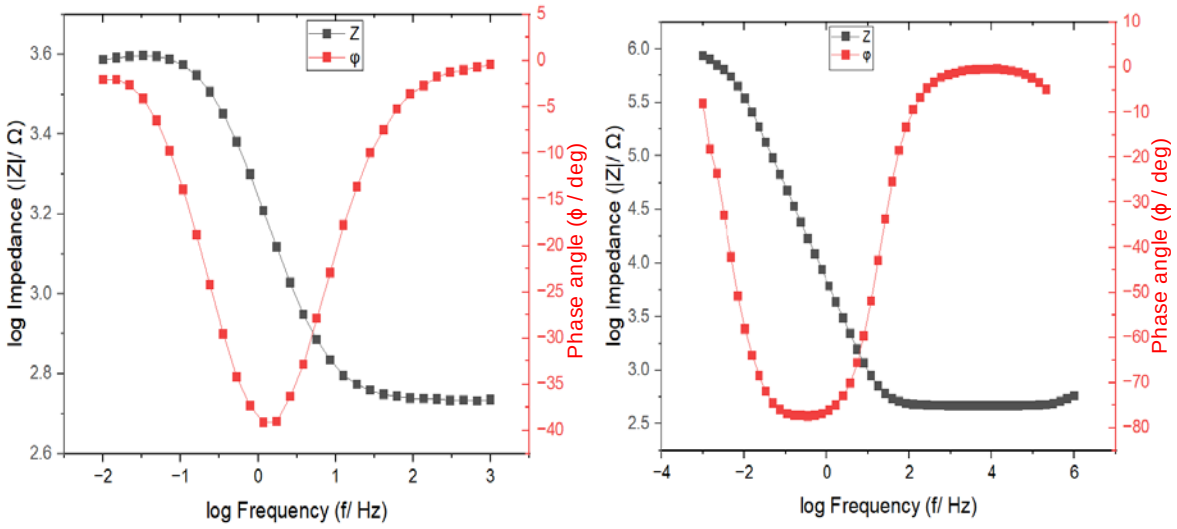

Figure 3.8: Magnitude (black trace) and phase angle (red trace) Bode plots of blank solution (left) and 1.5 vol.% C.Inh #4 inhibitor solution (right).

For the blank solution, the following features are observed:

- High-Frequency Region (log f > 2): In the magnitude plot (black trace), |Z| is relatively constant at approximately $10^{2.7}$ Ω (around 500 Ω to 600 Ω), and the phase angle approaches 0°. This behavior is characteristic of the solution resistance (R_s), representing the ohmic resistance of the electrolyte.
- Mid-Frequency Region (log f between -1 and 1): The magnitude of |Z| decreases with increasing frequency, and a distinct phase angle peak is observed around −38°. This region corresponds to the time constant associated with the charge transfer process (R_{ct}) in parallel with the double-layer capacitance (C_{dl}) at the bare or partially corroding metal-electrolyte interface. The peak indicates the frequency range where capacitive and resistive elements contribute significantly.
- Low-Frequency Region (log f < -1): The magnitude of |Z| tends to level off at approximately $10^{3.6}$ Ω (around 4 kΩ), and the phase angle approaches 0°. This low-frequency impedance value primarily represents the sum of the solution resistance and the charge transfer resistance (R_s+R_{ct}), indicating the overall resistance to corrosion.

The presence of 1.5% C.Inh #4 inhibitor significantly alters the electrochemical response of the steel, demonstrating its effective corrosion inhibition.

For the 1.5 vol.% C.Inh #4 inhibitor solution, the following features are observed:

- High-Frequency Region (log f > 2): Similar to the blank, the impedance magnitude remains around $10^{2.7}$ Ω and the phase angle is near 0°. This indicates that the solution resistance (Rs) is largely unaffected by the addition of the inhibitor, as expected.
- Mid-Frequency Region (log f between -2 and 2): A profound change is observed in this region. The impedance magnitude (|Z|) is significantly higher across this range compared to the blank, and the phase angle exhibits a much broader and more intense peak, reaching approximately −75°. This dramatic shift towards a phase angle closer to −90° is indicative of a highly capacitive and protective film forming on the steel surface. The broader peak suggests a wider distribution of time constants, likely due to the inherent heterogeneity of the adsorbed inhibitor layer (e.g., surface roughness, varying film thickness, or different adsorption sites).
- Low-Frequency Region (log f < -2): The impedance magnitude at low frequencies is drastically increased, reaching approximately $10^{5.8}$ Ω (around 630 kΩ). This represents a

~157-fold increase in the total impedance ($R_s + R_{ct}$) compared to the blank solution (4 kΩ). This substantial increase in low-frequency impedance is a direct quantitative measure of the significantly enhanced corrosion resistance provided by the inhibitor, primarily due to a large increase in the charge transfer resistance (R_{ct}).

3.1.3 Effect of Immersion Time

With a 1.5 vol.% concentration of C.Inh #4, the effect of immersion time was tested. The impedance data of the working electrode was measured after 3 hours, 24 hours, 48 hours and 72 hours and is shown in Figure 3.9.

It is observed that the diameters of the semi-circles increased with immersion time suggesting an increase in charge transfer resistance. This increase can be attributed to the adsorption of the inhibitor molecules onto the metal surface, forming a protective film. As the inhibitor molecules adsorb onto the metal surface, they hinder the exchange of electrons between the metal and the electrolyte, thereby increasing the resistance to charge transfer. At longer immersion times, the adsorption process would approach equilibrium and the inhibitor reaches maximum coverage.

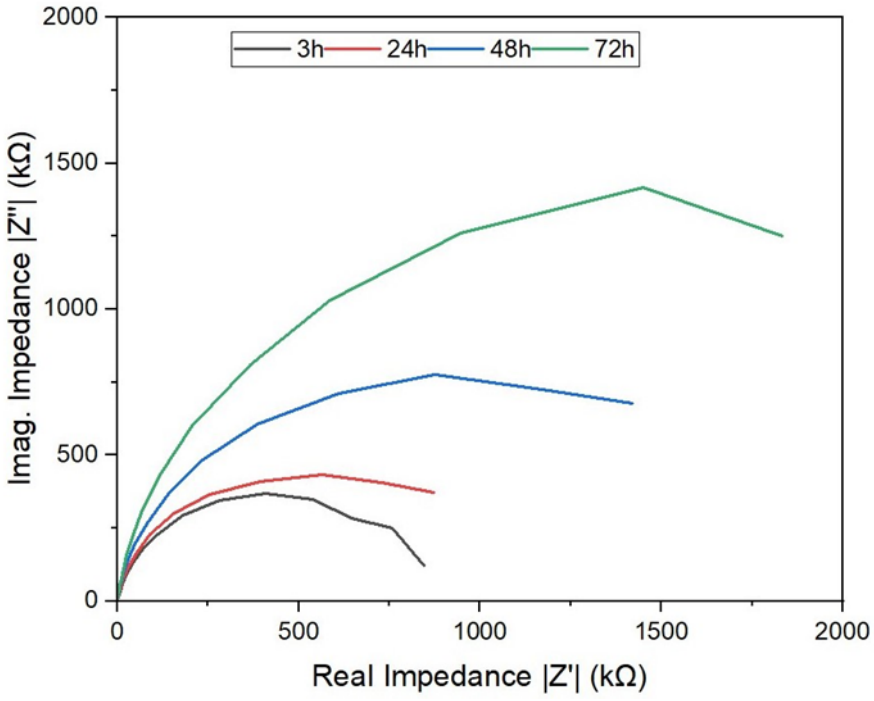

Figure 3.9: Nyquist plot showing the influence of 1.6310 steel electrode immersion time in 1.5% concentration of C.Inh #4 inhibitor.

The Bode plot showing the influence of immersion time on the frequency response of the system is shown in Figure 3.10.

At higher frequencies (typically above 10^2 Hz or 10^3 Hz), the magnitude plots for all immersion times are observed to be similar or to merge, in the area annotated (a). This behavior is primarily governed by the solution resistance (R_s), which represents the ohmic resistance of the electrolyte between the WE and the RE tip. Since the bulk composition and conductivity of the electrolyte solution (1.5 vol.% inhibitor in 0.004 mol/dm^3 NaCl) are expected to remain relatively constant over the 72-hour immersion period, the Rs values, which dominate the impedance response at high frequencies, do not change significantly. Therefore, the merging of the magnitude plots at high frequencies indicates the consistent and stable ohmic resistance of the solution throughout the immersion experiment.

The phase plots in Figure 3.10 also exhibit a similar trend at higher frequencies. While the phase angles at high frequencies remain close to 0° (annotated (b) and dominated by solution resistance), significant variations are observed at lower frequencies. The maximum phase angle, which is indicative of the capacitive behavior of the interface, generally shifts towards lower frequencies and becomes broader/more negative with increasing immersion time as observed in the area annotated (c). This suggests an increase in the overall time constant of the system. Furthermore, by observing the mid-frequency region of the magnitude plots (d), where the impedance is primarily governed by the combination of the charge transfer resistance and double-layer capacitance, it is evident that the impedance magnitude at lower frequencies increases substantially with immersion time. This directly indicates a significant increase in the charge transfer resistance (R_{ct}) as the inhibitor film develops and becomes more protective. Concurrently, the slope of the magnitude plot in the capacitive region (where it approaches log f = -1) remains relatively constant across different immersion times. This consistency in the capacitive slope, along with the values of the Constant Phase Element (CPE) parameter α (Table 3.2), suggests that the double-layer capacitance (C_{dl}) values may remain relatively similar or undergo only minor changes over time, while the dominant effect is the increasing resistance to charge transfer. This implies that the primary mechanism of improved inhibition 48 hours after immersion is the formation of a more resistive barrier layer, rather than a substantial change in the dielectric properties or thickness of the double layer itself.

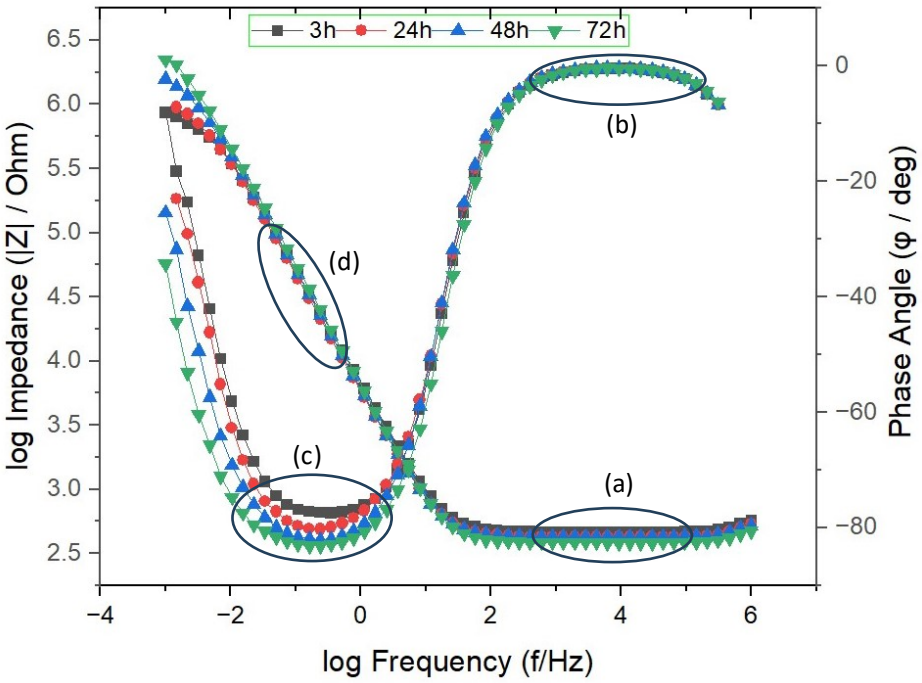

Figure 3.10: Bode plot showing the effect of immersion time in 1.5% inhibitor solution

A summary of the equivalent circuit modeling parameters for the blank solution and the 1.5 vol.% inhibitor solution over various immersion times, along with the effect of immersion time on R_{ct}, are shown in Table 3.2 and Figure 3.11. Q represents the impedance of the Constant Phase Element (CPE). α values, indicative of double-layer behavior and describing surface inhomogeneities and non-ideality, were reported to vary between 0.80 and 0.95.

The inhibition efficiencies at different immersion times were evaluated from EIS data using the values of the polarization resistance, and reported in Table 3.2. The polarization resistance R_p is the sum of the charge transfer resistance and the resistance of all other circuit elements used in the circuit modelling. In the simple Randles Circuit with CPE model used in this study, $R_p \approx R_{ct}$

Therefore, $IE(\%) = \frac{R_{ct,inh} - R_{ct,blank}}{R_{ct,inh}} \bullet 100\%$ (3.2)

Table 3.2: Equivalent circuit parameters for blank and 1.5% C.Inh #4 showing effect of immersion time on impedance and inhibitor layer parameters.

Time (h)	R_s (Ω)	R_{ct} (MΩ)	C_{dl} (µF)	Q (µF•$S^{(n-1)}$)	α	IE (%)
Blank	538.8 ± 9.5	0.004±1E-4	110.2±5.5	106.1±5.5	0.839	-
3	464.3 ± 4.5	0.86 ± 0.02	40.8 ± 1.5	28.9 ± 1.5	0.902	99.5 ± 0.1
24	427.3 ± 5.2	1.02 ± 0.01	44.0 ± 1.4	32.1 ± 1.4	0.916	99.6 ± 0.1
48	428.6 ± 7.3	1.73 ± 0.04	40.8 ± 0.9	30.3 ± 0.9	0.930	99.8 ± 0.1
72	385.6 ± 2.7	2.95 ± 0.82	37.2 ± 0.5	27.6 ± 0.5	0.936	99.9 ± 0.4

The time-dependent increase in the charge transfer resistance in the system is reflected in Figure 3.11.

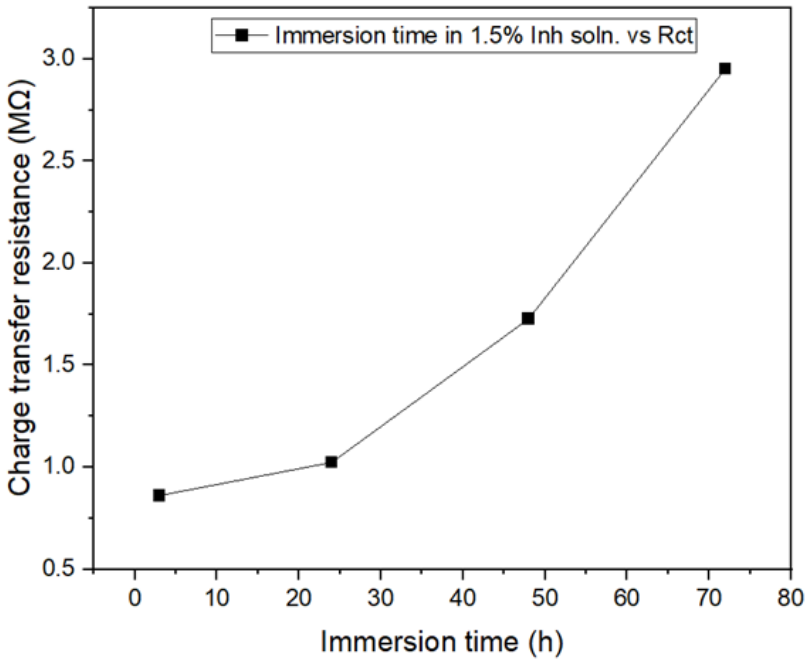

Figure 3.11: Charge transfer resistance vs immersion time for 1.5 vol.% C.Inh #4 inhibitor solution.

It can therefore be concluded that while the inhibitor exhibited rapid kinetics in its interaction with the metal surface, corrosion inhibition significantly improved with increasing immersion time, as evidenced by the increase in charge transfer resistance shown in Figure 3.11. This has been attributed in literature to the progressive enhancement in adsorption and increased uniformity and density of the inhibitor layer over extended immersion time [89,177,178].

3.2 Characterization of Samples Obtained Post-WAS Cutting

In this section, evaluation of the performance of the selected inhibitor (C.Inh #4) under conditions more closely representative of the actual WAS cutting process is described. This evaluation was based on insights derived from initial immersion tests (Section 3.1.1), which established C.Inh #4 as the most effective among the tested inhibitors for preventing corrosion, as visual checks confirmed. Additionally, information obtained from the comprehensive electrochemical investigations with the inhibitor (Section 3.1.2), quantified its inhibition efficiency and determined an optimal concentration range. The primary objective of these post-WAS cutting experiments was to provide a validation of the laboratory-scale findings (Section 3.1.2) by assessing the inhibitor's ability to protect the steel particles produced in a real WAS cutting scenario.

Following a controlled WAS cutting of a non-radioactive RPV steel block, using a water-abrasive suspension mixed with 1.5 vol.% of the selected inhibitor (C.Inh #4) and 60 mg/l of the additive, Liquitech 227P, further electrochemical and surface analytical investigations were conducted. In the electrochemical experiments, freshly polished 1.6310 steel coupons serving as WE were immersed in solutions (Tap water, tap water + 1.5 vol.% Inhibitor, and the WAS, after separation of solids) obtained directly from the WAS cutting operation at ANT Lübeck. The results are presented in the following subsections.

3.2.1 Electrochemical Measurements with WAS Cutting Solutions

3.2.1.1 Open Circuit Potential Measurements

The evolution of the OCP of 1.6310 steel coupons measured in the different solutions sampled from the WAS cutting experiment is shown in Figure 3.12.

The OCP measurements showed steady electrode potentials over a 2.5-hour measurement period after a 10-minute depassivation of the steel electrode at -1 V. The blank solution (tap water) showed a steady OCP around -680 mV vs RE over the measurement period, in contrast to the OCP measured in the WAS and tap water + 1.5 vol.% inhibitor solutions. The OCP measurement in the WAS, showed similar evolution to tap water + 1.5 % Inhibitor solution. For both samples, the electrode potential stabilized after 105 minutes (1.75 hours) at around -200 mV vs RE. The observed increase in OCP suggests a significant slowing down of the corrosion rate in the samples containing the inhibitor.

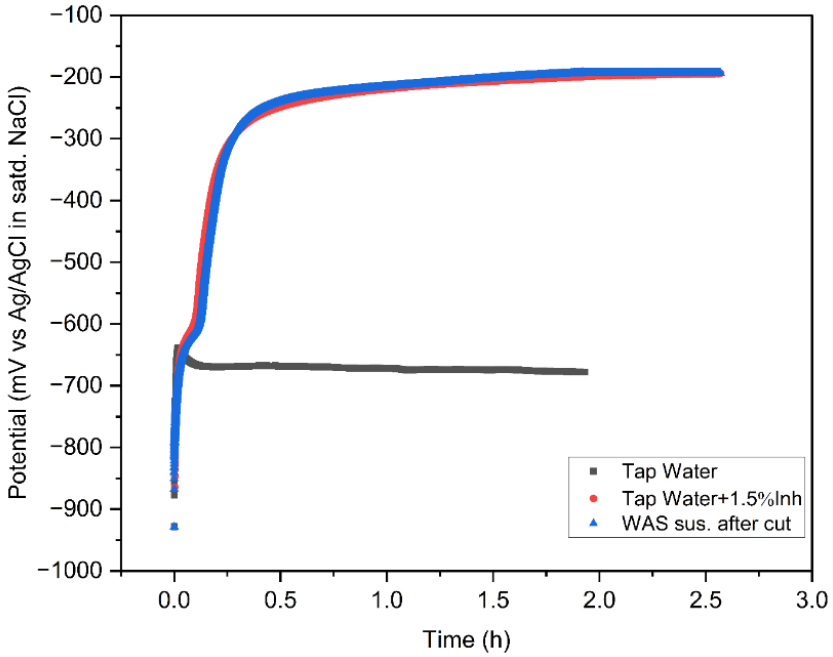

Figure 3.12: OCP measurements for 1.6310 steel in tap water, Tap water with 1.5 vol.% C.Inh #4, and the WAS sampled from the cutting vessel at ANT Lübeck.

3.2.1.2 Potentiodynamic Polarization Measurements

The PDP curves of the 1.6310 coupons measured in the blank (tap water), tap water + 1.5 vol.% C.Inh #4 and WAS are shown in Figure 3.13.

It is observed from Figure 3.13 that in the absence of the inhibitor, the corrosion of the steel progressed faster in the blank solution, evidenced by the high current densities for both the cathodic and anodic reactions. For the 1.6310 coupons in the tap water and WAS containing 1.5 vol.% C.Inh #4, the corrosion potentials were significantly increased compared to the blank. The cathodic polarization curves for both inhibited samples exhibited similar slopes and properties, suggesting a significant repression of oxygen reduction, consistent with the neutral to alkaline pH values of these solutions. The mechanism of the cathodic reaction in this pH range is oxygen reduction and the cathodic current is limited by oxygen diffusion. In the presence of the inhibitor adsorbing onto the steel surface, the diffusion rate of oxygen to the cathodic sites is severely limited, consequently slowing down the cathodic reaction [73]. The anodic reaction can also be seen to have been impeded significantly by the presence of the inhibitor. Two distinct regions can be observed in the anodic curves measured in both WAS and tap water containing 1.5 vol.% C.Inh #4: (1) an initial region (a) with a slight increase in current density, followed by (2) a region (b) characterized by a near-zero slope, indicative of passivation. The first region (a) of the anodic polarization curve is associated with active

dissolution from Fe → Fe^{2+} oxidation [179]. This is followed by the second region (b) attributed to diffusion–controlled behavior of the inhibitor film. The presence of the inhibitor ensures that the current density is as low as possible suggesting that electron transfer as a result of metal ion dissolution is significantly minimized.

In the passivation region, the metal is almost completely protected by the inhibitor layer and nearly no oxidation of the metal ion can occur. Metal passivation, either by the presence of inhibitors or a passive oxide layer, begins at a certain potential known as the passivation potential, E_p. From Figure 3.13, E_p is around 0.05 V. Beyond this potential, the anodic current associated with metal dissolution decreases drastically to a minimal value. The passivation potential is influenced by the acidity of the solution, shifting to more positive values as the solution pH decreases [180–182].

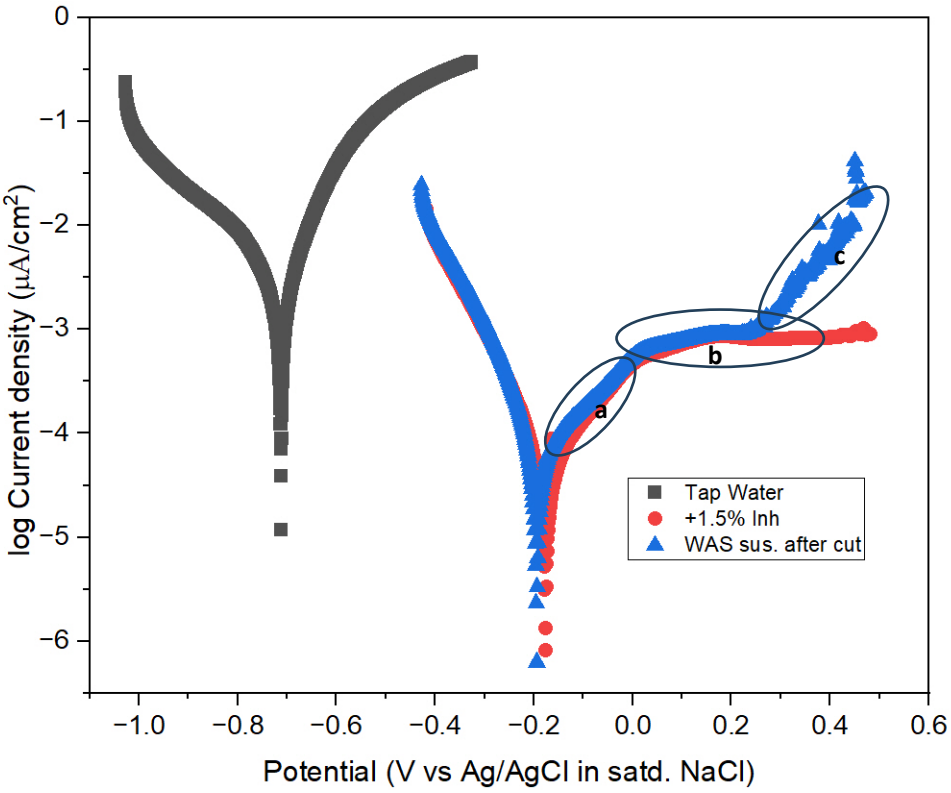

Figure 3.13: Potentiodynamic polarization curves for the blank, WAS and tap water + 1.5% Inhibitor. The annotated sections denote different passivation phenomena.

For the WAS + 1.5 vol.% C.Inh #4, an additional region (c) is observed starting after an anodic polarization potential of 0.2 V vs RE. At this point, there is a breakdown in the passivation produced by the inhibitor layer, with a sudden increase in the anodic current density. The protective layer provided by the inhibitor might deteriorate in the presence of aggressive ions in the solution, leading to localized corrosion initiation on the underlying metals. The onset of

passivation breakdown in region (c) could be due to deleterious action of phosphonates from the additive, the lowering of the WAS pH making the steel susceptible to corrosion, and the action of aggressive Cl^- in the tap water. The dissolution of passive films due to attack of aggressive anions (e.g Cl^-) typically occurs above a specific potential known as the film breakdown potential, denoted as E_b [183,184].

The pH of the WAS was measured to be 5.6 ± 0.2 compared to 7.4 ± 0.2 for Tap water and 7.8 ± 0.2 for Tapwater + 1.5% Inhibitor solutions respectively. This lowered pH in the WAS is directly attributable to the presence of the proprietary additive, Liquitech 227P, with pH measured to be 4.8 ± 0.1. As detailed in Section 2.2.3, Liquitech 227P is a dimethyl phosphonate-based sequestering agent. Phosphonates, particularly polyphosphonates, are known to be inherently acidic due to the presence of multiple phosphonic acid (P-OH) groups, which can deprotonate in solution and thus lower the pH of the cutting fluid.

PDP curves illustrating the polarization behavior of the steel in tap water with the additive only are provided in Figure A2 (appendix), indicating that the additive alone did not significantly inhibit corrosion.

In Table 3.3, the electrochemical parameters for the samples obtained from the WAS cutting experiment are listed.

Table 3.3: Electrochemical parameters from PDP analysis of 1.6310 steel in WAS cutting samples

Solution	β_a (mV/dec)	β_c (mV/dec)	i_{corr} (µA)	E_{corr} (mV)	CR (mmpy)	IE (%)
Tap water	122.7 ± 2.5	262.7 ± 3.5	5.74 ± 0.21	712.7±30.0	0.36 ± 0.01	-
Tap water + Inh	350.2 ± 3.1	97.6 ± 3.1	0.51 ± 0.05	231.2 ±15.2	(2.94±0.30) E-2	91.1± 0.9
WAS + Inh	262.9 ± 4.2	106.2 ± 1.9	0.78 ± 0.01	270.1±13.5	(4.90±0.06) E-2	86.4± 0.5

The corrosion rate significantly decreased in both the WAS and the Tap water with inhibitor. Inhibition efficiencies greater than 85% were calculated from the corrosion currents (i_{corr}).

3.2.2 Surface Characterization of the Steel Swarf after the WAS cut

3.2.2.1 Scanning Electron Microscopy (SEM-EDX)

The suspension of steel-abrasive mixture (containing steel particles, abrasive particles, C.Inh #4 inhibitor, and cutting additive) collected after the WAS cut was stored in borosilicate glass

containers prior to analysis. Samples of the steel-abrasive mixture were collected, dried with argon, and then analyzed using Scanning Electron Microscopy (SEM-EDX) to determine changes in the morphology and composition of the steel/abrasive particles at 48 hours, 216 hours, 456 hours, and 18 months after the WAS cutting process. Figure 3.14 shows some SEM images of the steel and abrasive mixture 48 hours after the cut.

Table 3.4 gives the elemental composition (in at. %) of the marked areas on the surfaces in the SEM image (Figure 3.14b) of the mixture, 48 hours after the cut. Point 1 (blue square) represents a steel particle while Point 2 (orange square) represents an abrasive particle in the mixture. The elemental analysis of Point 1 shows the absence of significant oxygen counts (below detection limits) on the steel surface 48 hours after the cut. While XPS measurements (discussed in Section 3.2.2.2) observed a thin, intrinsic oxide layer, the EDX results combined with the visual integrity of the surface by SEM (Figure 3.14, 3.15) indicates that extensive macroscopic oxidation of the steel particles has not occurred in the presence of the inhibitor. The composition of point 2 in Table 3.4 on the abrasive particle showed a significant presence of oxygen, magnesium, aluminum, silicon and iron, predominant in the mineral components of the abrasive (See Table 2.2).

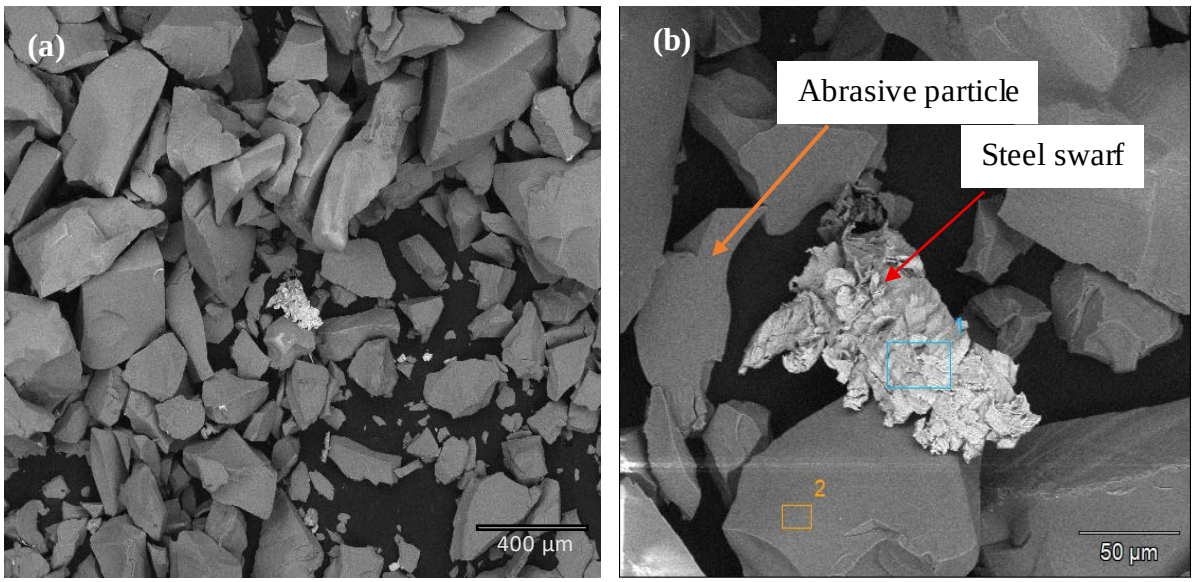

Figure 3.14: Backscattered electron (BSE) images showing steel swarf and abrasive particles, 48 hours after the WAS cut. Points 1 and 2 in (b) represent a steel swarf and an abrasive particle.

Table 3.4: Composition (atom %) of steel and abrasive particles 48 hours after the WAS cut

	C	O	Mg	Al	Si	Ca	Mn	Fe
Steel particle (Point 1)	5.2	n.d.	0.6	1.0	1.8	n.d.	2.1	89.3
	±1.9		±0.8	±0.6	±0.6		±1.1	±4.5
Abrasive particle (Point 2)	1.7	65.0	3.9	8.8	13.5	2.0	-	5.1
	±1.2	±3.0	±0.7	±0.8	±0.9	±0.5		±0.2

*Errors are reported as ±3σ (three standard deviations), representing a 99.73% confidence interval for the elemental quantification by EDX.
n.d – not detected

Figure 3.15 presents additional SEM images of the steel-abrasive mixture after longer immersion periods of 216 hours and 456 hours, respectively. Visually, these images do not reveal the widespread formation of distinct iron corrosion products or significant morphological changes indicative of severe general corrosion on the steel particle surfaces. The surfaces of the micrometer-size steel particles largely retain their metallic appearance and roughness from the impact of the high-pressure WAS.

While SEM imaging primarily provided morphological information and may not definitively confirm the absolute absence of very thin, amorphous, or sub-microscopic corrosion layers, the consistent visual integrity of the steel surfaces across the extended immersion times strongly suggests that the C.Inh #4 inhibitor effectively prevented extensive macroscopic corrosion, ensuring that the steel particles would be separable by magnetic filtration. This observation is further supported by the quantitative elemental analysis from EDX (Table 3.4 for 48h, and later XPS data in Section 3.2.2.2), which showed a very low or undetectable oxygen content on the steel particles in the presence of the inhibitor. The lack of visible corrosion products by SEM, coupled with the electrochemical data (Section 3.2.1) demonstrating high inhibition efficiencies, indicates that the inhibitor maintained the surface integrity against aggressive corrosion over these periods. More detailed chemical state analysis by XPS (Section 3.2.2.2) provided further insights into the composition of any passive or adsorbed layers.

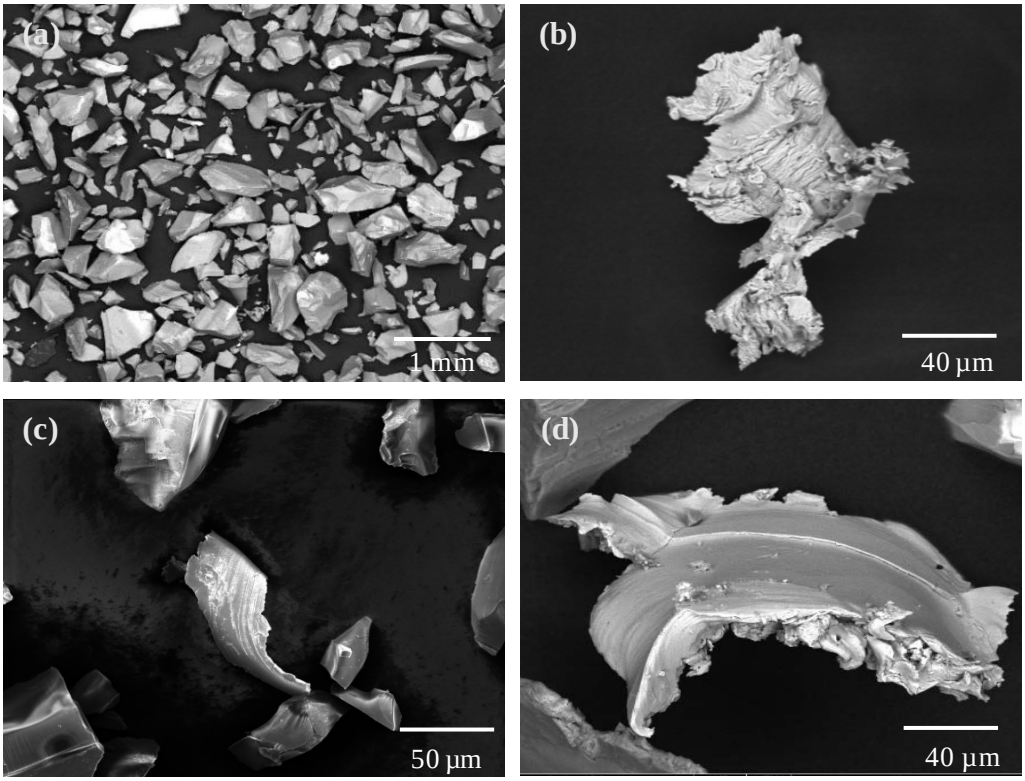

Figure 3.15: SEM images showing steel and abrasive particles in suspension after the WAS cut (a) and (b) 216 hours, (c) and (d) 456 hours.

3.2.2.2 X-ray Photoelectron Spectroscopy

To gain insights on the inhibitor composition and the nature of the film it forms on the steel surface, a comparative XPS analysis of the bulk C.Inh #4 inhibitor and a 1.6310 steel coupon treated with the inhibitor was performed and shown in Figure 3.16. The XP survey spectra of C.Inh #4 shows the presence of oxygen, nitrogen and sulphur in the inhibitor formulation. The binding energies of the N 1s and S 2p elemental lines (400.4 eV and 169 eV, respectively) suggest the presence of amine and sulfur-containing groups (e.g., sulfates/sulfonates) in C.Inh #4. As observed in Figure 3.16, the steel coupon treated with C.Inh #4 inhibitor shows the presence of oxygen, nitrogen and a carbon-rich layer on the steel surface. In contrast, the spectrum of the immersed steel coupon is devoid of any peak contributions from sulphur suggesting that sulphur is not bound to the steel surface. Given that a native iron oxide/hydroxide layer spontaneously forms on steel surfaces upon exposure to ambient conditions, the interaction of C.Inh #4 predominantly occurs with this pre-existing surface oxide rather than a pristine metallic iron surface. The most probable mechanism for the formation of the protective layer, therefore, involves the interaction of carbon and nitrogen-

containing functional groups from the inhibitor molecules (amines) with the steel's oxidized surface. The observed O 1s peak at ~530 eV and the detected oxidized iron species (Fe 2p) confirm the presence of surface oxides and hydroxides, further supporting that the interaction of the inhibitor with these charged surface species is a key inhibition mechanism. This interaction likely modifies the properties of the native oxide layer or forms a stable adsorbed film on top of it, hindering further corrosion.

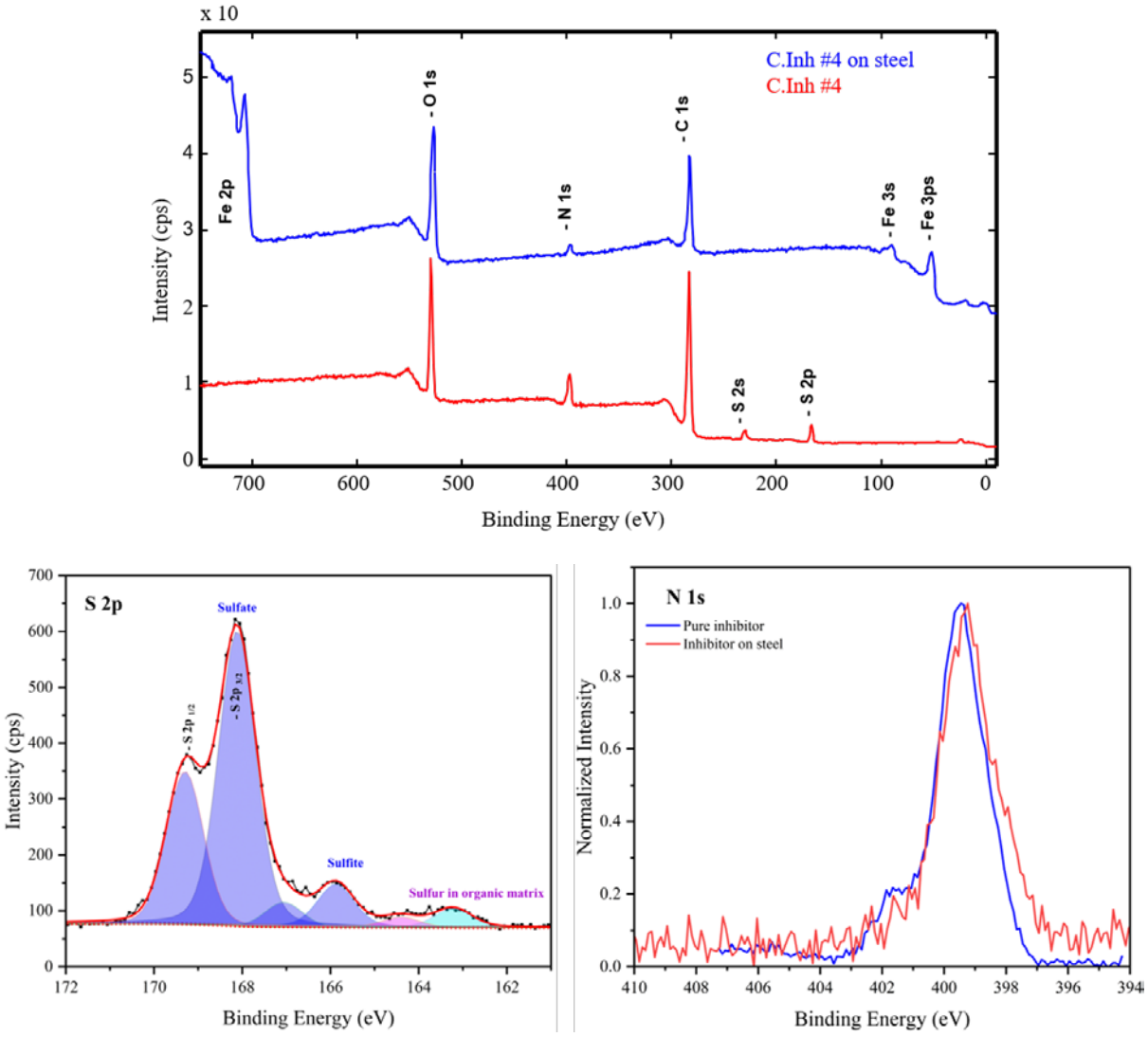

Figure 3.16: Top – combined XP survey spectra of C.Inh #4 and 1.6310 steel surface treated with the inhibitor. Bottom left - High-resolution S 2p XP spectrum of the pure C.Inh #4 inhibitor, with deconvolution. The experimental data (black dots) are fitted with a Shirley background and Gaussian-Lorentzian functions (red line). The spectrum reveals the presence of multiple sulfur species: sulfate (SO_4^{2-}) and sulfite (SO_3^{2-}) - blue shaded peak, and sulfur in an organic matrix - cyan shaded peak). Bottom right – Combined N 1s spectra of C.Inh #4 and of 1.6310 steel surface treated with the inhibitor.

Furthermore, the chemical composition of the film formed on a 1.6310 steel coupon immersed in the WAS cutting solution during the cutting experiment was also analyzed by angle-dependent XPS with the spectra for C 1s, N1s, Fe 2p and O 1s shown in Figure 3.17.

By varying the angle between the normal of the sample surface and the analyzer axis, the information depth is varied. Spectra recorded at 20° between the normal of the sample surface and the analyzer axis have a larger information depth than at higher angles. At 20° metallic iron is pronounced at Fe 2p, whereas at 70° the Fe (hydr)oxide dominates. Spectra of C 1s and N 1s are similar at all recorded angles indicating that the inhibitor film is located on the top of the iron oxide, native to the steel surface. When exposed to ambient conditions, a native iron oxide layer typically forms on steel surfaces after preparation. This could account for some of the oxidation observed in the sample. At 70°, the hydroxide and hydrate portion at the O 1s spectrum is enhanced compared to the oxidic portion. The WAS used for the cut consisted of Tap water with 1.5 vol.% C.Inh #4 and 60 mg/l concentration of the additive (Liquitech 227P). The survey XP spectrum characterizing the additive is provided in Figure A3 (appendix).

The XP spectra contained in Figure 3.17 provide information about the surface chemistry and composition of the steel particles after WAS cutting with 1.5 vol.% C.Inh #4 inhibitor. In the C 1s spectra, the COO peak at 288.2 eV corresponds to carboxylate groups, indicating the presence of organic acids or their derivatives on the surface, likely from the corrosion inhibitor. The prominent peak at a binding energy of 285 eV marked C_xH_y suggests the presence of hydrocarbons, possibly from organic contaminants or dried residual inhibitor on the surface. In the N 1s spectra, a nitrogen-containing species with a binding energy of 400.3 eV strongly suggests the presence of an amine group on the steel surface. These groups identified to be present on the surface give a clue as to the composition of the corrosion inhibitor. In the Fe 2p spectra, peaks at 710 eV, and 707 eV binding energies correspond to different oxidation states of iron – Fe-(III) and Fe-(0) respectively. The elemental line of Fe-(II) between those of Fe-(III) and Fe-(0) is not resolved but is expected to be present. The detection of Fe-(0) indicates the presence of elemental iron within the information depth of XPS (~ 2.7 nm range for Fe-oxide, Fe 2p spectrum) [185]. In the O1s spectra, the observed peaks between 530 eV and 532 eV suggest the presence of various oxygen-containing species, including iron oxides (Fe_2O_3), and functional groups like hydroxyl (-OH), alcohol (-CO) or carboxyl (-COO) groups. The presence of carboxyl groups (-COO) and nitrogen-containing species indicates the possibility of adsorption of the organic corrosion inhibitor on the steel surface, resulting in a detectable layer that has minimized the corrosion rate.

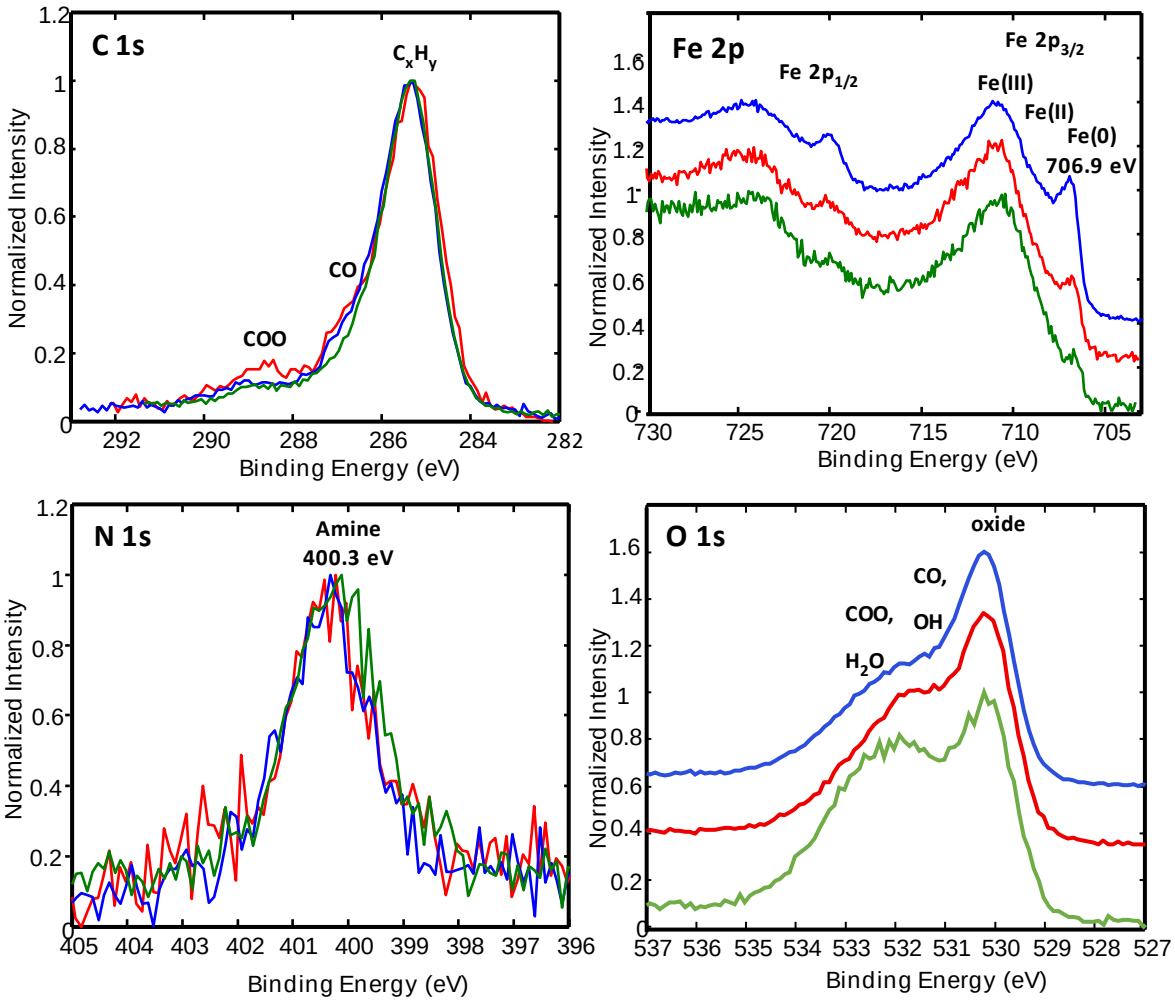

Figure 3.17: Angle-dependent XP spectra of a polished steel coupon immersed in the WAS basin 48 hours after the cut. The angle between the surface normal and analyzer axis: 20° (blue curves), 45° (red curves) and 70° (green curves). The acceptance angle of the analyzer was ±20°.

3.2.2.3 Long-Term Corrosion Monitoring after the WAS Cutting Process.

This section examines the long-term corrosion behavior of steel particles generated during the WAS cutting process, after 18 months of immersion in the cutting suspension. The SEM images, EDX and XP spectra of the steel are reported in Figures 3.18 – 3.26 and Tables 3.5 – 3.7 to provide a comprehensive understanding of the surface morphology and chemical composition of the 1.6310 steel surface following prolonged exposure to the WAS environment.

Figure 3.18 and Table 3.5 give a wide-area surface morphology and elemental composition of the surface of a 1.6310 steel coupon, immersed in the WAS cutting basin during the WAS cutting process, after 18 months in solution.

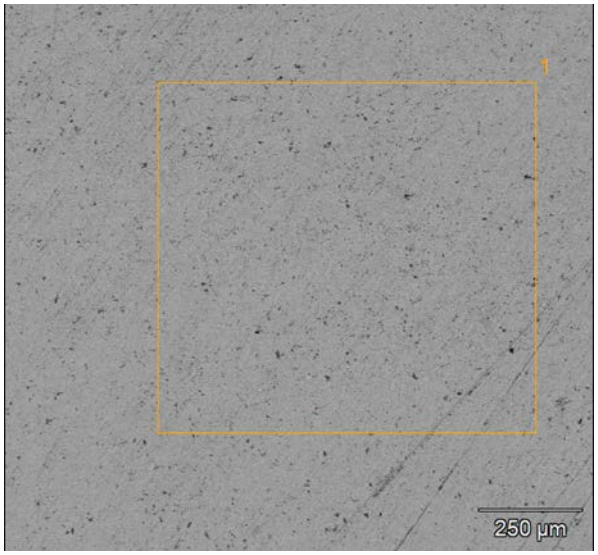

Figure 3.18: BSE image of the surface of a 1.6310 steel coupon immersed in the WAS after 18 months in solution. The marked area '1' indicates the region subjected to EDX analysis, with its elemental composition detailed in Table 3.5.

Table 3.5: Composition in at.% of the surface area "1" (Fig. 3.18) of a 1.6310 steel coupon immersed in the WAS for 18 months.

	C	O	Al	Si	Cr	Mn	Fe	Mo
Composition (wt. %)	6.1 ±0.5	2.0 ±0.2	0.8 ±0.2	1.2 ±0.3	0.2 ±0.2	1.1 ±0.7	88.4 ±1.7	0.2 ±0.1

The BSE image in Figure 3.18 reveals a surface exhibiting minimal evidence of widespread general corrosion. While the 1.6310 steel itself contains a small percentage of silicon (0.28 wt.%), darker, localized features are observed across the SEM images in Figure 3.18, and magnified in Figure 3.19). These features may represent the onset of localized corrosion or could indicate the presence of co-deposited particulate matter from the cutting fluid, such as aluminosilicate (clay) particles. Such particles would appear darker in BSE images due to their lower average atomic number compared to iron, and their presence could also offer nucleation sites for further deposition or localized reactions. This possibility is supported by later localized EDX analyses (Figure 3.19 and Table 3.6), which show significant concentrations of Al, Si, and O in some of these darker regions, consistent with inorganic contaminants.

Despite these localized features, the overall elemental composition of the larger surface area ("1") shown in Table 3.5 shows a relatively low oxygen content and a high iron-to-oxygen atomic ratio, suggesting that a significant, widespread corrosion layer had not formed over the extended immersion period. This indicates that the inhibitor, C.Inh #4, maintained a degree of

protective efficacy against general corrosion long-term. However, when comparing this to the steel surface after 48 hours (where oxygen was below EDX detection limits, Table 3.4), the observed 2.0 at.% oxygen after 18 months does indicate a degree of surface oxidation on the over time. This suggests a gradual diminishing or alteration of the inhibitor layer's protective ability in prolonged contact with the solution. Considering that the inhibitor was labeled biodegradable by the manufacturer would support the observation. A higher magnification image (10 µm field width) was subjected to EDX analysis at three points (1, 2 and 3), for localized corrosion investigation.

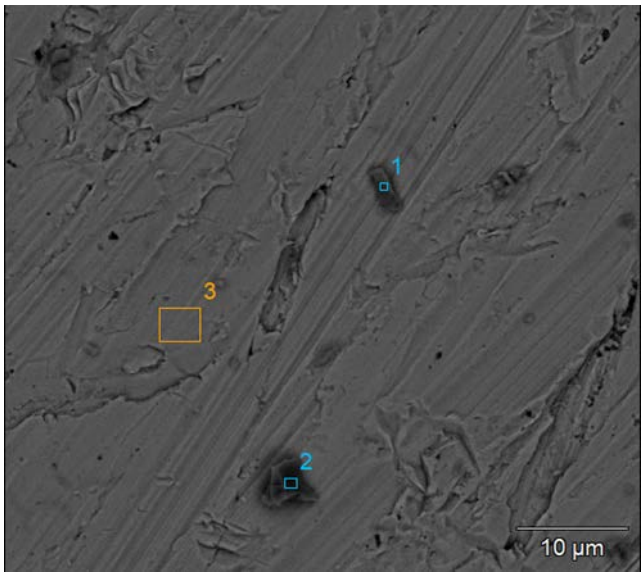

Figure 3.19: BSE image of the 1.6310 steel coupon surface after 18 months of immersion in the WAS, displaying three marked regions (1, 2, and 3) for localized EDX analysis, with their elemental composition detailed in Table 3.6.

Table 3.6 presents the elemental composition of three distinct points on the steel surface shown in Figure 3.19. Points 1 and 2, which correspond to these darker features, exhibit high concentrations of oxygen, aluminum, and silicon, consistent with the presence of inorganic particulate contaminants. In contrast, Point 3 represents an area more characteristic of the bulk steel surface, showing a high iron content (93.9 at.%) and a very low oxygen content (below detection limits). The composition of Point 3, with its high metallic iron signal and minimal oxygen, indicates the absence of significant localized general oxidation at this specific location after long-term immersion in the WAS.

Considering the information depth of SEM-EDX analysis, very thin oxide layers are typically not detected if the underlying metallic signal is dominant. While EDX indicated absence of

bulk corrosion products on the steel surface, XPS (as discussed in Section 3.2.2.2) could still detect the presence of a thin native oxide layer on the steel surface, even if macroscopically insignificant.

Table 3.6: Composition of three sample points (1,2,3) in at. % on the surface of the steel shown in Figure. 3.19 by SEM-EDX.

	C	O	F	Mg	Al	Si	Ca	Mn	Fe	Ni
Point 1	4.1 ± 0.6	48.6 ± 1.2	1.2 ± 1.4	3.7 ± 0.3	9.3 ± 0.3	13.7 ± 0.3	2.9 ± 0.2	0.4 ± 0.2	16.1 ± 0.6	-
Point 2	3.4 ± 0.7	59.9 ± 1.5	- -	5.4 ± 0.3	8.9 ± 0.4	13.1 ± 0.4	1.8 ± 0.2	-	7.5 ± 0.6	-
Point 3	3.1 ± 0.6	-	-	-	-	0.7 ± 0.2	-	1.5 ± 0.4	93.9 ± 1.8	0.8 ± 0.5

The XP spectrum of the steel surface is shown in Figure 3.20 and 3.21. The broad-scan XPS spectrum (Figure 3.20) confirms the presence of carbon, nitrogen, oxygen, calcium and iron on the surface. The presence of nitrogen suggests that some components of the inhibitor film persist on the surface even after long-term immersion.

The N 1s spectrum of the steel after 18 months (Figure 3.21) shows a new peak at a higher binding energy of 401.6 eV in addition to the 400.4 eV binding energy peak typical of nitrogen from an amine group. The Fe 2p spectrum shows a Fe $2p_{1/2}$ peak at ~725 eV, a Fe $2p_{3/2}$ peak at ~711 eV and a satellite of Fe $2p_{3/2}$, indicating iron at the +3-oxidation state. Present in the spectrum are also peaks showing the presence of Fe (II) and Fe (0) at lower binding energies and lower intensities compared to Fe (III). The presence of Fe (0) signal confirms that the oxide layer remains relatively thin, allowing photoelectrons from the underlying metallic iron to be detected. The presence of a high concentration of oxygen in the XPS analysis (from the O 1s signal) is in agreement with the SEM analysis suggesting the onset of localized corrosion all over the steel surface as residence time in solution reached 18 months.

It is worth noting that the performance of C.Inh #4 inhibitor, far exceeds the initially estimated corrosion inhibition time needed (2 weeks) for processing the steel-abrasive mixture obtained from the WAS cutting of the RPV steel.

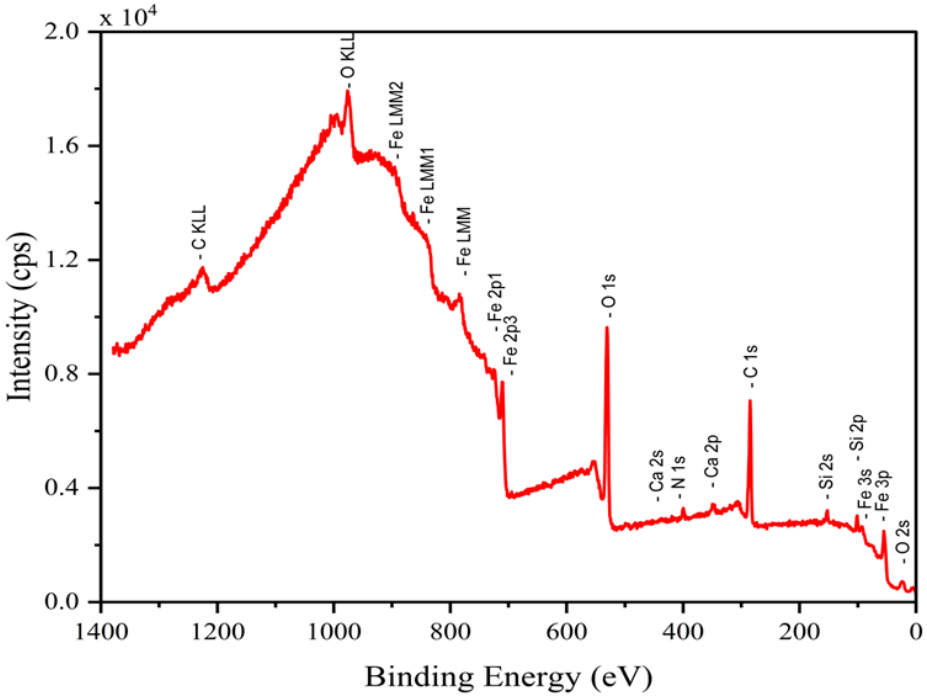

Figure 3.20: XP survey spectrum of a polished 1.6310 steel coupon surface after 18 months of immersion in the WAS, rinsed with Milli-Q water prior to measurement.

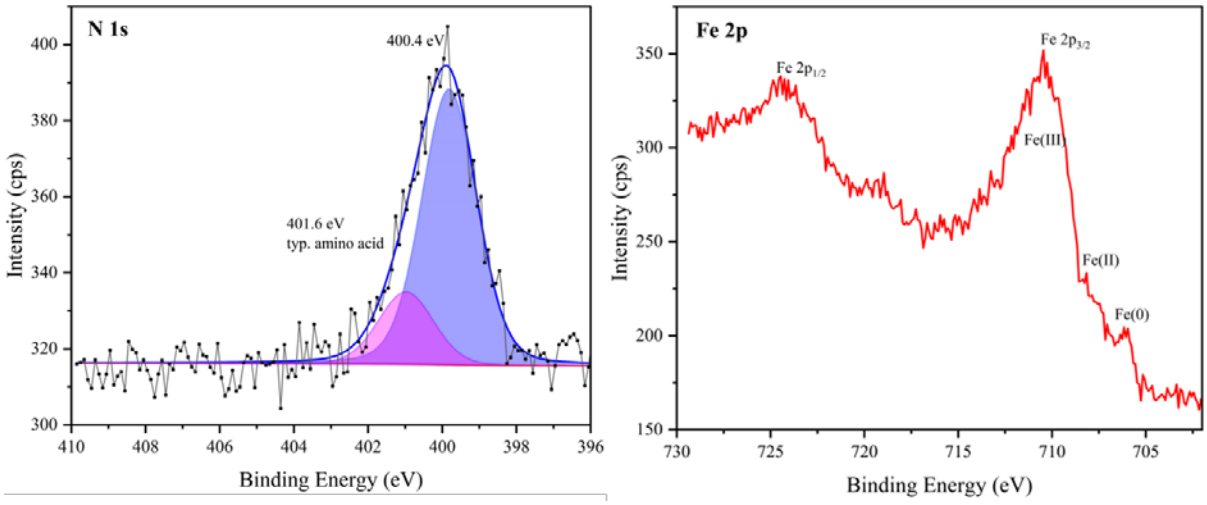

Figure 3.21: N 1s and Fe 2p XP spectra of a 1.6310 steel coupon surface after 18 months of immersion in the WAS. The N 1s spectrum (left) reveals two nitrogen species, including a prominent amine group peak at ~400.4 eV and an additional peak at 401.6 eV. The Fe 2p spectrum (right) shows peaks corresponding to various iron oxidation states: metallic iron Fe (0), Fe-(II), and Fe-(III).

Figures 3.22 and 3.23 provide further insights into the long-term surface state of the 1.6310 steel coupon after 18 months of immersion in the WAS cutting suspension. Figure 3.22 displays SEM images, which reveal the presence of numerous darker, localized features scattered across the steel surface. These features exhibit distinctive morphologies, including irregular,

filamentous, or clustered structures, which are visually characteristic of microbial colonization and biofilm formation [186,187]. Further EDX analysis of these localized features was conducted, as presented in Figure 3.23 for points 1 and 2, with their atomic compositions detailed in Table 3.7. The EDX spectra from these darker areas show significantly higher atomic concentrations of carbon, nitrogen and oxygen compared to the surrounding steel matrix (e.g., Point 1: 35.4% C, 7.8% O; Point 2: 2.6% C, 3.7% O). This elemental composition is characteristic of organic matter and biological structures [188], suggesting the presence of microorganisms forming a biofilm on the steel surface.

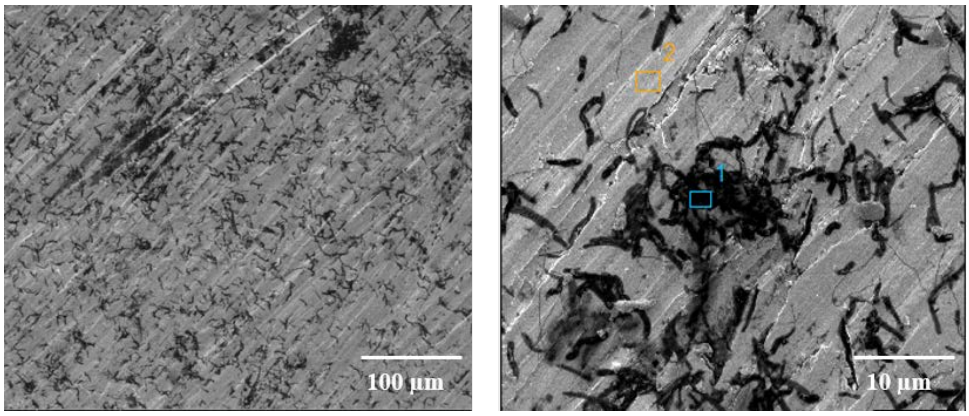

Figure 3.22: SEM images of 1.6310 steel surface at different magnifications showing bacterial presence (darker features) after immersion in WAS for 18 months. Points 1 and 2 EDX spectra are found in Figure 3.23.

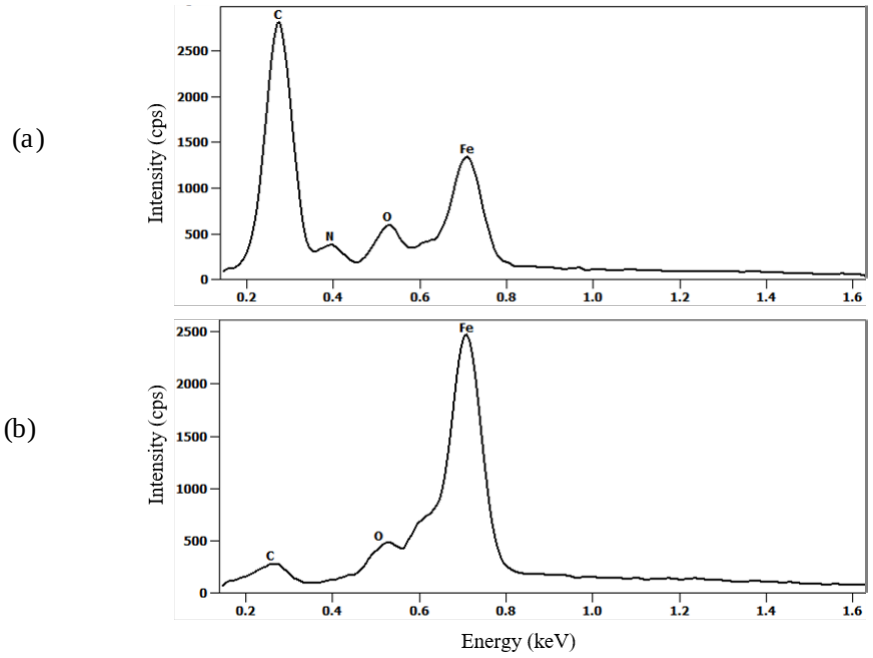

Figure 3.23: EDX analysis of points a and b in Fig. 3.22 on the 1.6310 steel surface after 18 months in WAS. (a) EDX spectrum for point 1; (b) EDX spectrum for point 2. Electron beam energy: 2.5 kV.

Table 3.7: Elemental composition (in at. %) of points 1 and 2 in Fig. 3.23.

	C	O	N	Fe
Point 1	29.0 ± 0.9	12.4 ± 2.5	9.2 ± 0.9	49.4 ± 2.5
Point 2	2.5 ± 0.3	7.3 ± 1.4	-	90.2 ± 2.7

The possible presence of microorganisms suggests that the tap water, despite the addition of a corrosion inhibitor, was not sterile and contained viable microbial species. While some microorganisms are known to be tolerant to or even metabolize certain corrosion inhibitors, their presence could lead to the formation of a biofilm on the steel surface [186]. This biofilm can trap moisture, nutrients, and even corrosion products and creates microenvironments at the metal surface that differ significantly from the bulk solution chemistry, potentially altering the effectiveness of the inhibitor. This phenomenon could lead to localized corrosion processes beneath the biofilm, otherwise known as microbiologically influenced corrosion (MIC) [187].

3.3 Separation and Characterization of C.Inh #4 Inhibitor Composition

To explain fully the corrosion inhibition mechanism of C.Inh #4 and to provide a foundation for understanding its behavior in the presence of ionizing radiation, a comprehensive characterization of its chemical composition was necessary. Since C.Inh #4 is a commercial formulation, the precise molecular structures of its active components were initially unknown. In this section, details of the analytical approach combining results from XPS, NMR and EI-MS, to identify the key constituents of C.Inh #4 are presented. Resolving the structures of the constituent compounds of the inhibitor enabled the correlation of its overall performance with specific molecular properties and interactions.

3.3.1 Chemical Composition of Adsorbed Inhibitor

Information from the safety datasheet of C.Inh #4 indicated that it is an “amine-based” inhibitor formulation. The XP spectra of the pure inhibitor and of the surface of 1.6310 steel treated with the inhibitor were presented in Figure 3.20. Comparison of the pure inhibitor's XP spectrum (red trace) with that of the steel surface after immersion in the inhibitor solution (blue trace) provided initial insights into the elemental composition and surface interactions. The pure inhibitor spectrum exhibited prominent peaks corresponding to carbon (C 1s), oxygen (O 1s), and nitrogen (N 1s), confirming these elements as key components of the organic compounds within the formulation. Additionally, distinct sulfur peaks (S 2s and S 2p) were observed in the

pure inhibitor spectrum, with the S 2p binding energy (typically 168-169 eV) consistent with sulphate and sulfone core levels [189,190].

As already highlighted in the previous section, the XP spectrum of the steel surface after inhibitor treatment showed significant peaks for C 1s, O 1s, and N 1s, indicating the successful adsorption or interaction of carbon-, oxygen-, and nitrogen-containing species from the inhibitor onto the steel surface. The N 1s binding energy at approximately 400.3 eV confirmed the presence of amine groups on the adsorbed layer, consistent with the "amine-based" nature of the formulation. However, the S 2s and S 2p peaks, clearly present in the pure inhibitor, were absent from the steel surface spectrum. This strongly suggests that the sulfur-containing compound(s) present in the bulk inhibitor formulation either did not adsorb onto the steel surface, or adsorbed in negligible quantities that were below the XPS detection limit, and therefore likely do not contribute directly to the formation of the protective layer.

3.3.2 Nuclear Magnetic Resonance (NMR) Spectroscopy

To elucidate the molecular composition of C.Inh #4, a series of NMR experiments were performed. The ^{1}H NMR spectrum for C.Inh #4 in D_2O (Figure 3.27) revealed distinct proton environments, indicative of a multi-component mixture. Multiplets (m) observed between 0.8 to 1.5 ppm were characteristic of aliphatic protons (-CH_3 or -CH_2-) within hydrocarbon chains. The observed splitting patterns suggest the presence of multiple adjacent protons, consistent with relatively long alkyl chains [191]. A triplet (t) at approximately 2.3 ppm suggested a -CH_2- group adjacent to an electron-withdrawing group, such as a carbonyl or carboxyl moiety [192]. Doublet peaks in the aromatic region (7.0 to 8.0 ppm) indicated the presence of aromatic protons, with splitting patterns suggesting substitution on the aromatic ring [191]. Highly intense triplet signals at 2.8 and 3.7 ppm were particularly notable, suggesting a -CH_2-CH_2- substructure where each -CH_2- group is bonded to different electronegative functional groups [192].

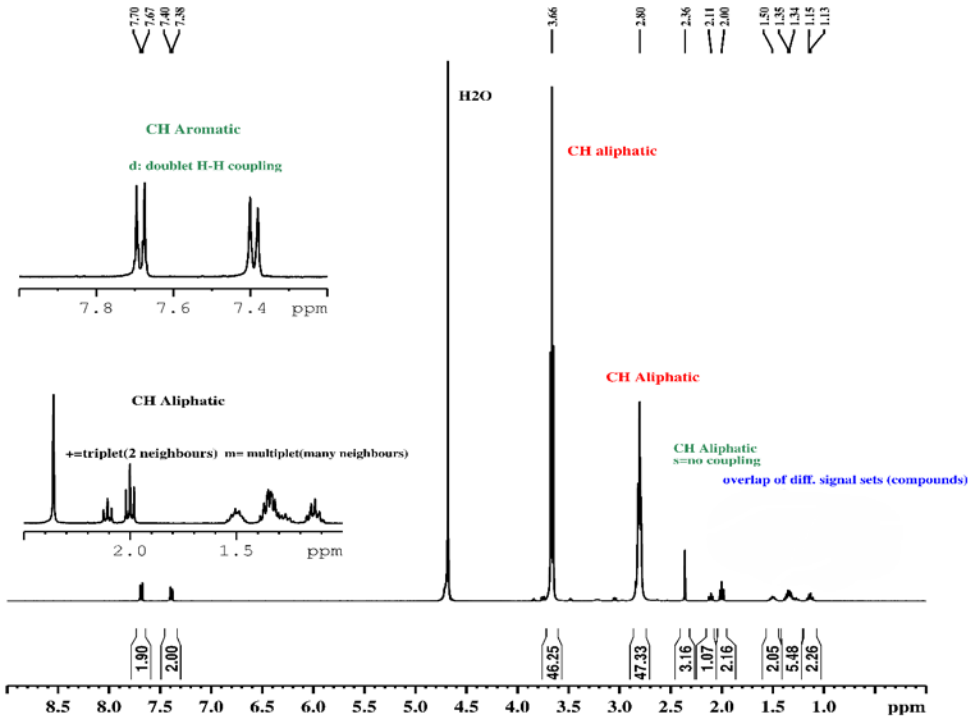

Figure 3.24: [1]H NMR spectrum (chemical shift (in ppm) vs signal intensity) of C.Inh #4. Insets and annotations show aliphatic and aromatic regions and possible groups present in the constituent molecules of the inhibitor.

The ^{1}H,^{1}H COSY NMR spectrum (Figure 3.25) provided crucial connectivity information between protons, allowing for the identification of distinct molecular species within the mixture [193]. Based on the observed cross-couplings, three distinct, uncoupled spin systems were identified, providing compelling evidence for the presence of at least three different compounds within C.Inh #4:

- **Spin System 1 (Aromatic Component):** This system is evidenced by the cross-couplings observed solely within the aromatic region (around 7.5 ppm), and a distinct cross-coupling between these aromatic signals and a singlet (methyl group) at 2.4 ppm (as indicated in Figure 3.25). The absence of cross-peaks between this system and other regions of the spectrum confirms it as a self-contained molecular entity.
- **Spin System 2 (Ethanolamine Derivative):** The highly intense signals at 2.8 and 3.7 ppm showed strong cross-couplings isolated from other spin systems, unequivocally confirming the x-CH_2-CH_2-y substructure. Given their high intensity, this compound represents a major constituent of C.Inh #4 and is consistent with ethanolamine, diethanolamine, or triethanolamine.

- **Compound 3 (Aliphatic Component):** Multiple cross-peaks are observed only within the broad aliphatic region (0.8-2.0 ppm), with no cross-couplings to either the aromatic system or the 2.8/3.7 ppm system. This indicates a third, independent spin system, corresponding to a compound dominated by aliphatic chains.

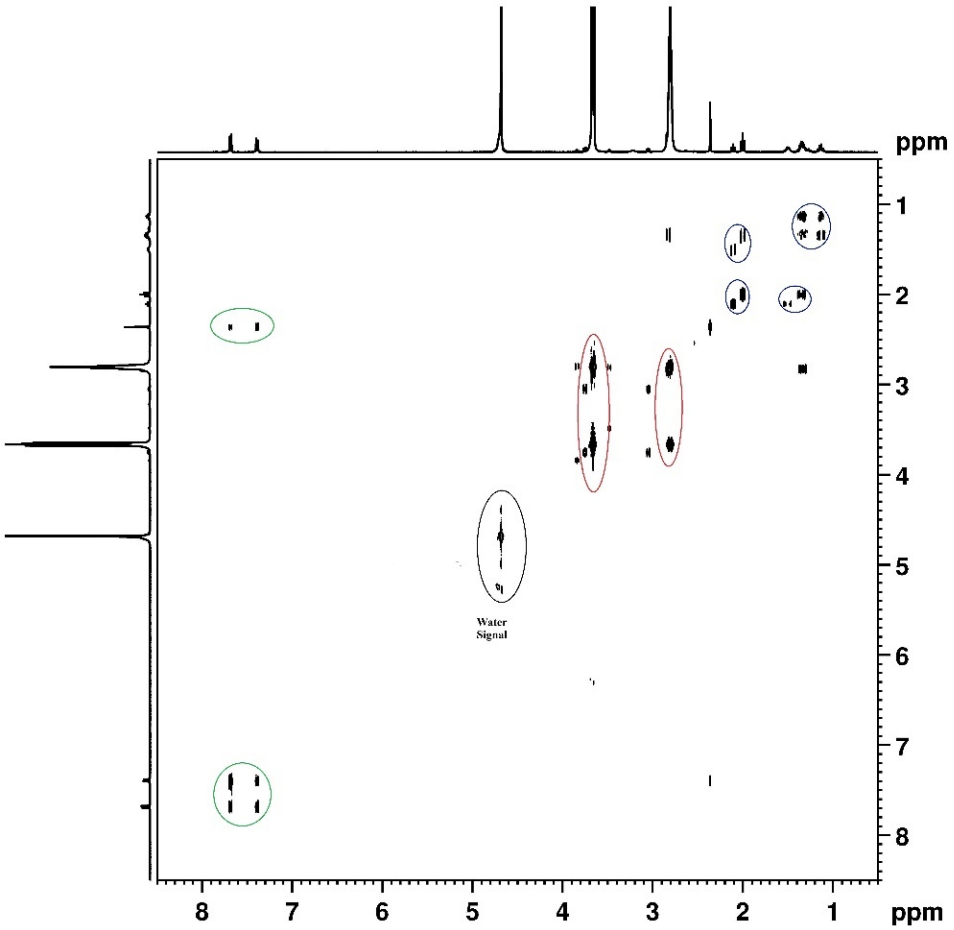

Figure 3.25: Two-dimensional Homonuclear Correlation Spectroscopy (^1H, ^1H COSY) NMR spectrum of the C.Inh #4 formulation in D_2O. Cross-peaks, such as those highlighted by the red and green ellipses, indicate scalar (spin-spin) coupling between protons on adjacent or nearby atoms within the same molecule, thereby revealing direct through-bond connectivities. The prominent signal around 4.7 ppm, labeled "Water Signal," corresponds to residual H_2O protons present in the deuterated solvent (D_2O).

The ^{13}C NMR spectrum (Figure 3.26) indicates the nature of carbon atoms present in the inhibitor, providing further support for the interpretations [191,192]. A peak corresponding to a -CH_3 group was observed, consistent with the aromatic component (Spin System 1). Multiple -CH_2- peaks were identified, some with high intensity, reinforcing the presence of

ethanolamine-like structures (Spin System 2) and other alkyl chains (Spin System 3). Importantly, the presence of a signal around 183.75 ppm indicated a carboxylic acid (-RCOOH) or ester (-RCOOR') moiety. For the aromatic component identified in Spin System 1, the combination of ^{1}H and ^{13}C shifts, along with the absence of a carbonyl functionality directly attached to the aromatic ring, suggested an oxygen-based substituent (likely a hydroxyl group) attached to the toluene ring.

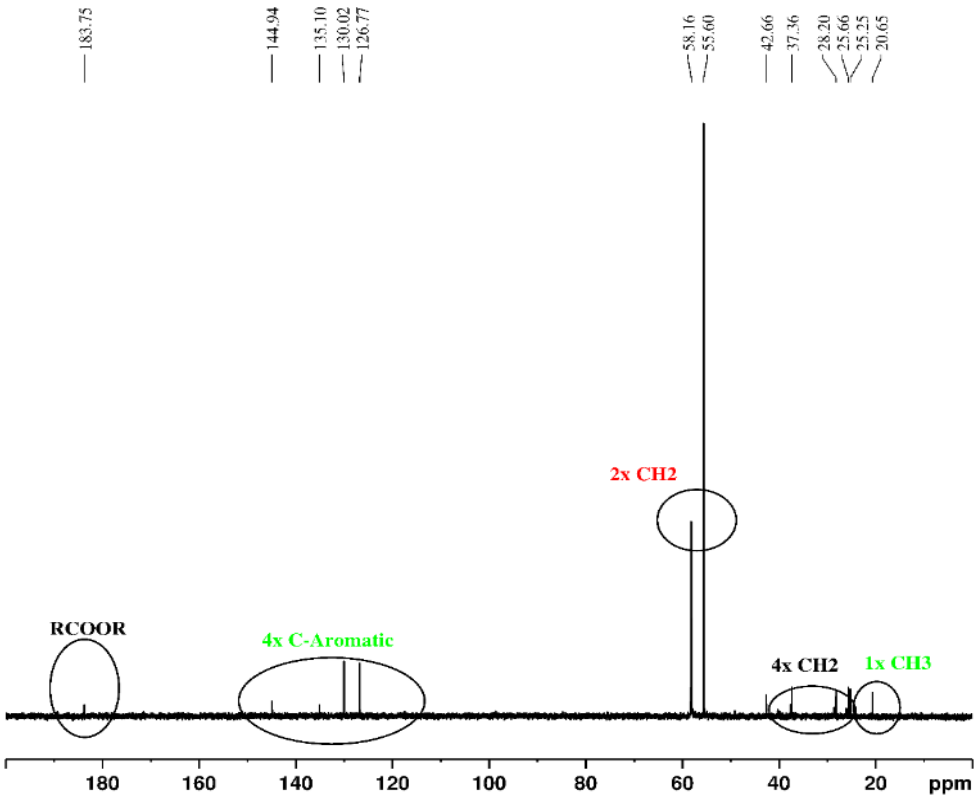

Figure 3.26: ^{13}C-NMR spectrum of C.Inh #4 formulation in D_2O. Key assignments include characteristic peaks for carboxylic acid/ester carbons (RCOOR, ~183.75 ppm), aromatic carbons (4x C-Aromatic, ~126-145 ppm), methylene carbons (2x CH_2 , ~55-58 ppm; 4x CH_2,~25-42 ppm), and a methyl carbon (1x CH_3, ~20.65 ppm).

Following column chromatography of C.Inh #4, four fractions were collected (vis Fraction 1 – 4) and their ^{1}H NMR spectra were compared to the original C.Inh #4 mixture (Figure 3.27). Fraction 1 showed distinct peaks consistent with an ethanolamine derivative, further supporting the presence of the compound identified in Spin System 2.

Overall, the NMR data established C.Inh #4 as a complex mixture containing at least three main components: a major ethanolamine derivative, an aromatic compound resembling a substituted toluene, and a largely unresolved component containing long aliphatic chains.

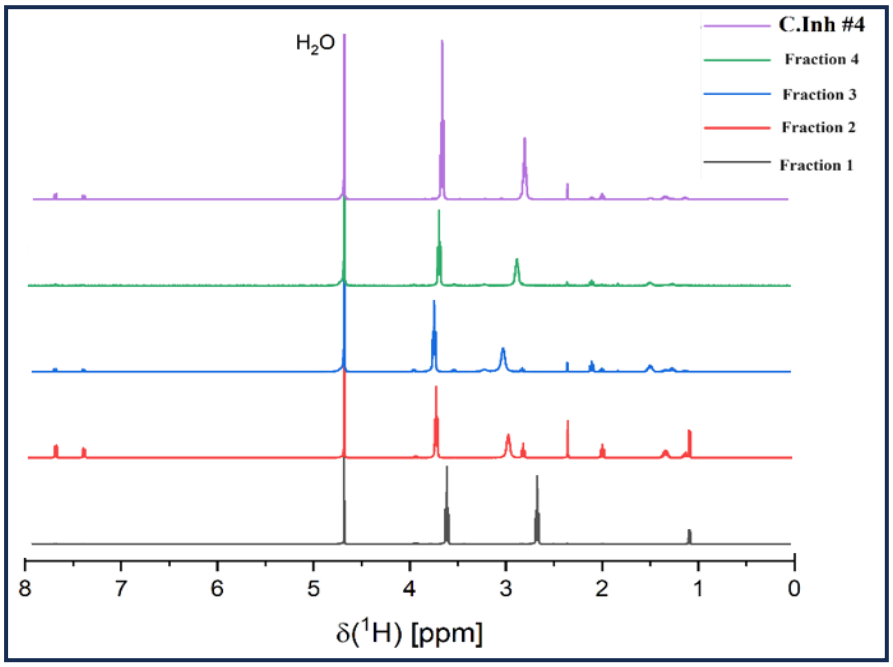

Figure 3.27: Comparison of ¹H NMR spectra for the original C.Inh #4 formulation (purple trace) and four distinct fractions (Fraction 1: black, Fraction 2: red, Fraction 3: blue, Fraction 4: green) obtained through column chromatography of C.Inh #4.

3.3.3 Electron Ionization Mass Spectrometry and Definitive Identification

To complement the NMR analyses and provide definitive molecular identification, particularly for components less resolved by NMR, Electron Ionization Mass Spectrometry (EI-MS) was performed. As described in Section 2.2.5, the analysis was conducted using a Gas Chromatography-Mass Spectrometry (GC-MS) system. The GC-MS data (Figure 3.28) presented two distinct chromatographic peaks, observed within retention time windows of 0.99-1.26 min and 2.47-2.91 min. These distinct peaks indicate the presence of at least two major eluting species that were subsequently characterized by their mass spectra. The notation "MS: 0.99-1.26 min" refers to the mass spectrum (or integrated mass spectral data) acquired for the compound(s) eluting from the gas chromatograph within that specific retention time range [194].

The upper spectrum (corresponding to the earlier eluting species, likely from the NMR Spin System 2) showed a prominent signal at m/z 118.0966, which can be assigned to a fragment of triethanolamine (TEA). The protonated molecule peak of TEA ($C_6H_{16}NO_3$) is expected at m/z 150.1130, and a signal at m/z 150.1242 was observed, strongly supporting the presence TEA. The fragmentation pattern, including the loss of CH_3OH and further ethanol chains, was consistent with TEA's known fragmentation pathways [195].

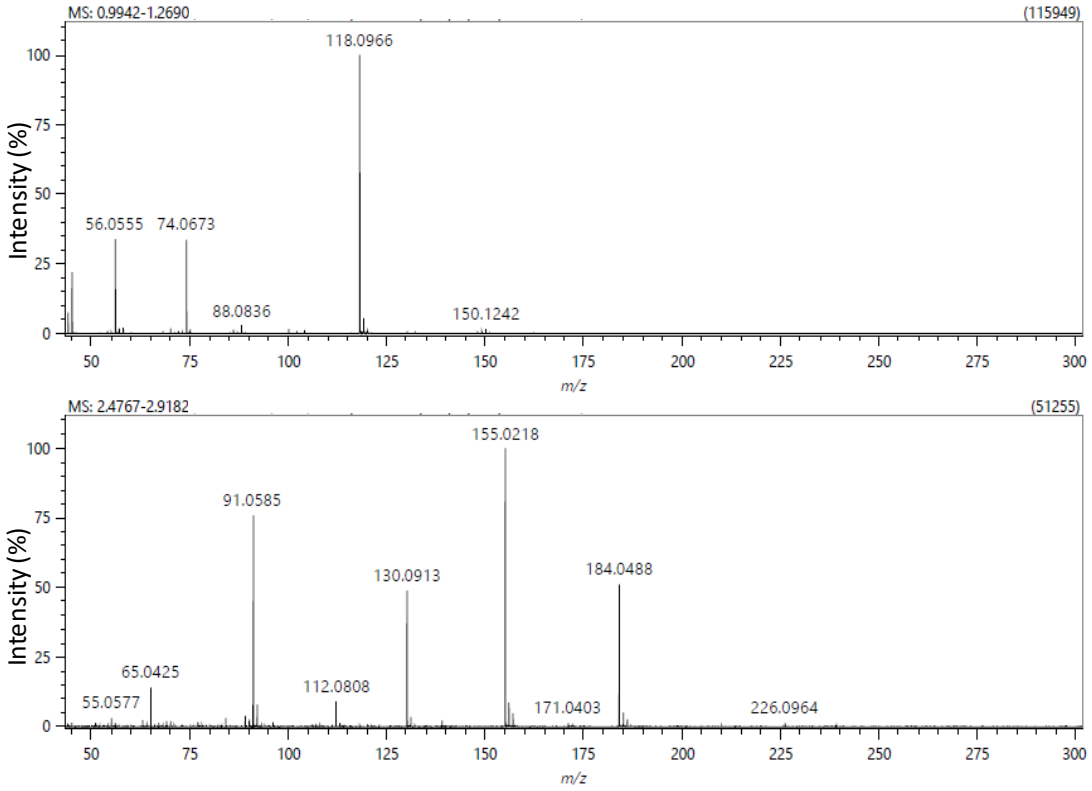

Figure 3:28: Electron Ionization Mass Spectra (EI-MS) of the C.Inh #4 Formulation.

The lower spectrum (corresponding to the later eluting species, initially assigned as aromatic compound identified in the NMR Spin System 1) exhibited a more complex fragmentation pattern. This spectrum displayed significant fragments containing sulfur such as m/z 155.0218, assigned to $[C_7H_7SO_2]^+$, and m/z 184.0488, assigned to $[C_7H_7SO_2NHCH_2]^+$. These sulfur-containing fragments, coupled with the presence of the tolyl ion (m/z 91.0585), provided strong evidence for a sulfur-containing aromatic compound with an aliphatic chain in the formulation.

Following the comprehensive preliminary analytical findings, the manufacturer of C.Inh #4 was contacted to confirm the identity of the major constituents. This communication definitively identified three primary active compounds in the formulation: 2,4,6-Tri (6-aminohexanoic acid)-1,3,5 triazine (TACT), 6-(4-Methylphenylsulfonamido) hexanoic acid, and Triethanolamine (TEA), with TEA and TACT being themselves corrosion inhibitors [81,84]. To provide confirmation of these identities, pure samples of TEA and TACT were acquired, and their ^{1}H NMR spectra were directly compared with that of the C.Inh #4 formulation. Figure 3.29 presents the comparative NMR data: the green spectrum represents pure TEA, the red spectrum corresponds to pure TACT, and the black spectrum is that of the C.Inh #4 formulation.

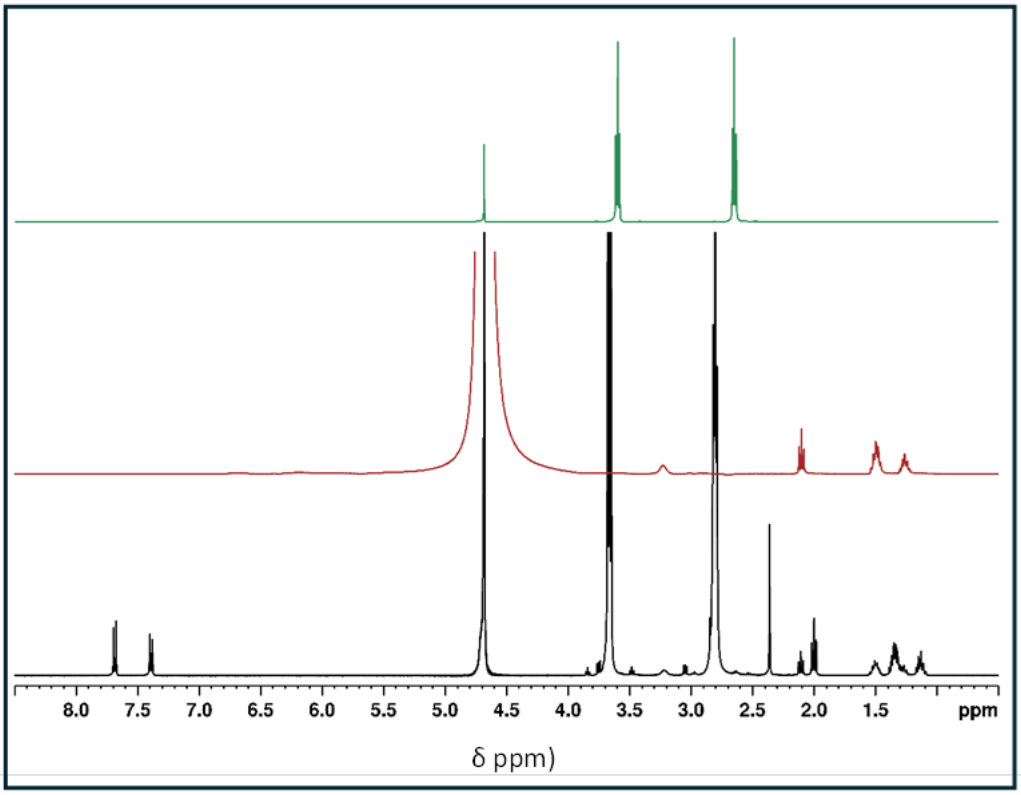

Figure 3.29: Comparative ¹H NMR spectra of pure Triethanolamine (TEA, green), pure 2,4,6-Tri (6-aminohexanoic acid)-1,3,5 triazine (TACT, red), and the C.Inh #4 formulation (black).

It can be observed from Figure 3.29 that the black spectrum of C.Inh #4 is clearly a superposition of the characteristic signals from both pure TEA and pure TACT.

The prominent triplets in the black spectrum at approximately 2.8 ppm and 3.7 ppm precisely match the characteristic signals observed in the pure TEA spectrum (green), confirming the presence of TEA's -CH_2-CH_2- substructures adjacent to nitrogen and oxygen, respectively. This aligns with the initial NMR interpretation of Compound 2.

Similarly, the aromatic signals in the black spectrum (around 7.5 ppm) and the triplet at approximately 3.2 ppm, along with other aliphatic signals (e.g., around 0.8-1.7 ppm and 2.2 ppm), are in direct correspondence with the peaks observed in the pure TACT spectrum (red).

With the additional information supplied by the manufacturer, a comprehensive reconciliation of analytical findings for the three compounds was as follows:

Triethanolamine: Its presence is strongly supported by the characteristic triplet signals in the C.Inh #4 NMR spectrum (matching pure TEA) and the molecular ion fragment in the EI-MS (m/z 150.1242). This corresponds to the previously identified compound in Spin System 2.

2,4,6-Tri (6-aminohexanoic acid)-1,3,5 triazine: Its presence is confirmed by the specific aromatic and aliphatic signals in the C.Inh #4 NMR spectrum that perfectly match pure TACT (Figure 3.31). TACT contributes significantly to the nitrogen content detected by XPS (Section 3.3.1).

6-(4-Methylphenylsulfonamido) hexanoic acid: This compound directly accounts for the sulfur-containing fragments (m/z 155.0218, 184.0488) observed in the EI-MS (Figure 3.31) and the sulfur peaks detected in the bulk inhibitor's XPS (Section 3.3.1). Its structure, containing a methylphenyl (tolyl) group and a hexanoic acid chain, also aligns with the initial NMR observations of "aromatic with tolyl group" and contributes to the broader aliphatic signals initially grouped under Spin System 3.

The absence of sulfur peaks in the XPS spectrum of the adsorbed layer on the steel surface (Section 3.3.1), despite the confirmed presence of 6-(4-Methylphenylsulfonamido) hexanoic acid in the bulk formulation, suggests that this sulfur-containing component either does not adsorb significantly onto the steel surface, or its adsorption is too weak or sparse to be detected by XPS. This implies that its contribution to the direct formation of the protective surface film may be negligible, with the primary surface-adsorbing species being TEA and TACT. In addition, based on the "CHON" principle described in Chapter 2 as an inhibitor selection criterion, further study on 6-(4 Methylphenylsulfonamido)-hexanoic acid was discontinued because of the presence of sulfur in the compound. The findings in this section aligns with common commercial formulations where TACT is typically dissolved in triethanolamine and used as a biodegradable corrosion inhibitor for water-based lubricants and metal working fluids [58–60].

In conclusion, the formulation of C.Inh #4 has been identified using complementary methods. The structures of TEA and TACT are given in Figure 3.33

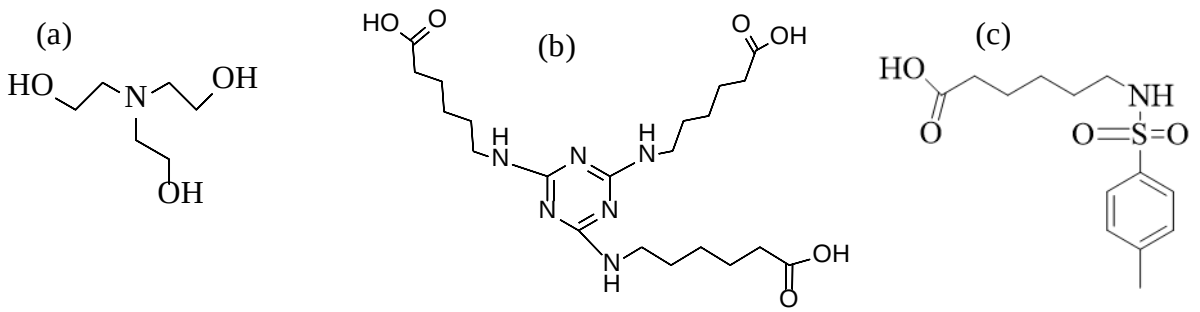

Figure 3.30: Chemical structures of the key components of C.Inh #4: (a) Triethanolamine – $C_6H_{15}NO_3$ (TEA), (b) 2,4,6-Tri (6-aminohexanoic acid)-1,3,5 triazine - $C_{21}H_{36}N_6O_6$ (TACT), and (c) 6-(4-Methylphenylsulfonamido) hexanoic acid.

3.4: Corrosion Inhibition of RPV Steel with Unirradiated TEA and TACT Inhibitors

Following the definitive identification of Triethanolamine, and 2,4,6-Tri (6-aminohexanoic acid)-1,3,5 triazine as primary active constituents of C.Inh #4 (Section 3.3), further investigation into their individual corrosion inhibition properties on 1.6310 ferritic steel are presented. Understanding their unirradiated behavior and mechanisms is crucial, establishing a baseline for interpreting ionizing radiation effects (Section 3.5).

In this section, the electrochemical performance, adsorption characteristics, and film properties of TEA and TACT in a near-neutral bicarbonate medium, mirroring WAS cutting conditions are covered.

3.4.1 Electrochemical Measurements of 1.6310 Steel in TEA and TACT Solutions

3.4.1.1 Open Circuit Potential Measurements of 1.6310 Steel in TEA and TACT Solutions

OCP measurements for 1.6310 steel (with an exposed surface area of 0.84 cm^2) in 0.06 mol/dm^3 $NaHCO_3$ solution containing TEA and TACT inhibitors, performed at room temperature in aerated conditions, are presented in Figure 3.31. As discussed in Chapter 2.2 (Electrochemical Measurements), 0.06 mol/dm^3 $NaHCO_3$ was utilized as electrolyte for these further studies, a selection informed by an industrial partner involved in the project. These experiments with TEA and TACT were performed to simulate representative industrial application conditions.

For all tested TACT concentrations (100 ppm, 200 ppm, 300 ppm, and 400 ppm), the OCP exhibited a rapid and significant positive shift from the initial negative potential due to the pre-measurement depassivation step, similar to observations in Section 3.1.2.1. This swift ennoblement of the potential suggests a rapid interaction of TACT molecules with the steel surface. The OCP values for all TACT concentrations stabilized quickly, typically within the first 0.5 hours, at significantly more noble potentials, ranging from approximately -240 mV to -190 mV vs. Ag/AgCl. This represents a substantial positive shift of approximately 440-490 mV compared to the blank solution. Notably, increasing TACT concentration from 100 ppm to 400 ppm leads to a progressive, albeit slight, shift towards more noble potentials and potentially faster stabilization, suggesting an enhanced protective effect with increasing surface coverage. However, a slight deviation is observed where the OCP at 300 ppm (-212.4 mV) is marginally lower (less noble) than at 400 ppm (-197.9 mV). This minor deviation from the

otherwise consistent trend lies within the expected variability of electrochemical measurements and can be attributed to a number of factors such as instrument noise, local fluctuations in electrode kinetics from variations in surface preparation, or transient changes in solution conditions. In addition, at concentrations of 300 ppm and above, TACT's high inhibition efficiency (over 98%, Table 3.9) suggests that the steel surface is already approaching saturation coverage. Small differences in OCP within this saturation regime could arise from subtle, localized film heterogeneity, or the dynamic equilibrium of adsorption/desorption. The consistently high and stable OCP values across this concentration range indicate that TACT effectively passivates the steel surface, significantly reducing its susceptibility to corrosion.

The OCP behavior at different TEA concentrations showed a varied, concentration-dependent trend as shown in Figure 3.31.

At 1000 ppm, the OCP initially shifts positive but then stabilizes at approximately -600 mV vs. Ag/AgCl. While this is slightly more noble than the blank (-680 mV), it remains a relatively negative potential, indicating only partial corrosion inhibition at this low concentration, consistent with the lower inhibition efficiency observed in Table 3.10. At 3000 ppm, the OCP exhibits a rapid initial positive shift, similar to higher concentrations. However, it then undergoes a pronounced transient drop in potential (between approximately 0.2 and 0.5 hours), before slowly recovering and stabilizing around -400 mV vs. Ag/AgCl. This transient dip suggests an initial, perhaps incomplete, film formation followed by a temporary breakdown or rearrangement of the protective layer, before a more stable, albeit less noble than optimal, state is achieved. This behavior correlates directly with the "jump" in inhibition efficiency observed in the potentiodynamic polarization curves (Figure 3.36 Table 3.10), where 3000 ppm marks a critical concentration for effective inhibition. When the concentration was increased to 5000 ppm, 8000 ppm, and 10000 ppm, the OCP curves showed rapid and substantial positive shifts, stabilizing quickly at nearly similar noble potentials (ranging from approximately -220 mV to -190 mV vs. Ag/AgCl). These potentials are comparable to, or even slightly more noble than, those achieved with TACT, indicating highly effective corrosion inhibition at these higher TEA concentrations. The similarity in the stabilized OCP values across these high concentrations suggests that the steel surface reaches a saturation point for TEA adsorption, beyond which further concentration increases have a negligible effect on the open-circuit potential.

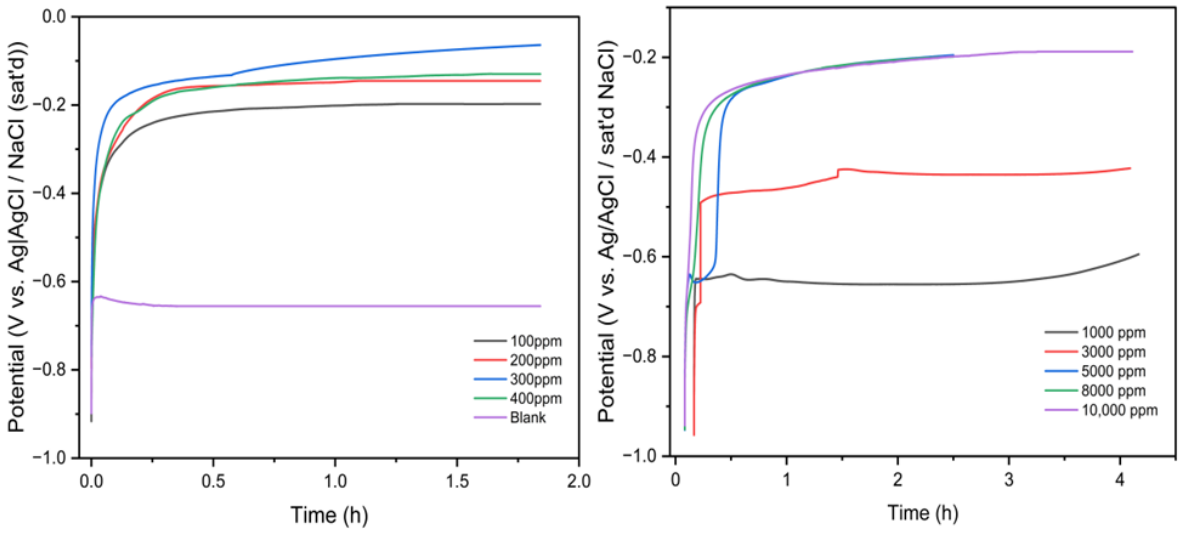

Figure 3.31: OCP measurement of 1.6310 steel coupons immersed in 100 ppm – 400 ppm concentrations of TACT in 0.06 mol/dm^3 $NaHCO_3$ solution (left) and in 1000 ppm – 10,000 ppm concentrations of TEA in 0.06 mol/dm^3 $NaHCO_3$ solution (right) both at r.t. and in aerated conditions.

3.4.1.2 Electrochemical Impedance Spectroscopy Measurements of 1.6310 Steel in TEA and TACT solutions.

The results of EIS measurements performed after OCP stabilization are presented in Figures 3.32 – 3.34 representing the Nyquist (Complex Plane) and Bode plots. In addition, an equivalent circuit model – Randles with CPE was used to fit the EIS data and extract parameters given in Table 3.8.

The Nyquist plots in Figures 3.32, show single, depressed semicircles for all the measured concentrations of TEA and TACT. This characteristic shape indicates that the corrosion process occurring in these systems is primarily charge transfer-controlled, and the depression is attributed to surface inhomogeneities, roughness, or a distribution of relaxation times at the steel-electrolyte interface [92,196]. The diameter of the semicircle, corresponding to the charge transfer resistance (R_{ct}), increases with increase in inhibitor concentration for both TEA and TACT. At 1000 ppm TEA concentration, the semicircle diameter is relatively small ($R_p \approx 14.3$ kΩ), indicating partial inhibition. A dramatic increase in diameter is observed as the concentration rises to 3000 ppm ($R_p \approx 145.0 \pm 4.5$ kΩ), and further to 5000 ppm ($R_p \approx 357.0 \pm 9.7$ kΩ). This confirms that a critical concentration is required for TEA to form a highly resistive film.

Interestingly, the R_p value then shows a decrease at 8000 ppm ($Rp \approx 215.1 \pm 6.5$ kΩ) before increasing again at 10000 ppm ($R_p \approx 483.2$ kΩ), reaching the highest observed resistance. This deviation from the trend at very high concentrations can be attributed to several factors in

addition to those suggested in the OCP results (Section 3.4.1.1). The decrease at 8000 ppm might be due to over-concentration effects, where a less ordered or more porous multilayer forms, or a change in the adsorption mode that is less efficient for barrier protection. However, at the extremely high concentration of 10,000 ppm, a re-ordering or compaction of the multilayered film might occur, leading to a more effective barrier. Alternatively, at such high concentrations, the increased bulk viscosity of the solution could significantly impede the diffusion of corrosive species to the electrode surface, leading to a diffusion-limited corrosion rate that manifests as a higher apparent R_p. This suggests that beyond a certain optimal concentration, the inhibition mechanism might involve a combination of surface film properties and bulk solution effects.

TACT, in contrast, exhibited a much larger semicircle diameter even at significantly lower concentrations. At 100 ppm, Rp ≈ 69.0 kΩ, which is already substantially higher than TEA at 1000 ppm. The diameter continues to increase with concentration, reaching Rp = 220.0 ± 6.6 kΩ at 300 ppm and Rp = 252.0 ± 7.6 kΩ at 400 ppm. These results indicate that TACT provides protective resistance at comparatively high efficiency at much lower concentrations (e.g., 100 – 300 ppm) compared to TEA (which requires ≥ 3000 ppm). This difference in efficiency can be attributed to their distinct adsorption mechanisms, as further explored in Section 3.4.2.

Table 3.8: EIS parameters extracted from the Randles with CPE EEC model fittings for 1.6310 steel in TEA and TACT solutions. χ^2 values were ~10^{-4} for the model fittings.

	Conc. (ppm)	R_s (Ω)	R_{ct} (kΩ)	Q ($\mu Fs^{(\alpha-1)}$)	α	CPE_{dl} (μF)	IE (%)
	Blank	98.6 ± 5.2	2.8 ± 0.5	168.0 ±5.2	0.70	180.5 ± 4.3	-
	1000	90.3 ± 3.8	14.3 ± 0.4	130.3 ± 3.3	0.85	112.7 ± 8.5	80.4
	3000	155.7 ± 3.1	145.0 ± 4.5	50.0 ± 1.5	0.80	82.7 ± 4.0	98.1
TEA	5000	82.0 ± 1.6	357.0 ± 9.7	43.5 ± 1.3	0.82	79.5 ± 3.2	99.2
	8000	107.9 ± 2.2	215.1 ± 6.5	46.6 ± 1.7	0.91	67.8 ± 2.7	98.7
	10,000	55.1 ± 1.1	483.2 ± 15.5	41.4 ± 2.9	0.93	51.5 ± 2.7	99.4
	100	128.0 ± 2.6	69.0 ± 3.1	61.1 ± 1.8	0.69	116.9 ± 9.5	95.9
TACT	200	138.1 ± 2.8	84.3 ± 2.5	40.5 ± 1.2	0.88	47.3 ± 2.5	96.7
	300	120.2 ± 2.4	220.0 ± 6.6	28.3 ± 0.9	0.82	42.5 ± 1.9	98.7
	400	132.5 ± 2.6	252.0 ± 7.6	18.6 ± 0.6	0.65	12.9 ± 2.7	98.8

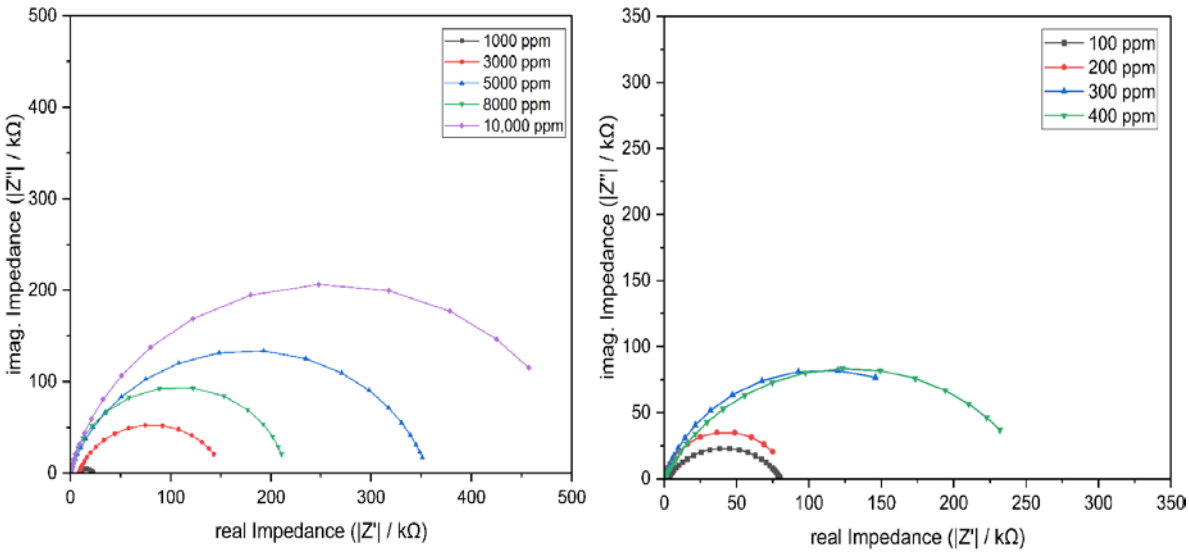

Figure 3.32: Nyquist plots of 1.6310 steel in 0.06 mol/dm^3 $NaHCO_3$ with varying TEA inhibitor concentrations.

The Bode plots in Figures 3.33 and 3.34, the phase angles shift to more negative values (~−70° to −80°) at high concentrations for both TEA and TACT indicating an increase in capacitive behavior. A single well-defined time-constant (single peak) is observed for both inhibitors at all measured concentrations indicating that the corrosion process is primarily controlled by the kinetics of electron transfer reactions at the interface, rather than by mass transport (diffusion) limitations or multiple, distinct layers with different electrochemical properties. Also, this implies that inhibition from both TEA and TACT is from a single, uniform protective layer (e.g., a monolayer or a compact, homogeneous multilayer) that acts as the main barrier to corrosion. For all concentrations of both inhibitors, the impedance magnitude at high frequencies remains relatively constant and similar to the blank solution's resistance (R_u in Table 3.11, typically around 100Ω). This confirms that the inhibitors primarily affect the electrode-electrolyte interface. The consistent increase in R_p and the shift of the phase angle peaks towards lower frequencies and higher values with increasing concentration confirm the formation of a more compact and protective barrier layer for both inhibitors.

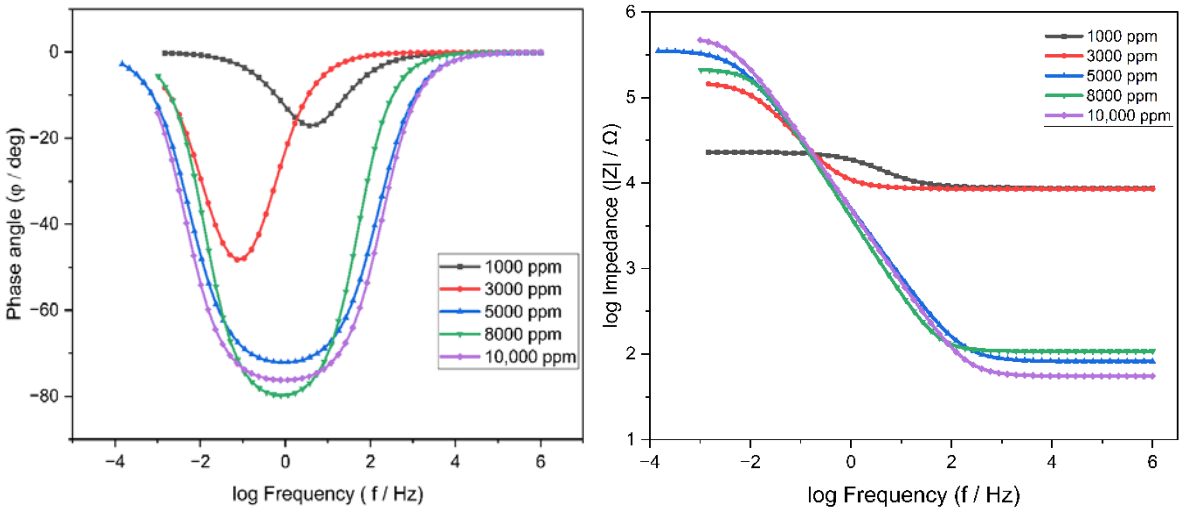

Figure 3.33: Bode plots of 1.6310 steel in 0.06 mol/dm^3 $NaHCO_3$ with varying TEA inhibitor concentrations.

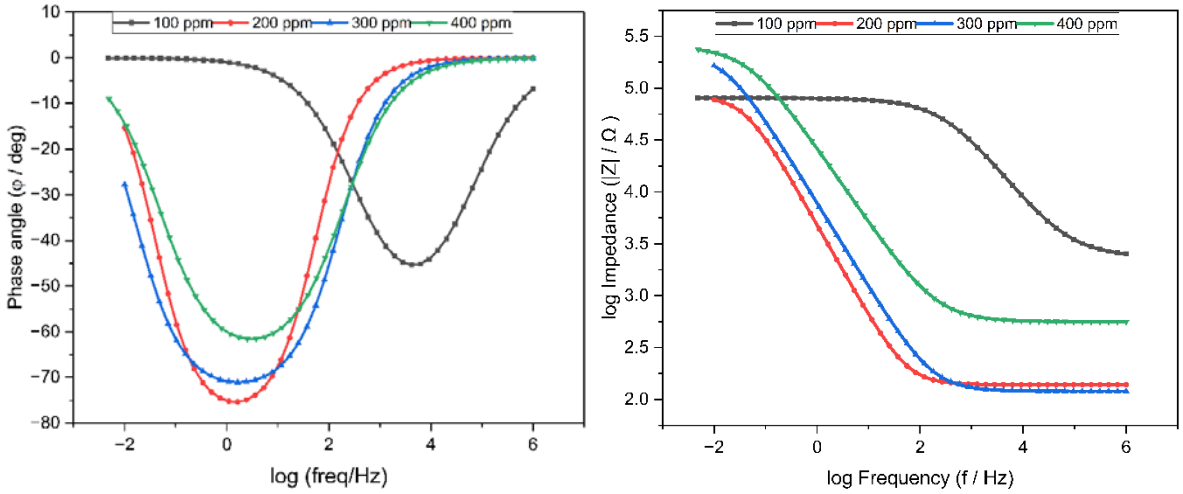

Figure 3.34: Bode plots of 1.6310 steel in 0.06 mol/dm^3 $NaHCO_3$ with varying TACT inhibitor concentrations

3.4.1.3 Potentiodynamic Polarization Measurements of 1.6310 Steel in TEA and TACT solutions.

Figures 3.35 and 3.36 show the potentiodynamic polarization curves for solutions with different concentrations of TACT and TEA respectively, from experiments performed immediately after EIS experiments with the same electrode in each case. Tables 3.9 and 3.10 give the extracted Tafel Extrapolation parameters and corrosion rates. The potentiodynamic polarization curves for TEA and TACT demonstrate their effectiveness as mixed-type inhibitors, significantly suppressing both anodic (metal dissolution) and cathodic (oxygen reduction) reactions on the 1.6310 steel surface. In addition, the corrosion current (i_{corr}),

reflecting the rate of electrochemical reactions (charge transfer) on the metal surface, decreased with higher inhibitor concentrations possibly due to higher surface coverage of the inhibitors on the metal electrode.

For TACT, even at a low concentration of 100 ppm, the anodic and cathodic branches were remarkably shifted to low current densities compared to the blank. A very low i_{corr} (0.18±0.01 µA) is recorded in Table 3.9. A distinct passivation region is evident on the anodic branch, signifying the formation of a protective film. With further increase in concentration to 200 ppm, 300 ppm, and 400 ppm, only marginal additional shifts towards lower current densities and more noble potentials are observed. The i_{corr} values remain very similar (e.g., 0.14±0.01 µA at 200 ppm and 300 ppm, 0.11±0.01 µA at 400 ppm), with inhibition efficiencies consistently >98%. This indicates that TACT reaches its saturation coverage and maximum protective effect at or below 100 ppm, with additional concentration providing negligible further benefit. The anodic branches for these concentrations show wide passivation plateaus with consistently steep cathodic slopes confirming sustained mixed-type inhibition.

Similar results have been reported in literature by Yoo et al [84]. In their work, 200 ppm TACT inhibited the corrosion of mild steel in 1 mol/dm^3 HCl up to 98%, with E_{corr} around -399 mV vs Ag/AgCl.

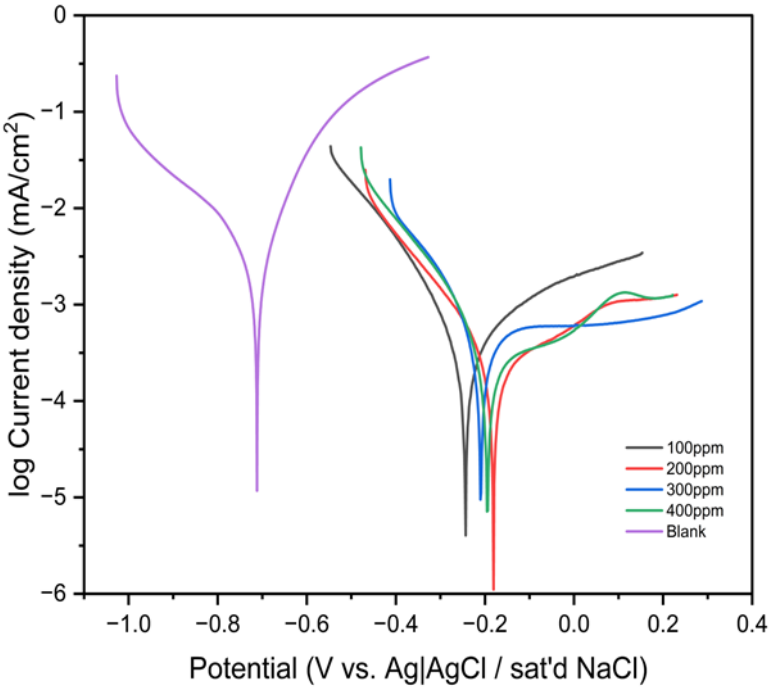

Figure 3.35: Potentiodynamic polarization curves of 1.6310 steel immersed in solutions with 100 – 400 ppm TACT concentrations. Measurements were at r.t, in aerated conditions.

At 1000 ppm TEA, partial inhibition is provided by the inhibitor molecules. The cathodic and anodic branches are shifted to lower current densities compared to the uninhibited blank, but the i_{corr} remains relatively high (4.62±0.01 µA, Table 3.10). The curve indicates that the protective film is incomplete or less effective, allowing significant corrosion to proceed. A slight improvement in inhibition is observed at 2000 ppm, with i_{corr} at 4.26±0.02 µA. The shape of the curve remains similar to 1000 ppm, indicating that the critical concentration for effective passivation has not yet been reached. 3000 ppm concentration marks a critical threshold for TEA's effectiveness as an obvious shift is observed, with both anodic and cathodic branches moving significantly towards much lower current densities. The i_{corr} drops to 0.26±0.01 µA, yielding a high inhibition efficiency. A clear and broad passivation region emerges on the anodic branch, where the current density remains very low over a wide potential range (~ -0.1 V to +0.3 V vs. Ag/AgCl), indicating the formation of a stable and highly protective film.

At much higher concentrations (>5000 ppm), the PDP curves become remarkably similar, indicating that a state of saturation coverage of the steel surface has been reached by the inhibitor. The i_{corr} values remain very low (e.g., 0.08±0.01 µA for 5000 ppm) with E_{corr} values > 200 mV. The anodic branches show robust passivation regions, and the cathodic slopes are steep, confirming strong suppression of both reactions. The slight non-monotonic behavior in R_p values between 5000 ppm and 8000 ppm (as discussed in the EIS section) is a subtle effect not overtly visible in the overall shape of these PDP curves, which remain highly protective.

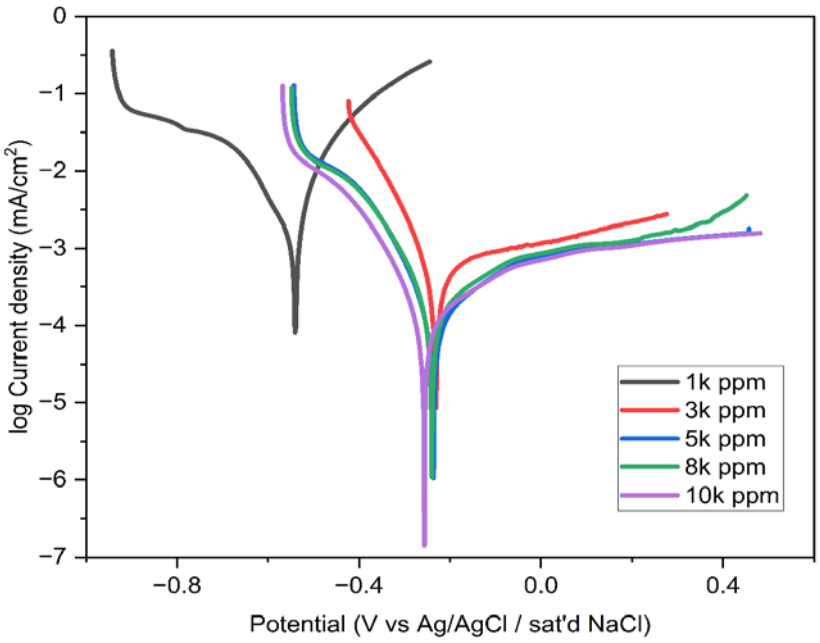

Figure 3.36: Potentiodynamic polarization curves of 1.6310 steel in solutions with 1000 – 10,000 ppm TEA concentrations. Measurements were at r.t, in aerated conditions.

It is clear from Tables 3.9 and 3.10 that an increase in concentration led to a decrease in corrosion rate and an increase in inhibition efficiency correlated with an increase in effective inhibitor surface coverage. This suggests that both inhibitors effectively reduce corrosion by interacting with the steel surface.

TEA (5000 ppm) shows excellent inhibition, reducing CR from 0.11 ± 0.01 mm/y to 0.0005 mm/y. With 100 – 400 ppm TACT, over 90% inhibition efficiency is achieved. In comparison, 10 times less concentration of TACT is required to achieve the same level of corrosion inhibition as with TEA.

Table 3.9: Tafel Extrapolation parameters for 1.6310 Steel in Blank and TACT solutions

Conc. (ppm)	E_{corr} (mV)	i_{corr} (µA)	β_a (mV/dec)	β_c (mV/dec)	CR (mm/y)	IE (%)	θ
blank	-733.5 ± 9.0	8.12 ± 0.03	109.1 ± 1.5	301.2 ± 3.0	0.11 ± 0.01	-	-
100	-242.2 ± 7.2	0.18 ± 0.01	132.1 ± 1.5	93.2 ± 1.5	(2.56 ± 0.08)E-3	97.7	0.98
200	-234.3 ± 8.0	0.14 ± 0.01	210.7 ± 1.5	83.6 ± 1.5	(2.00 ± 0.06)E-3	98.3	0.98
300	-212.4 ± 3.0	0.14 ± 0.01	104.6 ± 1.5	52.6 ± 1.0	(2.01 ± 0.06)E-3	98.2	0.98
400	-197.9 ± 2.5	0.11 ± 0.01	138.4 ± 1.5	55.0 ± 1.0	(1.57 ± 0.05)E-3	98.6	0.99

Table 3.10: Tafel Extrapolation parameters for 1.6310 Steel in TEA solutions

Conc. (ppm)	E_{corr} (mV)	i_{corr} (µA)	β_a (mV/dec)	β_c (mV/dec)	CR (mm/y)	IE (%)	θ
1000	-540.0 ± 23.0	4.62 ± 0.01	123.9 ± 1.5	289.5 ± 15.0	0.07 ± 0.01	43.1	0.43
2000	-393.6 ± 13.0	4.26 ± 0.02	99.5 ± 1.0	155.7 ± 12.0	0.06 ± 0.001	47.5	0.48
3000	-217.8 ± 22.1	0.26 ± 0.01	86.4 ± 1.0	62.9 ± 10.0	(3.64±0.10)E-3	96.8	0.97
4000	-222.0 ± 21.0	0.07 ± 0.01	67.8 ± 1.0	52.0 ± 8.2	(1.58±0.05)E-3	99.1	0.99
5000	-214.1 ± 9.0	0.08 ± 0.01	81.8 ± 1.0	45.9 ± 3.5	(0.50±0.02)E-3	99.0	0.99

The requirement for a relatively high concentration of TEA to achieve effective inhibition, particularly when compared to TACT which chemisorbed and had long hydrocarbon chains providing more coverage (Section 3.4.1), can be attributed to its primary physisorption mechanism (Section 3.4.2). Physisorption relies on weaker interactions and typically necessitates a higher bulk concentration to achieve and maintain a significant degree of surface coverage compared to inhibitors that utilize stronger chemisorption. Thus, a higher concentration of TEA is needed to establish a sufficiently dense protective layer capable of

effectively impeding the corrosion process. Similar results have been obtained in literature using TEA and its derivatives as corrosion inhibitors for steels in different media. Tocharat et al [197], reported that even at a concentration of 2.4% (~24,000 ppm), pure TEA had an inhibition efficiency of 77% and still showed rust spots with cast iron chips in 0.1 M NaCl. Li et al [198] reported TEA used synergistically with sodium silicate (SS) for inhibiting the corrosion of 45 Steel in 3.5% NaCl solution. Their results indicate that the inhibition effect of the composite inhibitor (TEA + SS) improved as the TEA concentration increased up to 3 g/L (3000 ppm), beyond which it started to decrease due to competitive adsorption. Furthermore, Kim et al [199] used TEA synergistically with $NaNO_3$ for inhibiting the corrosion of ductile cast iron in tap water. Their findings indicate that at least 2.5% TEA was needed for synergistic inhibition with 1000 ppm of the nitrite.

These findings support the observation in Figure 3.36 that a concentration around 3000 ppm (0.3 vol.%) is a significant threshold for TEA's effectiveness, even when potentially acting synergistically.

3.4.1.4 Comparative Electrochemical Analysis of C.Inh #4, TEA, and TACT

A comparative analysis of the electrochemical results obtained for the commercial inhibitor formulation C.Inh #4 (discussed in Section 3.1.2) and its two primary active components, TEA and TACT, discussed in Section 3.4.1 is provided. This comparison is crucial for understanding how the individual components contribute to the overall performance of the commercial formulation and for validating the insights gained from the compositional analysis.

All three systems (1.6310 steel immersed in electrolytes with C.Inh #4, TEA at high conc., TACT at low conc.) effectively shifted the OCP to more noble values, indicating a reduced thermodynamic driving force for corrosion. TACT achieved this at significantly lower concentrations, while TEA required a higher threshold. The behavior of C.Inh #4 appeared to be a combined effect, with its overall inhibition effect likely influenced by the efficient passivation provided by its components.

Furthermore, all three systems effectively reduced corrosion rates by acting as mixed-type inhibitors. TACT consistently outperformed TEA in terms of concentration required for comparable inhibition. For instance, TACT achieved >97% IE at 100 ppm, while TEA required 3000 ppm to reach 96.8% IE. The 1.5 vol.% C.Inh #4 (equivalent to approximately 15000 ppm) achieved 93.8% IE, which is lower than the peak efficiency of pure TEA (99.0% at 5000 ppm)

and TACT (>98% at 100 ppm). This is attributable to the lack of precise information regarding the concentrations of TEA and TACT in the formulation, as well as differences in the electrolyte used for the study in both cases.

From the EIS data, the three systems demonstrated significant increases in R_p/R_{ct} and improved capacitive behavior, confirming the formation of protective films. Quantitatively, TACT achieved comparable R_{ct} values at significantly lower concentrations than TEA. For example, 300 ppm TACT ($R_p \approx 220$ kΩ) provided similar protection to 8000 ppm TEA ($R_p \approx 215$ kΩ), which represents 27 times less concentration requirement. The C.Inh #4 formulation, at its optimal concentration (1.5 vol.% or 15000 ppm), achieved an R_{ct} of 2.95 MΩ after 72 hours, which is higher than the maximum Rp observed for individual TEA or TACT at their tested concentrations. This suggests that the formulation, possibly due to positive synergistic effects can achieve a very high level of surface protection, particularly over longer immersion times.

3.4.2 Adsorption Modelling of TEA and TACT on 1.6310 Steel Surface

To gain deeper insight into the nature of the interaction between the inhibitor molecules (TEA and TACT) and the 1.6310 steel surface, and to understand the mechanism governing the formation of the protective layer, the experimental data relating inhibitor concentration to surface coverage were subjected to adsorption isotherm analysis. Modeling the adsorption process using established isotherms, such as the Langmuir, Freundlich, or Temkin models, allowed for the quantitative determination of adsorption parameters such as ΔG^{θ}_{ads}. These parameters provide crucial information regarding the type of adsorption (e.g., physisorption or chemisorption), the strength of the inhibitor-surface interaction, and the thermodynamics of the adsorption process, thereby contributing to a comprehensive understanding of the corrosion inhibition mechanism for both TEA and TACT in the tested environments.

Table 3.11 presents the concentration and surface coverage values for TEA and TACT at various studied concentrations, from which model fitting was performed. Figure 3.37 shows the plot of C/θ vs C for TACT, and Figure 3.38 shows the plot for TEA, both with their corresponding fitting equations.

Table 3.11: Concentration and surface coverage values for electrochemical measurements in TEA and TACT solutions at room temperature.

Inhibitor	Conc (ppm)	Conc (mol dm^{-3})	IE (%)	θ	C/θ (mol dm^{-3})
TEA	1000	6.70E-3	43.1±0.2	0.43±0.02	(1.56±0.01) E-02
	2000	1.34E-2	47.5±0.3	0.48±0.03	(2.87±0.01) E-02
	3000	2.01E-2	96.8±0.1	0.97±0.01	(2.08±0.01) E-02
	4000	2.68E-2	99.1±0.1	0.99±0.01	(2.72±0.01) E-02
	5000	3.35E-2	99.0±0.1	0.99±0.01	(3.39±0.01) E-02
TACT	100	2.0E-4	97.7±0.1	0.98±0.01	(2.04±0.10) E-04
	200	4.0E-4	98.3±0.1	0.98±0.01	(4.08±0.10) E-04
	300	6.0E-4	98.2±0.1	0.98±0.01	(6.12±0.11) E-04
	400	9.0E-4	98.6±0.1	0.99±0.01	(9.09±0.10) E-04

The linearity of the plots in Figures 3.37 and 3.38, with slope values close to unity, indicates that Langmuir-type adsorption is a suitable model for both TEA and TACT adsorption over the investigated concentration ranges. The goodness of fit is quantitatively supported by the high coefficient of determination (R^2) values: R^2 =0.998 for TACT and a relatively high value for TEA (approaching 1 if only values ≥ threshold concentration of 3000 ppm is considered). It is important to note that the R^2 value, while indicating the proportion of variance in the dependent variable predictable from the independent variable, is a measure of model fit and does not typically carry an uncertainty value in the same way as a directly measured or derived parameter. The adsorption equilibrium constant, K_{eq}, is obtained from the inverse of the intercept of these linear plots ($1/K_{eq}$ = intercept). Subsequently, ΔG^{θ}_{ads} is obtained using Eqn. 1.17.

From the plots in Figure 3.37 and 3.38, the intercepts for TEA and TACT are 1.47E-02 and 1.28E-06 mol dm^{-3} respectively, and the adsorption equilibrium constants, K_{eq}, are (6.80±2.27) E+01 and (7.78±2.42) E+05 dm^3 mol^{-1} respectively. Calculation of the ΔG^{θ}_{ads} values for TEA and TACT gives -20.4 ± 0.8 kJ/mol and -43.5 ± 0.8 kJ/mol respectively.

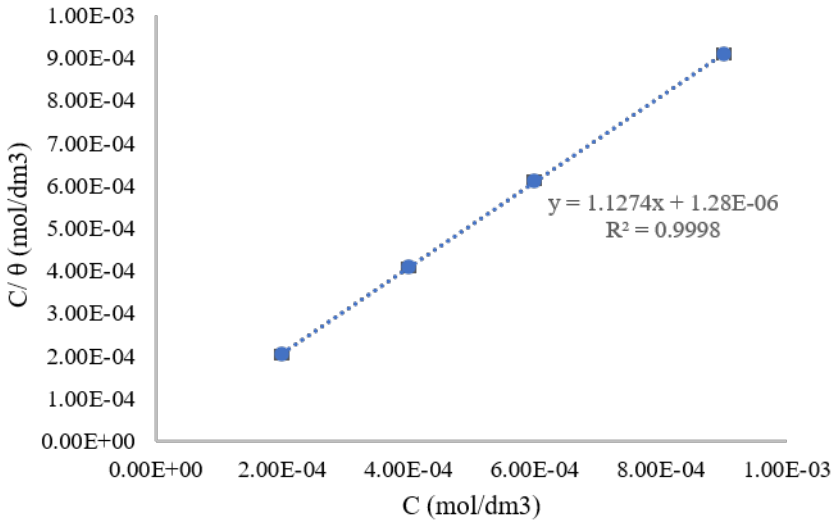

Figure 3.37: Plots of C/θ vs C for TACT at 25°C, over a concentration range. K_{eq} and ΔG^{θ}_{ads} values are estimated from the intercept and slope of the plot.

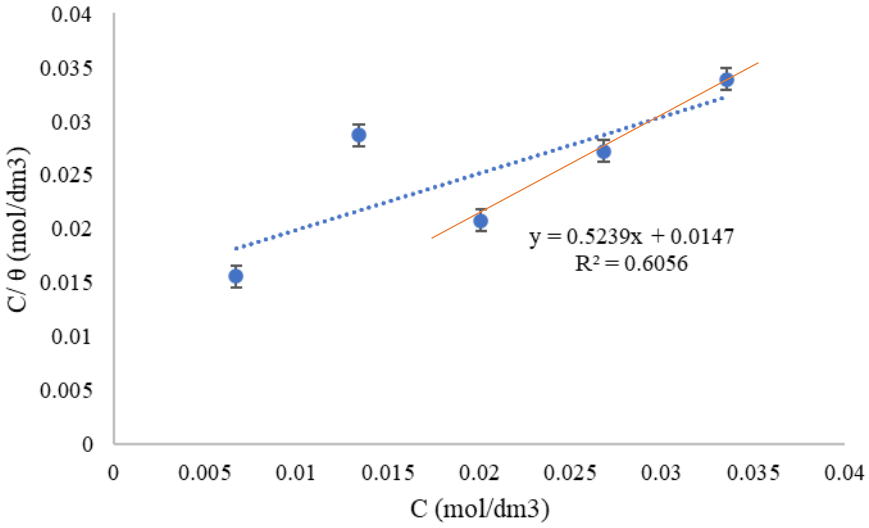

Figure 3.38: Plots of C/θ vs C for TEA at 25°C, over a concentration range. K_{eq} and ΔG^{θ}_{ads} values are estimated from the intercept and slope of the plot.

The type of adsorption mechanism can be inferred from the calculated values of ΔG^{θ}_{ads} according to the "20/40 criteria" [73,200] which defines physisorption as $\Delta G^{\theta}_{ads} > -20$ kJ/mol, mixed physisorption/chemisorption as $\Delta G^{\theta}_{ads} \in [-20,-40]$ kJ/mol, and chemisorption as $\Delta G^{\theta}_{ads} < -40$ kJ/mol. This criteria has formed the basis of mechanistic description of inhibitor adsorption in corrosion literature [79,121,172].

From the results obtained in this study, it can be inferred that TEA adsorbs by means of physisorption while TACT combines physisorption and chemisorption to form a monolayer

protection on the steel surface. This is in agreement with the results of Yoo and coworkers [84] who calculated -35.8 kJ/mol as the ΔG_{ads}^{θ} for the adsorption of TACT in 1 mol/dm^3 HCl.

Recently, Walczak et al [201], Latour et al [96] and Kokalj [78] have argued that the premise of equating inhibition efficiency to the surface coverage (IE = θ) for the determination of ΔG_{ads}^{θ} and thereafter the strength of adsorption of an inhibitor, is not necessarily valid. The reasons for this argument are that the assumptions for Langmuir-type adsorption are rarely perfectly met under experimental conditions, leading them to suggest treating K_{eq} as a "semi-quantitative descriptor of the isotherm shape rather than as input for determining ΔG_{ads}^{θ}" [201]. However, this formalism for determining ΔG_{ads}^{θ} is used in this study as a complementary approach to fully unraveling the adsorption mechanism of the inhibitors under investigation.

From the obtained results in the present study, a more negative ΔG_{ads}^{θ} value for TACT compared to TEA means TACT adsorbed more strongly by combining physisorption and chemisorption, making it more effective at preventing corrosion. In addition, TEA required higher concentrations for effective inhibition compared to TACT.

3.4.3 Characterization of TEA and TACT treated Steel Surfaces

3.4.3.1 Surface Morphology

Characterization of the surface morphology of the steel coupons after immersion in the blank solution (0.06 mol dm^{-3} $NaHCO_3$) and blank solutions with 5000 ppm TEA and 300 ppm TACT, were performed with SEM-EDX. A comparison of the SEM images is given in Figure 3.39

Figure 3.39(a) and (c) clearly show uniform corrosion across the surface of the steel after exposure to the blank solution without the addition of any inhibitor, characterized by generalized roughness across the surface. In contrast, the steel surfaces after exposure to TEA and TACT-containing solutions (Figure 3.39(b) and (d)) show no visible signs of surface oxidation or extensive corrosion products. For blank solutions, corrosion rate of 1.6310 steel in 0.06 mol dm^{-3} $NaHCO_3$ solution was measured to be 0.11 ± 0.01 mm/y (Table 3.9) compared to 0.16 ± 0.02 mm/y in 0.004 mol dm^{-3} NaCl solution (Table 3.1). This confirms that the addition of $NaHCO_3$ to the WAS (cutting suspension) provides a minor decrease in the corrosion rate of the steel without any additional inhibitor, even though the observed corrosion rate is still too high for the intended practical application. This is in agreement with the results

of Zhu et al [202],Thomas et al [118], Gilroy and Mayne [203], Rangel et al [204] who have studied the impact of $NaHCO_3$ on iron/carbon steel/mild steel corrosion.

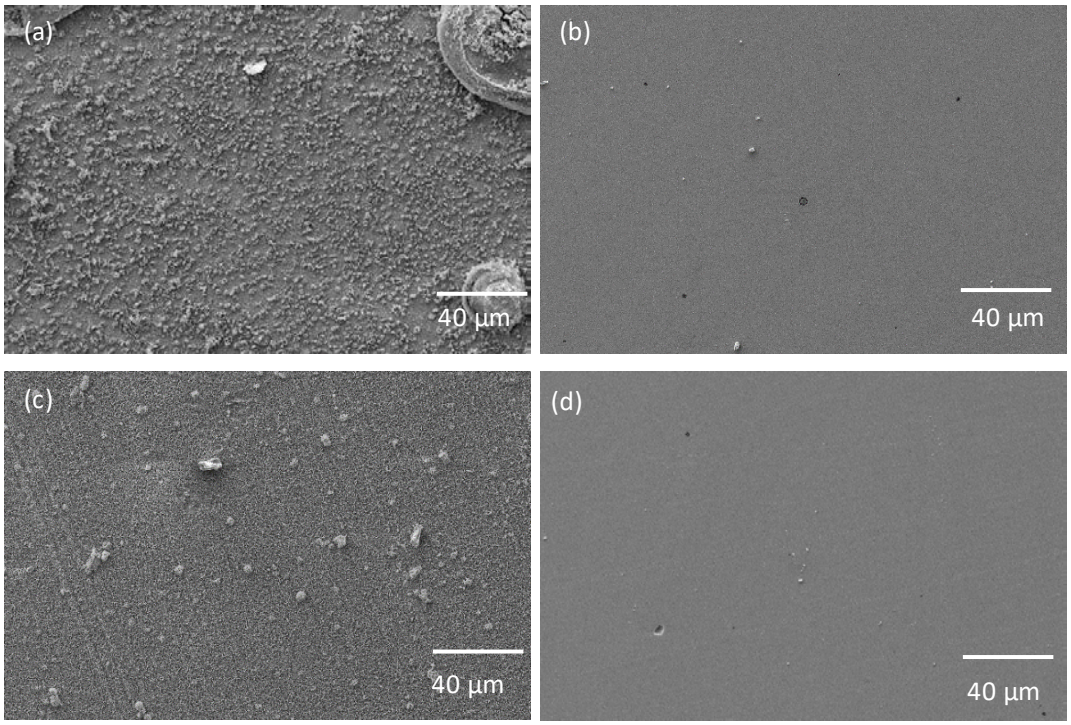

Figure 3.39: SEM images of the steel coupons after 2 weeks contact time in (a) and (c) blank 0.06 mol dm^{-3} $NaHCO_3$ soln., (b) 5000 ppm TEA-inhibited soln., and (d) 300 ppm TACT-inhibited soln.

The EDX spectra of the steel coupons surfaces in the blank, blank + 5000 ppm TEA, and blank + 300 ppm TACT are also in Figure 3.45.

The EDX spectrum of the steel surface in the blank 0.06 mol/dm^3 $NaHCO_3$ solution reveals a significant presence of oxygen (50.5 at. %) and carbon (15.9 at. %), alongside iron (31.0 at. %). The high oxygen content, coupled with the visible corrosion products in the corresponding SEM image (Figure 3.40), strongly indicates the formation of an iron oxide/hydroxide layer. In near-neutral bicarbonate solutions, the initial corrosion of iron often leads to the precipitation of ferrous hydroxide ($Fe(OH)_2$), which can then oxidize to ferric hydroxides ($Fe(OH)_3$ or FeOOH) and ultimately iron oxides (Fe_2O_3, Fe_3O_4) [205,206]. The substantial carbon content, together with oxygen, suggests the incorporation of iron carbonates or ferrous bicarbonate species within this corrosion product layer [204]. This mixed oxide/carbonate layer provides a degree of inherent passivation, as reflected by the lower corrosion rate compared to NaCl solutions, but it is not fully protective, leading to corrosion. The nature of the passive oxide

film formed on mild and ferritic steels like 1.6310 would be similar to those of pure iron in similar corrosive environments. Bockris et al [207] proposed one layer of γ-Fe_2O_3, Nagayama and Cohen [206,208] proposed a two-layer model containing an inner Fe_3O_4 and an outer γ-Fe_2O_3, while Sato et al [209] proposed a two-layer model with inner anhydrous γ-Fe_2O_3 and outer hydrated γ-Fe_2O_3.

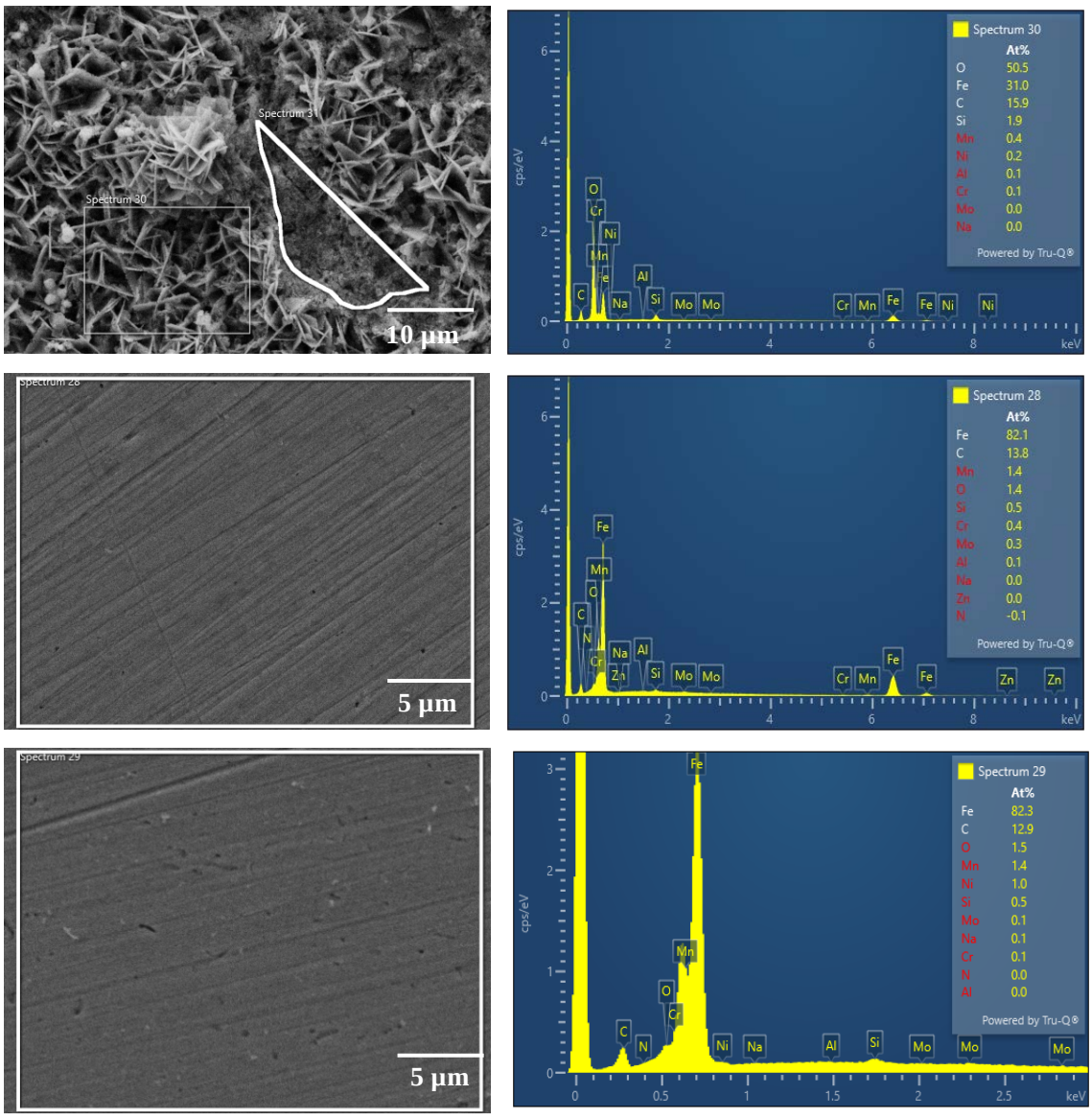

Figure 3.40: SEM images and EDX spectra showing the surface composition of steel coupons immersed in blank 0.06 mol/dm^3 $NaHCO_3$ solution (top row), blank + 5000 ppm TEA solution (middle row), and blank + 300 ppm TACT solution (bottom row).

The SEM image and EDX spectrum of the steel surface immersed in 5000 ppm TEA solution (Figure 3.40, middle row) shows a different composition. The iron content is significantly higher (82.1 at.%), while the oxygen content is drastically reduced (1.4 at.%). The very low

oxygen content, in contrast to the blank, indicates that TEA effectively inhibits the extensive formation of iron oxides and hydroxides. A similar observation is seen in the TACT-treated steel coupon. The TACT-treated surface also exhibits a high iron content (82.3 at.%), a very low oxygen content (1.5 at.%) and a relatively high carbon content (12.9 at.%).

3.4.3.2 Surface Chemical Composition

The chemical composition of the steel surface immersed in each of the inhibitors was investigated with XPS and reported in the spectra in Figure 3.41.

Fe oxide peaks in the Fe 2p spectra for both TEA and TACT are significantly shifted to higher binding energies compared to metallic iron at ~707 eV. The peak at around 710 eV has been shown to be consistent with the presence of both Fe_2O_3 and Fe_3O_4 [209]

The N 1s and Fe 2p XPS spectra for the steel coupons immersed in TEA and TACT show the presence of nitrogen at binding energy of ~ 400.3 eV typical of amine-groups on the surface of the steel. The N 1s peak in both cases corresponds well to what might be expected for a nitrogen atom donating electron density to the iron surface via its lone pair (Willenbruch et al.[211] report a value of 399.8 eV for ammonia on an iron surface). Since amines are basic with lone pair of electrons on nitrogen in addition to π-electron clouds on aromatic rings (in the case of TACT), they easily interact with positively charged surface of iron oxides and hydroxides developed as a result of the solution pH relative to the point-of-zero charge (PZC) of the oxide. Thus, it can be expected that the inhibitors adsorbed to the partially oxidized metal surface via coordination.

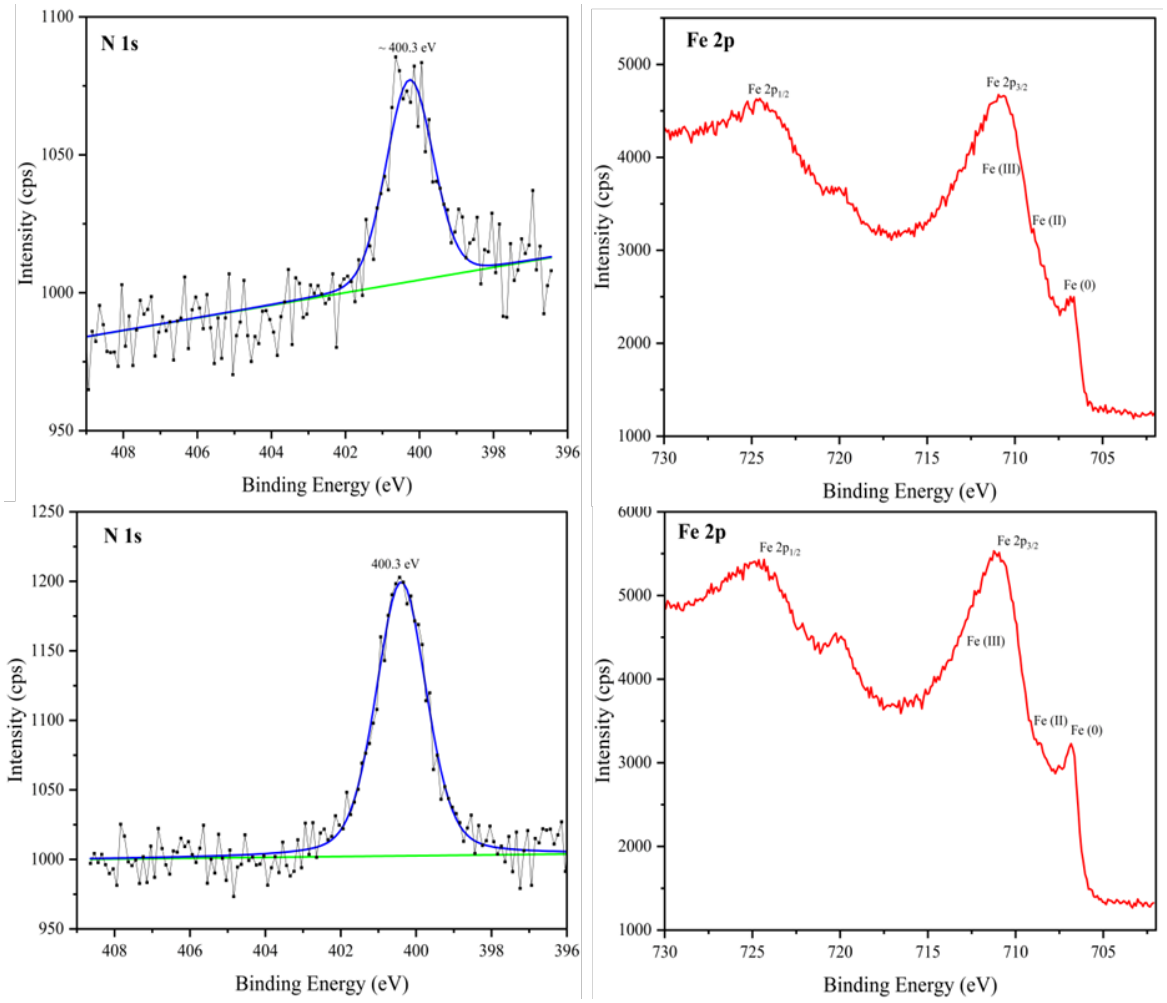

Figure 3.41: N1s spectra with curve fit: Blue curve – Gaussian-Lorentzian function, dotted black – measured spectrum, green – Shirley background, and Fe 2p XPS spectra (red) of 1.6310 steel immersed in 300 ppm TACT (top row) and in 5000 ppm TEA (bottom row) solutions.

TEA is known to form stable complexes with iron in neutral and alkaline pH ranges, and these complexes significantly influence the electrochemical processes of iron in these solutions as demonstrated in the work of Bechtold and Mohr [212]. This ability to form stable complexes with iron ions in aqueous solution has significant implications for TEA as a corrosion inhibitor for steel surfaces. In near-neutral environments where the steel surface is covered by a layer of iron oxides and hydroxides, TEA molecules in the electrolyte can interact with the iron species within this surface layer. This interaction can occur through the coordination capabilities of TEA, which acts as a polydentate ligand capable of binding to metal ions via its nitrogen atom and/or the oxygen atoms of its hydroxyl groups [213]. Electrostatic interactions could also occur between the negatively charged surface oxide/hydroxides and some protonated TEA molecules (TEA pKa ~8.0 and the aqueous solution pH ~ 8.7). The adsorption of TEA molecules and the formation of insoluble TEA-Fe surface complexes can create a physical barrier layer that

impedes mass transport on the steel surface; the diffusion of aggressive species (e.g. oxygen and chloride ions) to the metal surface and the outward migration of metal ions. This barrier effect, further enhanced by the inherent corrosion-reducing tendency of HCO_3^- in the system, contributed to the observed significant reduction in corrosion current densities and the shift towards more noble potentials seen in the electrochemical measurements (Section 3.4.1).

While there is limited information on the complexation of TACT with iron/iron oxides, 1,3,5 triazine derivatives have been reported to inhibit steel corrosion by coordinating with the metal surface through electron donation to the empty d-orbital of Fe atom or with surface Fe^{2+} ions from the N atoms in the organic molecule. Also, electrostatic attractions could occur between the largely unprotonated inhibitor molecules (given the near-neutral electrolyte solution) and the charged steel surface via dipole-dipole interactions between the electric field of the double-layer or with charged sites on the metal oxide surface (e.g., interaction with surface Fe^{2+} or Fe^{3+} ions) and the polar bonds and dipole moments of the inhibitor molecules [88,97]. Thus, electrostatic interactions contribute to the overall adsorption of TACT on the steel surface [214,215]. Once adsorbed, the planar triazine ring of TACT lies against the steel surface. With its large molecular structure, a 2D geometric coverage is created, which blocks active corrosion sites and provides physical impedance to charge transfer processes. In addition, the hexanoic acid chains form outward-oriented hydrophobic layer which further reduces penetration of water and dissolved oxygen and creates a concentration gradient that slows diffusion processes.

3.4.4 Adsorption Quantification with QCM

3.4.4.1 TEA Adsorption

After achieving a stable baseline with water, 5000 ppm TEA solution was injected into the Fe-coated QCM sensor at a flow rate of 0.1 ml/min for 5-minute intervals, alternating with 5-minute injections of water. This cycle was repeated multiple times to observe the adsorption and desorption behavior. The fundamental frequency varies with injection time as observed in Figure 3.42.

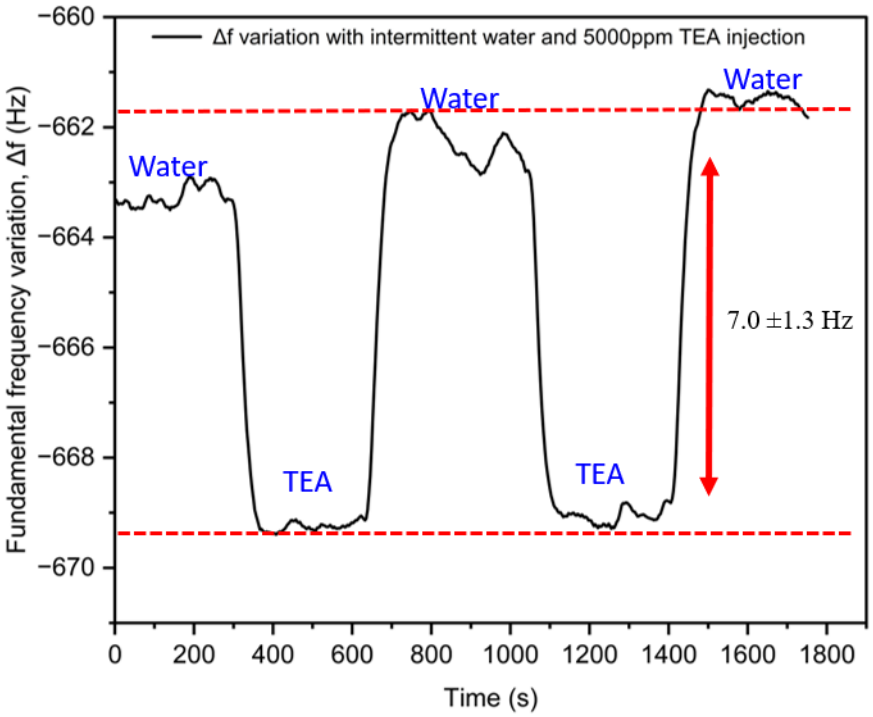

Figure 3.42: Fundamental frequency variation during alternating injections of water and 5000 ppm TEA solution at 0.1 ml/min flow rate, with 300-second (5-minute) intervals for each injection step.

The effect of a longer injection time (to monitor adsorption kinetics and equilibrium adsorption) was investigated by injecting the TEA solution for about 60 minutes at the same flow rate. The variation in fundamental frequency with time can be observed in Figure 3.48.

From Figures 3.42 and 3.43, the surface mass loading increased with prolonged TEA injection time, evidenced by an observed increase in Δf from 7.7 Hz to 10.5 Hz. This suggests that equilibrium adsorption required more than 5 minutes to fully develop or achieve maximum coverage on the Fe-QCM sensor surface under the given experimental conditions.

Using the Sauerbrey equation, the mass loading on the sensor corresponding to the observed variations in fundamental frequency increased from 136 ng/cm² to 186.5 ng/cm² ± 26.0 ng/cm², likely due to surface rearrangement or multilayer adsorption over time.

Even for prolonged exposure, the interaction of TEA with the sensor surface remained reversible. This suggests a weak interaction between TEA molecules and the steel surface. Consistent with a predominantly physisorption mechanism (Section 3.4.2), the QCM measurements reveal a weak and reversible binding of TEA to the Fe-coated QCM surface. This characteristic interaction helps explain why relatively high concentrations were necessary to achieve the significant inhibition efficiencies observed electrochemically.

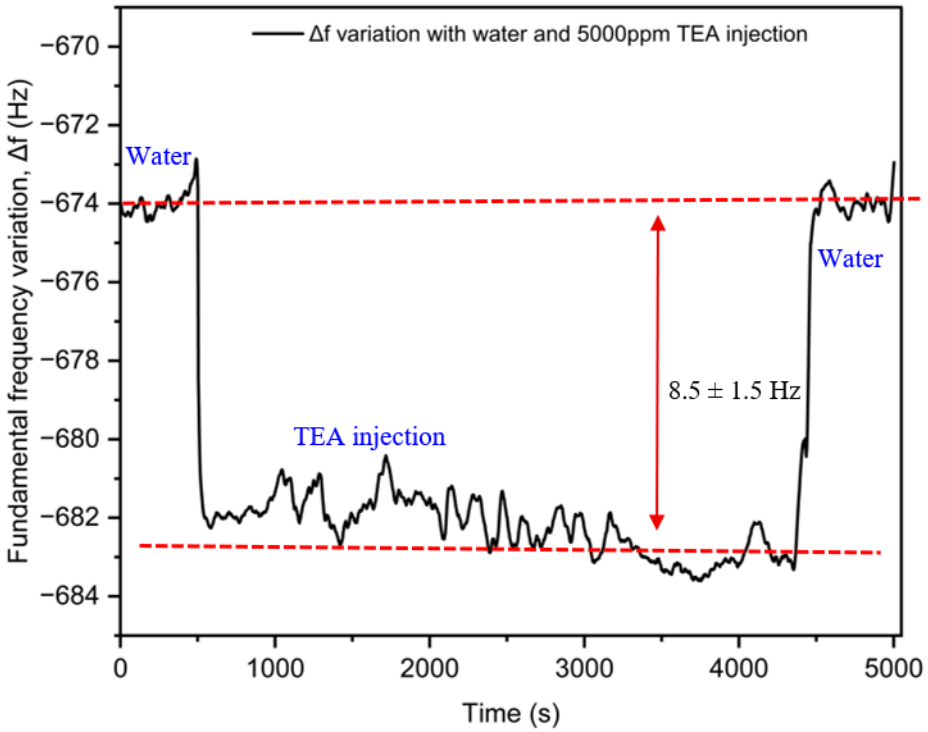

Figure 3.43: Fundamental frequency variation during prolonged injection (3600 seconds) of 5000 ppm TEA solution at 0.1 ml/min flow rate, for monitoring adsorption kinetics and equilibrium.

Effect of flow rate on the adsorption of TEA on Fe-coated QCM:

By increasing the flowrate from 0.1 ml/min to 0.4 ml/min, the effect of hydrodynamic forces on the interaction between TEA and the Fe-QCM sensor was observed and reported in Figure 3.44.

Across all three tested flow rates (0.1, 0.2, and 0.4 ml/min), the initial frequency drop was consistent, typically around 8–10 Hz. Fast and similar adsorption kinetics was observed during the initial phase. At flow rates of 0.2 ml/min and 0.4 ml/min, a positive Δf shift was observed after the initial adsorption. This suggests that TEA molecules were being displaced or removed from the sensor surface. The increased hydrodynamic forces may have exceeded the binding strength of the weak interactions between TEA and the Fe on the surface of the sensor, leading to desorption of TEA molecules.

The steeper slope of the positive shift at 0.4 ml/min indicates a more pronounced desorption or displacement effect. The observed desorption at higher flow rates suggests that TEA is unlikely to provide robust or long-lasting protection in environments with high fluid dynamics, as it may not maintain a stable protective layer. At 0.1 ml/min, the steady and stable frequency after adsorption indicates that the flow rate provides sufficient time for TEA molecules to uniformly adsorb and form a homogeneous layer.

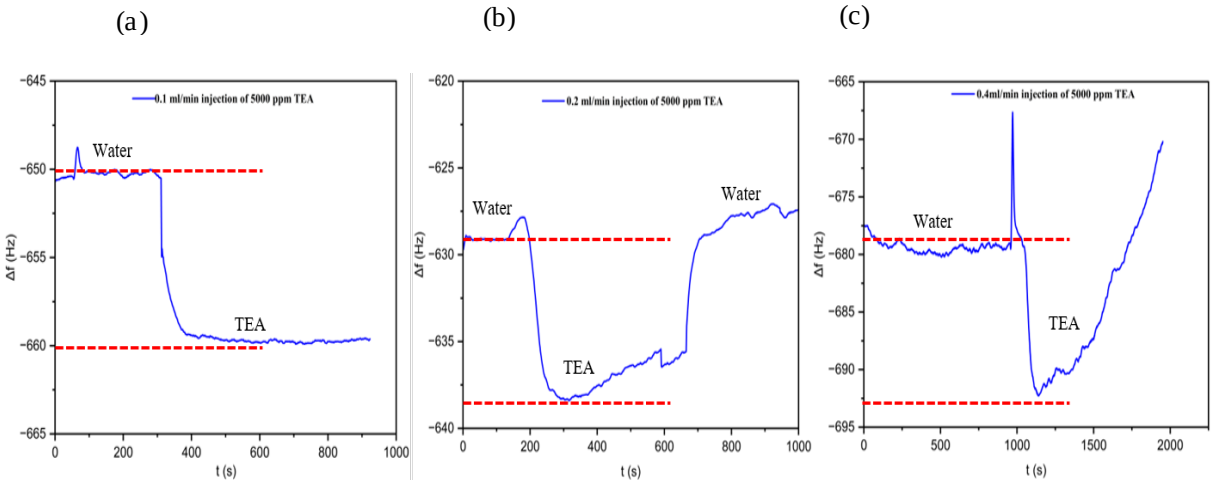

Figure 3.44: Fundamental frequency variation during the injection of 5000 ppm TEA solution at (a) 0.1, (b) 0.2 and (c) 0.4 ml/min flow rate flowrates respectively (from left to right).

3.4.4.2 TACT Adsorption

After achieving a stable baseline, 300 ppm TACT solution was injected at a flow rate of 0.1 ml/min for 5 minutes, followed by water reinjection. The resulting variation of fundamental frequency is reported in Figure 3.45.

The equivalent mass loading of TACT on the Fe-QCM surface was calculated using the Sauerbrey equation (Table 3.12). In contrast to TEA, when the flow was switched back to water, the frequency did not return to the baseline. This indicates that some TACT molecules remained irreversibly adsorbed on the sensor surface. This observation could infer that TACT forms stronger bonds with the Fe coating of the sensor, likely through coordination bonds, hydrogen bonding, or other chemical interactions.

TACT remained strongly attached to the surface even after rinsing with water, demonstrating its potential to form a durable, protective layer.

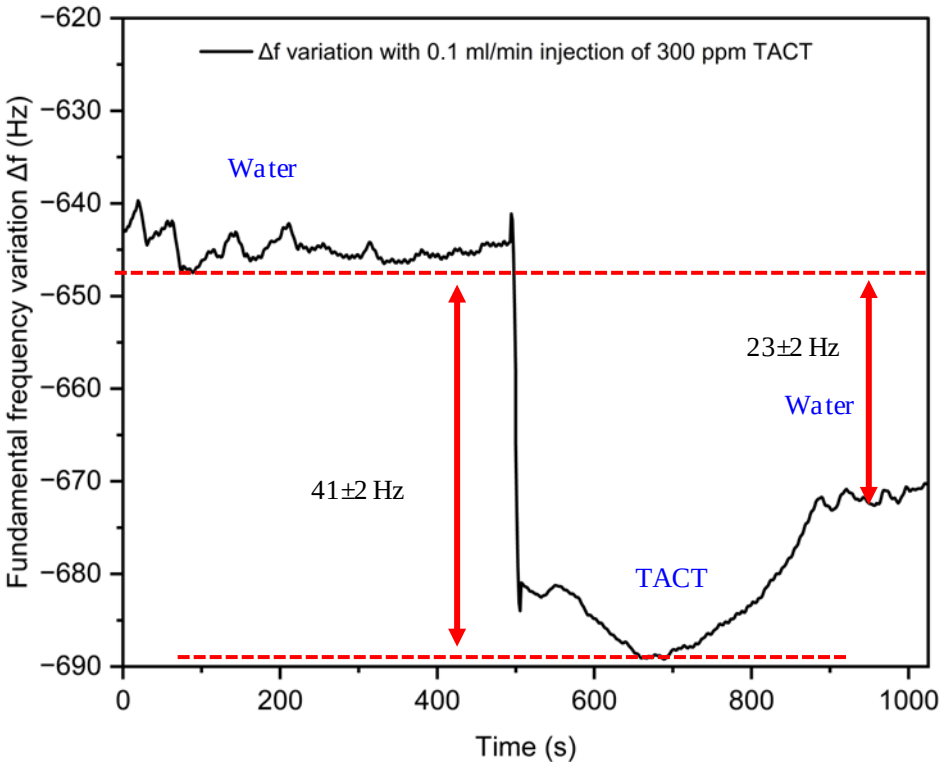

Figure 3.45: Fundamental frequency variation with the injection of 300 ppm TACT solution at 0.1 ml/min flow rate.

3.4.4.3 Film thickness from QCM data and comparison with Ellipsometry data

To calculate the thickness of the adsorbed organic films from the QCM data, a few assumptions were made with regards to the behavior of the films.

- The film behaves like a rigid body and does not exhibit significant viscoelastic properties.
- The energy dissipation shift (ΔD) is small.
- The adsorbed organic film is uniformly distributed across the sensor surface.
- The film is non-porous and has a uniform density.

If the film is dense and rigid, its behavior will closely approximate that of a solid material, and thus the bulk densities of the pure materials (TACT or TEA) are used for the calculation instead of modeling the effective film density in solution.

$$h_{(nm)} = \frac{\Delta m_{\left(\frac{ng}{cm^2}\right)}}{\rho_{\left(\frac{g}{cm^3}\right)}} \times 10^{-2} \qquad (3.8)$$

Where Δm is the mass loading in ng/cm², calculated from the Sauerbrey equation and ρ is the density of the molecule with $\rho_{TACT} = 1.28$ g/cm³ and $\rho_{TEA} = 1.13$ g/cm³.

Table 3.12: Estimation of inhibitor adsorbed layer thickness from mass change values.

S/N	Sample ID	Δf (Hz)	Δm (ng/cm^2)	h (nm)
1	TACT (Dynamic)	41.00 ± 1.45	(4.1 ± 0.3) E+02	3.10 ± 0.20
2	TACT (Static)	23.10 ± 1.45	(7.3 ± 0.3) E+02	5.50 ± 0.20
3	TEA (Dynamic)	-	-	-
4	TEA (Static)	8.50 ± 1.50	(1.5 ± 0.3) E+02	1.33 ± 0.24

Ellipsometry measurements were also performed to complement the QCM results in validating the estimated thickness values of adsorbed inhibitor layers.

In 'static mode,' the sensor was immersed in an unstirred inhibitor solution, allowing adsorption under equilibrium conditions. while in 'dynamic mode,' the sensor was exposed to a flowing inhibitor solution, simulating real-world conditions and highlighting flow effects on adsorption. Based on reported values of Tseng and Thompson [216], the refractive indices of the samples were taken as TACT, n = 1.604 and TEA, n = 1.485.

Table 3.13: Comparison of inhibitor adsorbed layer thickness using QCM & Ellipsometry.

S /N	Sample	Ellipsometry	QCM
1	TACT (Dynamic)	1.80 ± 0.12 nm	3.10 ± 0.20 nm
2	TACT (Static)	4.44 ± 0.25 nm	5.50 ± 0.20 nm
3	TEA (Dynamic)	-	-
4	TEA (Static)	1.96 ± 0.20 nm	1.33 ± 0.24 nm

The combined results from QCM and Ellipsometry, as presented in Tables 3.13, offer complementary insights into the physical characteristics and formation mechanisms of the adsorbed inhibitor films of TEA and TACT on the steel surface. These techniques, while both measuring film thickness, do so based on different physical principles, allowing for a better interpretation of the film properties.

Under both static and dynamic conditions, TACT films formed thicker adsorbed layers compared to TEA films. For instance, in static conditions, TACT yielded thicknesses of 4.4 nm (Ellipsometry) and 5.5 nm (QCM), whereas TEA formed films of ~2 nm (Ellipsometry) and 1.3 nm (QCM). These results support the findings that TACT provides better inhibition

efficiency at lower concentrations via a stronger adsorption mechanism (chemisorption combined with physisorption) as discussed in Section 3.4.2.

For TACT, the film thickness measured under dynamic (flow) conditions was notably thinner than under static conditions (3.1 nm QCM dynamic vs. 5.5 nm QCM static; 1.8 nm Ellipsometry dynamic vs. 4.4 nm Ellipsometry static). This indicates that hydrodynamic forces can remove loosely bound molecules or alter the conformation of the adsorbed layer, leading to a more compact or less extensive film under flow. For TEA, while a direct dynamic Ellipsometry measurement was not performed, the QCM data (Figures 3.42-3.44) clearly showed that TEA's adsorption is reversible and susceptible to desorption under increased flow rates, resulting in thinner layers.

A notable observation is the difference in measured thickness between QCM and Ellipsometry for the same sample, particularly for TACT. QCM measurements generally yielded slightly larger thicknesses than Ellipsometry. This discrepancy is significant and can be attributed to the fundamental differences in the operating principle of both measurement techniques. The Sauerbrey equation, while a good approximation for rigid films, relates frequency change to the total coupled mass on the sensor surface. This includes not only the dry mass of the adsorbed inhibitor molecules but also any trapped solvent (water) or associated hydration layers, as well as contributions from the viscoelastic properties of the film [139,217]. If the adsorbed layer is soft, porous, or highly hydrated, the QCM will register a larger effective mass, leading to a larger calculated thickness (assuming a rigid film model and bulk density).

In contrast, Ellipsometry determines film thickness based on changes in the polarization state of light reflected from the surface, which is primarily sensitive to the dry film thickness and its refractive index [142,143]. The refractive indices of adsorbed layers could deviate from the assumed values. It is also less sensitive to loosely bound water or the viscoelastic properties of the film. The observed discrepancy for TACT (QCM thickness significantly greater than Ellipsometry thickness) suggests that the TACT film is likely more hydrated, less rigid, or more porous than the TEA film. This aligns with the complex molecular structure of TACT, which possesses multiple flexible hexanoic acid chains and hydrophilic functional groups that can trap or associate with water molecules within the adsorbed layer. In contrast, the closer agreement between QCM and Ellipsometry for TEA suggests a relatively less hydrated or more compact film, consistent with its weaker physisorption and smaller molecular size.

The measured thicknesses for TACT (up to 5.5 nm) are significantly larger than the estimated length of a single TACT molecule chain (~1.3 nm) or the dimensions expected for a flat-lying monolayer. This strongly supports the conceptual model of TACT forming a multilayered structure or adsorbing in a more extended, upright conformation on the steel surface [76,79,177]. The strong chemisorption component of TACT adsorption likely provides a stable anchor layer, onto which further molecules can adsorb or entangle, leading to a thicker, potentially hydrated, and robust physical barrier. This thick, stable, and persistent layer, even under dynamic conditions (albeit thinner), directly contributes to TACT's better and more durable corrosion inhibition performance.

The thinner films observed for TEA (around 1.7-2.0 nm) are consistent with a densely packed monolayer, multilayer adsorption, or from the formation of a slightly hydrated monolayer by physisorption [81]. The high reversibility and susceptibility to desorption from flow rate increase observed by QCM (Figures 3.42-3.44) further emphasize that TEA forms a less robust, more transient protective layer under flow conditions, as a continuous supply is needed to maintain adequate surface coverage against desorption. While some literature reports chemisorption of TEA on other metal substrates (e.g., magnesium by Shang et al.[218]), its interaction with steel in our system is consistent with a predominantly physisorptive character or weak, reversible chemisorption. This also suggests that TEA, on its own, may form a less stable and thinner protective layer, which could potentially limit its long-term surface protection, especially in dynamic environments [97].

3.4.5 Conceptual Adsorption/Inhibition Model for TEA and TACT on Steel Surfaces

The corrosion inhibition of ferritic steel (1.6310) in near-neutral aqueous media by TEA and TACT has been explained by their distinct adsorption mechanisms and the characteristics of the protective films they form on the steel surface. The steel surface, when exposed to aerated near-neutral solutions, is typically covered by a thin, native iron oxide/hydroxide layer. The proposed conceptual models for TEA and TACT adsorption and inhibition are derived from a synthesis of the results obtained in previous sections of this chapter.

3.4.5.1 TEA Inhibition Model

From the ΔG_{ads} values and QCM observations, TEA primarily adsorbs onto the steel surface via physisorption or weak, reversible chemisorption, acting as a mixed type inhibitor. This mechanism is conceptually illustrated in Figure 3.46

The possible interactions between TEA and the steel surface are:

(1) The lone pair on the nitrogen atom of TEA can interact with positively charged sites on the iron oxide/hydroxide surface. In near-neutral solutions, some TEA molecules may be protonated, leading to electrostatic attraction with negatively charged surface sites.
(2) The hydroxyl (-OH) groups of TEA can form hydrogen bonds with surface hydroxyl groups on the iron oxide/hydroxide layer.
(3) The nitrogen and oxygen atoms, possessing lone pair electrons, may form weak dative bonds or coordinate interactions with surface iron atoms or iron ions within the oxide layer [219].
(4) TEA is known to form stable complexes with Fe^{2+} and Fe^{3+} ions in aqueous solution [212,213]. The formation of these complexes in the near-surface region can provide a barrier preventing the diffusion of corrosive species to the metal surface. TEA-Fe^{3+} complexes are known to be highly soluble, and TEA-Fe^{2+} less soluble. This could also explain the desorption at high flow rates observed from QCM measurements.

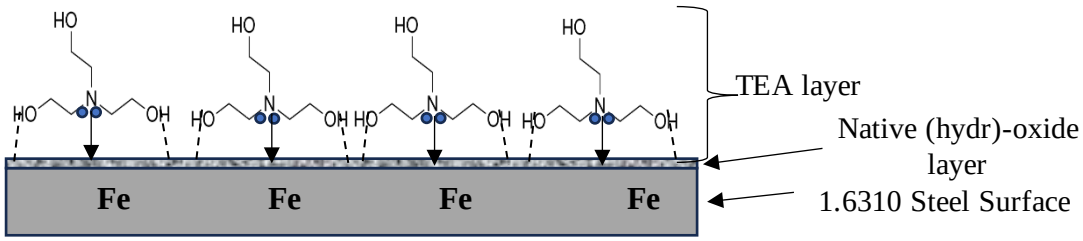

Figure 3.46: Conceptual adsorption model of TEA on the 1.6310 steel surface

3.4.5.2 TACT Inhibition Model

Results from this study support the conclusion that TACT is a mixed-type inhibitor, adsorbing through a combination of physisorption and strong chemisorption, as seen in Figure 3.47.

The possible interactions between TACT and the steel surface are:

(1) The lone pairs on the nitrogen atoms within the central triazine ring and the terminal amine groups of the hexanoic acid chains can form strong coordinate (dative) bonds with vacant d-orbitals of surface iron atoms or Fe^{2+}/Fe^{3+} ions in the native oxide layer [214,220]. The π-electron system of the triazine ring can also participate in back-donation with the metal surface, further strengthening the chemisorption.

(2) Electrostatic attractions can occur between inhibitor molecules and the charged steel surface via dipole-dipole interactions between the electric field of the double-layer or with charged sites on the metal oxide surface.

(3) Carboxyl (-COOH) groups at the experimental pH range are partly deprotonated ($-COO^-$) and can coordinate with Fe ions on the metal surface. Carboxyl and amine ($-NH_2$) groups can also form hydrogen bonds with surface hydroxyls.

(4) The triazine ring of the adsorbed inhibitor provides geometric coverage of the steel surface and a physical barrier to charge transfer and mass transport.

(5) The long aliphatic hexanoic acid chains contribute significantly to the hydrophobicity of the adsorbed layer, creating a more effective physical barrier that repels water and aggressive ions.

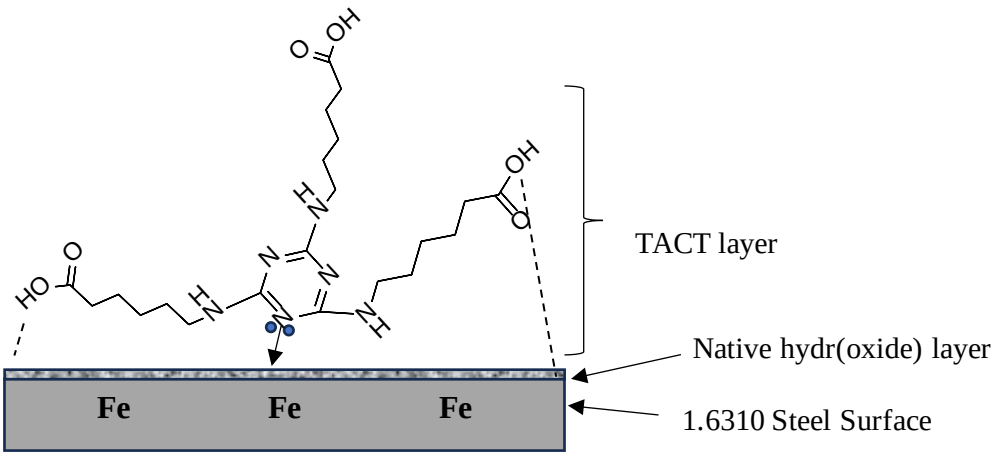

Figure 3.47: Conceptual adsorption model of TACT on the 1.6310 steel surface

3.5: Corrosion Inhibition with Irradiated TEA and TACT

The corrosion inhibitors (5000 ppm TEA and 300 ppm TACT) were irradiated to mimic real conditions encountered in the WAS cutting of activated RPV steels. Radiation transport simulation using the PENELOPE code enabled the estimation of expected dose rates from a reference radioactive steel-abrasive mixture. A dosimetry system was established to validate absorbed dose rates from radioactive sources in the KIT-INE controlled area. Ex-situ electrochemical experiments with aqueous phases of the irradiated solutions and freshly polished 1.6310 steel coupons were conducted and compared with results for the unirradiated inhibitors. NMR spectroscopic measurements aimed at uncovering radiation-induced changes to the molecular structures were performed after each irradiation dose. Surface analyses of steel coupons immersed in inhibitor solutions and irradiated, were conducted to observe the influence of ionizing radiation on the steel surface morphology of corrosion-inhibited steel.

3.5.1 Radiation Transport Simulations

Radiation transport simulations obtained using PENELOPE are summarized in Table 3.14 for three cases: irradiation of water sample in vials with an activated spring section, irradiation of water sample in vials with a spent MOX fuel segment, and the reference case of steel-abrasive mixture (SAM) in 1 m^3 of water.

Table 3.14: Summary of key simulation results for the different source/material configurations. All uncertainties are statistical uncertainties from Monte Carlo simulations.

Quantity	Irradiation of vial with activated spring (A = 8.42 E+08 Bq)	Irradiation of vial with MOX fuel (A =6.4 E+10 Bq)	Reference case of SAM in water (A=1.0 E+09 Bq)
Average Energy Deposition per Decay in Water (keV/history)	1.16 ± 0.01	0.180 ± 0.001	968.24 ± 1.55
Average Absorbed Dose per Decay in Water (MeV/g / history)	(1.16 ± 0.01) E-04	(1.80 ± 0.01) E-05	(9.98 ± 1.60) E-07
Average Absorbed Dose Rate in Water (mGy/h)	56.30 ± 0.34	664.00 ± 2.32	0.558 ± 0.001

The average absorbed dose rate in water estimated from the simulations enabled the planning of inhibitor irradiation experiments. With the MOX fuel, 664 ± 2 mGy/h is expected as dose rate to the irradiation vial containing the inhibitor solution, as described in Section 2.2.6 and in Figure 2.11. With the activated spring, an average absorbed dose of 56.30 ± 0.34 mGy/h is expected in the sample to be irradiated. For the SAM in water reference case, an average absorbed dose rate of 0.558 ± 0.001 mGy/h is expected in the water.

Cylindrical Dose Distribution in SAM Reference Case:

The simulation results show a non-uniform dose rate distribution throughout the water volume. Figure 3.48 illustrates the half-cylindrical dose distribution as a function of height from the bottom of half (from center to one radius dimension) of the cylindrical water phantom with the SAM at the base.

With a source activity of 1E+09 Bq the maximum dose rate of 0.014 keV/g/history corresponding to 8.07 ± 0.08 mGy/h was observed at the interface between the steel-abrasive layer and the water. This high dose region extends approximately 3 cm into the water and decreases with distance from the source. At a distance of 123.4 cm from the source layer, the dose rate decreases to 1E-06 keV/g/history (corresponding to 5.77 ± 0.10 E-04 mGy/h), representing the dose at the top layer of the water phantom.

The expected average dose rate in the simulation's reference case would amount to approximately 4.89 ± 0.01 Gy (i.e. 0.558 mGy/h · 24 h · 365) for one year of exposure assuming no changes in the source activity. This means that the inhibitor would be exposed to this absorbed dose in the solution containing the SAM. This dose value would scale in the real scenario with respect to actual source activities and exposure time.

The SAM simulation results therefore provide an estimation of expected dose rates from a steel-abrasive mixture after WAS cutting and before separation in the NaMaSK system under investigation. It also provides a baseline for quantifying radiation effects on the organic corrosion inhibitors required for this study. Simplifications in the simulation model, such as not fully accounting for the complex geometry of the real distributed source or the contributions of other radionuclides present in the activated steel, could lead to greater dose rates in actual radioactive steel-abrasive mixtures.

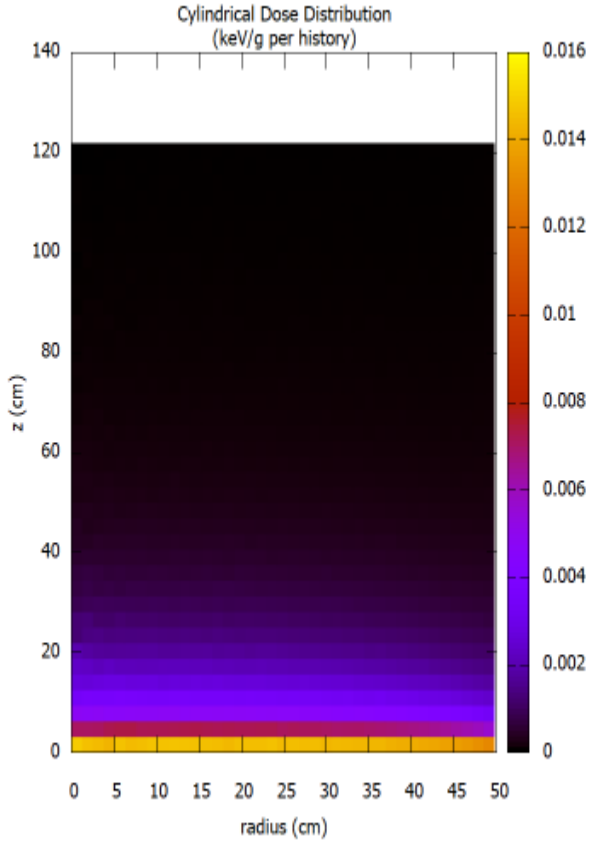

Figure 3.48: Half-cylindrical dose distribution for the Steel-Abrasive Mixture (SAM) in a 1m^3 water volume during radiation transport simulations.

3.5.2 Dosimetry and Dose Validation

3.5.2.1 Solid State Dosimetry

The results of the evaluation of the 20 TLDs after 4 hours of irradiation in the autoclaves with the activated spring source are presented in Figure 3.49, showing the dose distribution by position of the TLDs in the autoclave (Fig 2.12). Table B1 (Appendix) provides a tabular description of each TLD's absorbed dose and the mean absorbed dose rate after 4 hours of irradiation. For the irradiation experiment with samples arranged in a carousel having the irradiation source at the center (described in detail in Section 2.2.6, Fig. 2.11), the absorbed dose and dose rate for each TLD are evaluated in Table B2 (Appendix) and summarized in Figure 3.50.

Figures 3.52 and 3.53, along with the detailed data in Tables B1 and B2, clearly demonstrate that the absorbed dose to the TLDs was dependent on their position relative to the source, exhibiting statistically significant differences across the measurement locations.

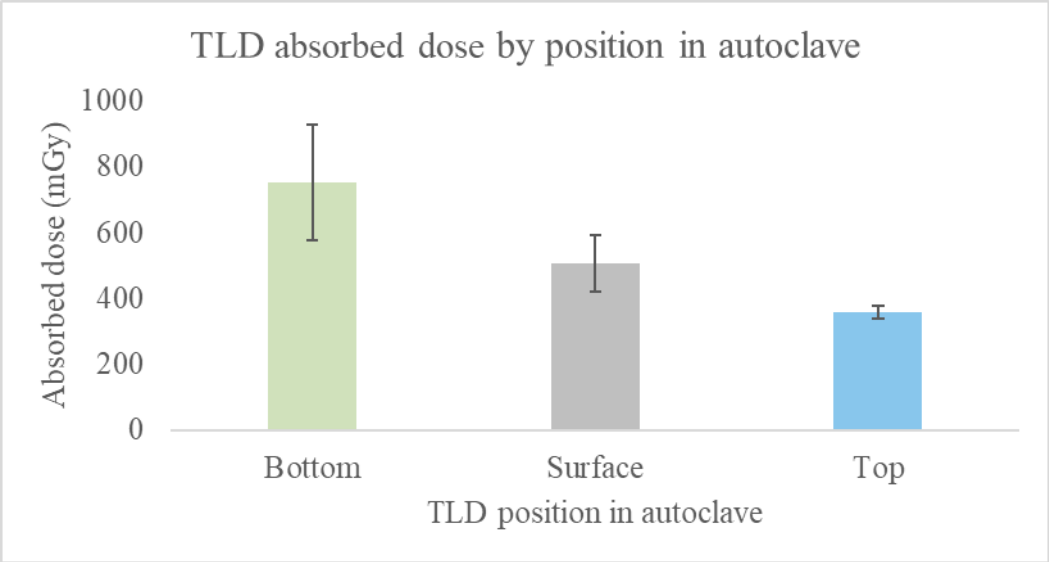

Figure 3.49: Dose distribution by position of TLDs arranged in an autoclave and irradiated with an activated stainless-steel spring. Error bars represent statistical uncertainties from the TLD measurements.

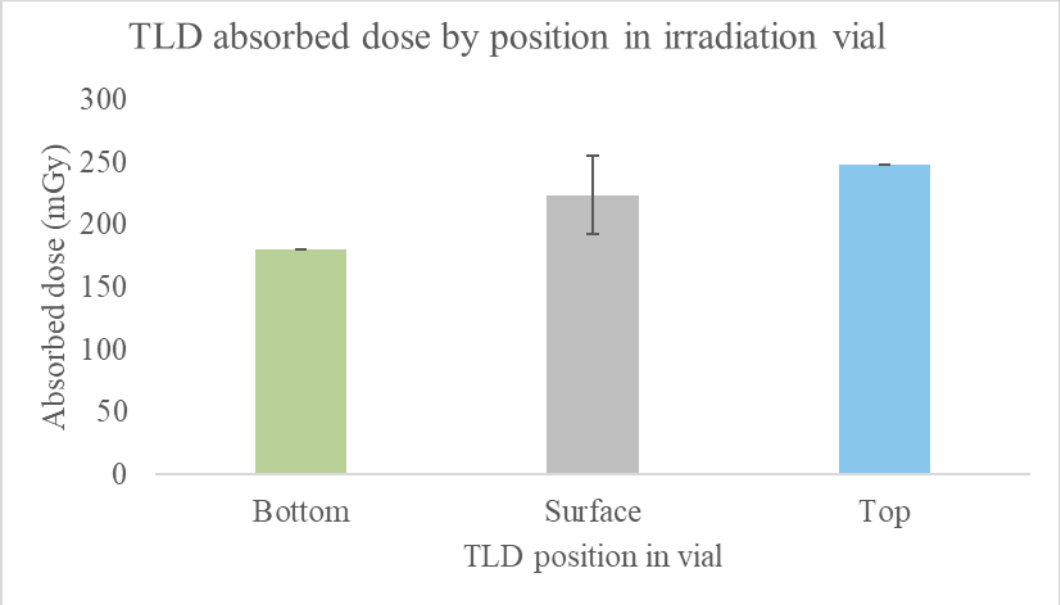

Figure 3.50: Dose distribution by position of TLDs arranged and irradiated in the polyethylene carousel setup with an activated stainless-steel spring at the center. Error bars represent statistical uncertainties from the TLD measurements.

For the autoclave setup (Figure 3.49, Table B1), the TLDs positioned at the bottom of the autoclave, closest to the activated stainless steel spring source, received the highest mean absorbed dose. TLDs on the cylindrical surface received an intermediate mean dose, while TLDs placed at the top of the autoclave, furthest from the source, received the lowest mean dose.

For the TLDs in the irradiation vial (carousel setup, Figure 3.50, Table B2), a similar position-dependent dose distribution was observed, though with a different geometry.

These measured dose ranges across TLD positions do not overlap, quantitatively confirming that significant differences in absorbed dose exist between the different positions. This position-dependent dose is physically expected due to the inverse square law of radiation intensity with distance from the source, and the specific geometry of the setup where the source was placed at the base of the autoclave. An average absorbed dose of 5.3±1.8 E+02 mGy was calculated for this setup. For a 4-hour irradiation period, the average dose rate measured with the TLDs was 132.9 ± 44.2 mGy/h. The large uncertainty reflects the spatial dose variation based on source and TLD arrangement. For the TLDs in the irradiation vial, the average dose rate was estimated to be 55.4 ± 8.0 mGy/h.

3.5.2.2 Fricke Dosimetry

Fricke dosimetry was employed as a chemical dosimetry method to experimentally determine the absorbed dose to the inhibitor solutions and blanks during irradiation experiments. This technique also served as a crucial validation tool for the solid-state dosimetry (TLDs) and the numerical computation of radiation fields around the sources using Monte Carlo simulations.

Figure 3.51 presents the UV-Vis spectra of the Fricke solutions, illustrating the increase in absorbance at 304 nm following irradiation from various sources in the INE-ABL. The clear increase in the absorption band for irradiated samples compared to the unirradiated (blank) Fricke solution qualitatively confirms the radiation-induced formation of Fe^{3+}, serving as the basis for quantitative dosimetry. Calibration samples irradiated to nominal doses of 30 Gy and 50 Gy also show progressively higher absorbance values, establishing the linearity and responsiveness of the dosimetry system.

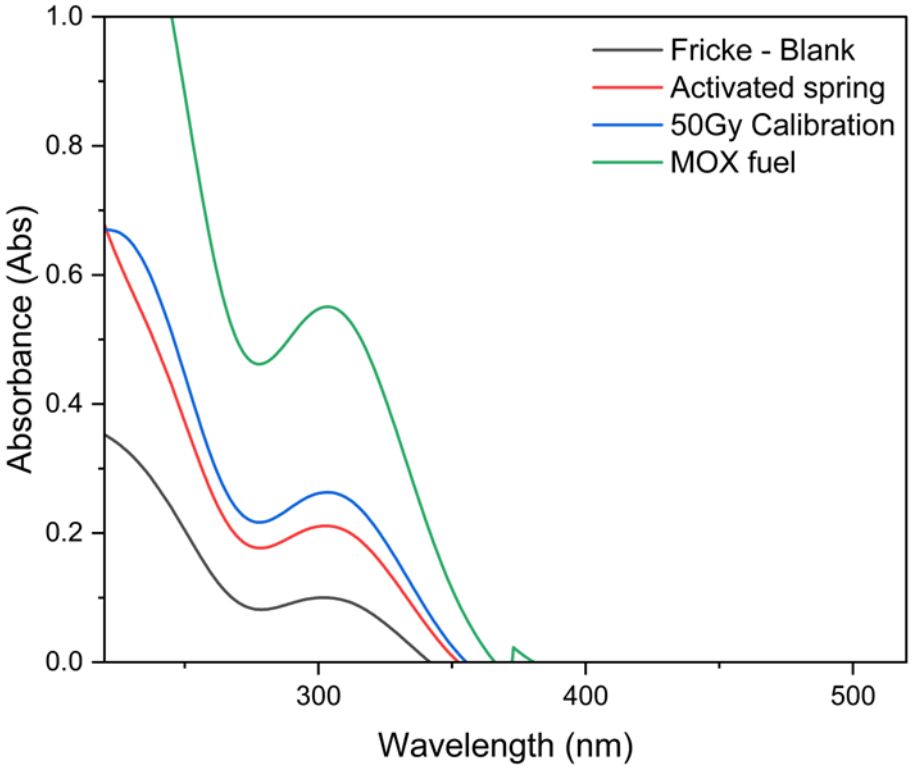

Figure 3.51: UV-vis spectra of Fricke-blank solution (unirradiated), a 50 Gy calibration sample, Fricke solution irradiated with the activated stainless-steel spring for 3 weeks, and Fricke solution irradiated with MOX fuel segment for one week in the INE-ABL.

A summary of the quantitative results from the Fricke dosimetry, including the measured absorbance changes and the calculated absorbed doses, is presented in Table 3.15.

Table 3.15: Absorbance values from UV-Vis measurements and absorbed dose calculation for Fricke dosimetry with different sources.

Radiation Source	Change in absorbance ($\Delta Abs \pm 0.004$) at 25°C	Absorbed dose to Fricke, D_F (Gy)	Absorbed dose to water, D_W (Gy)
Fricke - Blank	-	-	-
30 Gy Calibration	0.097	27.0 ± 3.5	27.1 ± 3.5
50 Gy Calibration	0.163	45.3 ± 5.0	45.5 ± 5.0
Activated spring	0.114	32.0 ± 4.1	32.1 ± 4.1
MOX fuel	0.452	126.9±2.5	127.4±2.5

The calibration results demonstrate the reliability of the Fricke dosimetry system. The measured doses of 27.1 ± 3.5 Gy and 45.5 ± 5.0 Gy for nominal 30 Gy and 50 Gy irradiations, respectively, are in good agreement with the expected values, falling within the stated

uncertainties. This confirms the accuracy and precision of the Fricke solution preparation and spectrophotometric analysis procedure.

For the experimental irradiation sources, the Fricke dosimetry yielded specific absorbed dose to water values. The 3-week irradiation with the activated spring source resulted in an absorbed dose of 32.1 ± 4.1 Gy. This translates to an average dose rate of 63.7 ± 8.1 mGy/h (calculated from 32.1 Gy/ (3 weeks × 7 days/week × 24 h/day) ≈ 0.0637 Gy/h = 63.7 mGy/h). This value exhibits good comparability with the dose rate of 55.41 ± 8.03 mGy/h determined independently using TLDs for the same setup (Section 3.5.2.1), providing strong cross-validation for the dose estimations. For the MOX fuel segment, a significantly higher absorbed dose of 127.4 ± 2.5 Gy was measured after a 1-week irradiation period, corresponding to a dose rate of approximately 7.60 ± 0.15 E+02 mGy/h. This value shows a discrepancy when compared with the dose rate of 6.64 ± 0.02 E+02 mGy/h obtained from the Monte Carlo simulation of the same setup. The difference of approximately 94.3 mGy/h (representing about a 14% deviation) is statistically significant given the combined uncertainties of both methods. This discrepancy suggests that the simplified geometry, materials and source definitions employed in the simulation may not fully capture all the complexities of the experimental setup.

The dosimetric results confirmed that for high dose irradiation up to 2.5 kGy, the second setup using MOX fuel as radiation source was preferred. High doses up to 2.5 kGy were required to obtain discernible results from the radiolysis of the inhibitors and to provide a conservative figure for justifying the performance of the inhibitors in real scenarios.

3.5.3 Post-Irradiation Analyses:

The corrosion inhibitors (5000 ppm TEA and 300 ppm TACT) were irradiated up to absorbed dose values of 35 Gy, 0.35 kGy, 2.00 kGy and 2.50 kGy by exposing the samples to the radiation sources in the experimental setup described in Section 2.2.6. The pH of the solutions before and after irradiation were measured. Ex-situ electrochemical experiments with aqueous phases of the irradiated solutions and freshly polished 1.6310 steel coupons were conducted and compared with results for the unirradiated inhibitors. NMR spectroscopic measurements aimed at uncovering radiation-induced changes to the molecular structures were performed after each irradiation dose. Surface analyses of steel coupons irradiated in-situ in the inhibitor solutions at the different absorbed dose values, were conducted to observe the influence of ionizing radiation on the steel surface chemistry in the presence of the inhibitors.

3.5.3.1 pH Measurements:

A comparison of the pH values of the samples measured immediately after irradiation, are provided in Table 3.16. It is observed that absorbed dose affected the pH of the inhibitor solutions.

Decrease in pH values of demineralized water when exposed to γ-irradiation has been reported in literature [221]. From Table 3.16, the pH of TEA (in Milli-Q water) decreases with increase in absorbed dose, while pH variations in TACT are minor and within measurement uncertainty. While no explicit study on the dependence of TEA's pH on dose could be found in literature, the results observed in the present study could be attributed to the generation of H^+ ions from the radiolysis of water and the possible formation of organic acids from TEA breakdown. With TEA (in 0.06 mol/dm^3 $NaHCO_3$) a buffering effect can be observed even after 2.5 kGy irradiation.

Table 3.16: Measured pH values (±0.2) of blank and irradiated inhibitors with respect to absorbed dose.

Solutions	Absorbed dose				
	Unirradiated	35 Gy	0.35 kGy	2.00 kGy	2.50 kGy
Blank 1 (Milli-Q)	7.1	7.0	6.8	6.4	6.2
Blank 2 (0.06 mol/dm^3 $NaHCO_3$)	8.5	-	-	-	8.2
5000 ppm TEA (in Blank 1)	9.7	9.0	8.5	8.0	8.0
5000 ppm TEA (in Blank 2)	8.7	-	-	-	8.6
300 ppm TACT (in Blank 1)	7.0	7.1	7.2	7.2	7.4
300 ppm TACT (in Blank 2)	7.6	-	-	-	8.0

3.5.3.2 Ex-situ Electrochemical Measurements:

The PDP curves comparing the unirradiated and irradiated 5000 ppm TEA and 300 ppm TACT solutions at different dose values are shown in Figure 3.52 and Figure 3.53 respectively. An additional curve illustrates the influence of bicarbonate ions on the corrosion behavior of the metal electrode in the presence of the inhibitors and ionizing radiation. A summary of Tafel Extrapolation parameters from the potentiodynamic experiments of TEA and TACT are presented in Table 3.17.

Table 3.17: Tafel Extrapolation and corrosion rate values for 1.6310 steel in irradiated TEA (5000 ppm) and TACT (300 ppm) solutions. TACT/TEA-BC indicate inhibitors in 0.06 mol/dm^3 $NaHCO_3$

Dose (kGy)	Sample	β_a (mV/dec)	β_c (mV/dec)	i_{corr} (µA)	E_{corr} (mV)	CR (mm/y)
	TACT	282.2 ± 3.0	70.4 ± 2.5	0.17± 0.01	-230.20±6.0	3.58±0.20 E-03
0.35	TEA	103.5 ± 2.0	120.3 ± 3.0	0.09±0.01	-240.2±5.0	1.90±0.02 E-03
	TACT	262.1±3.0	180.30±4.0	0.29±0.02	-300.05±8.0	6.11±0.40 E-03
2.0	TEA	311.3±4.0	170.4±4.5	0.15±0.01	-418.9±10.0	3.17±0.02 E-03
	TACT	340.2±4.0	160.6±4.0	0.35±0.02	-385.5±15.0	7.38±0.42 E-03
2.5	TEA	330.0±4.0	205.2±4.0	0.25±0.02	-420.1±12.0	5.28±0.42 E-03
	TEA-BC	350.2±4.0	108.7±9.0	0.22±0.02	-400.3±10.0	4.64±0.42 E-03
	TACT-BC	159.7±2.0	150.2±6.0	0.40±0.05	-480.5±20.0	8.44±1.01 E-03

As shown in Table 3.17, both inhibitors showed a degradation in performance with increasing radiation dose, leading to higher corrosion rates. The corrosion potentials for both inhibitors exhibited a consistent negative shift with increasing dose, as annotated in Figures 3.52 and 3.53. This suggests that the tendency for the steel corrosion increased with absorbed dose, as both inhibitors were affected by radiation-induced species. The specific interactions with the steel surface and the electrochemical reactions might differ, however, for both inhibitors.

The Tafel plots for the TEA-inhibited system shown in Figure 3.52 and summarized in Table 3.17 reveal the influence of ionizing radiation and bicarbonate ions on the corrosion inhibition of low alloy ferritic steel. In the unirradiated state, TEA provides a degree of corrosion inhibition, characterized by an E_{corr} of approximately -214.1 mV and a CR of 0.5E-3 mmpy, corresponding to ~99% inhibition efficiency relative to the uninhibited system (see Table 3.10). Upon exposure to ionizing radiation, the corrosion kinetics are significantly altered. Increasing radiation doses generally lead to a decrease in the corrosion potential (as illustrated in Figure 3.55) and increase in the corrosion current density, indicating a reduction in the inhibitor's effectiveness and an acceleration of the corrosion process. The E_{corr} shows no significant shift at 0.35 kGy; however, it decreases to -420 mV at higher doses (2.0 kGy and 2.5 kGy. This suggests that radiation-induced species likely influence both anodic and cathodic reaction rates in a dose-dependent manner. The cathodic Tafel slopes appear to decrease at higher radiation doses, potentially indicating changes in the rate-determining step of the cathodic reaction or

the involvement of new cathodic processes driven by radiolysis products. The addition of 0.06 mol/dm^3 $NaHCO_3$ to the 2.5 kGy irradiated TEA system results in a slight positive shift in E_{corr} (to approximately -400 mV) with a slight decrease in the corrosion current.

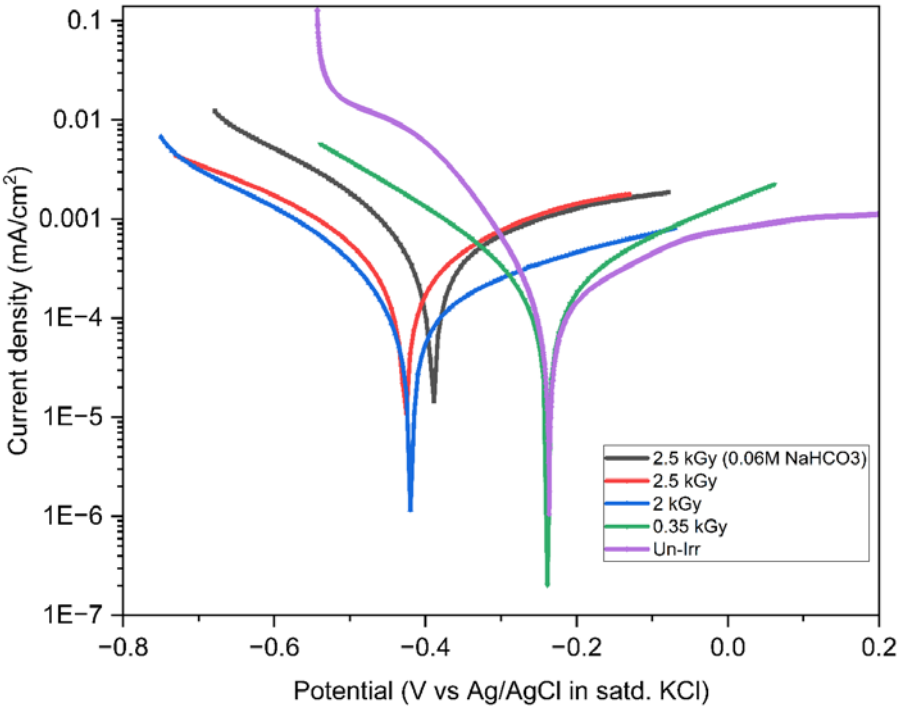

Figure 3.52: Potentiodynamic polarization curves (Tafel plots) for 1.6310 low alloy ferritic steel in 5000 ppm TEA solution. Samples were exposed to ionizing radiation doses of 0.35 kGy, 2 kGy, and 2.5 kGy, as well as a sample irradiated to 2.5 kGy in the presence of 0.06 mol/dm^3 $NaHCO_3$ solution.

For the unirradiated sample, TACT provides inhibition with an E_{corr} around -0.25 V and an estimated i_{corr} of approximately 0.14 µA. Similar to TEA, increasing radiation doses lead to a progressive increase in the corrosion current, signifying a decrease in TACT's inhibitory capacity (Figure 3.60). The E_{corr} for TACT generally shifts towards more negative potentials with increasing radiation dose, reaching approximately -400 mV at 2.5 kGy. The Tafel slopes also change with radiation dose, reflecting altered reaction kinetics. The introduction of 0.06 mol/dm^3 $NaHCO_3$ to the 2.5 kGy irradiated TACT system caused a substantial increase in the corrosion current (markedly higher than for the TEA system) and a significant negative shift in E_{corr} (to approximately -500 mV). This negative shift, coupled with the high corrosion current, indicates a strong influence of carbonates on accelerating the anodic dissolution of steel in the presence of TACT under the experimental condition.

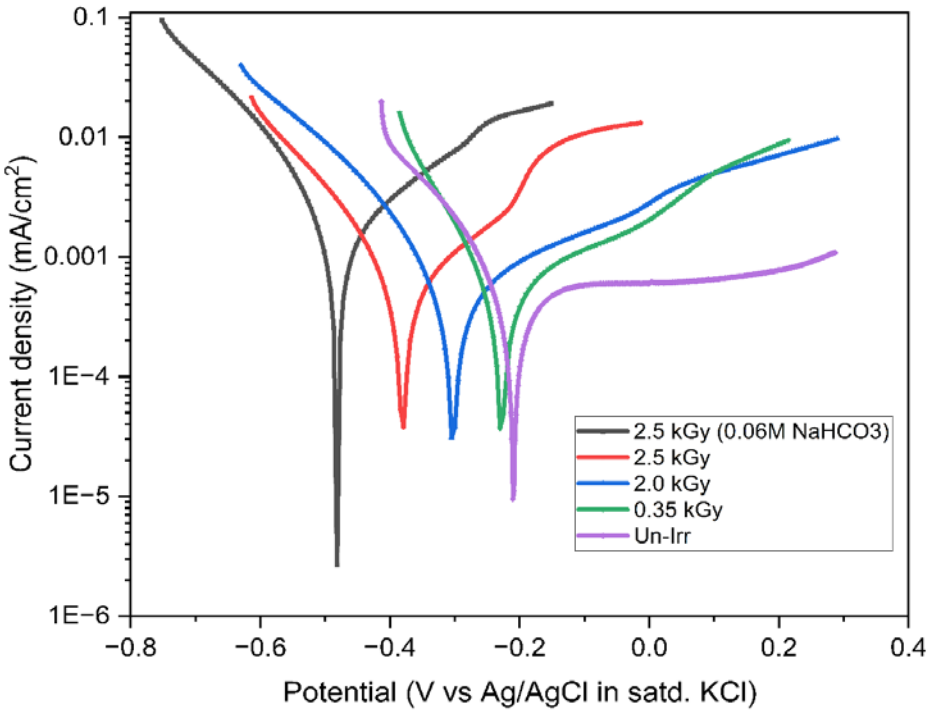

Figure 3.53: Potentiodynamic polarization curves (Tafel plots) for 1.6310 low alloy ferritic steel in 300 ppm TACT solution. Samples were exposed to ionizing radiation doses of 0.35 kGy, 2 kGy, and 2.5 kGy, as well as a sample of 300 ppm TACT in 0.06 mol/dm^3 $NaHCO_3$ solution irradiated to 2.5kGy.

Comparison of TEA and TACT Inhibition Behavior:

To comprehensively assess the impact of ionizing radiation on the protective capabilities of TEA and TACT, the corrosion rates of 1.6310 steel in both unirradiated and irradiated inhibitor solutions were compared. The relevant CR values, extracted from Tafel extrapolation parameters (Tables 3.9, 3.10, and 3.17), are summarized in Table 3.18. For this comparison, optimal unirradiated concentrations (5000 ppm for TEA and 300 ppm for TACT) were selected, as these concentrations demonstrated high inhibition efficiencies prior to irradiation.

Table 3.18: Comparative Corrosion Rates (CR) of 1.6310 Steel in Unirradiated and Irradiated TEA (5000 ppm) and TACT (300 ppm) Solutions.

Inhibitor	Absorbed Dose (kGy)	Corrosion Rate CR (mm/y)	Relative factor of increase in CR (vs. Unirradiated)
TEA	Unirradiated (0)	(0.50±0.02) E-03	1
	0.35	(1.90±0.02) E-03	3.8
	2.0	(3.17±0.02) E-03	6.3
	2.5	(5.28±0.42) E-03	10.6
TACT	Unirradiated (0)	(2.01±0.06) E-03	1
	0.35	(6.11±0.02) E-03	3.0
	2.0	(7.38±0.42) E-03	3.7
	2.5	(8.44±0.63) E-03	4.2

The data in Table 3.18 demonstrate a dose-dependent decrease in the inhibition efficiency for both TEA and TACT, as evidenced by a progressive increase in the corrosion rate with increasing absorbed radiation dose. This indicates that the radiolytic products of water and/or the degradation of the inhibitors themselves compromised their protective capabilities.

In the unirradiated state, 500ppm TEA provided a lower corrosion rate ((0.50±0.02) E-03 mm/y) compared to TACT at 300 ppm ((2.01±0.06) E-03 mm/y). This confirms TEA's excellent performance at its optimal high concentration, while TACT achieved strong inhibition at a significantly lower concentration.

Both inhibitors showed an increase in CR even at relatively low doses. For TEA, the CR increases by a factor of 3.8, while for TACT, it increases by a factor of 3.0. This suggests that even relatively minor radiolytic changes affected the inhibitors' performance.

At 2.5 kGy, TEA's corrosion rate increased significantly by a factor of 10.6 compared to its unirradiated state, reaching (5.28±0.42) E-03 mm/y. This substantial increase aligns with the more pronounced molecular degradation observed in the TEA NMR spectra (Figure 3.54, where peak broadening and new product formation indicate a loss of structural integrity.

For TACT, corrosion rate also increased with dose, but to a lesser extent relative to its unirradiated performance, with a 4.2-fold increase at 2.5 kGy, reaching (8.44±0.63) E-03

mm/y. This comparatively smaller increase in CR (relative to its unirradiated state) is consistent with the greater molecular stability of TACT observed in its NMR spectra (Figure 3.62), where the core triazine structure appears more resistant to radiolytic breakdown.

Despite TACT's higher relative radiation stability (smaller factor of increase in CR), TEA ultimately maintains a lower absolute corrosion rate at the highest absorbed dose in the present study (2.5 kGy) compared to TACT ((5.28±0.42) E-03 mm/y for TEA vs. (8.44±0.63) E-03mm/y for TACT). This could be attributed to TEA's higher initial concentration providing a larger reservoir of inhibitor, or the nature of its degradation products still offering some residual protection, even if the parent molecule is compromised. Also, both inhibitors maintained high inhibition efficiencies (above 95% compared to the unirradiated) even at the highest absorbed dose of 2.5 kGy, demonstrating notable radiation resistance in the experimental condition.

TEA and TACT differ in their behavior when exposed to radiation in the presence of $NaHCO_{3(aq)}$. The presence of 0.06 mol/dm^3 $NaHCO_3$ at 2.5 kGy irradiation led to a significant acceleration of corrosion for the TACT system, whereas for the TEA system, a decrease in corrosion was observed with the presence of $NaHCO_3$. This indicates that hydrogen carbonate ions likely interfered with the formation or stability of the protective inhibitor layer. In the presence of TEA, bicarbonate ions effectively maintained the alkaline pH of the system (Table 3.16), even as radiolytic species were formed. This stable alkaline environment is known to favor the stability of iron oxide/hydroxide passive films thereby indirectly contributing to preserving the integrity and protective capacity of the inhibitor layer.

In the absence of corrosion inhibitors, ferritic steels in aqueous media exposed to gamma radiation can experience increased corrosion rates due to the radiolysis of water, which generates redox active species ranging from highly oxidizing (•OH, H_2O_2, O_2) to highly reducing (e_{aq}^-, H•, H_2) species that react with the steel surface [103,222]. In contrast to oxidizing radiolysis products, the main reducing radiolysis species, H_2, is gaseous hence the dominant species in solution are •OH, H_2O_2(aq) and other oxidizing radiolysis species. The change in E_{corr} observed with irradiation has been attributed mainly to the build-up radiolytically generated H_2O_2. H_2O_2 acts as either a reductant or oxidant for the corrosion reaction depending on the nature of the oxide on the steel surface [223,224]. To observe the influence of γ-irradiation on metal electrodes, Fujita et al [225,226] irradiated a platinum electrode in solutions purged with Ar, CO_2, N_2O and O_2 and measured the potential difference against a non-irradiated electrode and reported less noble potential difference at the irradiated electrode, lower by 100-400 mV. Daub and coworkers [224] observed that the E_{corr} of carbon steels in 0.01 mol/dm3 sodium borate

solution at a pH of 10.6 increased upon γ-irradiation. This trend was corroborated by other researchers for stainless steels [106,227,228]. In the presence of inhibitors, Migahed and coworkers [105] observed a decrease in OCP and inhibition efficiency after some organic corrosion inhibitors (pH 5.4 and 6.4) were pre-irradiated up to 100 kGy by gamma irradiation and applied to 304 stainless steel in a 2 mol/dm^3 HCl solution. Dey and coworkers [104] concluded that the nature of the species formed by the reaction of the inhibitor and the radiolytic species – e_{aq}^-/H-atom dictate the effectiveness of such inhibitor in the presence of ionising radiation. Inhibitors that produce strong reducing radicals after reacting with e_{aq}^- / H· may still be effective corrosion inhibitors, provided they form insoluble complexes with the metal. Schwarz [229] performed a pulse radiolysis of triethanolamine using a Co-60 source and an electron beam. Among the radicals formed from the attack of e_{aq}^- on TEA, two main products were stable from the propagation till the termination steps: Diethanolamine HN(CH_2CH_2OH) and Acetaldehyde (CH_3CHO).

3.5.3.3 NMR Measurements

NMR spectra of ^{1}H NMR measurements performed after absorbed doses of 35 Gy, 0.35 kGy, 2 kGy and 2.5 kGy are compared with the spectra of the unirradiated inhibitors. These are shown in Figure 3.54 for 5000 ppm TEA and Figure 3.55 for 300 ppm TACT.

From Figure 3.54, unirradiated TEA, with the structure $N(CH_2CH_2OH)_3$, exhibits two prominent signals in its ^{1}H NMR spectrum. The triplet in the chemical shift region of 2.6 – 2.8 ppm and the broader triplet at 3.6-3.8 correspond to the -CH_2- groups adjacent to the nitrogen (N-CH_2) and the -CH_2- groups adjacent to the hydroxyl group (O-CH_2), respectively.

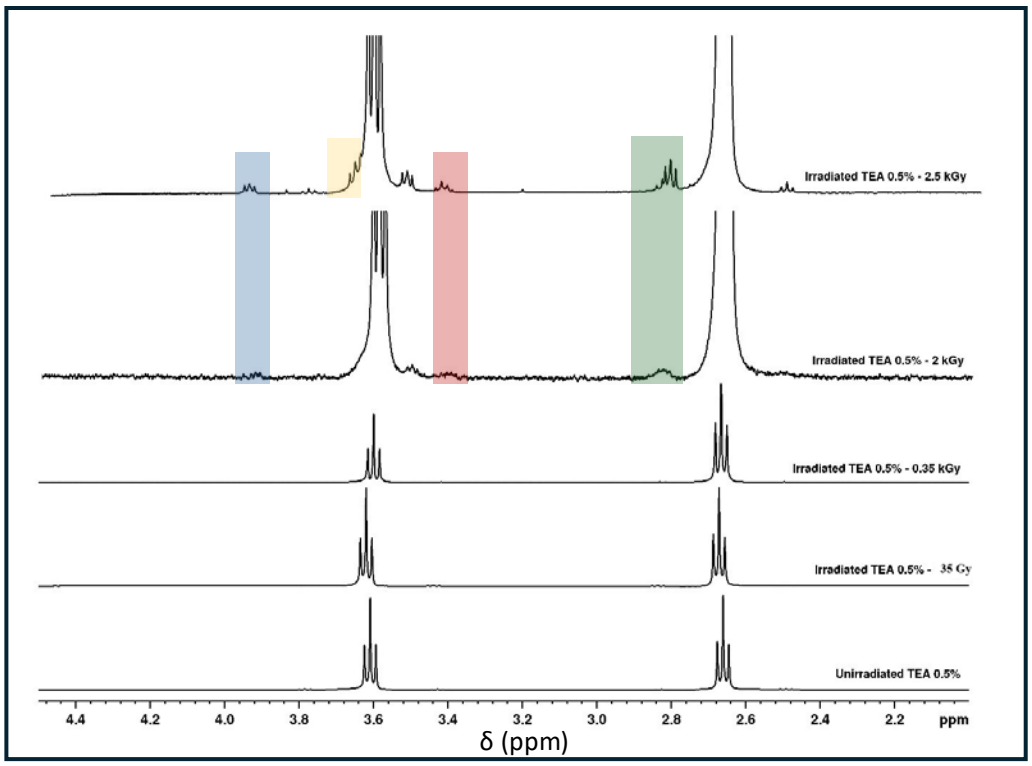

Figure 3.54: Comparison of ^{1}H-NMR spectra (400.18 MHz, 300 K) of unirradiated and irradiated 5000 ppm TEA solutions. Blue, red and green signals are newly identified compared to other spectra. Relative intensities are scaled independently to aid comparison.

The spectrum of the TEA sample irradiated at 35 Gy is almost identical to that of the unirradiated inhibitor. This suggests that at this very low dose, TEA experiences minimal, if any, radiolytic degradation detectable by ^{1}H NMR.

As the irradiation dose increases to 0.35 kGy and beyond, some changes are observed in the spectra relative to the unirradiated spectra:

1. Broadening of Existing Peaks: The two main TEA peaks (N-CH_2 and O-CH_2) at ~ 2.65 and 3.6 ppm become broader with increasing dose. This broadening indicates a loss of chemical homogeneity. The chemical environment of each type of proton becomes a distribution of slightly different environments. This is consistent with the formation of a range of radiolytic products, each with slightly altered chemical shifts.

2. New, Small Peaks: At higher doses (2 kGy and 2.5 kGy), new peaks with small intensities become visible around 3.4 ppm, and as a less intense shoulder around ~3.65 ppm. The region between 3.0 to 4.0 ppm contains the signals from protons from -CH_2- groups adjacent to oxygen or nitrogen. This suggests that the products formed are likely to have protons in similar chemical environments to those in the original TEA molecule, consistent with the formation of

degradation products such as diethanolamine, monoethanolamine, or fragments containing -CH_2-O- and -CH_2-N- linkages.

3. Dose-Dependent Degradation: The intensity of the new peaks, coupled with the broadening of the original TEA peaks, shows a dose-dependent degradation of TEA. Increasing absorbed dose results in greater radiolysis of the inhibitor solution.

The possible radiolysis mechanisms for the TEA solution include:

- C-N Bond Cleavage: Radiation can cause homolytic cleavage of the C-N bonds in TEA via OH attack. This would generate radicals, leading to the formation of smaller amine radicals (e.g., diethanolamine, monoethanolamine), aldehydes or alcohols [229].
- C-O Bond Cleavage: The cleavage of C-O bonds, leading to the formation of alcohols and imines, is a likely but less favored mechanism due to the higher bond dissociation energy of C-O compared to C-N [230,231].
- Hydrogen Abstraction: Studies reveal that OH radicals (and H atoms) can abstract a hydrogen atom from the protonated aliphatic amines usually at a position distant from the amino group (-NH_3^+ group). While for unprotonated amines, the OH (or O_{aq}^-) radicals can attack at every other position, leading to the formation of transients but the hydrogen abstraction by the radicals preferentially occurs on the amine group (-NH_2^+group) and on the alpha-position [232–234].These radicals are highly reactive and can participate in various reactions, including radical-radical coupling leading to the formation of dimers or larger oligomers. This could contribute to the observed broadening of the NMR signals at higher doses. In oxygenated solutions, (like in the present study) these carbon-centered radicals can form peroxyl radicals (R-O-O•), which subsequently decompose to form aldehydes, ketones, and carboxylic acids. This was the conclusion from the works of Clay & Rashid [232], Garrison et al [235], Fessenden & Neta [234]. The absence of significant down-field chemical shifts (> 7 ppm) suggests that aldehyde formation is not a dominant pathway under the experimental conditions, but the broadening and new small-intensity peaks could indicate minor contributions [236].

The NMR spectrum for the unirradiated TACT solution in Figure 3.55 indicates a triplet around ~3.2 ppm for the -CH_2- group adjacent to the triazine ring, a triplet around 2.2 ppm for the -

CH_2- adjacent to the carbonyl group (O=C-CH_2-). Multiplet signals at ~1.3 – 1.7 ppm from internal -CH_2- groups in the triazine ring.

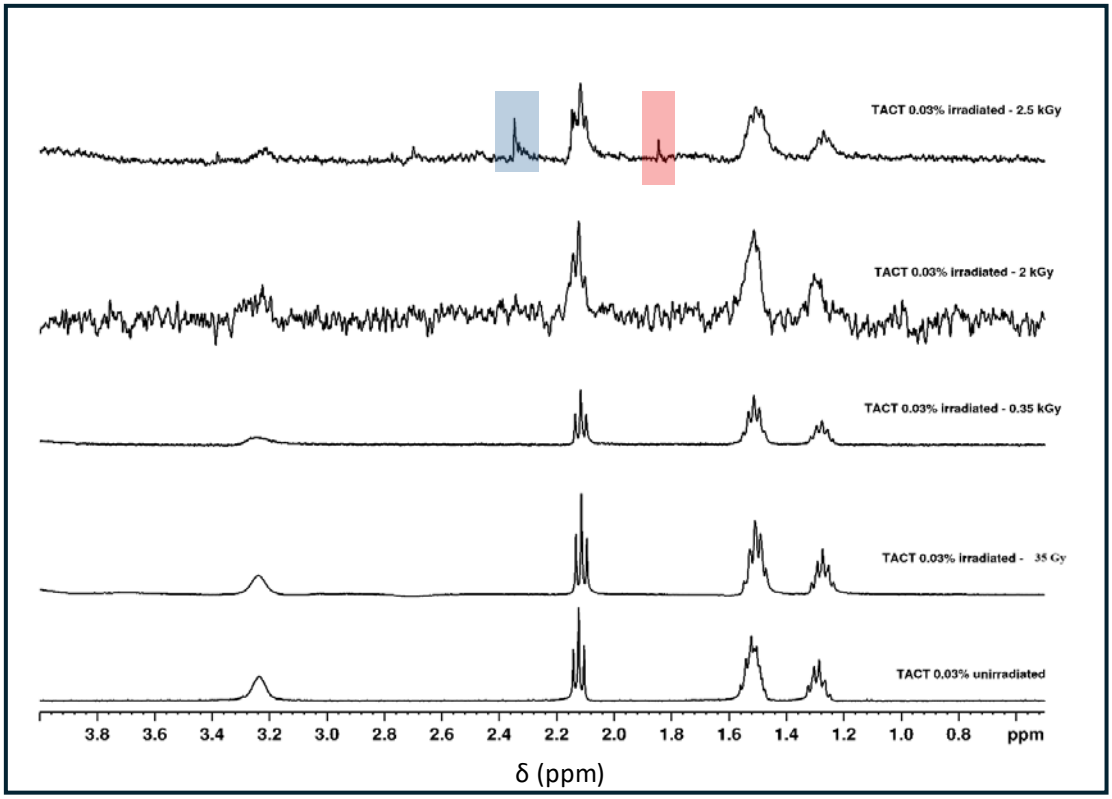

Figure 3.55: Comparison of ^{1}H-NMR spectra (400.18 MHz, 300 K) of unirradiated and irradiated 300 ppm TACT solutions. Blue and red bars denote possible new peaks from radiolysis. Relative intensities are scaled independently to aid comparison.

The key changes upon irradiation are peak broadening (at > 0.35 kGy dose), decreased intensity reflecting the radiolytic consumption of the parent TACT molecules, and the appearance of small new peaks at 2.5 kGy. Below 0.35 kGy absorbed dose, the molecule is relatively stable due to the stable triazine ring. The 2.5 kGy spectrum reveals very small, new, broad signals at 1.8 ppm and around ~2.3 ppm (red and blue bar in Fig. 3.55). These peaks, despite low intensity, signify the onset of molecular degradation and new chemical species formation from radiolysis, likely involving aliphatic side chains or amide bond cleavages, and resulting in minor degradation products with distinct proton environments. The increased apparent "noise" in the spectra at 2.0 kGy and 2.5 kGy, despite identical acquisition parameters as the rest, can be attributed to several factors stemming from the radiolytic degradation at these higher doses. This includes a reduced overall concentration of intact TACT molecules (leading to lower signal-to-noise ratio), the formation of a complex mixture of degradation products with overlapping and potentially very broad signals that distort the baseline, and the possible

generation of paramagnetic species (e.g., stable radicals or trace metal impurities undergoing redox changes) which can significantly broaden and suppress NMR signals, thus increasing the effective baseline noise [193].

The radiolytic degradation of TACT is more complex than that of TEA due to its more intricate structure. There is also a dearth of literature on the radiolysis mechanism specific to this molecule. The possible radiolysis mechanisms for the TACT solution include:

- Amide Bond Cleavage: Since amide bonds (R-CO-NH-R') are highly susceptible to cleavage by ionizing radiation, occurring primarily by hydrogen abstraction and OH radical attack [237–239], the cleavage of the amide bond would be a primary degradation pathway for TACT, leading to the formation of fragments containing the triazine ring and fragments of the aminocaproic acid side chains. E.g.

  TACT + hν → Triazine-NH_2 + HOOC-$(CH_2)_5$-NH-Triazine (and other fragments).

  The broadening and slight shifts of the existing TACT peaks (e.g., the triplet at 3.25 ppm and the triplet at 2.1 ppm) are consistent with the formation of a distribution of fragments where these bonds have been altered. New, unresolved signals contributing to the overall spectral envelope would also be expected in these regions.

- Hydrogen Abstraction: Similar to TEA, hydrogen abstraction from the methylene groups (-CH_2-) in the aminohexanoic acid chains can occur, leading to radical formation. These radicals can then undergo radical-radical coupling resulting in dimers and oligomers and oxidation to aldehydes/carboxylic acids. The increased broadening of the multiplets between 1.2 – 1.7 ppm and the appearance of minor new, broad signals in the 1.8 ppm and 2.3 ppm regions are consistent with the formation of various aliphatic and oxygenated aliphatic degradation products. These new signals represent the protons in these newly formed chemical environments.

The above mechanism is supported by the work of Cataldo and co-investigators [240] who performed radiolysis of 1,3,5 triazine, with γ-radiation between 50 and 350 kGy, and post-mortem studies using electronic absorption spectroscopy, liquid chromatography, FT-IR spectroscopy and differential scanning calorimetry (DSC). The results showed a low radiation stability of the molecule in the reported dose range. The observed radiolysis products include formamidine, triazine dimers and oligomers as well as gaseous products such as H_2, CH_4 and HCN. While the dose range in the present study are 20 times less than the above, the reported mechanisms are instructive.

The presence of characteristic peak positions across dose values in Figure 3.55, even with broadening and reduced intensity, indicates that the triazine ring exhibits greater stability to radiolysis compared to the more labile amide linkages and aliphatic chains. While TACT's NMR spectra indicated some radiolytic degradation, this persistence of the core functional groups suggests that its overall corrosion inhibition ability is largely retained. This conclusion is corroborated by the high IE (%) from electrochemical measurement after elevated doses.

G-values and Product Yields:

Schwarz performed pulse radiolysis of TEA and identified diethanolamine and acetaldehyde as main stable products from the propagation steps, and reported a G-value of 930 molecules/100 eV absorbed in the solution [229]. For the absorbed dose in the present study, a significant yield of diethanolamine and acetaldehyde is expected.

A G-value for TACT was not found in literature at the time of this report, however for triazine derivatives, Cataldo et al.[240] reported G-values for gamma-radiolysis products of 1,3,5-triazine such as H_2 (G=0.04 molecules/100 eV) and CH_4 (G=0.03 molecules/100 eV), with a total gaseous products yield, $G_{gas,}$ =0.22. This indicates that while simple gas products may have low yields, the overall degradation process is more complex, potentially involving other non-gaseous products, though their specific G-values were not quantified in that study. Other studies on triazine herbicides (e.g., atrazine) in aqueous solutions irradiated with electron beams or gamma rays indicate their degradation is driven by ·OH and e_{aq}^- reactions, leading to significant consumption of the parent molecule within kGy dose ranges [241,242], suggesting substantial overall degradation G-values.

In the present study, the qualitative observations from the NMR spectra provided direct evidence of these radiolytic transformations. The increasing peak broadening and the appearance of new, albeit small, signals at higher absorbed doses for both inhibitors signify a dose-dependent increase in the concentration of degradation products. The more pronounced changes observed for TEA (Figure 3.61) compared to TACT (Figure 3.62) qualitatively indicate a higher overall G-value for TEA degradation in this system, suggesting it is more susceptible to radiolytic breakdown.

3.5.3.4 Surface Composition of Irradiated Steel Coupons

Post-irradiation XPS measurements performed with the steel coupons immersed in the inhibitor solutions are reported in Figures 3.56 and 3.57 for different absorbed dose values. The N 1s

and Fe 2p spectra are compared with those of steel in contact with unirradiated inhibitor solutions.

XPS Spectra of Unirradiated and Irradiated 300 ppm TACT:

Figure 3.56 provides information about the chemical states of nitrogen (N 1s) and iron (Fe 2p) on the steel surface immersed in 300 ppm TACT before and after irradiation at different dose values (0.35 kGy and 2.5 kGy). The N 1s spectra (left column of Figure 3.56) show a weak N 1s peak at ~400.3 eV in the unirradiated sample, suggesting the presence of nitrogen-containing species, likely from TACT adsorption. The weak intensity of this N 1s signal, particularly when observed concurrently with prominent Fe 2p signals from the underlying steel substrate, is a direct indicator of a relatively thin inhibitor overlayer. After 0.35 kGy irradiation, the N 1s spectrum becomes more structured, with the binding energy of the main line at ~ 400.2 eV. The deconvolution of the N peak gives additional peaks at around 398.9 eV. The additional peaks suggest the presence of a fragment(s) with different nitrogen environments from the radiolysis of TACT. Organic compounds such as Aminoacetic acid (H_2NCH_2COOH) and Nitrilotriacetic acid ($N(CH_2COOH)_3$) have similar binding energies [243] and are possible products of TACT radiolysis. After 2.5 kGy, the N 1s peak at around 400.4 eV and 398.8 eV remains well defined, indicating the stability of -NH_2 and -CN groups even at higher radiation doses. This suggests that, despite some radiolytic degradation, TACT's key functional moieties (presumably the triazine core) persist. This ensured that the inhibitor could contribute to providing a protective layer on the steel surface, and thus its overall corrosion protection ability was not significantly compromised.

In the Fe 2p spectra (right column of Figure 3.56), the unirradiated sample clearly displays characteristic peaks for metallic iron (Fe(0) at ~707 eV) and ferrous iron (Fe(II) at ~710 eV), alongside a less intense peak for ferric iron (Fe(III)) at higher binding energies ~711 eV). This distribution of oxidation states indicates the presence of a thin, intrinsic iron oxide/hydroxide layer on the steel surface, with the underlying metallic iron still readily detectable. This confirms minimal initial oxidation and effective protection by the initial TACT adsorption, as highlighted in Section 3.4.3.2. For the 0.35 kGy irradiated sample, the Fe 2p spectrum shows a slight increase in the relative intensity of the Fe(III) peak compared to the unirradiated sample, suggesting a minor increase in surface oxidation. Nevertheless, the Fe(0) and Fe(II) components remain prominent, confirming that the TACT layer largely maintains its protective function against significant oxidation despite the exposure to radiation.

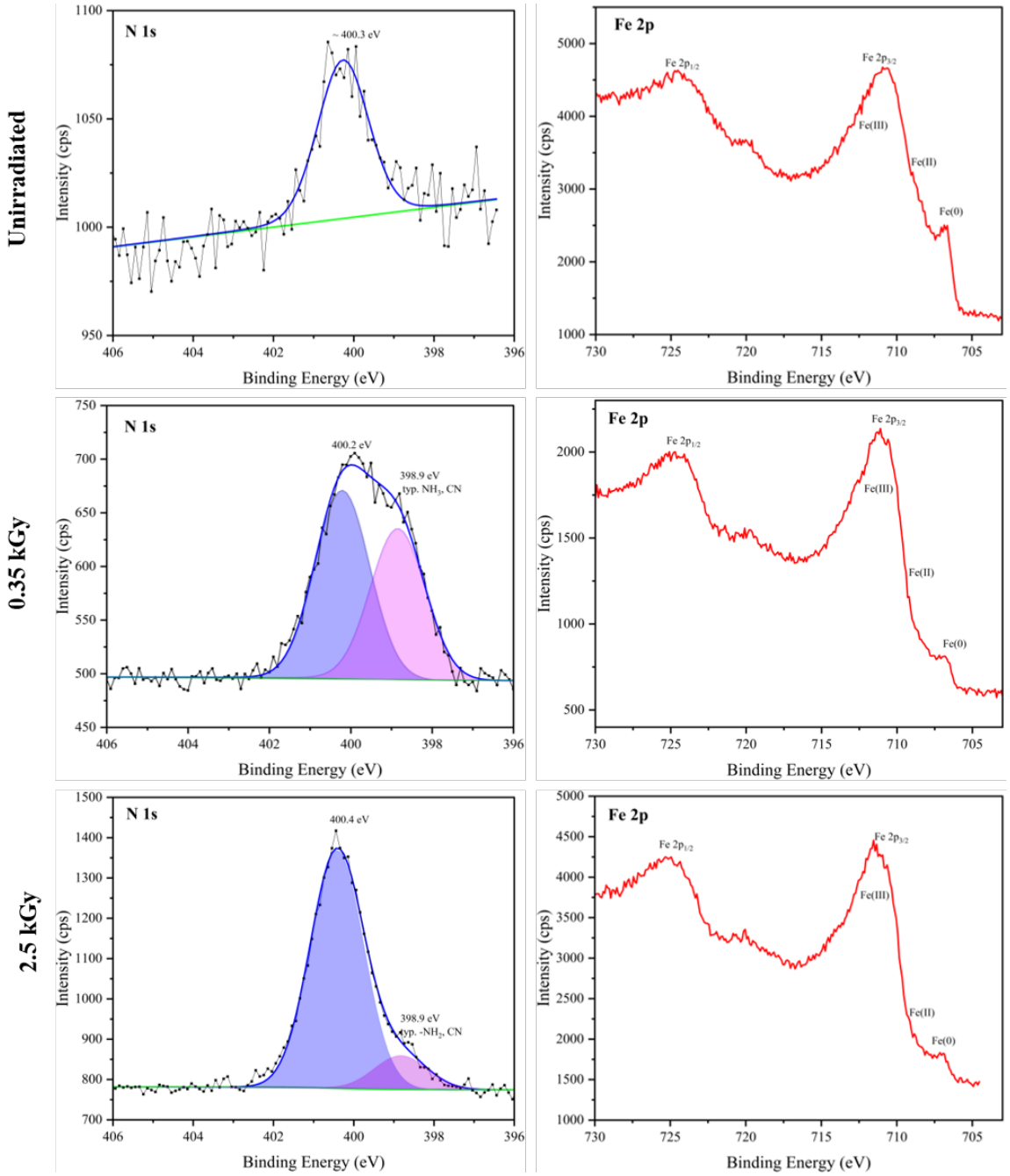

Figure 3.56: Comparison of Nitrogen (N 1s) and Iron (Fe 2p) spectra for steel in unirradiated and irradiated 300 ppm TACT solution at 0.35 kGy and 2.5 kGy absorbed dose values. N1s fitting indicate presence of other N species at higher doses.

After 2.5 kGy irradiation, a more noticeable change is observed. The Fe $2p_{3/2}$ peak assigned to Fe(III) becomes more intense, becoming the dominant iron species on the surface, while the Fe(0) peak is diminished and broadened. The Fe(II) component is still present but less intense compared to Fe(III). This shift towards higher oxidation states and the reduction in metallic iron content indicate a more significant degree of surface oxidation occurring at higher

radiation doses. This increased oxidation might be attributed to a partial breakdown of some inhibitor molecules or a reduction in the protective efficiency of the TACT layer under prolonged exposure to ionizing radiation, allowing corrosive species and radiolytic oxidants access to the steel surface. Despite this increased oxidation, the persistent presence of nitrogen (as discussed above) suggests that a substantial portion of the TACT layer, or its strongly adsorbed degradation products, remains on the surface, still providing some degree of protection against the complete oxidation of the steel surface.

XPS Spectra of Unirradiated and Irradiated 5000 ppm TEA:

Figure 3.57 shows a comparison of the N 1s and Fe 2p XPS spectra for steel coupons immersed in 5000 ppm TEA solution before and after exposure to ionizing radiation.

From the N 1s XPS spectra for the unirradiated sample in Figure 3.57, a strong peak at 400.3 eV suggests that TEA forms a well-adsorbed layer on the steel surface, likely through Fe-N interactions. A higher intensity is observed compared to TACT, possibly due to the higher relative concentration of the TEA (5000 vs 300 ppm). After 0.35 kGy irradiation, the binding energy remains at ~400.3 eV, suggesting that the chemical nature of TEA did not significantly change under irradiation up to this absorbed dose value. TEA therefore maintains its structural integrity at lower radiation doses (<0.35 kGy). With further increase in absorbed dose to 2.5 kGy, the peak at ~ 400.3 eV binding energy persists. The N 1s signal decreases in intensity, suggesting some desorption or breakdown of the inhibitor layer at higher radiation doses.

The Fe 2p spectrum for the unirradiated sample shows the presence of Fe(0) and Fe(III) peaks, with only a minor Fe(II) contribution, indicating low oxidation. This result is similar to that observed in TACT. At low dose value of 0.35 kGy, the Fe 2p spectrum still shows Fe(0) and Fe(III) as the main states. This suggests minor oxidation, but the TEA layer remains effective at preventing corrosion. After irradiation up to 2.5 kGy, a more intense Fe(III) peak is observed, with a decrease in Fe(0), indicating more advanced oxidation compared to 0.35 kGy. The Fe(0) peak is still visible, indicating that even with the presence of an oxide layer, metallic Fe can be detected at nanometer depth suggesting that the oxide layer is thin and that the inhibitor still protects the steel surface by a physical adsorption mechanism already discussed in the Section 3.4 with the unirradiated inhibitors.

The N 1s spectrum for TEA in 0.06 mol/dm^3 $NaHCO_3$ solution (purple spectrum in the 2.5 kGy N 1s) shows a lower intensity signal at the binding energy of the amine group (~400.3 eV)

compared to the solution in deionized water (blue trace). It can be inferred that the stability of TEA and its adsorption is strongly affected by the surrounding environment. CO_3^{2-} and HCO_3^- ions, present in the $NaHCO_3$ solution, are known to interact with iron and steel surfaces, contributing to passivation and forming surface complexes [204,205]. This interaction implies that carbonate/bicarbonate species could create a more effective barrier together with TEA than either species alone. The carbonate/bicarbonate ions may help stabilize TEA adsorption through electrostatic interactions or by forming bridging structures that enhance surface coverage and lower corrosion rate [244].

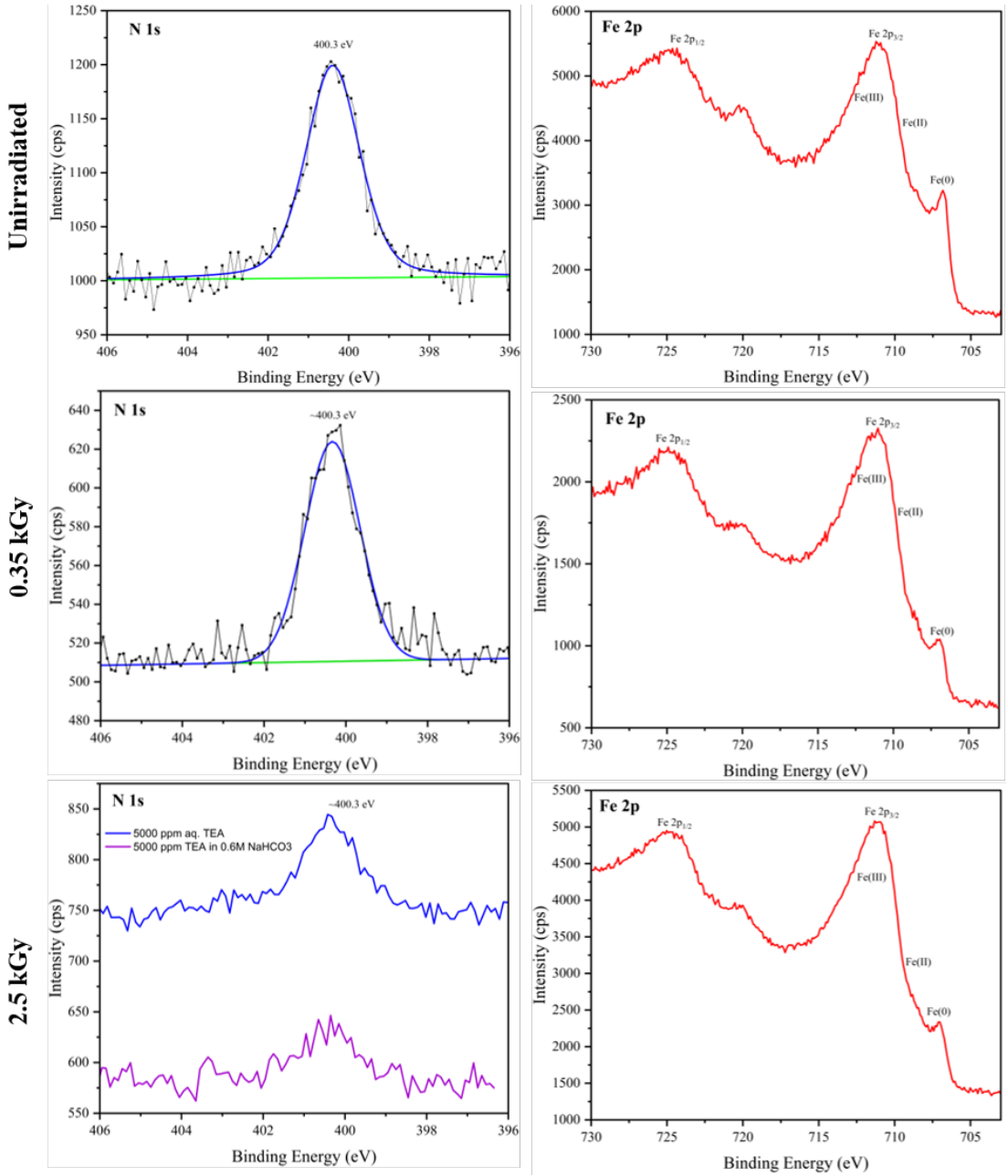

Figure 3.57: Nitrogen (N 1s) and Iron (Fe 2p) spectra for steel in unirradiated and irradiated 5000 ppm TEA solution. Effect of absorbed dose values of 350 Gy and 2.5 kGy are compared with unirradiated sample.

3.5.3.5 Surface Morphology of Irradiated Steel

A comparison of the surface morphology and elemental composition of the surfaces of 1.6310 steel coupons immersed in unirradiated TACT-inhibited and TEA-inhibited solutions, those immersed in the inhibitor solutions and further irradiated up to 2.5 kGy and coupons in blank solutions under the same conditions are presented in this section. Figures 3.58 and 3.59, along with the quantitative elemental compositions in Table 3.19, provide information on the surface morphology and elemental composition of the surfaces. The results complement the electrochemical data (Section 3.5.3.2) and NMR investigations (Section 3.5.3.3), to explain the observed effect of ionizing radiation on the corrosion inhibition of TEA and TACT.

The steel surface in the unirradiated blank solution (Figure 3.58: top, left) although initially prepared to a mirror finish, developed a visible homogeneous layer of precipitates/corrosion products after immersion in the blank solution. The corresponding EDX spectrum (Figure 3.59, top left) confirms a surface primarily composed of iron (42.2 ± 1.8 at. %) and nearly equal amount of oxygen (47.0 ± 1.7 at. %), along with carbon (9.8 ± 0.9 at. %) likely from adventitious contamination. The atomic ratio of Fe:O, approximately 1:1.11 (42.2:47.0) strongly indicates that the steel surface is covered by a significant layer of iron oxides and/or hydroxides. This corrosion product layer could provide some initial passivation in aerated conditions. In contrast, a heterogeneous and porous microstructure, consisting of nodular, cauliflower-like crystalline aggregates and high surface roughness is observed on the surface of the irradiated blank steel. This is characteristic of substantial corrosion product formation. The observed microstructural porosity and flake-like corrosion products suggest localized attack and potentially unstable passive film formation. The corresponding EDX spectrum (Figure 3.59, top right) shows a significant increase in oxygen content (61.1± 0.2 at. %) and a decrease in iron content (29.8 ± 1.6 at. %) compared to the unirradiated blank. This change in elemental ratio (1:2.05), coupled with the visual evidence, confirms extensive oxidation and the possible formation of a thick layer of hydrated iron oxides/hydroxides (likely Fe_2O_3). This observation is consistent with radiation-enhanced corrosion, where the radiolytic products of water (·OH, H_2O_2, etc.), acting as oxidants, significantly accelerate the corrosion process in the absence of effective inhibition [221,224].

Table 3.19: Composition in at. % of the surfaces shown in Figure 3.58. The elemental composition of 1.6310 steel surface in unirradiated solutions (Unir) of blank, 5000 ppm TEA and 300 ppm TACT, compared after irradiation up to 2.5 kGy.

	C	O	Al	Si	Mn	Mo	Fe	Ni
Blank	9.8	47.0	-	0.7	-	0.3	42.2	-
(Unir)	± 0.9	± 1.7		± 0.3		± 0.1	± 1.8	
Blank	5.8	61.1	0.3	3.0	-		29.8	-
(2.5 kGy)	± 0.2	± 0.2	± 0.2	± 0.2			± 1.6	
TACT	1.9	n.d.	0.5	1.0	1.8		94.8	-
(Unir)	± 0.7		± 0.3	± 0.5	± 0.6		± 2.9	
TACT	3.0	n.d.	-	0.7	1.4		94.9	-
(2.5 kGy)	± 0.6			± 0.3	± 0.7		± 1.8	
TEA	4.1	n.d.	0.4	0.7	1.6	0.3	92.0	0.9
(Unir)	± 0.6		± 0.2	± 0.2	± 0.5	± 0.2	± 2.4	± 0.6
TEA	1.9	n.d.	-	0.7	1.4	0.2	95.8	-
(2.5 kGy)	± 0.6			± 0.2	± 0.7	± 0.1	± 1.9	

n.d. – not detected

The surface of the steel immersed in unirradiated TACT solution (Figure 3.58, middle left) appears notably clean and smooth, similar to the freshly polished state, with minimal visible corrosion or deposits. A high iron content (94.9± 2.9 at.%) and a very low carbon content (1.9 at.%), with no detectable oxygen signal is seen in the EDX spectrum (Figure 3.59, middle left). The absence of oxygen, or its presence below the EDX detection limit (typically 0.1 – 1 at.%), is remarkable, providing some evidence that TACT prevented the formation of a substantial iron oxide layer, thus maintaining the metallic character of the surface necessary for magnetic separation. Post irradiation, the surface of the steel immersed in irradiated TACT solution (Figure 3.61, middle right) remains largely intact and smooth, visually indistinguishable from the unirradiated TACT-treated surface. No visible evidence of widespread corrosion or the rough, pitted morphology seen in the irradiated blank is observed. The corresponding EDX spectrum (Figure 3.59, middle right) continues to show a high iron content (94.9 ± 2.9 at.%) and no detectable oxygen signal. A slight increase in carbon content (3.0 ± 0.6 at.%) compared to the unirradiated TACT may be due to the accumulation of TACT degradation products or more extensive organic coverage. This visual and compositional stability of the TACT-treated surface under high-dose irradiation supports the electrochemical results (Section 3.5.3.2) where TACT maintained a relatively lower corrosion rate compared to the blank under irradiation.

This also aligns with the NMR findings (Section 3.5.3.3) which demonstrated TACT's molecular stability against radiolytic degradation even after 2.5 kGy irradiation.
The unirradiated TEA-treated surface (Figure 3.59, bottom left) also appears smooth and largely free of visible corrosion, similar to the TACT-treated surface. The EDX spectrum (Figure 3.59, bottom left) shows a high iron content (92.0± 2.4 at.%) and a moderate carbon content (4.1 at.%), with no detectable oxygen signal. This confirms TEA's effective corrosion inhibition in unirradiated conditions, consistent with electrochemical measurements showing high inhibition efficiency at 5000 ppm (Section 3.4.1). After irradiation, the irradiated TEA-treated surface (Figure 3.59, bottom right) visually remains largely smooth and unaffected by irradiation, showing no signs of widespread corrosion products, similar to that of TACT. The corresponding EDX spectrum (Figure 3.59, bottom right) reveals a high iron content (95.8 ± 1.9 at.%) and, notably, no detectable oxygen signal. The carbon content (1.9± 0.6 at.%) remains stable even after irradiation.

The surface analyses strongly correlate with the observations from NMR (Section 3.5.3.3) and electrochemical studies (Section 3.5.3.2), that while the inhibitors undergo slight performance reduction in the presence of ionizing radiation, they largely maintain their ability to suppress the formation of extensive corrosion products across the steel surface. TACT, in particular, exhibited greater radiation resistance compared to TEA, due to the triazine core ring-structure even though TEA, due to its ten-fold higher concentration usage, resulted in less absolute CR after 2.5 kGy irradiation. The pH changes observed (TEA pH decrease, TACT pH increase) further highlight the distinct radiolysis mechanisms for both inhibitors, influencing the long-term stability of adsorbed films and interaction with the steel surface.

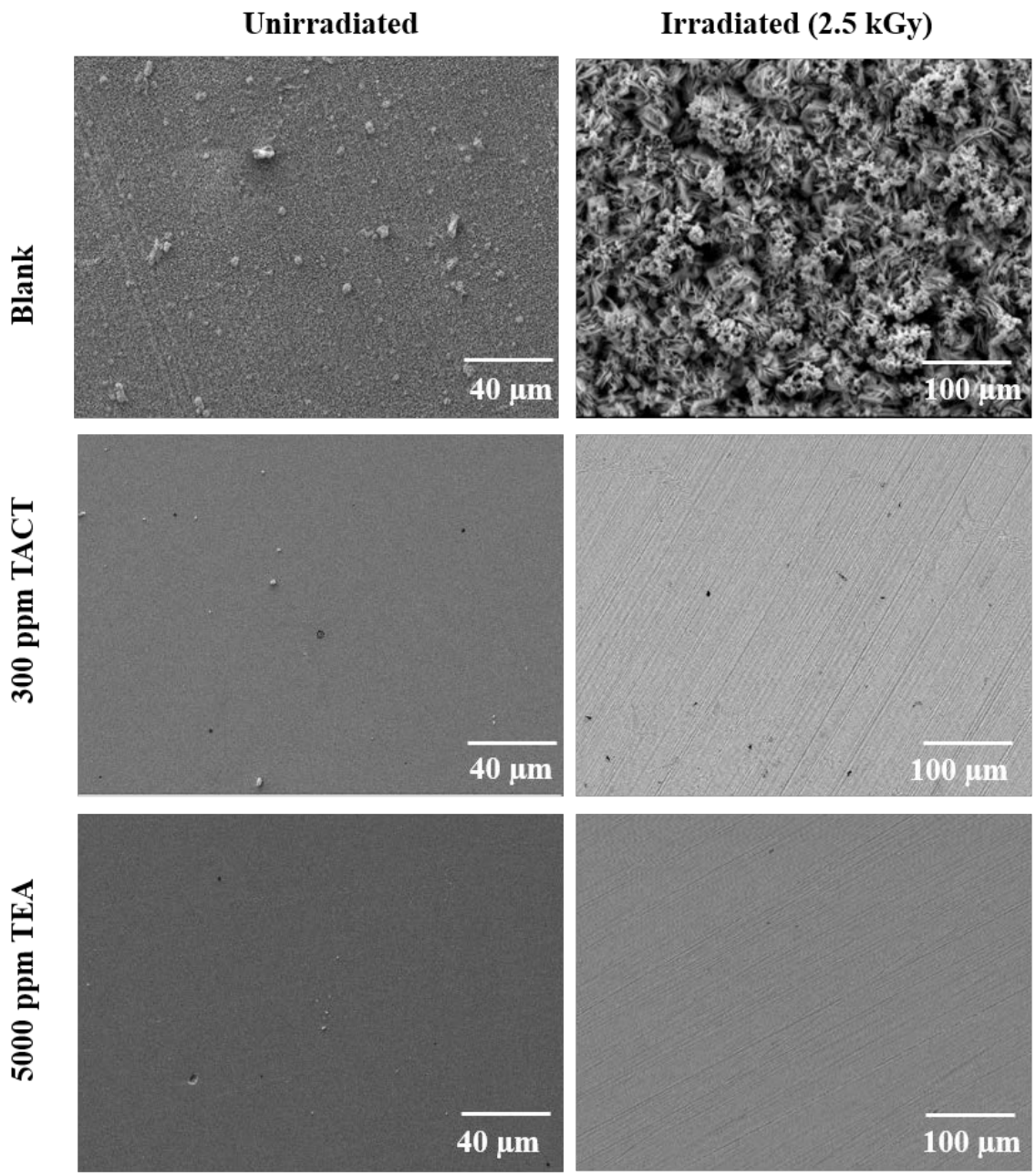

Figure 3.58: Comparison of surface morphology of 1.6310 steel immersed in unirradiated and 2.5 kGy irradiated blank (top row), 300 ppm TACT (middle row), and 5k ppm TEA (bottom row).

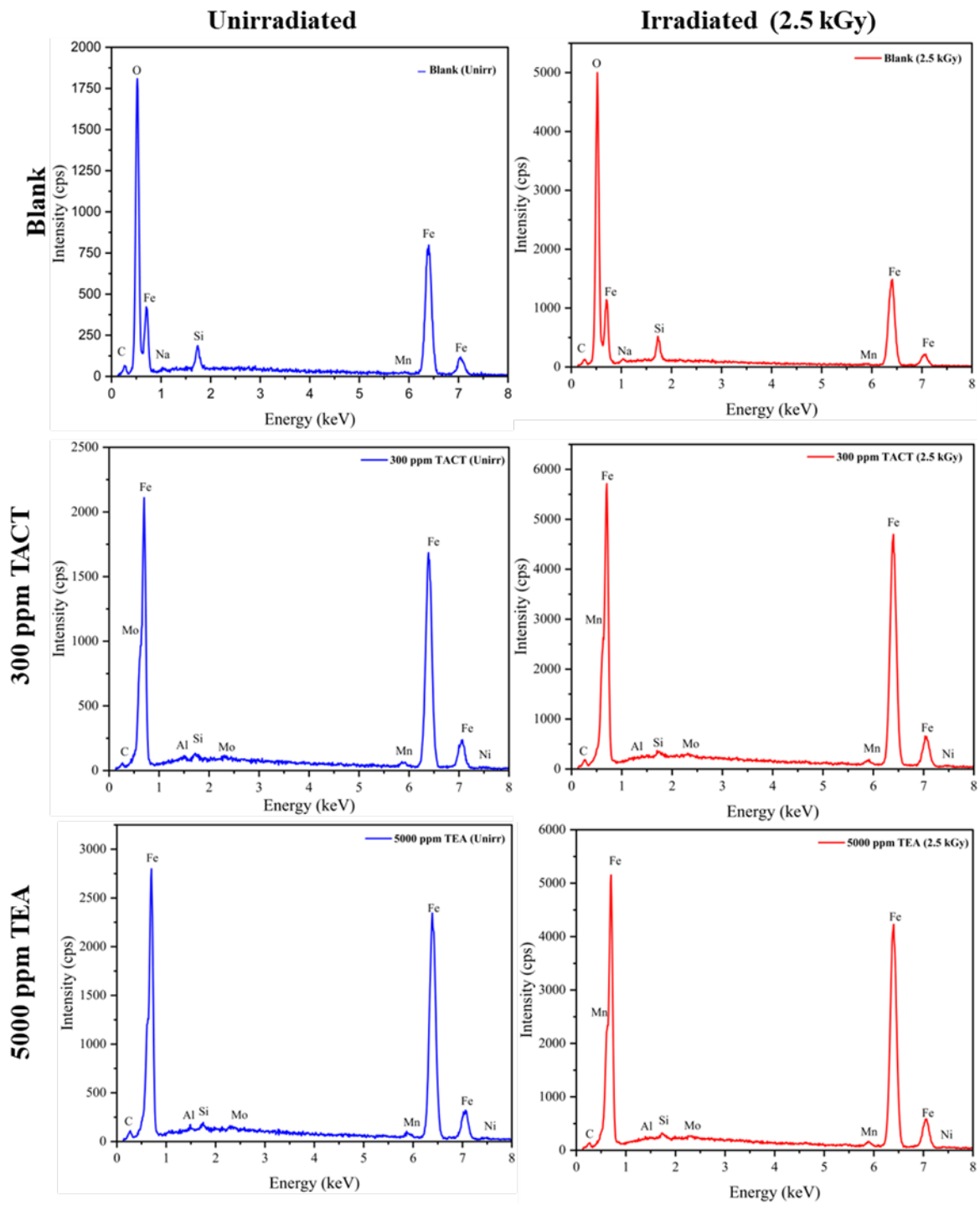

Figure 3.59: Comparison of EDX spectra of steel coupon surfaces in unirradiated (blue spectra) and 2.5 kGy irradiated blank and inhibitor solutions (red spectra). First row shows steel in blank solution, second row shows steel in 300 ppm TACT solution, and bottom row shows steel in 5000 ppm TEA solution.

CHAPTER FOUR: SUMMARY AND CONCLUSIONS

This dissertation presents a comprehensive investigation into the challenges associated with ferritic steel corrosion during and after Water Abrasive Suspension (WAS) cutting, a technique employed in nuclear decommissioning for the segmentation of reactor pressure vessels and internals. The effective management of corrosion in real dismantling scenarios is essential for efficient separation of the activated steel swarf from the abrasive particles by means of wet-sieving and magnetic filtration. Achieving efficient separation of the steel particles minimizes secondary radioactive waste volumes and enhances abrasive recyclability. The overarching goal was to identify effective corrosion inhibition strategies for Reactor Pressure Vessel (RPV) steel (1.6310) under conditions relevant to WAS cutting and subsequent separation processes, and to thoroughly understand the influence of ionizing radiation on inhibitor performance and steel corrosion. This chapter summarizes the key findings derived from the multi-technique experimental and computational approach, draws definitive conclusions in response to the stated aims, and discusses the broader implications of this research for nuclear decommissioning and future scientific endeavors.

4.1 Key Findings

4.1.1 Corrosion Inhibitor Selection and Characterization

The initial phase of this study focused on identifying and characterizing a suitable corrosion inhibitor for 1.6310 ferritic steel under conditions mimicking the WAS cutting environment.

- **Initial Screening and Optimal Concentration of C.Inh #4:** Immersion tests served as a qualitative initial screening, revealing that the commercial inhibitor formulation, C.Inh #4, significantly outperformed other tested candidates. Unlike other inhibitors, C.Inh #4 effectively prevented visible corrosion products on steel coupons after a 7-day immersion period (Section 3.1.1, Figure 3.2). Subsequent detailed electrochemical measurements (OCP, PDP, EIS) quantitatively confirmed C.Inh #4's potent inhibitory action. Potentiodynamic polarization studies (Section 3.1.2.2, Figure 3.4, Table 3.1) demonstrated that C.Inh #4 acts as a mixed-type inhibitor, effectively suppressing both anodic (metal dissolution) and cathodic (oxygen reduction) reactions. An optimal concentration of 1.5 vol.% was identified, achieving a high inhibition efficiency (IE%) of 93.8 ± 1.1 %. Electrochemical Impedance Spectroscopy (EIS) further corroborated

these findings, showing a substantial increase in charge transfer resistance (R_{ct}) from 0.004 MΩ (blank) to 0.86 ± 0.02 MΩ (at 3h) and up to 2.95 ± 0.82 MΩ after 72 hours of immersion (Section 3.1.2.3, Table 3.2), indicating the formation and continuous improvement of a robust protective film over time.

- **Performance in WAS Cutting Suspension:** Steel particles obtained from the WAS cutting experiment and left in the solution with the C.Inh #4 were reported to experience minimal surface oxidation even after 1 week. Validation experiments conducted with actual WAS cutting suspension, dosed with 1.5 vol.% C.Inh #4, confirmed its effectiveness under near-process conditions. OCP measurements showed a significant ennoblement of the potential compared to tap water, indicating reduced corrosion propensity (Section 3.2.1, Figure 3.12). PDP curves further revealed high inhibition efficiencies (e.g., 91.1 ± 0.9 % for Tapwater + Inhibitor), despite the complexity of the cutting fluid. Long-term immersion tests (up to 18 months) of 1.6310 steel coupons in the WAS cutting suspension, analyzed by SEM-EDX, revealed a remarkable absence of widespread macroscopic corrosion products (Section 3.2.2.1, Figures 3.14, 3.15), visually confirming the sustained protective action of C.Inh #4.
- **Compositional Elucidation of C.Inh #4:** To understand the mechanistic basis of C.Inh #4's performance, its chemical composition was thoroughly investigated using a combination of XPS, NMR spectroscopy (^{1}H, ^{13}C, COSY), and Mass Spectrometry (EI-MS). This multi-technique approach, complemented by direct confirmation from the manufacturer, definitively identified three major components: Triethanolamine (TEA), 2,4,6-Tri(6-aminohexanoic acid)-1,3,5 triazine (TACT), and 6-(4-Methylphenylsulfonamido) hexanoic acid (Section 3.3). The presence of sulfur in the third component led to its exclusion from further detailed study, adhering to the CHON principle for nuclear waste management.
- **Comparative Performance of Pure TEA and TACT:** Dedicated electrochemical studies on pure TEA and TACT in 0.06 mol/dm^3 $NaHCO_3$ solution provided critical insights into their individual contributions. TACT emerged as the more efficient inhibitor, achieving high inhibition efficiencies (>97% IE%) and robust passivation (e.g., $R_p \approx 220.0$ kΩ at 300 ppm) at significantly lower concentrations (100 – 300 ppm) (Section 3.4.1, Table 3.9). In contrast, TEA required a much higher critical concentration (≥3000ppm) to achieve comparable high inhibition (e.g., 99.0% IE at 5000 ppm, $R_p \approx 357.0$ kΩ) (Section 3.4.1, Table 3.10).

- **Adsorption Mechanisms and Film Characteristics:** Adsorption modeling using the Langmuir isotherm revealed that TEA primarily adsorbs via physisorption (ΔG_{ads}^{θ}= −20.4 ± 0.8 kJ/mol), consistent with its requirement for higher concentrations. TACT, conversely, utilizes a combination of physisorption and stronger chemisorption (ΔG_{ads}^{θ} = −44.5 ± 0.8 kJ/mol), explaining its remarkable efficiency at lower concentrations (Section 3.4.2). Quantitative adsorption measurements by Quartz Crystal Microbalance (QCM) and Ellipsometry further supported these findings (Section 3.4.4, Tables 3.13, 3.14). TACT formed thicker (up to 5.5 ± 0.2 nm by QCM) and more stable adsorbed layers that were less susceptible to desorption under flow, indicative of its robust binding. TEA formed thinner films (around 1.3-2.0 ± 0.2 nm) that were reversible and prone to desorption under increased flow rates.

4.1.2 Effects of Ionizing Radiation on Inhibitor Performance and Steel Corrosion

A major focus of this research was to quantify and understand the impact of ionizing radiation on the selected inhibitors and steel corrosion.

- **Radiation Field Characterization:** Monte Carlo radiation transport simulations using PENELOPE provided estimations of dose rates from a reference radioactive steel-abrasive mixture (SAM) in water, indicating a non-uniform dose distribution with the highest dose at the SAM-water interface (Section 3.5.1, Figure 3.55). Experimental dosimetry using Thermoluminescent Dosimeters (TLDs) and Fricke dosimetry validated these simulations and provided absorbed dose rates for the irradiation experiments (Section 3.5.2). TLD results unequivocally demonstrated position-dependent dose distributions within the experimental setups, confirming the need for careful dosimetric characterization.
- **Impact on Solution Chemistry (pH):** Ionizing radiation induced changes in the pH of the inhibitor solutions (Section 3.5.3.1, Table 3.16). TEA solutions showed a dose-dependent decrease in pH, likely due to the generation of H^+ ions from water radiolysis and the possible formation of organic acids from TEA breakdown. On the other hand, TACT solutions exhibited near-constant pH values with increasing dose.
- **Electrochemical Performance under Irradiation:** Ex-situ electrochemical measurements with irradiated inhibitor solutions revealed a dose-dependent decrease in the corrosion inhibition efficiency for both TEA and TACT (Section 3.5.3.2, Figures 3.52, 3.53, Table 3.17). For TEA, the corrosion rate increased by a factor of 10.6 at 2.5

kGy compared to its unirradiated state. For TACT, the increase was less pronounced, by a factor of 4.2 at 2.5 kGy. Therefore, the effect of ionizing radiation had more impact on the inhibition property of TEA than TACT.

- **Molecular Degradation (NMR):** ^{1}H NMR spectroscopy provided molecular-level evidence for radiolytic degradation (Section 3.5.3.3, Figures 3.54, 3.55). TEA exhibited more pronounced changes, including significant peak broadening and the appearance of new peaks with relatively smaller intensities, indicating molecular fragmentation (e.g., C-N and C-O bond cleavage, hydrogen abstraction, leading to smaller amines, aldehydes, and carboxylic acids). TACT, while also showing some broadening and minor new signals at high doses, demonstrated greater molecular integrity, with its core triazine ring remaining largely stable. This difference in molecular stability directly correlates with their relative electrochemical performance under irradiation.
- **Surface Composition and Morphology under Irradiation:** XPS and SEM-EDX analyses of steel coupons irradiated in the inhibitor solutions provided surface-specific insights (Section 3.5.3.4, 3.5.3.5, Figures 3.56, 3.57, 3.58, 3.59, Table 3.19). The irradiated blank sample showed severe oxidation and extensive corrosion products. In contrast, both TACT and TEA effectively prevented general macroscopic oxidation of the steel surfaces even after 2.5 kGy irradiation, largely preserving the metallic iron content (from EDX). XPS, with its higher surface sensitivity, revealed a dose-dependent increase in Fe(III) on both inhibited surfaces, indicating some radiation-induced oxidation, but the persistent presence of nitrogen (from the inhibitors) confirmed that protective layers remained. TACT-treated surfaces showed no detectable oxygen by EDX even after irradiation, highlighting its remarkable ability to maintain the metallic state.
- **Role of HCO_3^- Ions:** The presence of HCO_3^- ions in irradiated solutions had a complex and differing impact. For TEA, HCO_3^- ions appeared to have a synergistic effect, leading to a slight improvement in corrosion parameters at 2.5 kGy (Section 3.5.3.2, Table 3.17). For TACT, HCO_3^- did not have a significant effect on the corrosion parameters.
- **Microbiologically Influenced Corrosion (MIC):** Long-term immersion tests (18 months) of 1.6310 steel coupons in the WAS cutting suspension revealed the suspected presence of microorganisms and biofilm formation on the steel surface (Section 3.2.2.3, Figures 3.22, 3.23). This could attest to the biodegradable nature of C.Inh #4. While the inhibitor provided effective protection against general corrosion, the potential for

localized MIC due to possible biofilm formation highlights a long-term challenge that might require further consideration in real-world applications.

4.2 Conclusions

This research successfully addressed its dual objectives, providing critical insights into managing ferritic steel corrosion in WAS cutting environments relevant to nuclear decommissioning:

1. **Effective Inhibitor Identification:** C.Inh #4, a commercial formulation containing TEA and TACT, was definitively identified as a highly effective mixed-type corrosion inhibitor for 1.6310 ferritic steel in near-neutral aqueous media. It forms a robust protective film that significantly reduces corrosion rates and prevents macroscopic oxidation.
2. **TACT Inhibitor:** Comparative studies revealed that TACT is significantly more efficient than TEA, achieving comparable high inhibition efficiencies at concentrations approximately 10 to 27 times lower. This superior performance is attributed to TACT's stronger adsorption mechanism, combining physisorption and chemisorption, leading to the formation of thicker and more stable protective layers.
3. **Impact of Ionizing Radiation:** Ionizing radiation consistently reduced the inhibition efficiency of both TEA and TACT. However, TACT demonstrated greater molecular stability and a smaller relative increase in corrosion rate under irradiation compared to TEA. Despite this, TEA, at its higher effective concentration, maintained a lower absolute corrosion rate than TACT at the highest radiation doses, potentially as a result of the higher initial concentration and nature of its degradation products.
4. **Preservation of Steel Integrity:** Crucially, both inhibitors effectively prevented widespread macroscopic oxidation of the steel surface even after exposure to high radiation doses (up to 2.5 kGy), thus preserving the metallic integrity of the steel. This is vital for the efficiency of the downstream magnetic separation process proposed for secondary radioactive waste management of WAS suspensions.

4.3 Implications and Future Work

The findings of this dissertation have significant implications for optimizing WAS cutting procedures, enhancing steel-abrasive separation processes, and ensuring the long-term integrity of materials during nuclear decommissioning:

- **Guide for Inhibitor Selection:** The detailed mechanistic insights from this research provide a clear guide for the selection and design of effective inhibitors for WAS cutting of RPVs. An ideal inhibitor for this application should meet the following criteria:
  - It must exhibit a high binding affinity to the steel surface to resist removal by hydrodynamic shear forces in flow systems. This characteristic was demonstrated by TACT's strong chemisorption mechanism, which proved advantageous over TEA's weaker physisorption.
  - It should possess functional groups and/or long hydrocarbon chains to form a densely packed, robust, and water-repellent film that acts as an effective physical barrier to corrosive species.
  - It must have sufficient radiolytic stability to maintain its molecular structure and functional efficacy under the influence of ionizing radiation. This quality was shown to be superior in TACT compared to TEA.

- **Optimized Inhibition Strategy:** The identification of TEA and TACT as key active components provides a basis for developing tailored inhibitor formulations that combine their strengths, potentially leading to even more efficient and cost-effective solutions for WAS cutting.
- **Radioactive Waste Minimization:** The demonstrated ability of the inhibitors to prevent significant corrosion of steel particles, even under irradiation, directly contributes to minimizing the volume of radioactive secondary waste by preserving the magnetic properties of the steel for efficient separation.
- **Radiation Effects Mitigation:** The detailed understanding of radiolytic degradation pathways and their impact on inhibition efficiency provides a foundation for designing more radiation-resistant inhibitors or for optimizing inhibitor concentrations to account for radiation-induced losses in performance.

Further research could focus on:

- **Detailed Radiolytic Product Identification:** Employing advanced analytical techniques (e.g., LC-MS/MS, GC-MS) to definitively identify and quantify the specific degradation products of TEA and TACT under various irradiation conditions, including the presence of hydrogen-carbonate ions. This would allow for a more precise

understanding of their G-values and their individual contributions to corrosion or inhibition.

- **Mechanism of hydrogen-carbonate Interaction:** A deeper investigation into the complex and differing interactions of hydrogen-carbonate ions with irradiated TEA and TACT is warranted, potentially using in-situ spectroelectrochemical methods to probe surface film changes.
- **Synergistic Effects:** Further studies on the synergistic effects between TEA and TACT within the C.Inh #4 formulation, and with the phosphonate additive, could lead to optimized multi-component inhibitor blends.

This research has successfully addressed the dual objectives of optimizing corrosion inhibition during WAS cutting of RPV ferritic steel and understanding the influence of ionizing radiation on ferritic steel corrosion inhibition. The comprehensive experimental and analytical approach has led to the identification of a robust inhibitor formulation (C.Inh #4), which combines the benefits of TEA and TACT. The inhibitors not only form stable, protective films on the steel surface during the mechanical cutting process but also demonstrate resilience to the additional challenges posed by ionizing radiation. However, the commercial inhibitor formulation could be adapted to the needs in nuclear decommissioning by replacing the sulphur containing component.

REFERENCES

1. *A Taxonomy for the Decommissioning of Nuclear Facilities*. (International Atomic Energy Agency, Vienna, 2023).

2. Sterne, R. H. & Steele, L. E. Steels for commercial nuclear power reactor pressure vessels. *Nucl. Eng. Des.* **10**, 259–307 (1969).

3. Phythian, W. J. & English, C. A. Microstructural evolution in reactor pressure vessel steels. *J. Nucl. Mater.* **205**, 162–177 (1993).

4. Davies, L. M. A comparison of Western and Eastern nuclear reactor pressure vessel steels. *Int. J. Press. Vessels Pip.* **76**, 163–208 (1999).

5. Steele, L. Neutron irradiation embrittlement of reactor pressure-vessel steels. *At. Energy Rev.* **7**, 3–133 (1969).

6. Robertson, D. E., Thomas, C. W., Wynhoff, N. L. & Hetzer, D. C. Characterization of long-lived activation products in spent fuel assembly hardware and reactor pressure vessel steel. *Nucl. Eng. Des.* **118**, 463–486 (1990).

7. *Nuclear Power Reactors in the World*. Reference Data Series No. 2 (International Atomic Energy Agency, Vienna, 2024). ISBN 978-92-0-122224-4.

8. Babilas, E. & Brendebach, B. Selection and evaluation of decontamination and dismantling techniques for decommissioning of large NPPs components. *Prog. Nucl. Energy* **84**, 108–115 (2015).

9. *Decommissioning: Reactor Pressure Vessel Internals Segmentation.* (EPRI, Palo Alto, CA: 1003029, 2001).

10. Henderson, R. & Eickelpasch, L. Cutting Reactor Pressure Vessels and their Internals - Trends on Selected Technologies - 10247. in *36th Annual Radioactive Waste Management Symposium 2010 (WM 2010)* (WM Symposia, Arizona, 2010).

11. Maggini, A., Ciolini, R., Pistelli, S. & Garneri, E. Strategies and dismantling solutions for RPV internals of Trino NPP. *Prog. Nucl. Energy* **93**, 67–75 (2016).

12. Boing, L. E., Henley, D. R., Manion, W. J. & Gordon, J. W. *An Evaluation of Alternative Reactor Vessel Cutting Technologies for the Experimental Boiling Water Reactor at Argonne National Laboratory*. (1989) doi:10.2172/6346325.

13. Jeong, K., Choi, B., Moon, J., Hyun, D., Lee, J., Kim, I., Kim, G., Jeong, S., Lee, J., Song, H., & Son, B. An evaluation on the cutting technologies for decommissioning of the tube bundles in the RPV of NPPs. *Ann. Nucl. Energy* **83**, 342–345 (2015).

14. Bonavigo, L., De Salve, M., Zucchetti, M. & Annunziata, D. Radioactivity release and dust production during the cutting of the primary circuit of a nuclear power plant: The case of E. Fermi NPP. *Prog. Nucl. Energy* **52**, 359–366 (2010).

15. *Methods for the Minimization of Radioactive Waste from Decontamination and Decommissioning of Nuclear Facilities*. (International Atomic Energy Agency, Vienna, 2001).

16. Louis, H., Pude, F., Von Rad, Ch. & Versemann, R. Abrasive Water Suspension Jet Technology Fundamentals, Application and Developments. *Weld. World* **51**, 11–16 (2007).

17. Lee, G.R., Lim, B.J., Cho, D.W. & Park, C.D. Selection methodology of the optimal cutting technology for dismantling of components in nuclear power plants. *Ann. Nucl. Energy* **166**, 108808 (2022).

18. Troise, M., Bleynat, S., Dulla, S., Mauro, S., Pancotti, F. & Zanino, R. Development of a methodology to select suitable cutting techniques for the decommissioning of nuclear power plants considering site-specific requirements. *Proc. Int. Conf. Nucl. Eng. ICONE* **2023.3**, 1971 (2023).

19. Hyun, D. J. *et al.* Evaluation methodology of remote dismantling equipment for Reactor Pressure Vessel in decommissioning project. *J. Nucl. Fuel Cycle Waste Technol.* **1**, 83–92 (2013).

20. Versemann, R. Decommissioning nuclear plants: experiences in Germany. *Proc. Inst. Civ. Eng. - Energy* **161**, 101–113 (2008).

21. Steiner, H., Eickelpasch, N. & Tegethoff, H. Experience with the dismantling of three secondary steam generators in unit A in Gundremmingen by the 'ice-sawing' technique. *Nucl. Eng. Des.* **170**, 165–173 (1997).

22. Eickelpasch, N., Kalwa, H., Steiner, H. & Priesmeyer, U. The application of mechanical and thermal cutting tools for the dismantling of activated internals of the reactor pressure vessels in the Versuchsatomkraftwerk, Kahl and the Gundremmingen Unit A. *Nucl. Eng. Des.* **170**, 175–182 (1997).

23. Duspara, M., Paltinus, T., Maric´, D., Samardzic´, I., Ivandic´, Z. & Stoic´, A. New Approach of Recycling of Abrasives for Water Jet Cutting. in *Advances in Manufacturing Engineering and Materials* (eds. Hloch, S., Klichová, D., Krolczyk, G. M., Chattopadhyaya, S. & Ruppenthalová, L.) 29–35 (Springer International Publishing, Cham, 2019). doi:10.1007/978-3-319-99353-9_4.

24. Perianu, I. A., Cojocaru, R., Binchiciu, E.F. & Mnerie, G.V. Innovative solutions for waste removal (used abrasive) resulted from Water Jet Cutting process. *Eng. Innov.* **2**, 49–57 (2022).

25. Gentes, S., Müller, H.S., Kraps, U., Brandauer, M., Stiefel, S., Eckhardt, J.D., Haist, M., Krauß, C.O., Arnold, U. & Schneider, D. Abschlussbericht-Neuartige Entsorgungswege für Abrasivmittel aus der Wasserstrahl-Schneidtechnik (NENAWAS). (BMBF Karlsr. 2015).

26. Becker, F., Brandauer, M., Geckeis, H., Gentes, S., Heneka, A., Krauß,C.O., Plaschke, M., Schild, D. & Tobie, W. *Abschlussbericht über das Forschungsvorhaben 'MaSK'*. https://www.tib.eu/suchen/id/TIBKAT:1690836210/ (2019) doi:10.2314/KXP:1690836210.

27. Heneka, A. Abrasivaufbereitung aus dem Wasser-Abrasiv-Suspensionsschneideverfahren mittels Nasssiebung und Magnetseparation. (Karlsruher Institut für Technologie (KIT), Preprint at https://doi.org/10.5445/IR/1000169584 (2024).

28. Krauß, C. O., Becker, F., Chaudhry, M., Geckeis, H., Gentes, S., Heneka, A., Plaschke, M. & Schild, D. Separation System for the Treatment of Secondary Waste from the Waterjet-Abrasive-Suspension-Cutting. (2021) doi:10.5445/IR/1000139673.

29. Heneka, A., Krauß, C.O., Gentes, S., Becker, F., Geckeis, H., Lützenkirchen, J., Plaschke, M., Schild, D. & Tobie, W. A new technical approach for the minimization of secondary waste produced by water abrasive suspension cutting during disassembling of nuclear facilities. *Atw* **66**, 34–40 (2021).

30. Brandauer, M. Experimentelle Untersuchungen zur Separation von Korngemischen in einem Stabmagnetfilter. Preprint at https://doi.org/10.18419/OPUS-9719 (2017).

31. Krauß, C.O. Experimentelle und numerische Untersuchungen eines Magnetfiltersystems zur Minimierung von Sekundärabfall beim Rückbau kerntechnischer Anlagen. (2021) doi:10.5445/IR/1000130768.

32. ConSus, A. G. Technical Details: waterjet cutting. https://www.consus-gmbh.com/homepage.html#technical-details (2023).

Heneka, A. Abrasivaufbereitung aus dem Wasser-Abrasiv-Suspensionsschneideverfahren mittels Nasssiebung und Magnetseparation.

33. Orano Decommissioning. https://www.orano.group/en/unpacking-nuclear/dismantling-orano-s-global-strengths (2022).

34. EnBW. https://www.enbw.com/unternehmen/themen/rueckbau-kernkraftwerke/entsorgung.html (2022).

35. Misawa, T., Hashimoto, K. & Shimodaira, S. The mechanism of formation of iron oxide and oxyhydroxides in aqueous solutions at room temperature. *Corros. Sci.* **14**, 131–149 (1974).

36. Mizoguchi, T., Ishii, Y., Okada, T., Kimura, M. & Kihira, H. Magnetic property-based characterization of rust on weathering steels. *Corros. Sci.* **47**, 2477–2491 (2005).

37. Ouadah, M., Touhami, O., Ibtiouen, R., Khorchef, M. & Allou, D. Corrosion effects on the magnetic behavior of magnetic circuit of an induction machine. *Prog. Electromagn. Res. M* **68**, 79–87 (2018).

38. Singh, V., Lloyd, G. M. & Wang, M. L. Effects of temperature and corrosion thickness and composition on magnetic measurements of structural steel wires. *NDT E Int.* **37**, 525–538 (2004).

39. Sitek, J., Sedlačková, K. & Seberíni, M. Corrosion of Fe-Based Nanocrystalline Alloys. in *Material Research in Atomic Scale by Mössbauer Spectroscopy* (eds. Mashlan, M.,

Miglierini, M. & Schaaf, P.) 159–166 (Springer Netherlands, Dordrecht, 2003). doi:10.1007/978-94-010-0151-9_17.

40. Pardo, A., Otero, E., Merino, M.C., Lopez, M.D., Vazquez, M. & Agudo, P. The influence of Cr addition on the corrosion resistance of Fe73.5Si13.5B9Nb3Cu1 metallic glass in marine environments. *Corros. Sci.* **44**, 1193–1211 (2002).

41. Souza, C. A. C., De Oliviera, M.F., May, J.E., Botta, F.W.J., Mariano, N.A., Kuri, S.E. & Kiminami, C.S. Corrosion resistance of amorphous and nanocrystalline Fe–M–B (Mo,Zr, Nb) alloys. *J. Non-Cryst. Solids* **273**, 282–288 (2000).

42. Sipilä, K., Ferreirós, P., Ikäläinen, T., Mikkelson, A., Betova, I. & Bojinov, M. Decomposition products of oxygen scavengers and their effect on corrosion of steam generator materials – I. Diethyl-hydroxylamine and carbohydrazide. *Corros. Sci.* **240**, 112476 (2024).

43. İz, S. & Köylüoğlu, Ö. S. Investigation of the economic and sustainability aspects of cathodic protection method for corrosion prevention in marine structures. *J. Adhes. Sci. Technol.* **37**, 2861–2870 (2023).

44. Kumar, P.S., Mohan, D., Chandran, S., Rajesh, P., Rangarajan, S. & Velmurugan, S. Evaluation of nitrogen containing reducing agents for the corrosion control of materials relevant to nuclear reactors. *Mater. Chem. Phys.* **187**, 18–27 (2017).

45. Elliot, A. J., Chenier, M. P. & Ouellette, D. C. Radiolysis studies on the corrosion inhibitors 1 -hexyn-3-ol, cinnamonitrile, and 1,3-diethyl-2-thiourea. *Can. J. Chem.* **73**, 2137–2142 (1995).

46. Boxall, C., Bromley, M., Higgins, J., Berhane, G. & Wilbraham, R. Assessment of the corrosion vulnerability of common plant materials in the presence of key process streams. (2021).

47. Geckeis, H., Altmaier, M., & Fanghänel, S. *Annual Report 2014 / Institute for Nuclear Waste Disposal. (KIT Scientific Reports ; 7709)*. doi:10.5445/KSP/1000049786.

https://publikationen.bibliothek.kit.edu/1000049786 (2015)

48. Bilanin, W. *et al.* LWR water chemistry guidelines. *Prog. Nucl. Energy* **20**, 1–42 (1987).

49. Ateya, B. G. & Pickering, H. W. The distribution of anodic and cathodic reaction sites during environmentally assisted cracking. *Corros. Sci.* **37**, 1443–1453 (1995).

50. Bockris, J. O., Conway, B. E. & White, R. E. *Modern Aspects of Electrochemistry*. vol. 1 (Plenum Press, New York, 1985).

51. *Characterization of Corrosion Products on Steel Surfaces*. (Springer Berlin Heidelberg, 2006). doi:10.1007/978-3-540-35178-8.

52. Pourbaix, M. Atlas of Electrochemical Equilibria in Aqueous Solutions. (National Association of Corrosion Engineers, Houston, TX, 1974).

53. Engell, H. J. Stability and breakdown phenomena of passivating films. *Eletrochimic Acta* **22**, 987–993 (1977).

54. Qiu, J., Zhu, Y., Xu, Y., Li, Y., Mao, F., Wu, A. & Macdonald, D.D. Effect of chloride on the pitting corrosion of carbon steel in alkaline solutions. *J. Electrochem. Soc.* **169**, 031501 (2022).

55. Cheng, Y. F., Wilmott, M. & Luo, J. L. The role of chloride ions in pitting of carbon steel studied by the statistical analysis of electrochemical noise. *Appl. Surf. Sci.* **152**, 161–168 (1999).

56. Cottis, R. A. *Shreir's Corrosion*. (Elsevier Science, Oxford, 2010).

57. Faulkner, L. L. & Bard, A. J. *Electrochemical Methods and Applications*. (Wiley, New York, 2001).

58. Bockris, J. O. & Reddy, A. K. N. *Volume 2 Modern Electrochemistry*. (Springer US, Boston, MA, 1973). doi:10.1007/978-1-4613-4560-2.

59. Bockris, J. O., Drazic, D. & Despic, A. R. The electrode kinetics of the deposition and dissolution of iron. *Electrochimica Acta* **4**, 325–361 (1961).

60. Guidelli, R., Compton, R.G., Feliu, J.M., Gileadi, E., Lipkowski, J., Schmickler, W. & Trasatti, S. Defining the transfer coefficient in electrochemistry: An assessment (IUPAC Technical Report). *Pure Appl. Chem.* **86**, 245–258 (2014).

61. Ijsseling, F. P. Application of electrochemical methods of corrosion rate determination to systems involving corrosion product layers: Part 1: Linear polarization resistance measurement as an example of a simple method that can be performed with commercially available instruments. *Br. Corros. J.* **21**, 95–101 (1986).

62. Stern, M. & Geary, A. L. Electrochemical Polarization: I . A Theoretical Analysis of the Shape of Polarization Curves. *J. Electrochem. Soc.* **104**, 56 (1957).

63. Street, S.R., Xu, W., Amri, M., Guo, L., Glanvill, S.J.M., Quinn, P.D., Mosselmans, J.F.W., Vila-Comamala, J., Rau, C., Rayment, T. & Davenport, A.J. The Effect of Nitrate on Salt Layers in Pitting Corrosion of 304L Stainless Steel. *J. Electrochem. Soc.* **162**, C457–C464 (2015).

64. Agrisuelas, J., García-Jareño, J.J., Giménez-Romero, D., Gregori, J., Keddam, M. & Vicente, F. A Salt Layer Model for the Active Anodic Dissolution to Passive Transition of Nickel in Presence of Chloride. *ECS Trans.* **16**, 49–56 (2009).

65. Perez, N. *Electrochemistry and Corrosion Science*. (Springer, Cham, 2016). doi:10.1007/978-3-319-24847-9.

66. Bockris, J. O. & Reddy, A. K. N. Electrodics: More Fundamentals. in *Volume 2 Modern Electrochemistry* 991–1139 (Springer US, Boston, MA, 1970). doi:10.1007/978-1-4613-4560-2_3.

67. Kutznetsov, Yu. I. Organic corrosion inhibitors: where are we now? A review. Part II. Passivation and the role of chemical structure of carboxylates. *Int J Corros Scale Inhib* **5**, 282–318 (2016).

68. Hefter, G. T., North, N. A. & Tan, S. H. Organic corrosion inhibitors in neutral solutions; Part 1 - Inhibition of steel, copper, and aluminum by straight chain carboxylates. *Corrosion* **53**, (1997).

69. Verma, C., Quraishi, M. A., Chaudhery Mustansar, H. & Ebenso, E. E. *Organic Corrosion Inhibitors: Synthesis, Characterization, Mechanism, and Applications*. (John Wiley & Sons, Inc, New Jersey, 2022).

70. Mann, C. A., Lauer, B. E. & Hultin, C. T. Organic Inhibitors of Corrosion, Aliphatic Amines. *Ind. Eng. Chem.* **28**, 159–163 (1936).

71. Hackerman, N., Hurd, R. M. & Annand, R. R. Some structural effects of organic N-containing compounds on corrosion inhibition. *CORROSION* **18**, 37–42 (1962).

72. Hackerman, N. & Schmidt, H. R. The role of adsorption from solution in corrosion inhibitor action. *CORROSION* **5**, 237–242 (1949).

73. Donahue, F. M. & Nobe, K. Theory of organic corrosion inhibitors: Adsorption and linear free energy relationships. *J. Electrochem. Soc.* **112**, 886–891 (1965).

74. Quraishi, M. A., Chauhan, D. S. & Saji, V. S. Heterocyclic biomolecules as green corrosion inhibitors. *J. Mol. Liq.* **341**, 117265 (2021).

75. Mansfeld, F., Kendig, M. W. & Lorenz, W. J. Corrosion inhibition in neutral, aerated media. *J. Electrochem. Soc.* **132**, 290–296 (1985).

76. Ramesh, S. & Rajeswari, S. Corrosion inhibition of mild steel in neutral aqueous solution by new triazole derivatives. *Electrochimica Acta* **49**, 811–820 (2004).

77. Sehmi, A., Ouici, H.B., Guendouzi, A., Ferhat, M., Benali, O. & Boudjellal, F. Corrosion inhibition of mild steel by newly synthesized pyrazole carboxamide derivatives in HCl acid medium: Experimental and theoretical Studies. *J. Electrochem. Soc.* **167**, 155508 (2020).

78. Kokalj, A. Formation and structure of inhibitive molecular film of imidazole on iron surface. *Corros. Sci.* **68**, 195–203 (2013).

79. Musa, A. Y., Kadhum, A. A. H., Mohamad, A. B. & Takriff, M. S. Experimental and theoretical study on the inhibition performance of triazole compounds for mild steel corrosion. *Corros. Sci.* **52**, 3331–3340 (2010).

80. Zeng, Y., Kang, L., Wu, Y., Wan, S., Liao, B., Li, N. & Guo, X. Melamine modified carbon dots as high effective corrosion inhibitor for Q235 carbon steel in neutral 3.5 wt% NaCl solution. *J. Mol. Liq.* **349**, 118108 (2022).

81. Kim, K. T., Chang, H. Y., Lim, B. T., Park, H. B. & Kim, Y. S. New mechanism on synergistic effect of nitrite and triethanolamine addition on the corrosion of ductile cast iron. *Adv. Mater. Sci. Eng.* **vol.2016**, 14pages (2016).

82. El Ibrahimi, B., Jmiai, A., Bazzi, L. & El Issami, S. Amino acids and their derivatives as corrosion inhibitors for metals and alloys. *Arab. J. Chem.* **13**, 740–771 (2020).

83. Wang, X., Xu, W.L., Li, Y.Y., Jiang, Z.N., Zeng, X.Q. & Zhang, G.A. In-depth unveiling the interfacial adsorption mechanism of triazine derivatives as corrosion inhibitors for carbon steel in carbon dioxide saturated oilfield produced water. *J. Colloid Interface Sci.* **639**, 107–123 (2023).

84. Yoo, S.H., Kim, Y.W., Kim, N.K. & Kim, J.S. Effects of the chain length of tris(carboxyalkylamino)triazine on corrosion inhibition properties. *Korean Chem. Soc.* **36**, 346–355 (2015).

85. Kuznetsov, Y. I. *Organic Inhibitors of Corrosion of Metals*. (Springer Science & Business Media, 2013).

86. Hackerman, N., Snavely, E. S. & Payne, J. S. Effects of anions on corrosion inhibition by organic compounds. *J. Electrochem. Soc.* **113**, 677 (1966).

87. Raja, P. B. & Sethuraman, M. G. Natural products as corrosion inhibitor for metals in corrosive media — A review. *Mater. Lett.* **62**, 113–116 (2008).

88. Kokalj, A. Corrosion inhibitors: physisorbed or chemisorbed? *Corros. Sci.* **196**, 109939 (2022).

89. Fawzy, A., Abdallah, M., Zaafarany, I. A., Ahmed, S. A. & Althagafi, I. I. Thermodynamic, kinetic and mechanistic approach to the corrosion inhibition of carbon steel by new synthesized amino acids-based surfactants as green inhibitors in neutral and alkaline aqueous media. *J. Mol. Liq.* **265**, 276–291 (2018).

90. Ramaganthan, B. *et al.* Synthesized photo-cross-linking chalcones as novel corrosion inhibitors for mild steel in acidic medium: experimental, quantum chemical and Monte Carlo simulation studies. *RSC Adv.* **5**, 76675–76688 (2015).

91. Wood, M.H., Welbourn, R.J.L., Charlton, T., Zarbakhsh, A., Casford, M.T. & Clarke, S.M. Hexadecylamine Adsorption at the iron oxide–oil interface. *Langmuir* **29**, 13735–13742 (2013).

92. Akrout, H., Maximovitch, S., Bousselmi, L., Triki, E. & Dalard, F. Evaluation of corrosion non toxic inhibitor adsorption for steel in near neutral solution: L (+) ascorbic acid. *Mater. Corros.* **58**, (2007).

93. Otmačić, H. & Stupnišek-Lisac, E. Copper corrosion inhibitors in near neutral media. *Electrochimica Acta* **48**, 985–991 (2003).

94. Khamis, E. The Effect of temperature on the acidic dissolution of steel in the presence of inhibitors. *CORROSION* **46**, 476–484 (1990).

95. Langmuir, I. The constitution and fundamental properties of solids and liquids. Part I: solids. *J. Am. Chem. Soc.* **38**, 2221–2295 (1916).

96. Latour, R. A. The langmuir isotherm: A commonly applied but misleading approach for the analysis of protein adsorption behavior. *J. Biomed. Mater. Res. A* **103**, 949–958 (2015).

97. Zhu, Y., Free, M. L., Woollam, R. & Durnie, W. A review of surfactants as corrosion inhibitors and associated modeling. *Prog. Mater. Sci.* **90**, 159–223 (2017).

98. Collinson, E. & Swallow, A. J. The radiation chemistry of organic substances. *Chem. Rev.* **56**, 471–568 (1956).

99. Whillock, G. O. H. Corrosion in Radiolysis Induced Environments. in *Shreir's Corrosion* 1330–1339 (Elsevier, 2010). doi:10.1016/B978-044452787-5.00067-6.

100. Prevost-Bernas, A., Chapiro, A., Cousin, C., Landler, Y. & Magat, M. The radiolysis of some organic liquids. *Discuss. Faraday Soc.* **12**, 98–109 (1952).

101. Sellers, R. M. The radiation chemistry of nuclear reactor decontaminating reagents. *Radiat. Phys. Chem. 1977* **21**, 295–305 (1983).

102. Mincher, B. J., Modolo, G. & Mezyk, S. P. Review article: The effects of radiation chemistry on solvent extraction: 1. Conditions in acidic solution and a review of TBP radiolysis. *Solvent Extr. Ion Exch.* **27**, 1–25 (2009).

103. Spinks, J. W. & Woods, R. J. An Introduction to Radiation Chemistry. (John Wiley & Sons Inc., Hoboken, NJ USA 1990).

104. Dey, G.R., Naik, D.B., Kishore, K., Vinayakumar, C.K., Yuvaraju, B., Ventakeswaran, G. & Moorthy, P.N. Correlation between corrosion inhibition and radiation chemical properties of some organic corrosion inhibitors. *Radiat Phys Chem* **Vol. 51**, 171–174 (1998).

105. Migahed, M. A., Aly, R. O. & Al-Sabagh, A. M. Impact of gamma-ray-pre-irradiation on the efficiency of corrosion inhibition of some novel polymeric surfactants. *Corros. Sci.* **46**, 2503–2516 (2004).

106. Glass, R. S., Overturf, G. E., Van Konynenburg, R. A. & McCright, R. D. Gamma radiation effects on corrosion—I. Electrochemical mechanisms for the aqueous corrosion processes of austenitic stainless steels relevant to nuclear waste disposal in tuff. *Corros. Sci.* **26**, 577–590 (1986).

107. Buxton, G. V., Greenstock, C. L., Helman, W. P. & Ross, A. B. Critical Review of rate constants for reactions of hydrated electrons, hydrogen atoms and hydroxyl radicals (·OH/·O− in Aqueous Solution. *J. Phys. Chem. Ref. Data* **17**, 513–886 (1988).

108. Component Support Structures with Non-Integral Connections; Part 1: Component Support Structures with Non-Integral Connections for Components of the Primary Coolant Circuit of Light Water Reactors. (KTA 3205.1 (2018-10), KTA-Geschaeftsstelle, Salzgitter, Germany)

109. Sarkar, A., Kumawat, B. K. & Chakravartty, J. K. Ratchetting behavior of 20MnMoNi55 reactor pressure vessel steel. *J. Nucl. Mater.* **467**, 500–504 (2015).

110. ASTM Standard Practice for Preparing, Cleaning, and Evaluating Corrosion Test Specimens. (G01 Committee, ASTM International, West Conshohocken, PA: G1-90(1999) E1) doi:10.1520/G0001-90R99E01.

111. *Technical Data & Physical Characteristics for Barton Garnet Abrasives*. www.barton.com.

112. Taylor, R.J., May, I., Wallwork, A.L., Denniss, I.S., Hill, N.J., Galkin, B.Ya., Zilberman, B.Ya. & Fedorov, Yu.S. The applications of formo- and aceto-hydroxamic acids in nuclear fuel reprocessing. *J. Alloys Compd.* **271–273**, 534–537 (1998).

113. Bourg, S., Geist, A., Adnet, J.-M., Rhodes, C. & Hanson, B. C. Partitioning and transmutation strategy R&D for nuclear spent fuel: the SACSESS and GENIORS projects. *EPJ Nucl. Sci. Technol.* **6**, 35 (2020).

114. Paviet-Hartmann, P., Riddle, C., Campbell, K. & Mausolf, E. *Overview of Reductants Utilized in Nuclear Fuel Reprocessing/Recycling*. (American Nuclear Society - ANS, 2013).

115. Kahlert, H. Reference Electrodes. in *Electroanalytical Methods* (eds. Scholz, F. et al.) 291–308 (Springer Berlin Heidelberg, Berlin, Heidelberg, 2010). doi:10.1007/978-3-642-02915-8_15.

116. Botter, W., Scares, D. M. & Teschke, O. The influence of the Luggin capillary on the response time of a reference electrode. *J. Electroanal. Chem. Interfacial Electrochem.* **267**, 279–286 (1989).

117. Delgado, A. G., Parameswaran, P., Fajardo-Williams, D., Halden, R. U. & Krajmalnik-Brown, R. Role of bicarbonate as a pH buffer and electron sink in microbial dechlorination of chloroethenes. *Microb. Cell Factories* **11**, 128 (2012).

118. Thomas, J. G. N., Nurse, T. J. & Walker, R. Anodic passivation of iron in carbonate solutions. *Br. Corros. J.* **5**, 87–92 (1970).

119. Frankel, G. S. Electrochemical techniques in corrosion: Status, limitations, and needs. *J. Test. Eval.* **42**, 517–538 (2014).

120. Rammelt, U., Koehler, S. & Reinhard, G. Synergistic effect of benzoate and benzotriazole on passivation of mild steel. *Corros. Sci.* **50**, 1659–1663 (2008).

121. Obot, I. B. & Obi-Egbedi, N. O. Adsorption properties and inhibition of mild steel corrosion in sulphuric acid solution by ketoconazole: Experimental and theoretical investigation. *Corros. Sci.* **52**, 198–204 (2010).

122. *Electrochemical Impedance: Analysis and Interpretation*. (ASTM International, West Conshohocken, PA 19428-2959, 1993). doi:10.1520/STP1188-EB.

123. Lazanas, A. Ch. & Prodromidis, M. I. Electrochemical Impedance Spectroscopy─A tutorial. *ACS Meas. Sci. Au* **3**, 162–193 (2023).

124. Mansfeld, F. Electrochemical impedance spectroscopy (EIS) as a new tool for investigating methods of corrosion protection. *Electrochimica Acta* **35**, 1533–1544 (1990).

125. Jüttner, K. Electrochemical Impedance Spectroscopy (EIS) of corrosion processes on inhomogeneous surfaces. *Electrochimica Acta* **35**, 1501–1508 (1990).

126. Bagotsky, V. S. *Fundamentals of Electrochemistry*. (Wiley, 2005). doi:10.1002/047174199X.

127. Tan, Y. J., Bailey, S. & Kinsella, B. An investigation of the formation and destruction of corrosion inhibitor films using electrochemical impedance spectroscopy (EIS). *Corros. Sci.* **38**, 1545–1561 (1996).

128. Macdonald, D. D. Review of mechanistic analysis by electrochemical impedance spectroscopy. *Electrochimica Acta* **35**, 1509–1525 (1990).

129. Diard, J.P, Le Gorrec, B., & Montella, C. Handbook of Electrochemical Impedance Spectroscopy. Electrical Circuits Containing CPEs. (2020) doi:10.13140/RG.2.2.11979.62245.

130. Gamry Instruments. *Echem Analyst™ Software Operator's Guide*. https://www.gamry.com/assets/Uploads/Echem-Analyst-Manual-4-1-19.pdf (2019).

131. BioLogic Science Instruments. *EC-Lab® Software User's Manual*. 211 https://my.biologic.net/documents/ec-lab-software-manuals/ (2014).

132. ASTM Standard Practice for Conventions Applicable to Electrochemical Measurements in Corrosion Testing. (G01 Committee, ASTM International, West Conshohocken, PA: G3-14(2024)) doi:10.1520/G0003-14R19.

133. Burstein, G. T. A hundred years of Tafel's Equation: 1905–2005. *Corros. Sci.* **47**, 2858–2870 (2005).

134. Mansfeld, F. Tafel slopes and corrosion rates from polarization resistance measurements. *CORROSION* **29**, 397–402 (1973).

135. EUROPURE. Technisches Datenblatt Liquitech 227. (2017). www.europure.de

136. Powell, C. J. Practical guide for inelastic mean free paths, effective attenuation lengths, mean escape depths, and information depths in x-ray photoelectron spectroscopy. *J. Vac. Sci. Technol. Vac. Surf. Films* **38**, 023209 (2020).

137. Smekal, W., Werner, W. S. M. & Powell, C. J. Simulation of electron spectra for surface analysis (SESSA): a novel software tool for quantitative Auger-electron spectroscopy and X-ray photoelectron spectroscopy. *Surf. Interface Anal.* **37**, 1059–1067 (2005).

138. Schild, D. X-ray Photoelectron Spectroscopy. in *Hydrogen Technology* (ed. Léon, A.) 575–601 (Springer Berlin Heidelberg, Berlin, Heidelberg, 2008). doi:10.1007/978-3-540-69925-5_23.

139. Easley, A.D., Ma, T., Eneh, C.I., Yun, J., Thakur, R.M. & Lutkenhaus, J.L. A practical guide to quartz crystal microbalance with dissipation monitoring of thin polymer films. *J. Polym. Sci.* **60**, 1090–1107 (2022).

140. Sauerbrey, G. Verwendung von Schwingquarzen zur Wägung dünner Schichten und zur Mikrowägung. *Z. Für Phys.* **155**, 206–222 (1959).

141. Lack, F. R., Willard, G. W. & Fair, I. E. Some improvements in Quartz Crystal Circuit elements. *Bell Syst. Tech. J.* **13**, 453–463 (1934).

142. Azzam, R. M., Azzam, R. M. A. G., Bashara, N. M. & Bashara, N. M. *Ellipsometry and Polarized Light*. (North-Holland, Amsterdam, 1989).

143. Tompkins, H. G. & McGahan, W. A. *Spectroscopic Ellipsometry and Reflectometry: A User's Guide*. (Wiley, New York, 1999).

144. JEOL AccuTOF GCx Instrument at Organisch-Chemisches Institut, Universität Heidelberg. *JEOL AccuTOF GCx Instrument.*

https://www.uni-heidelberg.de/fakultaeten/chemgeo/oci/ms/equipment/ms-ocihd-accutof.html.

145. ASTM Standard Practice for Using the Fricke Dosimetry System. (E61 Committee, ASTM International, West Conshohocken, PA: 51026:2015, (2015)) doi:10.1520/E1026-23E01.

146. König, T., Dagan, R., Dardenne, K., Herm, M., Metz, V., Prüßmann, T., Rothe, J., Schild, D., Walschburger, A. & Geckeis, H. Chemical and spectroscopic investigations on the distribution and enrichment of radionuclides in fuel-cladding interfaces of irradiated high burn-up UOX and MOX fuels. (2022) doi:10.5445/IR/1000153314.

147. McEwen, M., Gamal, I. E., Mainegra-Hing, E. & Cojocaru, C. *Determination of the Radiation Chemical Yield (G) for the Fricke Chemical Dosimetry System in Photon and Electron Beams*. (2014) doi:10.4224/23002718.

148. Montelius, A. & Jung, B. ICRU Report 64. Dosimetry of High-Energy Photon Beams Based on Standards of Absorbed Dose to Water J. ICRU vol. 1, 1 (2001). *Acta Radiol.* **43**, 631–631 (2002).

149. Jayson, G. G., Parsons, B. J. & Swallow, A. J. The mechanism of the Fricke dosimeter. *Int. J. Radiat. Phys. Chem.* **7**, 363–370 (1975).

150. Salvat, F., Fernández-Varea, J. M. & Sempau, J. PENELOPE-2008: A Code System for Monte Carlo Simulation of Electron and Photon Transport. *Nucl. Energy Agency OECDNEA Rep. 6416, Issy-Moulineaux Fr.* (2009).

151. Sempau, J. Penelope/Peneasy user manual. *Dep. Phys. Tech. Univ. Catalonia* (2020).

152. Evans, J.C., Lepel, E.L., Sanders, R.W., Wilkerson, C.L., Silker, W., Thomas, C.W., Abel, K.H. & Robertson, D.R. *Long-Lived Activation Products in Reactor Materials*. (Pacific Northwest Laboratory, Richland, WA, 1984) doi:10.2172/6776358.

153. Browne, E. & Tuli, J. K. Nuclear Data Sheets for A = 60. *Nucl. Data Sheets* **114**, 1849–2022 (2013).

154. Loeb, A., Stanke, D. & Kemp, L. Decommissioning of the reactor pressure vessel and its peripheral facilities of the Nuclear Power Plant in Stade, Germany– in 37th Annual Radioactive Waste Management Symposium, WM 2011. (WM Symposia, Arizona, 2011).

155. Anunti, A., Larsson, H., Edelborg, M., Fuel, S. N. & Waste Management Co., S. (Sweden). Decommissioning study of Forsmark NPP. (2013).

156. Larsson, H., Anunti, A., Edelborg, M., Fuel, S. N. & Waste Management Co., S. (Sweden). Decommissioning Study of Oskarshamn NPP. (2013).

157. Rossini, S., Bertani, C., De Salve, M., Panella, B. & Pistelli, S. Radiological characterization of the reactor pressure vessel of Trino NPP for dismantling purposes. *Prog. Nucl. Energy* **107**, 17–30 (2018).

158. Kim, J. & Tseren, B. Occupational ALARA Planning for Reactor Pressure Vessel Dismantling at Kori Unit 1. *Int. J. Environ. Res. Public. Health **17**, 5346 (2020).*

159. Salvat, F. The PENELOPE code system. Specific features and recent improvements. *Ann. Nucl. Energy* **82**, 98-109. (2015).

160. Zhou, Y. *et al.* Corrosion control of mild steel in 0.1 M H2SO4 solution by benzimidazole and its derivatives: an experimental and theoretical study. *RSC Adv.* **7**, 23961–23969 (2017).

161. Obayes, H.R., Alwan, G.H., Alobaidy, A., Al-Amiery, A., Kadhum, A. & Mohamad, A. Quantum chemical assessment of benzimidazole derivatives as corrosion inhibitors. *Chem. Cent. J.* (2014) doi:10.1186/1752-153X-8-21.

162. Lowmunkhong, P., Ungthararak, D. & Sutthivaiyakit, P. Tryptamine as a corrosion inhibitor of mild steel in hydrochloric acid solution. *Corros. Sci.* **52**, 30–36 (2010).

163. Alahiane, M., Oukhrib, R., Albrimi, Y.A., Oualid, H.A., Bourzi, H., Akbour, R.A., Assabbane, A., Nahlé, A. & Hamdani, M. Experimental and theoretical investigations of benzoic acid derivatives as corrosion inhibitors for AISI 316 stainless steel in hydrochloric acid medium: DFT and Monte Carlo simulations on the Fe (110) surface. *RSC Adv.* **10**, 41137–41153 (2020).

164. Alahiane, M., Oukhrib, R., Berisha, A. & Alt Albrimi, Y. Electrochemical, thermodynamic and molecular dynamics studies of some benzoic acid derivatives on the corrosion inhibition of 316 stainless steel in HCl solutions. *J. Mol. Liq.* **328**, (2021).

165. Liu, C., Lin, G., Sun, Y., Lu, J., Fang, J., Yu, C., Chi, L. & Sun, K. Effect of octadecylamine concentration on adsorption on carbon steel surface. *Nucl. Eng. Technol.* **52**, 2394–2401 (2020).

166. Liao, Q.Q., Ge, H.-H. & Zhou, G.-D. Use of Octadecylamine for Shutdown Protection at Power Plants. *Mater. Perform.* **47**, 58–62 (2008).

167. Cao, S., Hu, J., Xie, J., Liang, Q. & Yin, L. Research on the film-forming characteristics of octadecylamine at high temperatures. *Anti-Corros. Methods Mater.* **60**, 14–19 (2013).

168. Baux, J., Caussé, N., Esvan, J., Delaunay, S., Tireau, J., Roy, M., You, D. & Pébère, N. Impedance analysis of film-forming amines for the corrosion protection of a carbon steel. *Electrochimica Acta* **283**, 699–707 (2018).

169. Bard, A. J. & Faulkner, L. R. *Electrochemical Methods: Fundamentals and Applications*. (John Wiley & Sons, Inc, New York, 2001).

170. Martinez, S. & Metikoš-Huković, M. A nonlinear kinetic model introduced for the corrosion inhibitive properties of some organic inhibitors. *J. Appl. Electrochem.* **33**, 1137–1142 (2003).

171. Huong, D. H., Duong, T. & Nam, P. C. Effect of the structure and temperature on corrosion inhibition of thiourea derivatives in 1.0 M HCl Solution. *ACS Omega* **4**, 14478–14489 (2019).

172. Laamari, M. R., Berrekhis, F., Benzakour, J. & Villemin, D. Adsorption and kinetic studies of piperidin-1-yl-phosphonic acid as a: Corrosion inhibitor of iron in sulphuric acid medium. *Journa Mater. Environ. Sci.* **3**, 485–496 (2012).

173. Gouy, M. Sur la constitution de la charge électrique à la surface d'un électrolyte. *J. Phys. Theor. Appl.* **9**, 457–468 (1910).

174. Chapman, D. L. A contribution to the theory of electrocapillarity. *Lond. Edinb. Dublin Philos. Mag. J. Sci.* **25**, 475–481 (1913).

175. Grahame, D. C. The electrical double layer and the theory of electrocapillarity. *Chem. Rev.* **41**, 441–501 (1947).

176. Stern, O. Zur Theorie der elektrolytischen Doppelschicht. *Z. Für Elektrochem. Angew. Phys. Chem.* **30**, 508–516 (1924).

177. Muralidharan, S., Phani, K. L. N., Pitchumani, S., Ravichandran, S. & Iyer, S. V. K. Polyamino-Benzoquinone Polymers: A new class of corrosion inhibitors for mild steel. *J. Electrochem. Soc.* **142**, 1478–1483 (1995).

178. Bentiss, F., Lagrenee, M., Traisnel, M. & Hornez, J. C. The corrosion inhibition of mild steel in acidic media by a new triazole derivative. *Corros. Sci.* **41**, 789–803 (1999).

179. El Miligy, A. A., Geana, D. & Lorenz, W. J. A theoretical treatment of the kinetics of iron dissolution and passivation. *Electrochim Acta* **20**, 273 (1975).

180. Sukhotin, A. M. & Kartashova, K. M. The passivity of iron in acid and alkaline solutions. *Corros. Sci.* **5**, 393–407 (1965).

181. Zhang, Y., Yin, X., Yan, Y., Wang, J. & Yan, F. Tribocorrosion behaviors of 304SS: effect of solution pH. *RSC Adv.* **5**, 17676–17682 (2015).

182. Li, X., Zhang, P., Huang, H., Hu, X., Zhou, Y. & Yan, F. An electrochemical study of pH influences on corrosion and passivation for a Q235 carbon steel in HNO_3 –$NaNO_2$, HAc–$NaNO_2$ and HCl–$NaNO_2$ solutions. *RSC Adv.* **9**, 39055–39063 (2019).

183. Zhang, B., Wang, J., Wu, B., Guo, X.W., Wang, Y.J., Chen, D., Zhang, Y.C., Du, K., Oguzie, E.E. & Ma, X.L. Unmasking chloride attack on the passive film of metals. *Nat. Commun.* **9**, 2559 (2018).

184. Wang, Z., Seyeux, A., Zanna, S., Maurice, V. & Marcus, P. Chloride-induced alterations of the passive film on 316L stainless steel and blocking effect of pre-passivation. *Electrochimica Acta* **329**, 135159 (2020).

185. Graat, P. C. J. & Somers, M. A. J. Simultaneous determination of composition and thickness of thin iron-oxide films from XPS Fe 2p spectra. *Appl. Surf. Sci.* **100–101**, 36–40 (1996).

186. Kip, N. & Van Veen, J. A. The dual role of microbes in corrosion. *ISME J.* **9**, 542–551 (2015).

187. Santhosh Kumar, A., Sivakumar, L., Rajadesingu, S., Sathish, S., Malik, T. & Parthipan, P. Sustainable corrosion inhibition approaches for the mitigation of microbiologically influenced corrosion -a systematic review. *Front. Mater.* **12**, 1545245 (2025).

188. Beech, I. B. & Gaylarde, C. C. Recent advances in the study of biocorrosion: an overview. *Rev. Microbiol.* **30**, 117–190 (1999).

189. Audi, A. A. & Sherwood, P. M. A. X-ray photoelectron spectroscopic studies of sulfates and bisulfates interpreted by Xα and band structure calculations. *Surf. Interface Anal.* **29**, 265–275 (2000).

190. Ota, H., Akai, T., Namita, H., Yamaguchi, S. & Nomura, M. XAFS and TOF–SIMS analysis of SEI layers on electrodes. *J. Power Sources* **119–121**, 567–571 (2003).

191. Pretsch, E., Bühlmann, P. & Badertscher, M. *Structure Determination of Organic Compounds: Tables of Spectral Data*. (Springer Berlin Heidelberg, Berlin, Heidelberg, 2009). doi:10.1007/978-3-540-93810-1.

192. Silverstein, R. M. & Bassler, G. C. Spectrometric identification of organic compounds. *J. Chem. Educ.* **39**, 546 (1962).

193. Claridge, T. D. W. *High-Resolution NMR Techniques in Organic Chemistry*. (Elsevier, Amsterdam London, 2016).

194. McLafferty, F. W. & Tureček, F. *Interpretation of Mass Spectra*. (University science books, Mill Valley, California, 1993).

195. Prince, E. L., McCabe, R. W. & Morton, L. H. G. The use of 1H Nuclear Magnetic Resonance Spectroscopy and Gas Liquid Chromatography/Mass Spectrometry to determine the effects of fungal biodeterioration on defined synthetic metal-working fluids. *Int. Biodeterior. Biodegrad.* **34**, 1–20 (1994).

196. Schalenbach, M., Durmus, Y. E., Tempel, H., Kungl, H. & Eichel, R. A. Double layer capacitances analysed with impedance spectroscopy and cyclic voltammetry: validity and

limits of the constant phase element parameterization. *Phys. Chem. Chem. Phys.* **23**, 21097–21105 (2021).

197. Tocharat, T., Tungasmita, D. N. & Tungasmita, S. Protection efficiency of triethanolamine decanedioate as a water-soluble corrosion inhibitor for steel in metalworking fluids. *Mater. Trans.* **66**, 310–317 (2025).

198. Li, C., Sun, Z., Kang, M., Yan, Z., Tan, Z., Li, Q., Wang, W., Tang, M., Li, G., Feng, Z. & Gao, Y. Study on the synergistic corrosion inhibition effect between sodium silicate and triethanolamine for 45 steel corrosion in 3.5% NaCl solution. *Int. J. Electrochem. Sci.* **16**, 211034 (2021).

199. Kim, K. T., Chang, H. Y., Lim, B. T., Park, H. B. & Kim, Y. S. Effect of ethanolamines on corrosion inhibition of ductile cast iron in nitrite containing solutions. *Corros. Sci. Technol.* **15**, 171–181 (2016).

200. Khamis, E., Bellucci, F., Latanision, R. M. & El-Ashry, E. S. H. Acid corrosion inhibition of nickel by 2-(Triphenosphoranylidene) succinic anhydride. *CORROSION* **47**, 677–686 (1991).

201. Walczak, M. S., Morales-Gil, P. & Lindsay, R. Determining Gibbs energies of adsorption from corrosion inhibition efficiencies: Is it a reliable approach? *Corros. Sci.* **155**, 182–185 (2019).

202. Zhu, J., Ma, B., Li, D., Zhang, Y. & Xu, L. Role of bicarbonate on CO_2 corrosion of carbon Steel. Preprint at https://doi.org/10.2139/ssrn.4658532 (2023).

203. Gilroy, D. & Mayne, J. E. O. The inhibition of the corrosion of iron in alkaline solutions. *Br. Corros. J.* **1**, 161–165 (1966).

204. Rangel, C. M., Fonseca, I. T. & Leitão, R. A. Some aspects of the electrochemical behaviour of mild steel in carbonate/bicarbonate solutions. *Electrochimica Acta* **31**, 1659–1662 (1986).

205. Li, W. S. & Luo, J. L. Uniformity of passive films formed on ferrite and martensite by different inorganic inhibitors. *Corros. Sci.* **44**, 1695–1712 (2002).

206. Nagayama, M. & Cohen, M. The Anodic Oxidation of Iron in a Neutral Solution. *J. Electrochem. Soc.* **109**, 781 (1962).

207. Bockris, J. O., Genshaw, M. A., Brusic, V. & Wroblowa, H. The mechanism of the passivation of iron in neutral solutions: An ellipsometric and coulometric investigation. *Electrochimica Acta* **16**, 1859–1894 (1971).

208. Nagayama, M. & Cohen, M. The Anodic Oxidation of Iron in a Neutral Solution. *J. Electrochem. Soc.* **110**, 670 (1963).

209. Sato, N., Kudo, K. & Noda, T. Single layer of the passive film on Fe. *Corros. Sci.* **10**, 785–794 (1970).

210. Marcus, P. & Grimal, J. M. The anodic dissolution and passivation of NiCrFe alloys studied by ESCA. *Corros. Sci.* **33**, 805–814 (1992).

211. Willenbruch, R. D., Clayton, C. R., Oversluizen, M., Kim, D. & Lu, Y. An XPS and electrochemical study of the influence of molybdenum and nitrogen on the passivity of austenitic stainless steel. *Corros. Sci.* **31**, 179–190 (1990).

212. Mohr, S. & Bechtold, T. Electrochemical behaviour of iron-complexes in presence of competitive ligands: A strategy for optimization of current density. *J. Appl. Electrochem.* **31**, 363–368 (2001).

213. Suzuki, Y. & Yokoi, H. Formation of soluble iron (III) complexes with triethanolamine and related compounds as studied by magnetic susceptibility measurements. *NIPPON KAGAKU KAISHI* 360–363 (1998) doi:10.1246/nikkashi.1998.360.

214. Verma, C., Thakur, A., Ganjoo, R., Sharma, S., Assad, H., Kumar, A., Quraishi, M.A. & Alfantazi, A. Coordination bonding and corrosion inhibition potential of nitrogen-rich heterocycles: Azoles and triazines as specific examples. *Coord. Chem. Rev.* **488**, 215177 (2023).

215. Hammud, H.H., Sheikh, N.S., Shawish, I., Bukhamsin, H.A., Al-Hudairi, D.E., Wee, A.L.X., Hamid, M.H.S.A., Maache, S.A., Al-Rasheed, H.H., Barakat, A., El-Faham, A. & Abd El-Lateef, H.M. Bis(dimethylpyrazolyl)-aniline- *s* -triazine derivatives as efficient corrosion inhibitors for C-steel and computational studies. *R. Soc. Open Sci.* **11**, 231229 (2024).

216. Tseng, Y.M. & Thompson, A. R. Densities and refractive indices of aqueous monoethanolamine, diethanolamine, triethanolamine. *J. Chem. Eng. Data* **9**, 264–267 (1964).

217. Dutta, A. K., Nayak, A. & Belfort, G. Viscoelastic properties of adsorbed and cross-linked polypeptide and protein layers at a solid–liquid interface. *J. Colloid Interface Sci.* **324**, 55–60 (2008).

218. Shang, W., He, C., Wen, Y., Wang, Y. & Zhang, Z. Performance evaluation of triethanolamine as corrosion inhibitor for magnesium alloy in 3.5 wt% NaCl solution. *RSC Adv.* **6**, 113967–113980 (2016).

219. Incorvio, M. J. & Contarini, S. X-ray photoelectron spectroscopic studies of metal/inhibitor systems: Structure and bonding at the iron/amine interface. *J. Electrochem. Soc.* **136**, 2493 (1989).

220. Wang, X., Xu, W. L., Liu, Z. Y. & Zhang, G. A. Unraveling the corrosion inhibition mechanism of triazine derivatives for carbon steel: Experimental and theoretical insights into interfacial adsorption. *Corros. Sci.* **220**, 111288 (2023).

221. Burns, W. G., Marsh, W. R. & Walters, W. S. The λ irradiation-enhanced corrosion of stainless and mild steels by water in the presence of air, argon and hydrogen. *Radiat. Phys. Chem. 1977* **21**, 259–279 (1983).

222. Hochanadel, C. J. Effects of Cobalt γ-radiation on water and aqueous solutions. *J. Phys. Chem.* **56**, 587–594 (1952).

223. Musa, A. Y. & Wren, J. C. Combined effect of gamma-radiation and pH on corrosion of Ni–Cr–Fe alloy inconel 600. *Corros. Sci.* **109**, 1–12 (2016).

224. Daub, K., Zhang, X., Noël, J. J. & Wren, J. C. Effects of γ-radiation versus H_2O_2 on carbon steel corrosion. *Electrochimica Acta* **55**, 2767–2776 (2010).

225. Fujita, N., Matsuura, C. & Saigo, K. Radiation-induced potential difference between electrodes with and without gamma rays. *Radiat. Phys. Chem.* **49**, 357–362 (1997).

226. Fujita, N., Matsuura, C. & Saigo, K. Evaluation of the potential difference induced between platinum electrodes with and without gamma-ray irradiation. *Radiat. Phys. Chem.* **50**, 457–463 (1997).

227. Marsh, G. P., Taylor, K. J., Bryan, G. & Worthington, S. E. The influence of radiation on the corrosion of stainless steel. *Corros. Sci.* **26**, 971–982 (1986).

228. Clark, W. E. The effect of gamma irradiation on the potential behavior of platinum and stainless steel electrodes. *J. Electrochem. Soc.* **105**, 483 (1958).

229. Schwarz, H. A. Chain decomposition of aqueous triethanolamine. *J. Phys. Chem.* **86**, 3431–3435 (1982).

230. Kass, S. R. π-Bond dissociation energies: C–C, C–N, and C–O. *J. Org. Chem.* **89**, 15158–15163 (2024).

231. Simić, M., Neta, P. & Hayon, E. Pulse radiolytic investigation of aliphatic amines in aqueous solution. *Int. J. Radiat. Phys. Chem.* **3**, 309–320 (1971).

232. Clay, P. G. & Rashid, M. The radiolysis of aqueous solutions of triethylamine and related amines. *Int. J. Radiat. Phys. Chem.* **3**, 367–376 (1971).

233. Taniguchi, H., Fukui, K., Ohnishi, S., Hatano, H., Hasegawa, H. & Maruyama, T. Free-radical intermediates in the reaction of the hydroxyl radical with amino acids. *J. Phys. Chem.* **72**, 1926–1931 (1968).

234. Fessenden, R. W. & Neta, P. Electron spin resonance study of radicals produced in irradiated aqueous solutions of amines and amino acids. *J. Phys. Chem.* **75**, 738–748 (1971).

235. Garrison, W. M., Jayko, M. E. & Bennett, W. Radiation-induced oxidation of protein in aqueous solution. *Radiat. Res.* **16**, 483 (1962).

236. Curtin, D. Y., Gourse, J. A., Richardson, W. H. & Rinehart, K. L. Use of nuclear magnetic resonance to distinguish between aliphatic, aldehyde and ketone derivatives. *J. Org. Chem.* **24**, 93–97 (1959).

237. Sugo, Y., Sasaki, Y. & Tachimori, S. Studies on hydrolysis and radiolysis of N,N,N′,N′-tetraoctyl-3-oxapentane-1,5-diamide. *Radiochim. Acta* **90**, 161–165 (2002).

238. Hayon, E., Ibata, T., Lichtin, N. N. & Simic, M. Sites of attack of hydroxyl radicals on amides in aqueous solution. *J. Am. Chem. Soc.* **92**, 3898–3903 (1970).

239. Hayon, E., Ibata, T., Lichtin, N. N. & Simic, M. Sites of attack of hydroxyl radicals on amides in aqueous solution. II. Effects of branching, alpha to carbonyl and to nitrogen. *J. Am. Chem. Soc.* **93**, 5388–5394 (1971).

240. Cataldo, F., Ursini, O. & Angelini, G. Study on the 1,3,5-triazine gamma-radiolysis. *J. Radioanal. Nucl. Chem.* **277**, 297–302 (2008).

241. Angelini, G., Bucci, R., Carnevaletti, F. & Colosimo, M. Radiolytic decomposition of aqueous atrazine. *Radiat. Phys. Chem.* **59**, 303–307 (2000).

242. Varghese, R., Mohan, H., Manoj, P., Manoj, V.M., Aravind, U.K., Vandana, K. & Aravindakumar, C.T. Reactions of hydrated electrons with triazine derivatives in aqueous medium. *J. Agric. Food Chem.* **54**, 8171–8176 (2006).

243. Yoshida, T. & Sawada, S. X-ray photoelectron spectroscopy of EDTA. *Bull. Chem. Soc. Jpn.* **47**, 50–53 (1974).

244. Kanematsu, M., Young, T.M., Fukushi, K., Sverjensky, D.A., Green, P.G. & Darby, J.L. Quantification of the effects of organic and carbonate buffers on arsenate and phosphate adsorption on a goethite-based granular porous adsorbent. *Environ. Sci. Technol.* **45**, 561–568 (2011).

APPENDICES

Appendix A

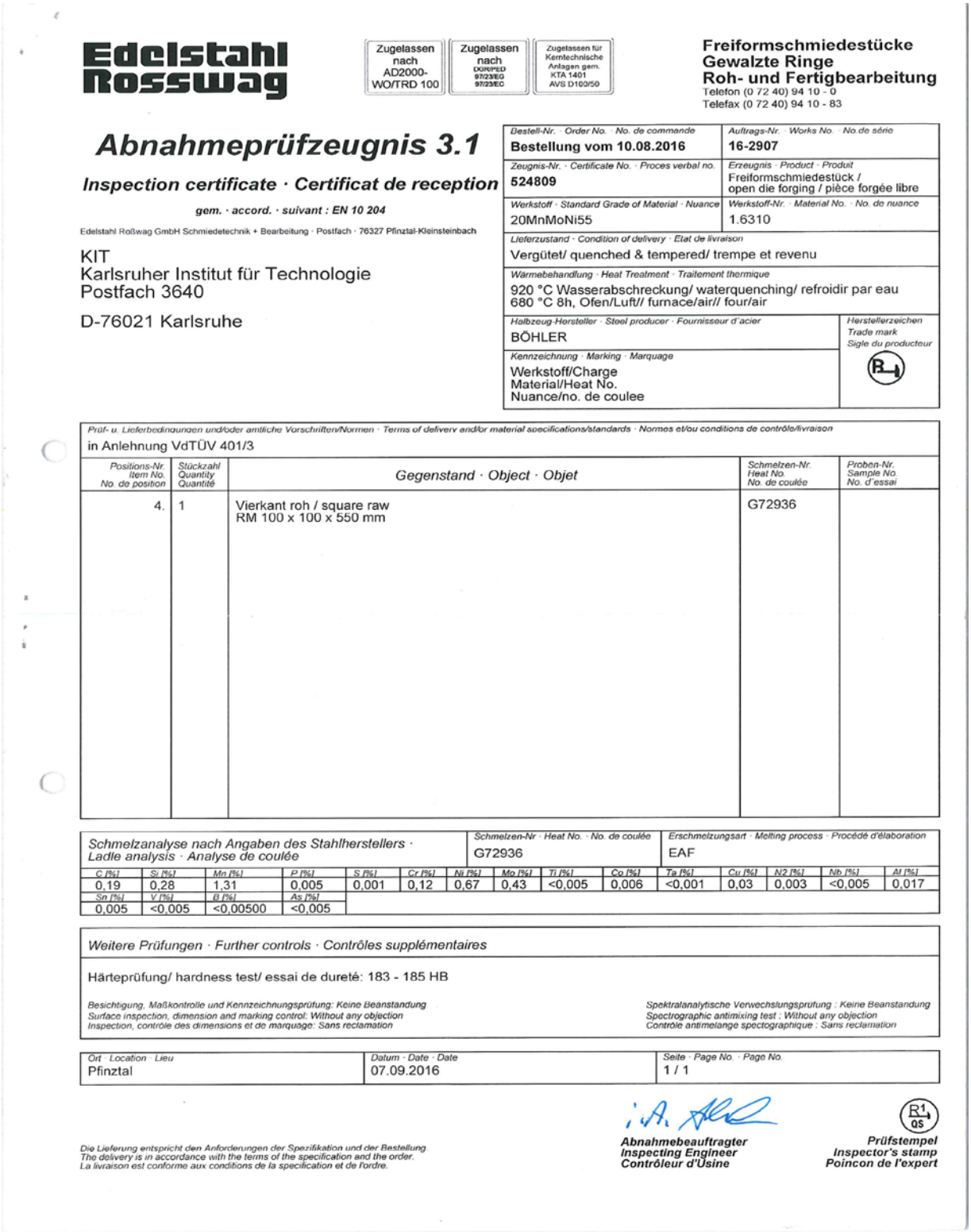

Edelstahl Rosswag

Zugelassen nach AD2000-WO/TRD 100 | Zugelassen nach DGRL/PED 97/23/EG 97/23/EC | Zugelassen für Kerntechnische Anlagen gem. KTA 1401 AVS D100/50

Freiformschmiedestücke
Gewalzte Ringe
Roh- und Fertigbearbeitung
Telefon (0 72 40) 94 10 - 0
Telefax (0 72 40) 94 10 - 83

Abnahmeprüfzeugnis 3.1

Inspection certificate · Certificat de reception

gem. · accord. · suivant : EN 10 204

Edelstahl Roßwag GmbH Schmiedetechnik + Bearbeitung · Postfach · 76327 Pfinztal-Kleinsteinbach

KIT
Karlsruher Institut für Technologie
Postfach 3640

D-76021 Karlsruhe

Bestell-Nr. · Order No. · No. de commande: **Bestellung vom 10.08.2016**	Auftrags-Nr. · Works No. · No.de série: **16-2907**
Zeugnis-Nr. · Certificate No. · Proces verbal no.: **524809**	Erzeugnis · Product · Produit: Freiformschmiedestück / open die forging / pièce forgée libre
Werkstoff · Standard Grade of Material · Nuance: 20MnMoNi55	Werkstoff-Nr. · Material No. · No. de nuance: 1.6310
Lieferzustand · Condition of delivery · Etat de livraison: Vergütet/ quenched & tempered/ trempe et revenu	
Wärmebehandlung · Heat Treatment · Traitement thermique: 920 °C Wasserabschreckung/ waterquenching/ refroidir par eau 680 °C 8h, Ofen/Luft// furnace/air// four/air	
Halbzeug-Hersteller · Steel producer · Fournisseur d'acier: BÖHLER	Herstellerzeichen · Trade mark · Sigle du producteur
Kennzeichnung · Marking · Marquage: Werkstoff/Charge Material/Heat No. Nuance/no. de coulee	

Prüf- u. Lieferbedingungen und/oder amtliche Vorschriften/Normen · Terms of delivery and/or material specifications/standards · Normes et/ou conditions de contrôle/livraison
in Anlehnung VdTÜV 401/3

Positions-Nr. Item No. No. de position	Stückzahl Quantity Quantité	Gegenstand · Object · Objet	Schmelzen-Nr. Heat No. No. de coulée	Proben-Nr. Sample No. No. d'essai
4.	1	Vierkant roh / square raw RM 100 x 100 x 550 mm	G72936	

Schmelzanalyse nach Angaben des Stahlherstellers · Ladle analysis · Analyse de coulée — Schmelzen-Nr · Heat No. · No. de coulée: G72936 — Erschmelzungsart · Melting process · Procédé d'élaboration: EAF

C [%]	Si [%]	Mn [%]	P [%]	S [%]	Cr [%]	Ni [%]	Mo [%]	Ti [%]	Co [%]	Ta [%]	Cu [%]	N2 [%]	Nb [%]	Al [%]
0,19	0,28	1,31	0,005	0,001	0,12	0,67	0,43	<0,005	0,006	<0,001	0,03	0,003	<0,005	0,017

Sn [%]	V [%]	B [%]	As [%]
0,005	<0,005	<0,00500	<0,005

Weitere Prüfungen · Further controls · Contrôles supplémentaires

Härteprüfung/ hardness test/ essai de dureté: 183 - 185 HB

Besichtigung, Maßkontrolle und Kennzeichnungsprüfung: Keine Beanstandung
Surface inspection, dimension and marking control: Without any objection
Inspection, contrôle des dimensions et de marquage: Sans reclamation

Spektralanalytische Verwechslungsprüfung : Keine Beanstandung
Spectrographic antimixing test : Without any objection
Contrôle antimelange spectographique : Sans reclamation

Ort · Location · Lieu	Datum · Date · Date	Seite · Page No. · Page No.
Pfinztal	07.09.2016	1 / 1

Die Lieferung entspricht den Anforderungen der Spezifikation und der Bestellung.
The delivery is in accordance with the terms of the specification and the order.
La livraison est conforme aux conditions de la specification et de l'ordre.

i.A.

Abnahmebeauftragter
Inspecting Engineer
Contrôleur d'Usine

Prüfstempel
Inspector's stamp
Poincon de l'expert

Figure A1: Inspection certificate for the determination of the chemical composition of 1.6310 Steel

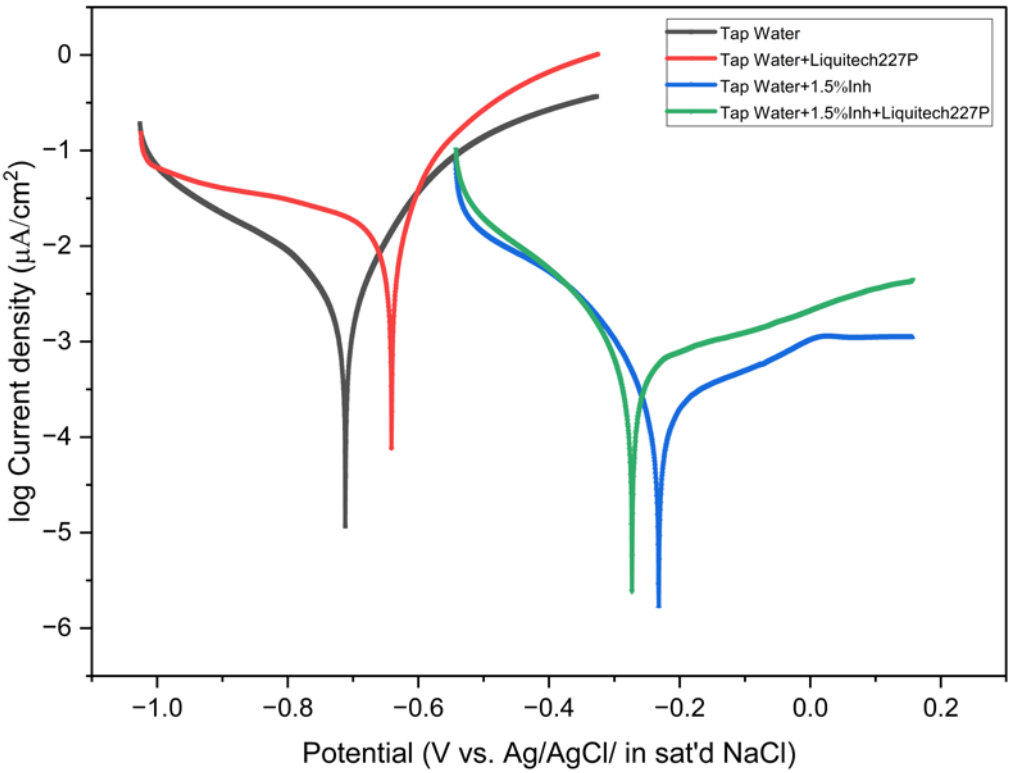

Figure A2: Potentiodynamic polarisation curves for Tapwater (pH 7.2) and Tapwater dosed with 1.5% inhibitor (pH 8.5), 60 ppm Liquitech 227P (pH 6.8), and a mixture of both (pH 7.1). Measurements were performed at room temperature.

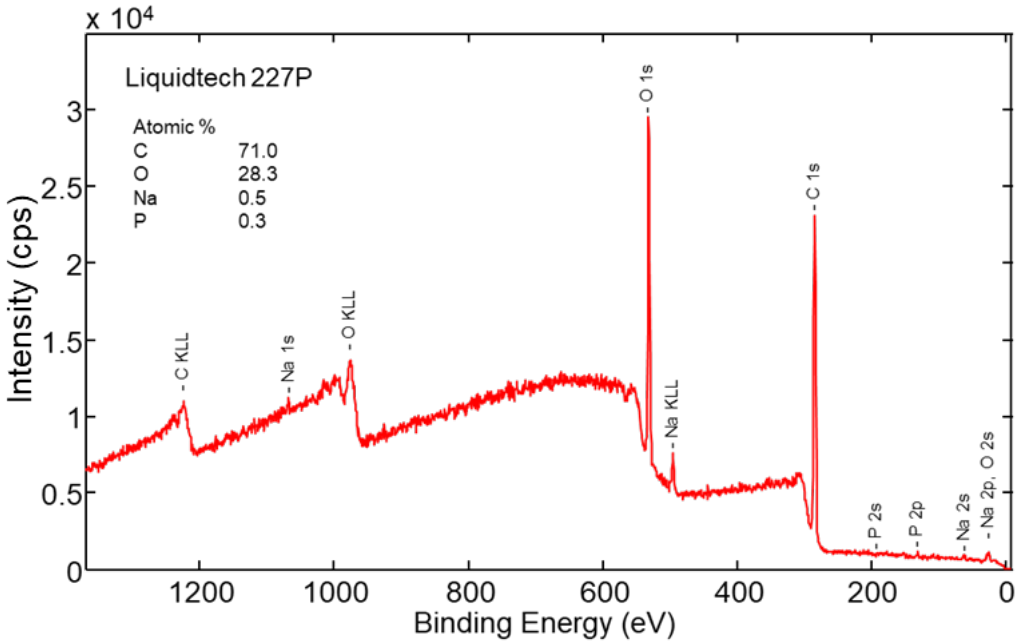

Figure A3: XPS survey of pure Liquitech 227P identified as a dimethyl phosphonate-based water treatment agent.

Appendix B

Table B1: TLD absorbed dose evaluation (activated stainless steel spring and autoclave, Figure 2.12)

Position	TLD No.	Absorbed dose (± 2% mGy)	Mean absorbed dose by position (mGy)
Bottom	S-1	806	
	S-2	868	
	S-3	591	7.5 ± 1.9 E+02
	S-4	516	
	S-5	985	
Cylindrical Surface	S-6	452	
	S-7	447	
	S-8	431	
	S-9	410	
	S-10	430	5.1 ± 0.9 E+02
	S-11	476	
	S-12	576	
	S-13	633	
	S-14	652	
	S-15	559	
Top	S-16	368	
	S-17	385	
	S-18	351	3.6 ± 0.2 E+02
	S-19	328	
	S-20	368	
	Mean	5.3± 1.8 E+02 mGy	**Mean dose rate: 132.9 ± 4.4 mGy/h**

Table B2: TLD absorbed dose evaluation (activated stainless steel spring and carousel setup)

Position	TLD No.	Absorbed dose (±2% mGy)	Mean absorbed dose by position (mGy)
Bottom	S-1	181	1.8 E+02 ± 0.5 E-01 (single TLD)
Cylindrical Surface	S-2	193	
	S-3	213	
	S-4	181	
	S-5	256	
	S-6	253	2.3 ± 0.3 E+02
	S-7	204	
	S-8	222	
	S-9	283	
	S-10	209	
Top	S-11	248	2.5E+02±0.4E+01 (single TLD)
	Mean	2.22± 0.3 E+02 mGy	**Mean Dose Rate: 55.4 ± 8.0 mGy/h**

Appendix C

Geometry input file for modeling SAM simulation (SAM.geo)

#Cylinderical drum of water representing WAS cutting suspension in a vessel

#Volume of drum 1m3

0000000000000000000000000000000000000000000000000000000000000000000000

SURFACE (1) water in cylindrical tank bottom

INDICES=(0, 0, 0, 1, 0)

Z-SHIFT=(0.000000000000000E+00, 0) (DEFAULT=0.0)

0000000000000000000000000000000000000000000000000000000000000000000000

SURFACE (2) water in cylindrical tank top

INDICES=(0, 0, 0, 1, 0)

Z-SHIFT=(+1.241700000000000E+02, 0) (DEFAULT=0.0)

0000000000000000000000000000000000000000000000000000000000000000000000

SURFACE (3) outer shape of water in the cylindrical vial

INDICES=(1, 1, 0, 0,-1)

X-SCALE=(+0.504600000000000E+02, 0) (DEFAULT=1.0)

Y-SCALE=(+0.504600000000000E+02, 0) (DEFAULT=1.0)

0000000000000000000000000000000000000000000000000000000000000000000000

BODY (1) Water

MATERIAL(1) Water

SURFACE (1), SIDE POINTER=(+1)

SURFACE (2), SIDE POINTER=(-1)

SURFACE (3), SIDE POINTER=(-1)

0000000000000000000000000000000000000000000000000000000000000000000000

SURFACE (4) outer shape of Steel/abrasive mixture in the drum

INDICES=(1, 1, 0, 0,-1)

X-SCALE=(+0.504600000000000E+02, 0) (DEFAULT=1.0)

Y-SCALE=(+0.504600000000000E+02, 0) (DEFAULT=1.0)

0000000000000000000000000000000000000000000000000000000000000000000000

SURFACE (5) top of Steel/abrasive mixture in the drum

INDICES=(0, 0, 0, 1, 0)

Z-SHIFT=(+3.104000000000000E+00, 0) (DEFAULT=0.0)

0000000000000000000000000000000000000000000000000000000000000000000000

BODY (2) Steel/abrasive mixture

MATERIAL(2) Steel/abrasive mixture (SAM)

SURFACE (1), SIDE POINTER=(+1)

SURFACE (4), SIDE POINTER=(-1)

SURFACE (5), SIDE POINTER=(-1)

BODY (1) Water

0000000000000000000000000000000000000000000000000000000000000000000000

END 0000000000000000000000000000000000000000000000000000000000000000

Sections of the PENELOPE input file for SAM simulation

```
[SECTION SOURCE BOX ISOTROPIC GAUSS SPECTRUM v.2014-12-21]
 ON                          STATUS (ON or OFF)
 Co-60.nuc                   PARTICLE TYPE (1=ELECTRON, 2=PHOTON, 3=POSITRON) OR RADIONUCLIDE FILENAME (e.g., Co-60.nuc)
  SUBSECTION FOR PHOTON POLARIZATION:
 0                           ACTIVATE PHOTON POLARIZATION PHYSICS (0=NO, 1=YES)
 0.0 0.0 0.0                  STOKES PARAMETERS (USED ONLY IF ACTIVATE POLARIZATION=1)
  SUBSECTION FOR PARTICLE POSITION:
 0.0  0.0  1.55               COORDINATES (cm) OF BOX CENTER
 50.46  50.46  3.10            BOX SIDES (cm)
 0.0  0.0                     FWHMs (cm) OF GAUSSIAN X,Y DISTRIBUTIONS
 0.0  0.0  0.0                EULER ANGLES [OMEGA,THETA,PHI](deg) FOR BOX ROTATION Rz(PHI).Ry(THETA).Rz(OMEGA).r
 0.0  0.0  0.0                TRANSLATION [DX,DY,DZ](cm) OF BOX CENTER POSITION
 2                           SOURCE MATERIAL (0=DON'T CARE, >0 FOR LOCAL SOURCE, <0 FOR IN-FIELD BEAM)
  SUBSECTION FOR PARTICLE DIRECTION:
 1.0  1.0  1.0                DIRECTION VECTOR; NO NEED TO NORMALIZE
 0.0  180.0                   DIRECTION POLAR ANGLE INTERVAL [THETA0,THETA1], BOTH VALUES IN [0,180]deg
 0.0  360.0                   DIRECTION AZIMUTHAL ANGLE INTERVAL PHI0 IN [0,360)deg AND DeltaPHI IN [0,360]deg
 1                           APPLY ALSO TO DIRECTION THE ROTATION USED FOR BOX POSITION (0=NO, 1=YES)
 [END OF BIGS SECTION]
[SECTION SOURCE PHASE SPACE FILE v.2009-06-15]
 OFF                          STATUS (ON or OFF)
 0                           PSF FORMAT (0=STANDARD penEasy ASCII, 1=IAEA BINARY)
 particles.psf                PSF FILENAME, REMOVE EXTENSION IF PSF FORMAT=1
 1                           SPLITTING FACTOR
 0.0  0.0  0.0                EULER ANGLES [Rz,Ry,Rz](deg) TO ROTATE POSITION AND DIRECTION
 0.0  0.0  0.0                TRANSLATION [DX,DY,DZ](cm) OF POSITION
 1                           VALIDATE BEFORE SIMULATION (1=YES, MAY TAKE A WHILE; 0=NO)
 0.000e0                      MAX PSF ENERGY (eV) (UNUSED IF VALIDATE=1 OR IAEA FORMAT. ADD 1023 keV FOR e+)
[END OF SPSF SECTION]
# >>>> PENGEOM+PENVOX >>>>>>>>>>>>>>>>>>>>>>>>>>>>>>>>>>>>>>>>>>>>>>>>>>>>
[SECTION PENGEOM+PENVOX v.2009-06-15]
 SAM.geo                      QUADRICS FILE NAME, USE '-' IF NONE
 -                           VOXELS FILE NAME, USE '-' IF NONE
 1                           TRANSPARENT QUADRIC MAT (USED ONLY IF QUAD&VOX)
 10                           GRANULARITY TO SCAN VOXELS (USED ONLY IF QUAD&VOX)
[END OF GEO SECTION]
[SECTION PENELOPE v.2019-08-06]
 MAT# FILE___(max 20 char) EABS(e-)  EABS(ph)  EABS(e+)  C1    C2    WCC     WCR     DSMAX   COMMENTS
  1   Water.mat            1.0e2     0.5e2     1.0e2     0.05  0.05  1.0e2   1.0e2   1.0     water in vessel
  2   SAM.mat              1.0e2     0.5e2     1.0e2     0.05  0.05  1.0e2   1.0e2   0.5     water in vessel
 -1 (SET MAT=-1 TO END THE LIST)
```